The University of Melbourne

School of Chemistry

Band Structure Engineering in II-VI Semiconductor Core/Shell Nanocrystals

Christian A. Potzner

Submitted in total fulfilment of the requirements
of the degree of Doctor of Philosophy

March 2011

Abstract

Semiconductor Quantum Dots (QDs) with their size dependent electronic and optical characteristics received immense attention over the last three decades due to the plethora of potential applications, and since they allow the observation and study of quantum confinement under ambient conditions. Coating these particles with another semiconductor material leads to the formation of a core/shell heterostructure which not only can significantly improve the chemical– and photo–stability but also enables band gap engineering in these systems. The ability to control the spatial probabilities of charge carriers within such systems opened up a variety of new optical properties previously not accessible with bare semiconductor nanocrystals.

In this thesis, core/shell structures with several material combinations are investigated with the aim to relate their optical properties to the confinement system imposed by the shell configuration. Utilising salt precursors and a layer–by–layer deposition technique termed SILAR, the experimental results demonstrate quantitative and highly uniform shell growth. It was found that the effect of lattice strain plays a vital role for the degree of epitaxy attainably in these materials, which significantly affects their uniformity and optical properties.

Studying the exciton confinement in classical Type–I CdSe/CdS and CdSe/ZnS heterostructures, the experimentally obtained results of different barrier potentials are in good agreement with theoretically predicted trends. Cryogenic optical measurements revealed an increase in confinement in CdSe/CdS structures as a function of shell growth at low temperature. For the first time, the evolution of the higher order transitions in CdSe/CdS core/shell heterostructures as a function of core size and shell thickness was quantitatively studied via low temperature photoluminescence excitation spectroscopy.

The ultimate success of applications based on the fluorescent properties of QDs requires high brightness and strong environmental robustness of these emitters. Since the luminescence efficiency of nanocrystal ensembles is directly related the number of non–radiative exciton recombination channels, present in the individual particles, reduction of these pathways is highly desirable. Following the argument that non–radiative recombination is intimately linked to the number of trap states available to the charge carriers, a graded seal core/shell/shell structure, based on a CdSe/CdS/ZnS system, was proposed with the aim to effectively confine the exciton in the core while minimising trap states. Investigating the effect of the CdS–to–ZnS shell thickness ratio, our results demonstrate the crucial effect of lattice strain in such particles. Strong blinking suppression was observed on the single nanocrystal level for the configuration

with a monolayer ratio of 1:4 between CdS and ZnS, demonstrating the viability of our structural considerations.

The capabilities of band gap engineering in core/shell heterostructures were further explored by investigation of a so–called Dual Quantum System (DQS) which is thought to host two potential regions for radiative exciton recombination. Thus, the corresponding photoluminescence spectrum should exhibit two emission peaks given that the recombination centres are sufficiently separated. Our results on theoretical calculations based on a core/barrier/shell model (CdSe/ZnS/CdSe) give insight into the principle structural requirements necessary to establish dual emission. Experimentally it was found that the successful preparation of such materials is highly challenging due to the specific structural and electronic requirements of a large barrier potential, a large core size and a thick barrier, which entail the corresponding adverse effects of lattice mismatch and low particle surface reactivity. Establishing dual emission, our optical studies show good agreement with the theoretically predicted trends and indicate de-coupled behaviour of the two recombination centres in these complex nanocrystal heterostructures.

Declaration

This is to certify that:

(i) The thesis comprises only original work undertaken by the author in the School of Chemistry, The University of Melbourne towards the PhD except where indicated,

(ii) Due acknowledgement has been made in the text to all other material used,

(iii) The thesis is less than 100,000 words in length, exclusive of table, diagrams, bibliographies, appendices and footnotes.

Christian Potzner

Acknowledgements

Looking back, the time spent on my PhD studies was certainly one of the most challenging, with multiple excitements and frustrations. Therefore, I would like to express my sincere gratitude to the following people for their continuous support and guidance towards the preparation of this thesis.

Firstly, I would like to thank my supervisor Paul for his constant support, enthusiasm and trust in my research. Having been given the freedom to direct my research on my own was challenging at times, but arguably more important allowed me to find and follow my own interests through the nano world.

To Joel van Embden and Daniel Gómez, for their excellent proof reading of this manuscript and their insightful comments, but more importantly for their continuous support and friendship throughout my studies.

To my colleagues from the 'blue lab' (past and present), for their friendship and the good times spent in and out of the lab. It was truly a pleasure and made the time at work so much more enjoyable. To keep this list short I will name only a few: Jack, Ann, Emma, Edin, Jo, Tich–Lam, Julia, Matthias and Anthony.

Also, to my family who always supported me on this journey, even though they had to see me moving to the 'other side of the world'.

Finally, to my beloved wife, Denisa, who undertook this adventure with me. Without her enduring support and faith in me I would not be where I am today. She comforted me through countless frustrations and managed always to put a smile on my face. For this, I thank her with all my heart.

Foreword

The contents of this thesis evolve around the synthesis of CdSe core based core/shell nanocrystal heterostructures and the investigation of their optical properties. Several combinations of shell material and thicknesses were analysed which greatly extend the degree of confinement control past the size tunable properties of bare quantum dots. The information presented in this manuscript is organised as follows:

In Chapter 1, the concepts of confinement and resulting size dependent properties of semiconductor nanocrystals are discussed. Furthermore the principles involved in the colloidal synthesis of such nanostructures are presented. A particular consideration is given to the role of ligands during synthesis and as passivating agents. The chapter concludes with discussion of fluorescence intermittency observable on the single particle level. The key aspects of blinking as well as the theoretical models to describe this phenomenon are presented.

In Chapter 2, the experimental methods and instruments employed throughout this thesis are described. Particular emphasis is given to the analytical methods of single particle fluorescence spectroscopy and electron microscopy.

In Chapter 3, we present studies on the effect of shell deposition in Type–I core/shell heterostructures. The synthetic conditions necessary to grow highly epitaxial semiconductor shells are discussed. The effect of lattice strain at the core/shell material interface is given particular emphasis. Optical studies on CdSe/CdS and CdSe/ZnS systems investigate the evolution of the band edge transition as a function of core size, shell material and temperature. Low temperature measurements were conducted to study the effect of shell thickness on the higher order transitions in CdSe/CdS nanocrystals.

In Chapter 4, the structural aspects to suppress fluorescence intermittency in colloidal semiconductor nanocrystals are discussed. The current literature and experimental advances towards non–blinking are reviewed. We present our results on the synthesis and optical properties of a graded seal CdSe/CdS/ZnS core/multi shell heterostructure as an alternative approach for blinking suppression. Analysing a parameter space of various shell thickness ratios between CdS and ZnS, we found the optimised structure to exhibit highly robust emission with strong blinking suppression on the single particle level. Studies on excitation power dependence reveal a highly single exponential fluorescence decay which is not affected by variations in laser intensity.

In Chapter 5, the concept of a Dual Quantum System and its synthesis are discussed. A detailed theoretical study in the framework of the effective mass approximation investigates

the relation between structural parameters and charge carrier localisation in order to establish the fundamental requirements for well–resolved dual emission. The aspects of the successful preparation of such a structure are presented with an emphasis on ligand chemistry and the challenges of surface reactivity and lattice mismatch. Analysing the optical properties of the Dual Quantum System, our results indicate de–coupled characteristics of the two exciton recombination centres.

Finally, this thesis is concluded summarising the key results of this work and an outlook toward future investigations.

Contents

Abstract iv

Declaration vii

Acknowledgements viii

Foreword x

List of Figures xvi

List of Tables xx

1 Introduction 1

1.1 Quantum Confinement in Semiconductor Nanocrystals 1

1.1.1 Band Structure 1

1.1.2 The Exciton 4

1.1.3 Infinite Potential Well Model 5

1.1.4 Finite Potential Well Model and Coulomb Interactions 8

1.1.5 Density of States 11

1.2 Principles of Colloidal Semiconductor Nanocrystal Synthesis 13

1.2.1 Colloidal Systems 13

1.2.2 Classical Nucleation Theory 14

1.2.3 Ensemble Dynamics 18

1.2.4 Growth Modes 19

1.2.5 Evolution of Quantum Dot Synthesis 25

1.2.6 Optical Effects of Capping Ligands 29

1.3 Blinking in Single Semiconductor Nanocrystals 33

1.3.1 Key Features of Fluorescence Intermittency 34

1.3.2 Theoretical Models of Blinking 38

1.4 Conclusion 43

Bibliography 43

2 Experimental Methods and Instrumentation 53
2.1 Chemicals and Solvents . . . 53
2.1.1 Solvents . . . 53
2.1.2 Chemicals for Nanocrystal Synthesis . . . 53
2.2 Nanocrystal Synthesis and Washing . . . 53
2.2.1 Reaction Setup . . . 53
2.2.2 CdSe Core Synthesis . . . 54
2.2.3 Post Preparative Washing and Storage of Nanocrystals . . . 57
2.3 Absorption and Photoluminescence Spectroscopy . . . 58
2.4 Cryogenic Photoluminescence Excitation Spectroscopy . . . 58
2.5 Extinction Coefficients and Particle Sizing . . . 59
2.6 Single Nanocrystal Spectroscopy . . . 60
2.6.1 Sample Preparation . . . 61
2.6.2 Confocal Setup . . . 62
2.6.3 Time–Correlated Single Photon Counting (TCSPC) . . . 64
2.6.4 Anti–Bunching — Evidence of Single Nanocrystal Probing . . . 66
2.6.5 Fluorescence Intermittency Analysis . . . 66
2.7 Electron Microscopy . . . 69
2.7.1 TEM Grid Preparation . . . 70
2.7.2 The FEI Tecnai F20 Electron Microscope . . . 71
2.7.3 Diffraction vs. Image Mode . . . 75
2.7.4 Scanning Mode (STEM) . . . 77
2.7.5 Atomic Number Contrast STEM (Z–STEM) . . . 78
2.7.6 Image Analysis . . . 82
Bibliography . . . 82

3 Synthesis and Optical Properties of II-VI Core/Shell Nanocrystal Heterostructures 87
3.1 Introduction . . . 87
3.2 Finite Potential Well Model for a Type-I Core/Shell Nanocrystal . . . 89
3.3 Preparation of Type-I Core/Shell Nanocrystals . . . 92
3.3.1 Experimental Details . . . 94
3.3.2 Monolayer Calculations . . . 95
3.3.3 Growth Temperature . . . 96
3.3.4 Ligand chemistry . . . 96
3.3.5 The Effects of Lattice Strain . . . 98
3.4 Electron Microscopy . . . 101

3.5 Electronic State Evolution . . . 103
3.5.1 Band Edge Transitions in CdSe/CdS and CdSe/ZnS Nanocrystals . . . 103
3.5.2 The Effect of Core Size . . . 106
3.5.3 The Effect of Temperature on the Band Edge Transition . . . 108
3.5.4 Higher Order Transitions in CdSe/CdS Nanocrystals . . . 110
3.6 Conclusion . . . 118
Bibliography . . . 118

4 Trap State Reduction in Core/Shell Semiconductor Nanocrystals 123
4.1 Introduction . . . 123
4.1.1 Elimination of Surface Traps . . . 123
4.1.2 Band Gap Engineering for Blinking Suppression . . . 125
4.2 Finite Potential Well Model for a Graded Type–I Core/Shell/Shell Nanocrystal 128
4.3 Preparation of Graded Seal CdSe/CdS/ZnS Core/Shell/Shell Nanocrystals . . 130
4.4 Electron Microscopy . . . 131
4.5 Optical Properties of graded Core/Shell/Shell Nanocrystals . . . 132
4.5.1 Absorbance and Emission . . . 132
4.5.2 Fluorescence Lifetime . . . 135
4.5.3 Environmental Robustness . . . 141
4.6 Single Particle Fluorescence Analysis . . . 142
4.7 Conclusion . . . 147
Bibliography . . . 148

5 Synthesis and Optical properties of a CdSe/ZnS/CdSe Dual Quantum System 153
5.1 Introduction . . . 153
5.2 Finite Potential Well Model for a Dual Quantum System . . . 154
5.3 Analysis of the Electronic Structure in a DQS . . . 155
5.3.1 The Effect of Barrier Width . . . 156
5.3.2 The Effect of Core Size and Well Thickness . . . 157
5.3.3 Conclusion . . . 161
5.4 Preparation of DQS core/shell Nanocrystals . . . 162
5.4.1 Experimental Details . . . 163
5.4.2 Amine Concentration . . . 165
5.4.3 Homogeneous Nucleation . . . 165
5.4.4 The Selenium Precursor . . . 166
5.4.5 The Effect of Metal Complexing Ligand . . . 166

5.5 Optical and Structural Characterisation 170
5.5.1 Electron Microscopy 170
5.5.2 Absorbance and Fluorescence Studies 172
5.5.3 Effects of Core Size and Barrier 176
5.5.4 Effects of Post–Synthetic Treatment 178
5.6 Conclusion 179
Bibliography 180

6 Concluding Remarks **185**

A Shell Growth Spreadsheet **187**

B Excitation Dependence of Single Particle Photoluminescence **189**

List of Figures

1.1 Nanocrystal Model . . . 2
1.2 Bandgap . . . 4
1.3 Excitation of ground state . . . 5
1.4 Infinite Spherical Potential . . . 9
1.5 Comparison of wavefunctions and radial probabilities for finite and infinite potentials . . . 10
1.6 Potential Comparison . . . 11
1.7 Density of States Scheme . . . 12
1.8 Surface Atoms Percentage . . . 14
1.9 LaMer Profile for Crystal Growth . . . 15
1.10 Free Energy Plot . . . 17
1.11 Ostwald ripening scheme . . . 20
1.12 Diffusion Sphere . . . 21
1.13 Diffusion and Reaction Limited Growth . . . 23
1.14 Temporal PSD evolution . . . 24
1.15 Ligand Binding Scheme . . . 25
1.16 Common ligands for colloidal NC synthesis . . . 27
1.17 Shape Control . . . 27
1.18 Robotic Nanomaterials Workstation . . . 28
1.19 Trap Emission arising from surface states . . . 29
1.20 Electronic Band gap structure of Ligand Passivation . . . 30
1.21 Ligand Surface Passivation Model . . . 32
1.22 Homogeneous and inhomogeneous broadening . . . 34
1.23 Blinking Trace with Corresponding On–time and Off–time Histograms . . . 35
1.24 Charging Model . . . 39
1.25 Surface Trap Model . . . 41

2.1 Reaction Setup for Nanocrystal Synthesis . . . 54
2.2 Temperature profile and absorbance spectra for CdSe core growth . . . 55
2.3 Size–tunable CdSe Nanocrystals . . . 56
2.4 Nanocrystal Washing . . . 57
2.5 Extinction Coefficient and Particle Sizing of CdSe Nanocrystals . . . 60

2.6 Nanocrystal Confocal Scan Image . . . 62
2.7 Single Particle Spectroscopy Setup . . . 63
2.8 TCSPC Histogram . . . 65
2.9 TCSPC schematic . . . 65
2.10 Antibunching Plot . . . 67
2.11 Bayesian Changepoint Detection . . . 68
2.12 TEM signals . . . 70
2.13 TEM Sample Contamination . . . 71
2.14 Schematic of electron lens . . . 73
2.15 Selected Area diffraction Pattern . . . 75
2.16 TEM Imaging and diffraction mode . . . 76
2.17 TEM condenser system . . . 77
2.18 Schematic diagram of detectors in a STEM . . . 79
2.19 Particle Size–distribution Analysis . . . 83

3.1 Core/Shell Model and Band Gap Scheme . . . 88
3.2 Scheme of Type–I core/shell model for finite potential well calculations . . . 89
3.3 Calculated Radial Probabilities for CdSe, CdSe/CdS and CdSe/ZnS . . . 91
3.4 Schematic of the SILAR protocol for core/shell Nanocrystals . . . 93
3.5 Wurtzite Crystal Faces . . . 95
3.6 Lattice Strain . . . 98
3.7 Temperature Profile of SILAR growth using Thermal Cycling . . . 99
3.8 Strain Effect . . . 100
3.9 TEM Analysis . . . 102
3.10 Absorbance and Emission Shifts — CdS vs. ZnS Shell . . . 104
3.11 Absorbance Evolution . . . 107
3.12 Absorbance Shift with first CdS layer deposition . . . 108
3.13 Normalised PL Spectra of CdSe/CdS at Room Temperature and 80 K . . . 109
3.14 Temperature Effect on CdSe/CdS Confinement . . . 111
3.15 PLE Spectra of CdSe Nanocrystals . . . 112
3.16 PLE Analysis . . . 113
3.17 PLE Scans Overview . . . 115
3.18 Higher Order Transition Evolution . . . 117

4.1 Scheme of Trap States in Nanocrystals . . . 124
4.2 Scheme of a Core/Shell Heterostructures for Blinking Suppression . . . 125
4.3 Scheme of a Graded Core/Shell/Shell Heterostructure . . . 127

4.4 CdS:ZnS Monolayer Ratios for Core/Shell/Shell Heterostructures 128
4.5 Radial Distribution Probabilities of CdSe/CdS/ZnS Nanocrystals 129
4.6 TEM Analysis of CdSe/CdS/ZnS core/multishell NCs 131
4.7 HAADF STEM images of CdSe/CdS/ZnS core/multishell NCs 132
4.8 Absorbance Analysis of CdSe/CdS/ZnS core/shell Growth 133
4.9 Photoluminescence Analysis of CdSe/CdS/ZnS core/shell Samples 134
4.10 Lifetime Analysis utilising a Stretched Exponential Fit 136
4.11 Lifetime Comparison of the Final CdSe/CdS/ZnS core/shell Samples 137
4.12 Lifetime Analysis of CdSe/CdS/ZnS core/shell Samples 139
4.13 Absorbance Comparison of the Final CdSe/CdS/ZnS core/shell Samples . . . 140
4.14 Lifetime Analysis of CdSe/CdS/ZnS core/shell Samples 141
4.15 Single Particle Spectroscopy of CdSe/CdS/ZnS core/shell Samples 143
4.16 Single Particle Spectroscopy of CdSe/CdS/ZnS core/shell Samples 144
4.17 Single Particle Spectroscopy of CdSe/CdS/ZnS core/shell Samples 145
4.18 Calculated Number of Absorbed Photons 146

5.1 Scheme of DQS bandstructure, 3D illustration and Photoluminescence spectra 154
5.2 Scheme of DQS model for finite potential well calculations 155
5.3 Effect of Barrier 157
5.4 Effect of Well Thickness (1S Exciton) 158
5.5 Dual Emission and Corresponding Wavefunction Probabilities 158
5.6 Effect of Well Thickness (2S Exciton) 160
5.7 Effect of Well Thickness for Small Core System 161
5.8 Absorption spectra of large CdSe cores 163
5.9 Reaction Scheme of Amide Formation 165
5.10 Homogeneous Nucleation 166
5.11 Photoluminescence Evolution - OA vs. TMPPA 167
5.12 TEM Analysis of ZnS Barrier- OA vs. TMPPA 168
5.13 PL Lifetime of CdSe/ZnS NCs grown with OA and TMPPA precursors 169
5.14 Emission Spectra of OA and TMPPA samples after CdSe Well Growth 170
5.15 TEM Analysis of the DQS 171
5.16 Optical Analysis of the DQS 173
5.17 DQS PLE and Lifetime Analysis 175
5.18 Effect of Core Size on PL Spectrum 176
5.19 Effect of Barrier Type on PL Spectrum and Fluorescence Lifetime 177
5.20 Well Emission Sensitivity 178

A.1 Excel Spreadsheet for SILAR Shell Growth 188

B.1 Single Particle Spectroscopy of CdSe/CdS/ZnS core/shell Samples 190
B.2 Single Particle Spectroscopy of CdSe/CdS/ZnS core/shell Samples 191
B.3 Single Particle Spectroscopy of CdSe/CdS/ZnS core/shell Samples 192
B.4 Single Particle Spectroscopy of CdSe/CdS/ZnS core/shell Samples 193

List of Tables

1.1 Electronic Parameters of II-IV bulk semiconductors 5

2.1 Synthetic Parameters for CdSe Nanocrystal Synthesis 55

3.1 Electronic Parameters of II-IV bulk semiconductors for Core/Shell Model . . 90
3.2 Structural Parameters for SILAR Shelling Calculations 95
3.3 Reaction Temperatures for SILAR shell growth - CdSe/CdS 97
3.4 Reaction Temperatures for SILAR shell growth - CdSe/ZnS 97
3.5 Core/Shell Volume Ratio 106

5.1 Electronic Parameters of II-IV bulk semiconductors for DQS Model 155
5.2 Reaction Temperatures for DQS barrier growth 164

1 Introduction

Semiconductor nanocrystals, also known as Quantum Dots (QD), are crystalline systems on the nanometer (10^{-9} m) scale (see Figure 1.1). As they cover the transition from the bulk to the atomic regime, they are the perfect model system to observe and study size–dependent physical properties that are governed by charge carrier motion. Once a crystal reaches this size regime, the free motion of charge carriers is strongly disturbed and due to boundary conditions becomes quantised [1]. It is those size–tunable quantum effects which make nanostructures most attractive and fuelled a field of intense research for the last three decades.

Today the most common route to produce high quality Quantum Dots with narrow size–distributions is via colloid chemistry. Since the seminal work of Murray, Norris and Bawendi in 1993 [2] a pursuit towards improved size–control [3], shape–control [4], heterostructures [5, 6] and "greener" synthetic routes [7–9] became and still remains an intense field of research.

The following chapter provides the reader with a basic understanding of quantum size effects in semiconductor nanocrystals. Furthermore it addresses the key synthetic concepts and recent advances to produce high quality colloidal QDs. Special attention will be given to the importance of ligands, which play a crucial role during particle growth as well as stabilisation and surface passivation. Finally the phenomenon of fluorescence intermittency (blinking) in single QDs and the theories attempting to describe this effect will be introduced.

1.1 Quantum Confinement in Semiconductor Nanocrystals

This section outlines the key concepts to describe the electronic structure in a crystalline solid and its influence on an exciton. Furthermore, the effects of quantum confinement in these crystals are addressed starting from a classical potential well model.

1.1.1 Band Structure

The electrons of a single free-standing atom occupy orbitals, which form a discrete set of energy levels. If several atoms are brought together into a molecule, these atomic orbitals split and produce a number of molecular orbitals equal to the number of atoms. When a large number of atoms (of order 10^{20} or more) are brought together to form a solid, the number of orbitals becomes exceedingly large, and the difference in energy levels becomes very small. Thus, they transform form discrete levels to continuous bands of energy. However, some

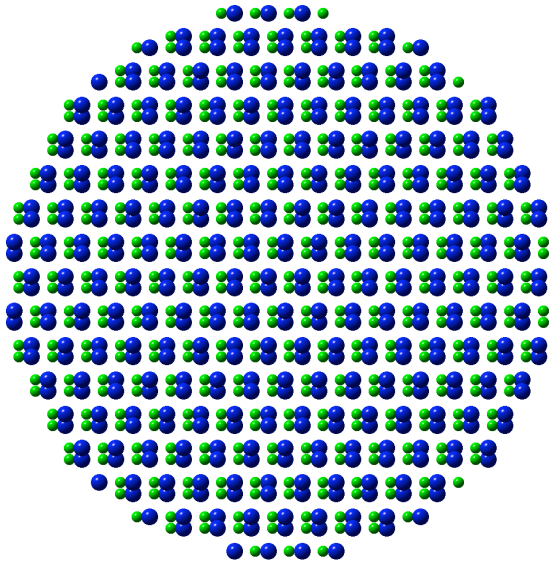

Figure 1.1 Planar view along the [111] axis of a spherical CdSe Nanocrystal model with a 3 nm diameter.

intervals of energy contain no orbitals, no matter how many atoms are bonded, forming band gaps. Since nanoscale crystals are intermediate between molecules and a solid, it is possible to study the transition from discrete energy levels to continuous bands in this size regime.

In order to interpret the electronic and optical properties of a given material within this nanoscale regime, it is important to understand its energy level structure. In the case of a bulk crystalline solid, the concept of band structures is very useful to explain the correlation between energy levels and the periodicity of the crystal lattice. Generally speaking, the band structure describes ranges of quantised energy that an electron (or hole) is 'allowed' or 'forbidden' to occupy. To derive the energy values E of such a system one can start with the non–relativistic time–independent Schrödinger equation

$$E\psi(r) = \left(-\frac{\hbar^2}{2m}\nabla^2 + V(r)\right)\psi(r) \quad , \tag{1.1}$$

where ∇^2 is the Laplacian operator, $V(r)$ is the potential energy term and $\psi(r)$ is the wave function. Due to the periodic nature of the lattice, several simplifications can be made, which lead to Bloch waves as solutions (eigenfunctions) for the energy levels (eigenvalues), given by:

$$\psi_{nk}(r) = e^{ik\cdot r}u_{nk}(r) \quad , \tag{1.2}$$

where k is the wavevector, which is related to the direction of motion of the electron in the crystal, and n being the band index, which numbers the energy bands. A Bloch wave

consists of a plane wave envelope function modulated by a periodic Bloch function ($u_{nk}(r)$) which accounts for the periodic potential of the crystal lattice. Due to the Born–von Karman boundary conditions for periodic systems, which state that

$$\psi(r + N_i a_i) = \psi(r) \qquad i = 1, 2, 3, ... \quad , \tag{1.3}$$

where a is the primitive lattice vector and N is any integer, k (and therefore the energy eigenvalues) can only assume certain (quantised) values given by

$$k = \frac{2\pi n}{Na} \qquad n = 1, 2, 3, ...N \quad . \tag{1.4}$$

A simple way to treat the influence of the lattice potentials in the band structure is provided by the effective mass approximation (EMA). A particle's effective mass m^* is the relative mass it appears to possess while translating in the crystal field. It can be shown that, under most conditions, electrons and holes in a crystal respond to electric and magnetic fields almost as if they were free particles in a vacuum, but with a different mass. As this free particle is considered to have no interactions with other electrons, it can be described by the following Hamiltonian:

$$\hat{H} = \left(-\frac{\hbar^2}{2m}\nabla^2 + V(r) \right) = -\frac{\hbar^2}{2m^*}\nabla^2 \quad , \tag{1.5}$$

where $V(r)$ represents the average potential the surrounding exerts on the electron (hole) and is accounted for within the effective mass m^*. Using the material dependent effective mass for electrons and holes the influence of the lattice potential may be considered through changes in momentum:

$$E = \frac{p^2}{2m^*} = \frac{\hbar^2 k^2}{2m^*} \quad . \tag{1.6}$$

It is important to note that in a real crystal, the situation is far more complex. Due to the periodic potentials, diffraction of the electron (or hole) waves occurs in the lattice and as such the dispersion relation is not even approximately quadratic, on a large K–scale. However, this study focuses on optical properties, which are mainly determined by the energy levels around the Fermi level (band gap). At the extrema of the valence and conduction bands, a parabolic band profile is valid (see Figure 1.2). Hence, for charge carriers with energies close to an extremum, EMA is a useful concept. There are several theories which attempt to predict the complete band structure in crystals, but will not be discussed here. Amongst the most common are the Nearly–free electron approximation and the Tight–Binding Model [10].

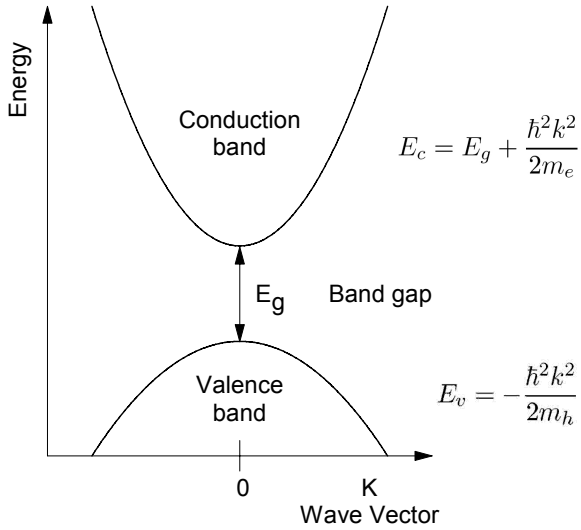

Figure 1.2 Single particle energy states as a function of the wavevector k in a direct band gap semiconductor.

1.1.2 The Exciton

An exciton is a bound state consisting of an electron and a hole. A vivid picture of exciton formation is as follows: A photon enters a semiconductor, exciting an electron from the valence band into a given level in the conduction band, and as consequence an empty level (a hole) is created in the valence band (Figure 1.3). Due to their mutual Coulomb attraction, the electron and hole form a bound state having slightly less energy than the unbound electron and hole. This bound state is termed an exciton. For semiconductors whose band gap is within the range of 1.4 up to 2.5 eV, excitons are typically induced by the interaction of the crystal with visible light (absorption of a photon) and consequently, the details concerning the electronic structure of the semiconductor crystal determine its optical response.

Excitons can be divided into two classes depending on their environment. In highly ionic structures, like alkali halide crystals, the specific dielectric constant ϵ is generally small which leads to strong Coulomb interactions between electron and hole. Therefore, the exciton tends to be small (size of unit cell) and strongly localised (Frenkel exciton). In semiconductors on the other hand, ϵ tends to be large, and as a result, the Coulomb interactions are effectively diminished via screening ($\sim$0.1 eV). Consequently the separation between electron and hole, known as the effective Bohr radius a_B, is considerably larger than the crystal lattice constant (Mott–Wannier exciton). The Bohr radius is described as follows:

$$a_B = \frac{4\pi\epsilon\hbar^2}{m^* e^2} \quad . \tag{1.7}$$

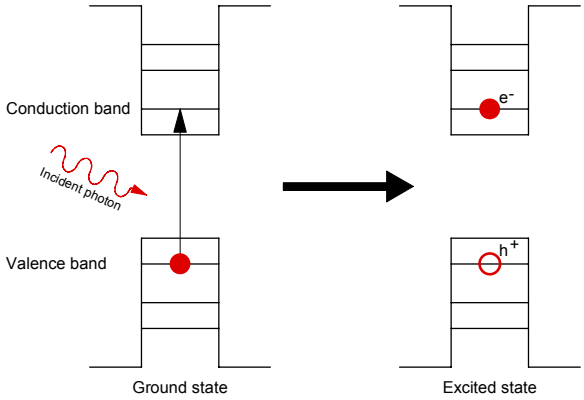

Figure 1.3 Exciton formation upon absorption of an incident photon. An electron (e^-) is excited from the valence band to a given level in the conduction band creating a hole (h^+) in the valence band.

	Band gap E_g $[eV]$	Electron effective mass m_e^*	Hole effective mass m_h^*	Exciton effective mass m_r^*	specific dielectric constant ϵ	Bohr radius a_B $[nm]$
CdSe	1.74	0.12	0.45	0.09	10.16	5.7
CdS	2.45	0.18	0.60	0.14	9.28	3.6
ZnS	3.62	0.20	0.80	0.16	8.30	2.8

Table 1.1 Electronic parameters of II-IV bulk semiconductors used in this thesis (Source: Landolt–Börnstein - Group IV Physical Chemistry (Springer); Volume 19, Subvolume B2, 2004).

Within the effective mass approximation, an exciton can be described analogously to a modified hydrogen atom:

$$\hat{H} = -\frac{\hbar^2}{2m_h^*}\nabla_h^2 - \frac{\hbar^2}{2m_e^*}\nabla_e^2 - \frac{e^2}{\epsilon \mid r_e - r_h \mid} \tag{1.8}$$

However, the binding energy is much smaller and the size much bigger than a hydrogen atom due to the effects of screening. Furthermore, the effective mass of the carriers is often a small fraction of the free electron mass. Table 1.1 shows the electronic parameters for the wurtzite II–VI semiconductors studied in this work.

1.1.3 Infinite Potential Well Model

Once a crystal approaches a size comparable to or less than a_B, an exciton will experience the presence of the structure's physical boundaries. This is the onset of quantum confinement and the electronic and optical properties of the crystal change considerably in this regime.

As a first approximation to describe quantum confinement, one can consider a particle in an *infinite* cubic potential well with a given lengths L_x, L_y and L_z. In this framework a potential $V(x, y, z)$ is regarded to be zero inside the box and infinite elsewhere, similar to the quantum mechanical description of translational motion. The Hamiltonian for such a system can therefore be written as:

$$\hat{H} = -\frac{\hbar^2}{2m}\nabla^2 + V(x, y, z) \quad . \tag{1.9}$$

Upon assigning a potential of zero inside the box and the assumption that the 3D wavefunction can be expressed as a product of three independent one–dimensional functions, the problem is reduced to solving a set of 1D Schrödinger equations:

$$E\psi(x) = -\frac{\hbar^2}{2m}\frac{\partial^2\psi(x)}{\partial x^2} \quad , \tag{1.10}$$

with the general solution of

$$\psi = A\sin kx + B\cos kx \quad . \tag{1.11}$$

As V is zero inside the well and infinite everywhere else, it follows that the wavefunction has to be zero at the boundaries as well, giving

$$\psi(0) = \psi(L) = 0 \quad . \tag{1.12}$$

Substituting 1.11 into 1.10 and evaluating for $x = 0$, we find that $B = 0$, which leads to a wave function of the form

$$\psi(x) = A\sin kx \quad , \tag{1.13}$$

and at $x = L$

$$\psi(L) = A\sin kL = 0 \quad . \tag{1.14}$$

Nodal solutions for equation 1.14 are

$$k = \frac{n\pi}{L} \tag{1.15}$$

with n being any *positive* integer. Normalization of the wavefunction provides the value for A. As the particle must be somewhere in the Box, the integral over the probability $|\psi(x)|^2$ over

all positions x must be equal to 1:

$$1 = \int_{-\infty}^{\infty} |\psi(x)|^2 dx = |A|^2 \int_0^L \sin^2(kx) dx = |A|^2 \frac{L}{2} \quad ,$$

or

$$|A| = \sqrt{\frac{2}{L}} \quad . \tag{1.16}$$

Substituting the results of equations 1.15 and 1.16 into equation 1.13 provides a set of independent, one–dimensional eigenfunctions

$$\psi_n(m) = \sqrt{\frac{2}{L}} \sin \frac{n\pi m}{L_m} \qquad m = x, y, z \quad . \tag{1.17}$$

For the three dimensional case:

$$\psi_n(x, y, z) = \sqrt{\frac{8}{L_x L_y L_z}} \sin \frac{n_x \pi x}{L_x} \sin \frac{n_y \pi y}{L_y} \sin \frac{n_z \pi z}{L_z} \quad . \tag{1.18}$$

As the particle in this model is regarded as *free*, equation 1.6 holds and its energies are quantised such that

$$E = \frac{\hbar^2}{2m} \left\{ \left(\frac{n_x \pi}{L_x} \right)^2 + \left(\frac{n_y \pi}{L_y} \right)^2 + \left(\frac{n_z \pi}{L_z} \right)^2 \right\} \qquad n = 1, 2, .. \tag{1.19}$$

Equation 1.19 shows that the energy difference ΔE between two given principal states (different quantum numbers n) decrease with increasing box size. Hence as soon as ΔE decreases below $k_B T$ the thermal energy provides the difference between the discrete energy levels and the levels are considered to form a band. The motion of a particle is therefore no longer quantised. This thermal–energy dependence of quantum effects is often a motivation for low–temperature experiments. This relationship of ΔE to box (crystal) size can be experimentally observed as a condensation of the absorption peaks of nanocrystals with increasing diameter.

Comparing the solution for k in equation 1.15 with 1.4, one can see that the allowed values for k double. This is due to the different applied boundary conditions. In the previous case where the potential V was regarded to be zero inside the box and infinite elsewhere, n was strictly positive. As the Born–von Karman boundary conditions apply for a particle in a periodic potential, n can also become negative or zero (the ground state).

Since quantum dots are generally spherical particles, a first improvement to the approximation would be to assume a spherical infinite potential well instead of a cubic one. This can be

done by employing the Hamiltonian operator in spherical polar coordinates, which is given by:

$$\hat{H} = -\frac{\hbar^2}{2m}\nabla^2 + V(r,\theta,\phi) \quad . \tag{1.20}$$

The respective eigenfunctions can be expressed as a product of the radial and angular components as

$$\psi_{n,l,m}(r,\theta,\phi) = R_{n,l}(r)Y_{l,m}(\theta,\phi) \quad , \tag{1.21}$$

where $R_{n,l}(r)$ is a linear combination of spherical Bessel and Neumann functions, and $Y_{l,m}(\theta,\phi)$ are spherical harmonics. The subscripts n, l and m are the principal, orbital and magnetic quantum numbers respectively. Using the same boundary conditions as previously employed for the cubic model, then solving separately the radial and angular components, one obtains the confinement energy for a spherical particle of mass m and radius a. Restricting the analysis to the lowest order spherically symmetric excited state, the energy is given by

$$E = \frac{\hbar^2}{2ma^2} \quad . \tag{1.22}$$

Considering now an exciton in a semiconductor nanocrystal, using the Hamiltonian described in equation 1.8, the energy of the lowest excited state (band gap) is given by:

$$E_{1S_e1S_h} = E_g + \frac{\hbar^2}{2m_e^* a^2} + \frac{\hbar^2}{2m_h^* a^2} \tag{1.23}$$

Equation 1.23 shows that, in the strong confinement regime, the band gap of a semiconductor scales inversely with the square of the particle size ($1/a^2$) and the carrier effective mass. Considering the electronic parameters in Table 1.1, it may be deduced that the major contributions to changes in the band gap energy arise from changes in electron state energy due to its small effective mass.

1.1.4 Finite Potential Well Model and Coulomb Interactions

Thus far, we have assumed that the wavefunction vanishes at the crystal surface due to an infinite potential, which is not an accurate representation of the real case. Confinement barriers in nanocrystals are *finite* (eV range). As a consequence of the increasing kinetic energy of charge carriers at the surface with decreasing diameter the probability of the exciton leaking into the surrounding matrix becomes significant, effectively reducing its spatial confinement. Figure 1.4 shows the severe overestimation in confinement energy evaluated by the infinite potential model for particle radii smaller than $\sim$3.5 nm.

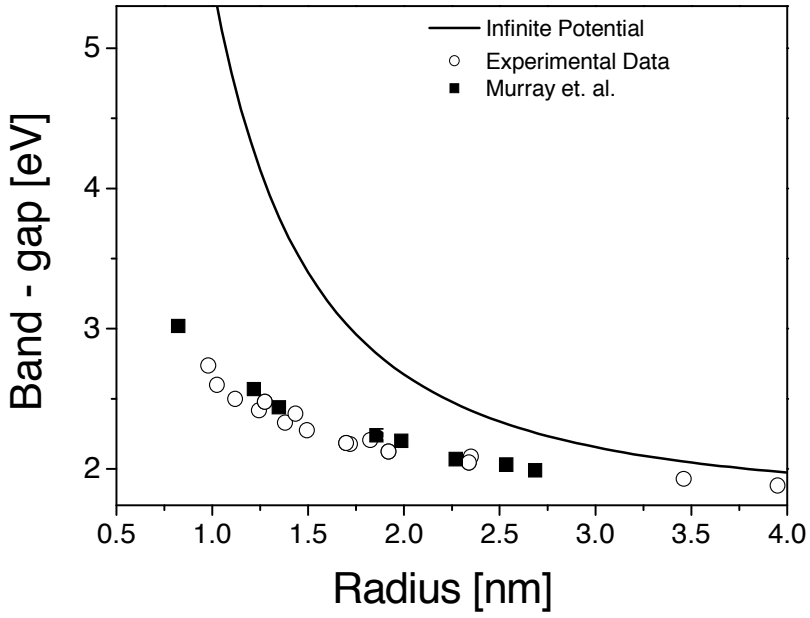

Figure 1.4 Plot of band gap energy vs. particle radius of CdSe nanocrystals comparing the infinite potential well model to experimentally obtained data [11]. The data points by Murray et al. were obtained from reference [2].

To adapt the model derived in Section 1.1.3 to a finite potential we have to adjust the boundary conditions for the spherical potential $V(r, \theta, \phi)$ as follows:

$$V(r,\theta,\phi) = \begin{cases} 0 & \text{if } |r| < a \\ V_m & \text{if } |r| \geq a \end{cases} \tag{1.24}$$

with the core and matrix regimes possessing the wavenumbers:

$$k = \begin{cases} \sqrt{\dfrac{2m^*E}{\hbar^2}} & \text{if } r < a \\ \sqrt{\dfrac{2m^*(V_m - E)}{\hbar^2}} & \text{if } r \geq a \end{cases} \tag{1.25}$$

The eigenfunction expression given in Equation 1.21 is still valid. However some additional conditions have to be fulfilled for the radial component $R_{n,l}(r)$: it must vanish sufficiently quickly within the matrix and not stringently at the core surface, and the eigenfunction (Equation 1.26) as well as the probability currents (Equation 1.27) must be continuous at the core–matrix interface.[10]

$$R_{n,l_c}(r)\big|_{r=a} = R_{n,l_m}(r)\big|_{r=a} \tag{1.26}$$

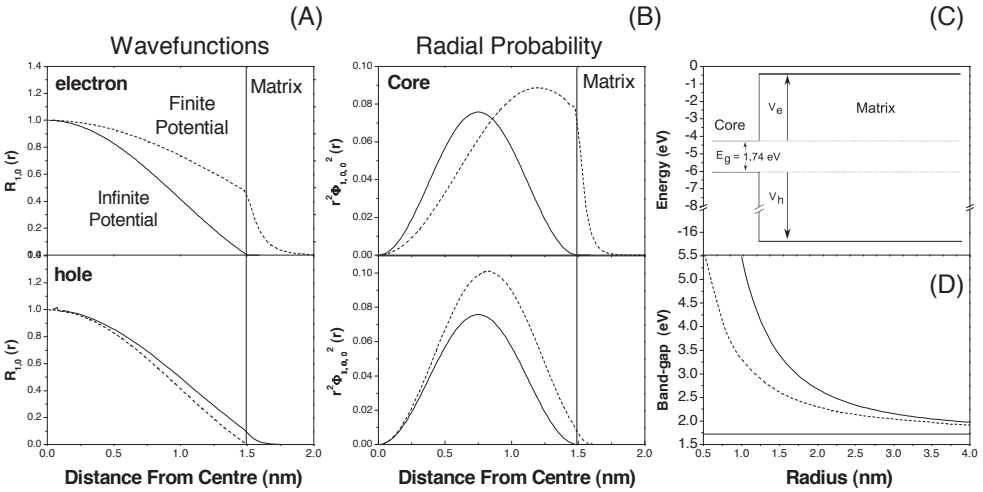

Figure 1.5 The $1S$ wavefunctions (A) and radial probabilities (B) for electrons and holes in a CdSe quantum dot having a 1.5 nm radius under finite and infinite barrier potentials. A potential energy diagram of bulk CdSe and the surrounding matrix (C). (D) Effect of the finite potential (dashed line) on particle size versus band gap predictions compared to the infinite case (solid line) [11].

$$\frac{1}{m_c^*}\frac{dR_{n,l_c}(r)}{dr}\bigg|_{r=a} = \frac{1}{m_m^*}\frac{dR_{n,l_m}(r)}{dr}\bigg|_{r=a} \tag{1.27}$$

Here m_c^* and m_m^* represent the effective masses of the charge carriers within the core and the surrounding matrix, respectively. Following these adjustments the eigenfunction is then harmonic inside the core while upon tunnelling at the surface into the matrix it decays exponentially. Figure 1.5 compares the wavefunctions (A) and radial probabilities (B) for a 1.5 nm radius CdSe nanocrystal with matrix potentials of $V_m^e = 4\ eV$ and $V_m^h = 10\ eV$ for the electron and hole, respectively (C) [12]. Employing a finite potential the charge carriers can now leak into the surrounding matrix and a finite probability exists for the electron (hole) to be delocalised at the particle surface. This leads to a unique case for semiconductor nanocrystal cores, wherein the optical properties of the particles are highly sensitive to the environment at the crystal surface. Due to the increasing kinetic energy of charge carriers, the extended wavefunction delocalisation becomes increasingly pronounced for smaller radii resulting in lower confinement energies. This is reflected in a distinct energy difference when compared to the infinite potential model (Figure 1.5 (D)).

So far we have completely neglected Coulomb interaction effects on the assumption that they are strongly screened due to the large dielectric constant in semiconductors. However, when in the strong confinement regime as appropriate to nanostructures, each carrier propagates within the Coulomb field of the other and as such the exciton binding energy becomes significant.

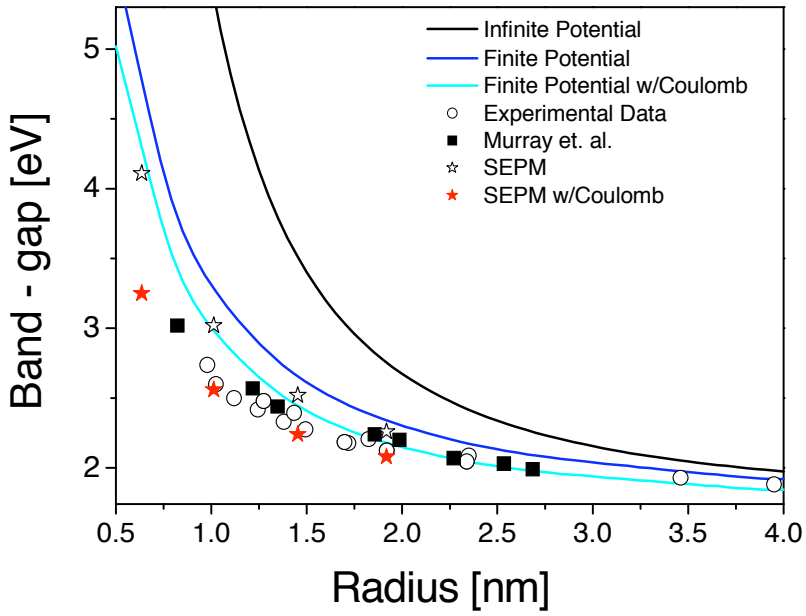

Figure 1.6 A plot of different confinement models and experimentally obtained size versus band gap data for CdSe [11].The results using the semi–empirical pseudopotential method were taken from reference [14]. The data points by Murray et al. were obtained from reference [2].

The contributions of Coulomb and polarisation effects were originally included as a first order perturbation of the Schrödinger equation for a two–particle system by Brus in 1984 [1, 13] giving:

$$E_{1S_e1S_h} = E_g + \frac{\hbar^2}{2m_e^* a^2} + \frac{\hbar^2}{2m_h^* a^2} - 1.786\frac{e^2}{\epsilon a} - 0.248\frac{e^4 m_0}{2\left(4\pi\epsilon\right)^2 \hbar^2 \pi \left(\frac{1}{m_e} + \frac{1}{m_h}\right)} \tag{1.28}$$

Figure 1.6 shows how the introduction of a finite potential leads to a significantly better approximation to the experimental data. However it is important to note, that non–parabolicity, band offsets as well as Coulomb interactions introduce large corrections to the hole states becoming especially significant for radii below 1 nm. In this range the EMA severely overestimates the predicted band gap and only high level *ab initio* calculations [14] can approximate the experimental data accurately.

1.1.5 Density of States

The Density of states (DOS), $D(E)$ describes the number of available states per unit volume and energy. The total number of states N is given by dividing the total volume by the volume

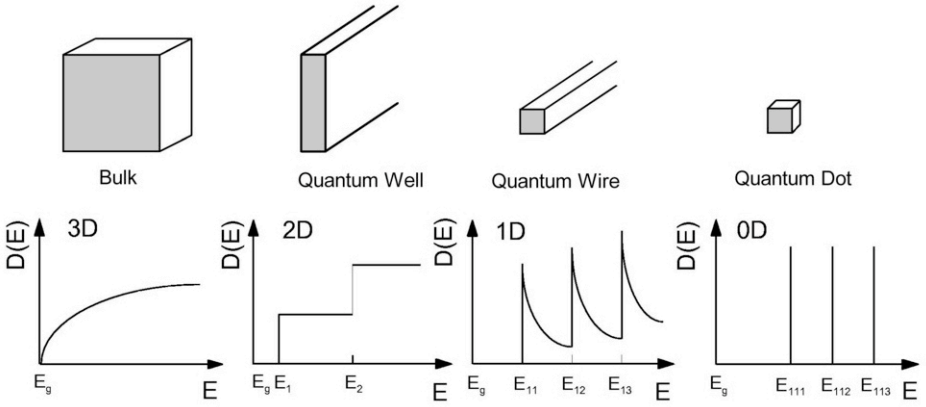

Figure 1.7 Density of States in different confinement systems. The function changes from a smooth square-root function of energy in a 3D bulk system to a staircase like function in a quantum well to states of discrete energy in a quantum dot

for a single state in k-space and the DOS can then be expressed as the derivative of N with changing energy:

$$D(E) = \frac{\partial N}{\partial E} = \frac{\partial N}{\partial k}\frac{\partial k}{\partial E} \quad . \tag{1.29}$$

An expression for $\partial k/\partial E$ can be found using equation 1.6 by differentiating k with respect to E:

$$\frac{\partial k}{\partial E} = \frac{m}{\hbar^2 k} \quad . \tag{1.30}$$

The relation for $\partial N/\partial k$ depends on the type of confinement as it dictates whether, and in which spatial direction, k is quantised. The expressions for a bulk, quantum well and quantum wire are $\frac{L^3k^2}{\pi^2}$, $\frac{L^2k}{\pi}$ and $\frac{L}{\pi}$ respectively. Substituting equation 1.30 and these expressions into equation 1.29 gives then the DOS for the respective system:

$$\begin{aligned}
\text{Bulk:} \quad & D(E)_{3D} = \frac{L^3\sqrt{2}m^{3/2}}{\hbar^3\pi^2}\sqrt{E} \quad , \\
\text{Q-Well:} \quad & D(E)_{2D} = \frac{m}{\hbar^2\pi} \quad , \\
\text{Q-Wire:} \quad & D(E)_{1D} = \frac{1}{\hbar 2\pi}\sqrt{\frac{2m}{E}} \quad .
\end{aligned}$$

It is significant that the 2D density of states does not depend on energy. Immediately, as the top of the energy-gap is reached, a significant number of states is available. In a quantum dot, the values of k are quantised in all directions and hence there is no k-space to be filled. All the available states exist only at discrete energies and can be represented by a Dirac delta function δ. The plots of DOS vs. E for the different confinement systems are shown in Figure 1.7.

1.2 Principles of Colloidal Semiconductor Nanocrystal Synthesis

The major significance of monodisperse particles is founded in the uniformity of their physico–chemical properties. Thus, direct correlation of the properties observed in ensemble measurements with those of a single particle is facilitated. Consequently, good control over the final size and size distribution is imperative to reliably study quantum size effects in semiconductor NCs ensembles. Since the seminal work by Murray et al. [2], much work has been devoted to developing adaptable reaction schemes for the preparation of high quality semiconductor nanocrystals. However, despite a tremendous experimental effort in synthetic development, the underlying mechanistic processes of nanocrystal nucleation and growth are still not fully understood, resulting in laborious trial–and–error approaches to finding the optimal set of reactants and conditions.

Having introduced the concepts of quantum confinement and its sensitivity to particle size, this section aims to provide an insight into the principles of the colloid chemistry involved in nanocrystal synthesis.

1.2.1 Colloidal Systems

Colloidal systems are defined as one substance microscopically dispersed in another. Depending on the phases of the two components those systems are classified as either aerosols (smoke, clouds), emulsions (milk) or sols (blood, paint). Surface interactions (repulsive or attractive) due to electrostatic or van der Waals forces become increasingly dominant with decreasing particle size and therefore controlling these forces in order to prevent particle aggregation and subsequent flocculation is of high importance. Figure 1.8 illustrates the increasing dominance of the surface once the radius enters the nano–size regime. For particles with a radius bigger than 100 nm, the surface atoms constitute less than $\sim$1 %. Once the particle size decreases towards the regime of quantum dots however, the surface atom percentage rises rapidly from $\sim$20 % ($r = 5\ nm$) to $\sim$70 % ($r = 1\ nm$).

One of the most effective methods to stabilize lyophobic colloidal particles is to cap them with ligands. By formation of a protective polymer or organic layer adhered to the crystal surface, aggregation of particles is entropically avoided in appropriate solvents. For effective steric stabilisation the ligands employed typically possess linear or branched, long–chain, alkyl groups with eight or more carbon units and are anchored to the surface atoms via functional group moieties. The nature of the moiety and the surface state to be passivated will largely control the bond strength. Common ligand classes used in semiconductor nanocrystal synthesis have carboxylate, amino, thiol, or phosphine functional groups. Utilising the wide range and versatility one can finely tune the steric stabilisation and solubility in various environments (polar, non–polar) by the choice of ligands.

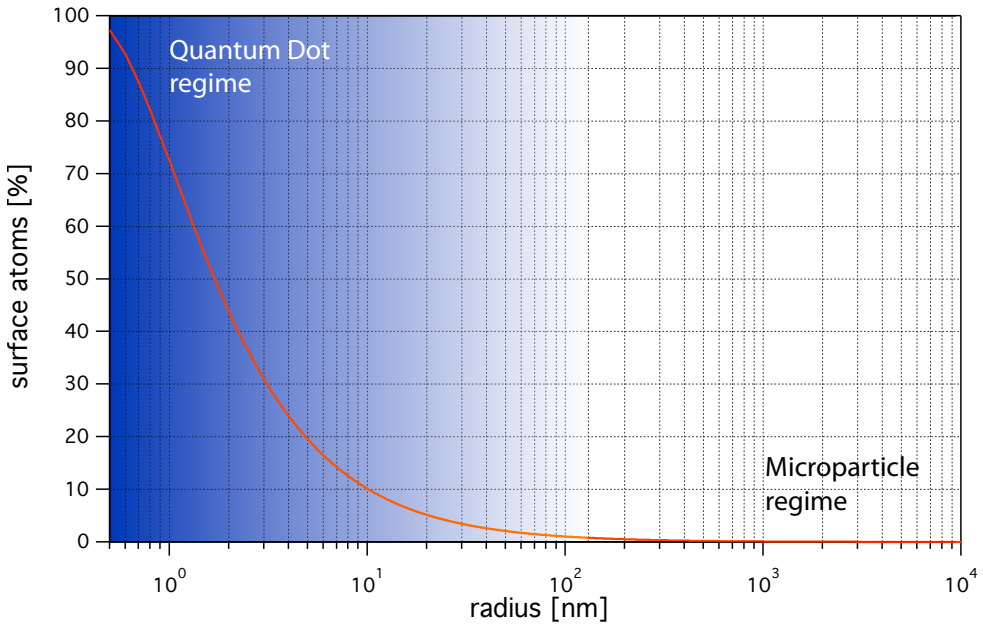

Figure 1.8 Plot of the surface atom percentage scaling with radius for a spherical particle.

Additionally one has to bear in mind that apart from colloidal stabilisation, ligands play three further distinct roles in NC chemistry. First, their presence during the nucleation process determines the reactivity and availability of the crystal precursors and monomers. Subsequently, they control the growth rate and final particle size distribution, and finally, they interact electronically with surface sites influencing the nanocrystal's optical properties. In the following, each of these aspects will be examined and discussed.

1.2.2 Classical Nucleation Theory

Classical nucleation theory (CNT) predicts the rate of generation of clusters based on solution supersaturation, reaction temperature and particle surface tension. It is worth noting that while the model is a good approximation for the evolution of micrometre sized particles, it has a major disadvantage when applied to nanocrystals. CNT considers initial nuclei sizes on the order of a few nanometres, which is approximately equal to the final NC size. Nevertheless, it is a useful theory to elucidate the principles involved in quantum dot formation.

The general process can be divided into homogeneous *nucleation* and *growth*, whereby the former corresponds to the initial formation of nuclei through separation of the solid phase from the solution phase. The thermodynamic driving force (supersaturation) for this phase transformation lies in the difference between the chemical potentials of the two phases forming

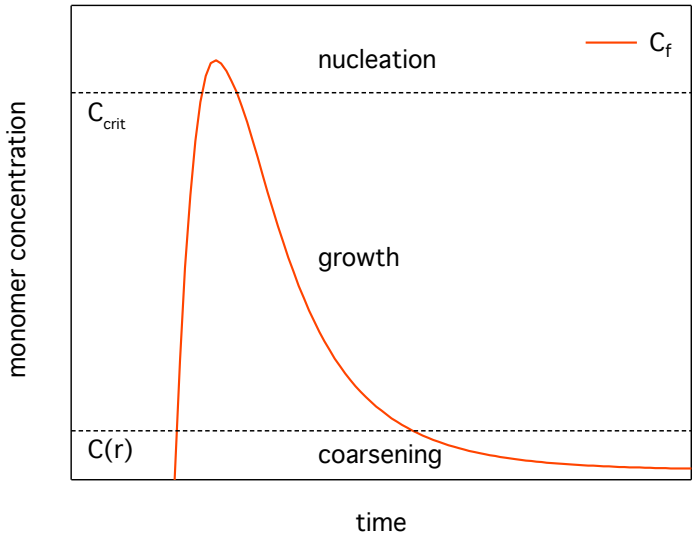

Figure 1.9 Monomer concentration profile during nucleation and growth according to LaMer [16]. The critical monomer concentration C_{crit} and equilibrium concentration $C(r)$ form the boundaries between the nucleation/growth and the growth/coarsening phase respectively.

the boundaries of a given system [15]. The thermodynamic barrier to nucleation is always higher than for growth as it requires the formation of a new surface. The extent of those barriers is dependent on the intrinsic properties of the system, such as monomer concentration, reaction temperature as well as nature and concentration of the surfactants employed.

According to LaMer [16], one of the key requirements for a monodisperse colloidal system is the separation of nucleation and growth. Figure 1.9 shows the well known LaMer diagram proposed by LaMer and Dinegar for describing the formation mechanism of monodisperse particles. After the induction period for accumulation of monomer to reach the critical concentration C_{crit}, the system enters the homogeneous nucleation stage, during which a 'burst' of spontaneous nucleation relieves the system of the high supersaturation. At the maximum concentration level, the system enters a pseudo steady state where the supply rate of monomer and its consumption for growth are equal. Because of the increasing consumption of monomer for the growth of nuclei, the free concentration of monomer C_f starts to decline and finally drops under the critical level for homogeneous nucleation at which point the system enters the growth stage and nucleation ceases.

In cases where the nucleation rate is high enough, the free monomer concentration stays above C_{crit} for only a brief moment and the nucleation stage is limited to a very short time window. Due to nuclei formation occurring in this 'burst' — as no additional nucleation is permitted in the growth stage — one expects the formation of monodispersed particles. The

growth phase continues to the point where C_f reaches the equilibrium monomer concentration $C(r)$, which is defined as the concentration needed in solution to sustain a particle with radius r. Once the monomer concentration drops below $C(r)$ coarsening will ensue.

It is important to note that while the LaMer model provides an excellent evaluative account of NC formation, it is overly simplistic and is unable to describe all the details of nanocrystal growth correctly. Instead of strictly separated stages there is strong experimental evidence that nucleation, growth and coarsening rather occur all at the same time [17] and each of them is only *dominant* at a certain time during the reaction.

As mentioned before, nucleation is linked to a thermodynamic potential barrier which is balanced by the energy gain of creating a new volume, and the energy cost due to creation of a new interface. The barrier to nucleation and the corresponding critical nucleus size can be directly determined by calculating the Gibbs free energy ΔG needed to create a new phase with radius r:

$$\Delta G = \frac{4}{3}\pi r^3 \Delta G_V + 4\pi r^2 \gamma \tag{1.31}$$

where ΔG_V is the free energy per unit volume (J/m^3) and γ is the surface free energy (J/m^2). The first term represents the energy gain of creating a new volume while the second term accounts for the energy loss due to the surface energy of the new interface. With ΔG_V given by

$$\Delta G_V = -\frac{RTln(S)}{V_m} \quad , \tag{1.32}$$

where R is the gas constant in units $JK^{-1}mol^{-1}$, T is the absolute temperature (K), S is the supersaturation, and V_m is the molar volume (m^3/mol). It is seen from Equation 1.31 that, if the temperature and supersaturation are too low, the energy that would be released by forming a crystal is not enough to create a new surface; thus nucleation does not proceed. The supersaturation is defined as the ratio between the monomer concentration in bulk solution $[C]_b$ and the equilibrium concentration for a surface with infinite curvature $[C]^0_\infty$:

$$S = \frac{[C]_b}{[C]^0_\infty} \tag{1.33}$$

Figure 1.10 (A) shows the gradient of ΔG under the assumption that the surface energy is independent of crystal size. It can be seen that, due to the dominant contribution of the surface component for very small nuclei, the free energy increases up to a critical radius r_{crit}, where

$$r_{crit} = -\frac{2\gamma}{\Delta G_V} = \frac{2\gamma V_m}{RTln(S)} \tag{1.34}$$

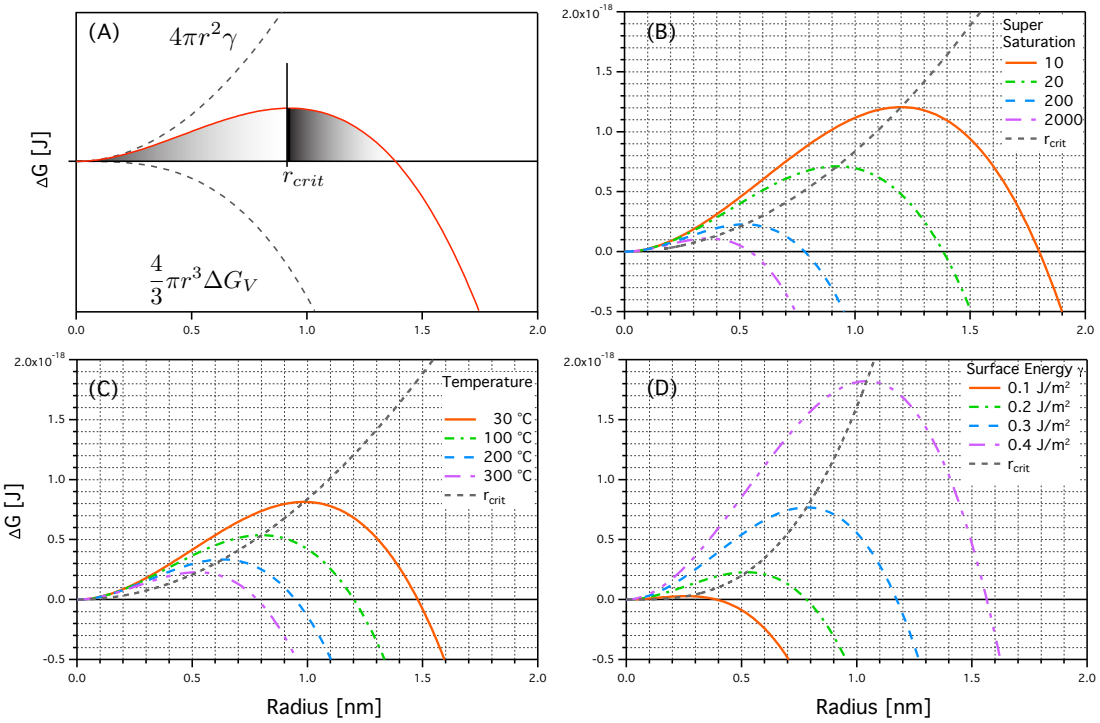

Figure 1.10 **(A)** Plot of the Gibbs free energy for nucleation and the respective energy contributions with increasing volume and surface. **(B)** The effect of supersaturation for a fixed surface energy γ of 0.2 J/m^2 and temperature of 300 $°C$. **(C)** The effect of temperature for a fixed surface energy γ of 0.2 J/m^2 and supersaturation of 200. **(D)** The effect of surface energy for a fixed supersaturation of 200 and temperature of 300 $°C$. The dashed grey lines in graphs **(B)** – **(D)** are a guide to the eye to illustrate the evolution of r_{crit}.

and

$$\Delta G_{crit} = \frac{16\pi\gamma^3}{(3\Delta G)_V^2} = \frac{4\pi\gamma}{3} r_{crit}^2 \qquad \text{for} \qquad \frac{d\Delta G}{dr} = 0 \quad . \tag{1.35}$$

As the size increases past the critical radius, growth becomes thermodynamically favourable. Consequently any crystals smaller than the critical sized nuclei possess a thermodynamic tendency to dissolve while any crystal larger than r_{crit} shall be thermodynamically driven to grow.

From equation 1.34 it is seen that the critical radius is controlled by the synthetic parameters of *surface energy*, *supersaturation* and *temperature*, which is illustrated in the plots (B), (C) and (D) of Figure 1.10. Supersaturation appears to have a strong effect on the nucleation barrier for values of less than $\sim$ 200. In this regime a doubling from 10 to 20 leads to a reduction of r_{crit} by 0.28 nm, which is about one atomic monolayer for a CdSe nanocrystal, as well as a decline in critical potential energy ΔG_{crit} by $\sim$ 40 %. Further increase of supersaturation to

200 shows another strong reduction in critical radius and potential energy by 0.4 nm and ~ 60 %. However once the regime past 200 is reached, the supersaturation has only a minor effect on the nucleation barrier. Since nucleation in realistic systems typically occurs in this high regime ($\sim 200 - 2000$), this parameter mainly provides the environment for the right nuclei size range but does not play a dominant role to fine control the critical radius. However, as will be discussed below, the high sensitivity and rapid increase of r_{crit} for low supersaturations has a major effect towards the end of NC growth when the monomers become depleted.

The effect of nucleation temperature (Figure 1.10 (C)) exhibits a similar trend, however with a more linear relationship between T and r_{crit}. Over the range of one order of magnitude, going from 30 $°C$ (ambient) to 300 $°C$, both the activation energy and r_{crit} decrease continuously. Typical temperatures for nanocrystal nucleation and growth fall into the range between 200 - 300 $°C$ which, like the supersaturation, has only a minor influence on the critical radius. However, in spite of thermodynamic considerations, accurate temperature control is of utmost importance in relationship to the involved reaction kinetics, such as precursor decomposition or collision forces and frequency.

From Figure 1.10 (D) it is clear that the surface free energy is the dominant factor determining the nucleation barrier. While the critical radius scales linearly with γ, the barrier height ΔG_{crit} rises exponentially with increasing surface free energy. As γ is largely controlled by the type and concentration of ligands at the particle surface, Figure 1.10 (D) highlights the importance of careful ligand choice. In this case, appropriate ligands control the passivation and stabilisation of the formed nuclei in order to lower and control γ.

1.2.3 Ensemble Dynamics

Given that the final crystal sizes are not much larger than the initially formed nuclei, the outcome of a NC synthesis (mean crystal size, particle size distribution, and concentration) is almost solely determined by the end of nucleation. Hence, precise control of the critical radius through the parameters discussed previously is one of the key factors in quantum dot synthesis. Drawing from these considerations the hot–injection method in lyophobic solvents established as one of the premier synthetic schemes to produce highly monodisperse nanocrystals [2]. This method is based on the rapid injection of a room temperature precursor solution into a hot mother solution ($\sim 300°C$) and particle growth at lower temperatures ($\sim 230 - 250°C$). The effect of this injection is two–fold. On the one hand, rapid precursor injection leads to a sharp rise in monomer concentration (increasing supersaturation) to overcome the nucleation barrier resulting in a 'burst' of nucleation. On the other hand, the quick temperature drop due to the cool injection solution and fast monomer consumption during the nucleation 'burst' leads to rapid supersaturation quenching, which causes nucleation to cease, and subsequently the

regime of particle growth becomes dominant. By maximising the separation of those two domains, the nuclei are expected to grow uniformly.

In an ideal system nucleation occurs simultaneously resulting in monodisperse crystal seeds. However in a realistic synthesis the critical radius and free energy barrier are subject to constant change due to the temporal variations in reaction conditions (Figure 1.11 (A)). This leads to a range of different sized seeds being formed as well as the re–dissolution of seeds that become unstable due to the changing conditions. Consequently a particle size distribution (PSD) emerges with its size range reflected by the degree of parameter stability. As discussed before, the increase of r_{crit} through a reduction in supersaturation (Figure 1.11 B)) (grey dashed line) favours the stability of larger particles, while smaller crystals become unstable. This becomes especially important once the monomer depletes ($C_f \leq C(r)$) and the low level supersaturation leads to a rapid increase of the critical radius. With r_{crit} approaching the size regime of the grown PSD, the smaller particles start to dissolve and in turn support the growth of the larger ones. This effect is called Ostwald ripening [18] and is typically characterised by a broadening of the PSD. This is an important factor to bear in mind as a typical nanocrystal synthesis is terminated before the onset of coarsening.

As a consequence of all these dynamics an experimental system always produces an ensemble size distribution rather then single sized particles. It is the objective of high quality synthetic techniques to balance those dynamics in order to narrow the PSD.

1.2.4 Growth Modes

Having presented the thermodynamic considerations of nanocrystal formation, we will now address the kinetic aspects and current models used to describe particle growth. In general, growth can be expressed as a sequence of monomer diffusion towards the nuclei surface and the reaction of monomers at the surface. Depending on which step occurs at a slower rate the growth mode is said to be either diffusion or reaction limited [19].

The trend of monomer diffusion towards (or away) from a surface is governed by their Brownian motion along a concentration gradient. Such gradients are induced by the removal of monomer from solution to populate the surface (growth). By considering the mass removed at the solid–liquid interface compared with the mass available in a region of the bulk solution near that interface the so called depletion depth h is obtained. The latter characterises the length scale of the mass transfer boundary layer (diffusion layer), and is a function of the concentration gradient (Figure 1.12). As stated by Fick's first law of diffusion, the total flux of monomers, I $(mol/m^2 s)$, towards a particle of radius r is given by

$$I = 4\pi x^2 D \frac{dC_f}{dx}\bigg|_{x \geq r} \quad , \tag{1.36}$$

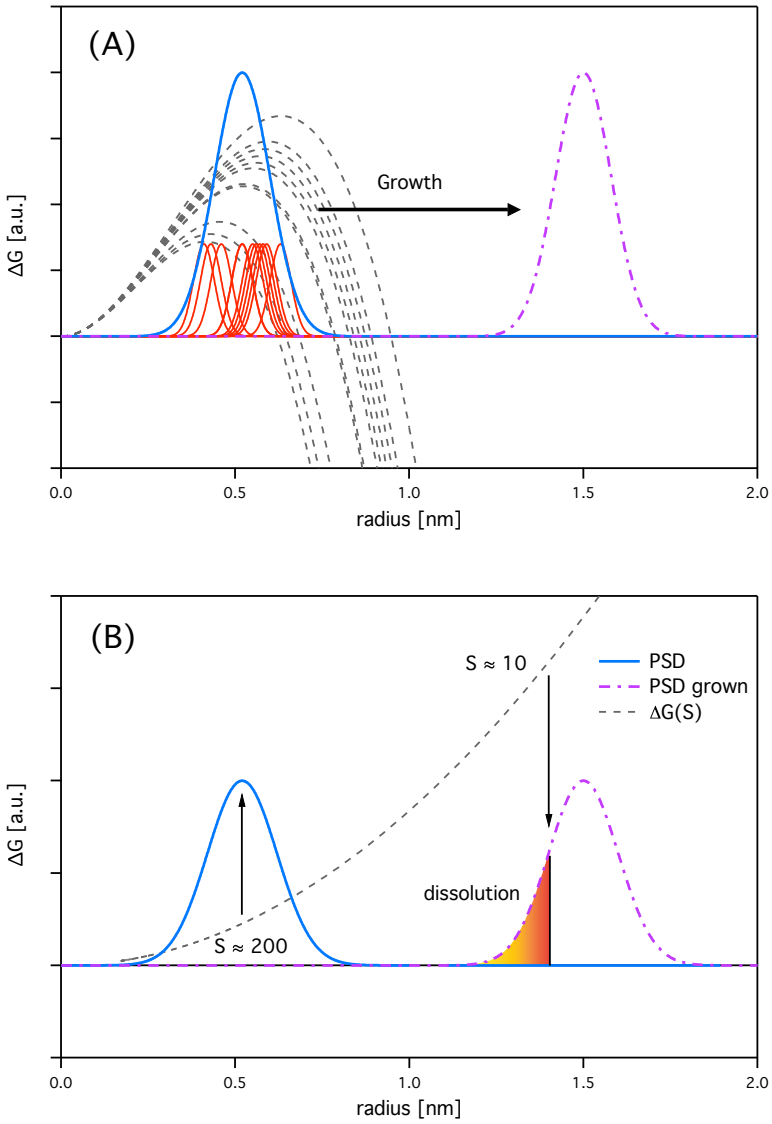

Figure 1.11 **(A)** Schematic of the PSD evolution. Temporal parameter changes indicated by the ΔG traces (grey dashed) result in a range of critical nuclei sizes (red distributions) from which the PSD (blue) emerges. Idealised growth shifts this distribution towards larger radii (purple). **(B)** Principle of Ostwald ripening. The evolution of the nucleation potential barrier with decreasing supersaturation $\Delta G_{crit}(S)$ (grey dashed) induces Ostwald ripening once r_{crit} reaches the PSD.

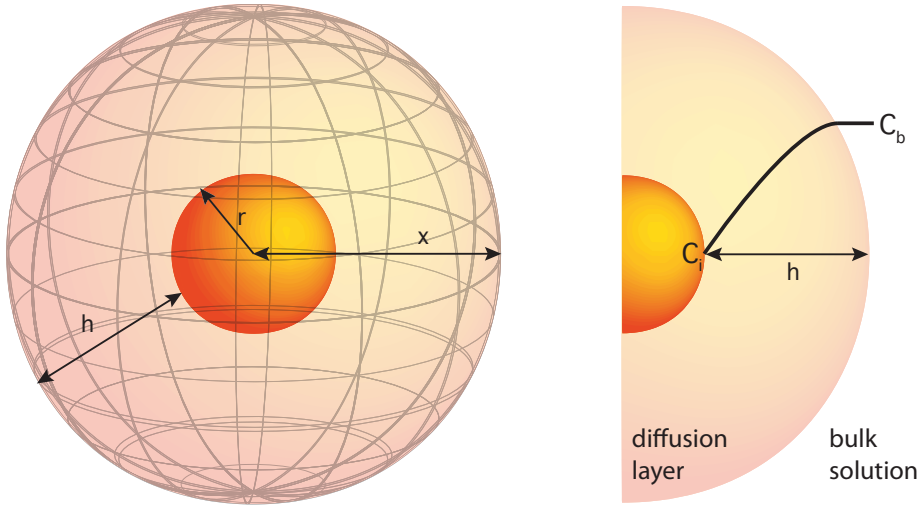

Figure 1.12 Left: A spherical particle of radius r surrounded by a diffusion layer with depletion depth h. Right: The profile of the monomer concentration gradient within the diffusion layer. C_b and C_i are the bulk and interface monomer concentrations respectively.

where D is the diffusion coefficient and C_f is the free monomer concentration at x. As illustrated in Figure 1.12, the boundary conditions for the integration of equation 1.36 are that at $x = r + h$ the monomer concentration equals the value in the bulk solution ($C_f = C_b$) and at $x = r$ it is equal to the interface concentration ($C_f = C_i$). Furthermore, I is constant irrespective of x, inasmuch as the diffusion of monomers towards the particle is in a steady state. Thus, after integration, the total diffusive flux of monomer to the particle surface is

$$I = 4\pi r D \frac{r+h}{h}(C_b - C_i) \quad . \tag{1.37}$$

Assuming that $r \lll h$ for nanoscale systems [19, 20], the flux expression is reduced to

$$I_{diff} = 4\pi r D(C_b - C_i) \quad . \tag{1.38}$$

Given that I is also related to the particle growth rate dV/dt, it can be expressed alternatively as:

$$I = \frac{dV}{dt}\frac{1}{V_m} = \frac{4\pi r^2}{V_m}\frac{dr}{dt} \quad , \tag{1.39}$$

where V_m is the molar volume of the monomer. When assuming purely diffusion limited growth, the monomers will react instantly once they reach the particle surface. Hence the interface concentration C_i is equal to the equilibrium concentration $C(r)$ (as defined in Section

1.2.2). After combining equations 1.38 and 1.39, the diffusion limited growth rate is then given by:

$$\frac{dr}{dt} = \frac{DV_m}{r}(C_b - C(r)) \quad . \tag{1.40}$$

Considering now the monomer reaction step at the surface, which is governed by the adsorption and desorption rate constants k_{ad} and k_{des}, respectively, I_{react} can be written as:

$$I_{react} = I_{ad} - I_{des} = \left(4\pi r^2 k_{ad} C_i\right) - \left(4\pi r^2 k_{des}\right) \quad , \tag{1.41}$$

where k is the rate constant of a first order surface reaction. Since the equilibrium monomer concentration $C(r)$ can be expressed by the ratio of k_{des}/k_{ad}, equation 1.41 is reduced to:

$$I_{react} = 4\pi r^2 k(C_i - C(r)) \quad . \tag{1.42}$$

In the case of purely reaction limited growth the monomer diffuses towards the particle surface but reacts at a rate which is dependent on the nature and concentration of surfactants in solution. Thus, the diffusion layer becomes irrelevant and the interface concentration C_i is equal to the bulk concentration C_b. Combination of equations 1.42 and 1.39 leads then to

$$\frac{dr}{dt} = kV_m(C_b - C(r)) \quad . \tag{1.43}$$

We now note that $C(r)$ is particle size dependent through the Gibbs-Thomson equation, since:

$$C(r) = C_\infty^0 exp\frac{2\gamma V_m}{rRT} \quad . \tag{1.44}$$

Furthermore, by combining equations 1.33 and 1.34 with equation 1.44, C_b can be expressed as

$$C_b = C_\infty^0 exp\frac{2\gamma V_m}{r_{crit}RT} \quad . \tag{1.45}$$

Subsequent substitution of these expressions into equations 1.40 and 1.43 respectively, gives the expressions for the growth rate in both the diffusion and reaction limits:

$$\frac{dr}{dt} = \frac{DV_m}{r} C_\infty^0 exp\frac{2\gamma V_m}{RT}\left(\frac{1}{r_{crit}} - \frac{1}{r}\right) \quad , \tag{1.46}$$

$$\frac{dr}{dt} = kV_m C_\infty^0 exp\frac{2\gamma V_m}{RT}\left(\frac{1}{r_{crit}} - \frac{1}{r}\right) \quad , \tag{1.47}$$

first described by Sugimoto et al. [19]. The two expressions are illustrated in Figure 1.13 showing the normalised radial dependence of the growth rate under diffusion and reaction control. It can be seen that for both modes the growth rates vary considerably in the size

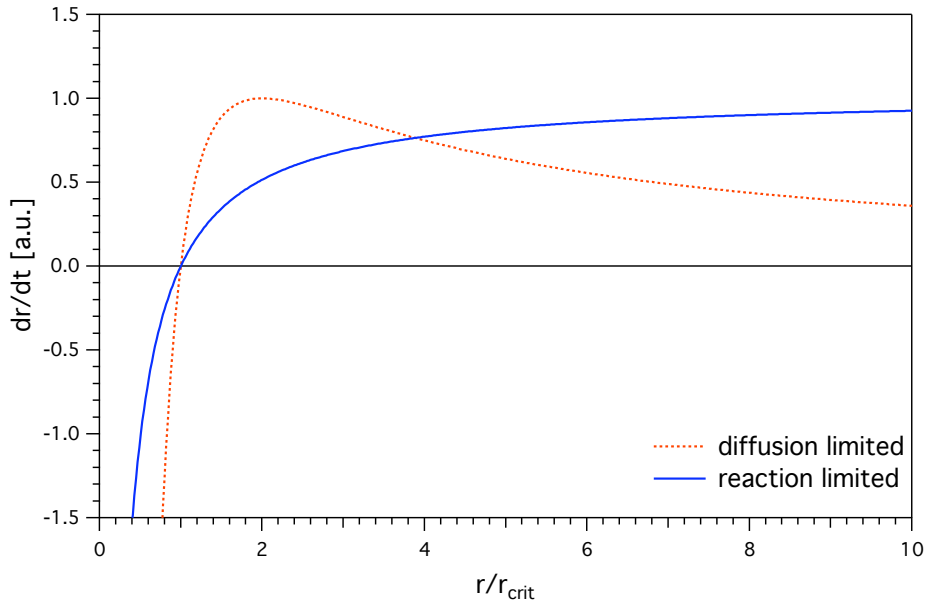

Figure 1.13 The growth rate as a function of particle size in the diffusion (red dotted line) and reaction limit (blue solid line).

range close to the critical radius. As demonstrated before, based on thermodynamics, particles with radii smaller than r_{crit} dissolve rapidly, while larger ones grow continuously with the zero growth rate occurring for $r = r_{crit}$. In the diffusion limited case the growth rate climbs steeply to a maximum followed by a gradual decline for larger particles. Consequently crystals in the size range close to the maximum will grow faster while the growth rate for larger particles declines continuously. Such a growth profile leads to narrowing of the PSD (*focussing*) during NC growth [20].

Considering the growth rate in the reaction limit, it seems that, since there is no dominant maximum, larger particles will always grow faster than smaller ones. Due to this self–accelerating effect, *defocusing* of the PSD is expected. Experimentally, *focusing* is commonly observed in the early growth stages and consequently, nanocrystal growth has been assumed to be predominantly diffusion limited [20–23]. However models based on diffusion limited growth exhibit major discrepancies when compared to experimentally determined kinetics. Recently developed theoretical models, providing insight into the underlying kinetics of nucleation and growth of nanocrystals, demonstrate that evolution of the PSD in the diffusion limit is not required for focusing, and that focusing can be achieved under pure reaction control [17, 24]. Figure 1.14 compares the temporal evolution of the PSD in the reaction and diffusion limits. In panel A the FWHM of the size distribution stays relatively constant for early reaction times ($\lesssim 100\ s$), whereas in the diffusion limit (panel B) focusing of the PSD is observed

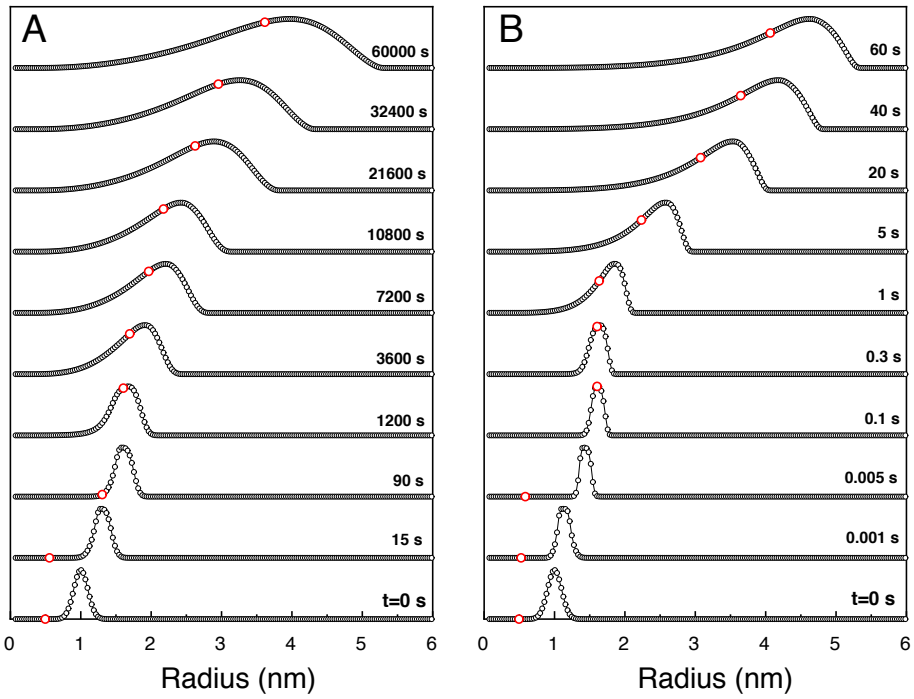

Figure 1.14 Temporal evolution of the PSD in the reaction (A) and diffusion limited (B) regime ($\gamma = 0.2\ Jm^{-2}$, $S = 500$, $D = 1e^{-12}\ m^2s^{-1}$). The red marker indicates the critical radius at the respective time. [17]

during early stages. In both cases, the onset of ripening is triggered once the critical radius approaches the mean radius of the PSD due to monomer depletion. However, examining the time scale at which the diffusion limited growth occurs, it is obvious that even when assuming a rather conservative diffusion coefficient of $10^{-12}\ m^2s^{-1}$ the reaction proceeds several orders of magnitude faster than experimentally observed. Thus we conclude that nanocrystal formation is reaction limited.

Due to the reaction limited mode, the control of NC nucleation and growth is fundamentally based on the control of the particle surface chemistry through the employed ligand system. The influence of suitable capping agents is two–fold as depicted in Figure 1.15. On the one hand, depending on their binding strength through functional groups, ligands control the particle growth rate k and can significantly lower γ, leading to the stabilisation of smaller particles in solution. On the other hand, the alkyl chain structure largely determines the solubility of free ligand and their complexes which in turn controls the supersaturation for a given system. As a result, an intensive field of research evolved over the last three decades investigating various ligand systems in order to maximise the control over nanocrystal nucleation and growth.

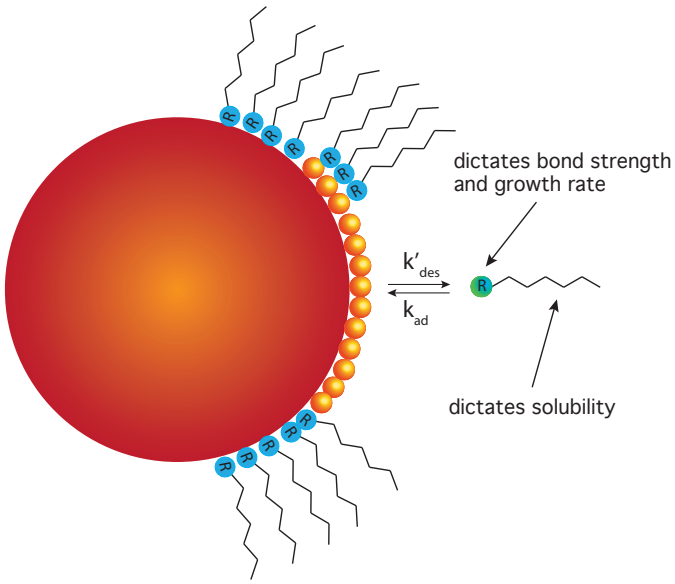

Figure 1.15 Schematic of reaction limited growth control through ligands. The bond strength between the functional groups (ligand) and the particle surface dictates the growth rate, while he alkyl chain structure controls the supersaturation in the system.

1.2.5 Evolution of Quantum Dot Synthesis

One of the first reports on colloidal CdS nanocrystal synthesis by Henglein et al. [25] involved a micelle route using sodium polyphosphate as a stabiliser in an aqueous environment. Through the deliberate inclusion of a capping agent, the formed nanoparticles were redispersible in water which allowed for further purification and processing. This was followed up by Steigerwald et al. [26] developing the first pseudo–organometallic route, where cadmium perchlorate and $Se(SiMe_3)_2$ were combined to form CdSe nanocrystals. Addition of phenyl(trimethylsilyl)selenide resulted in phenyl surface passivated particles which could be isolated by centrifugation and marks the first example of monomer passivation of a NC surface. The phenyl coating rendered the crystals soluble in pyridine and insoluble in petroleum ether, forming a solvent/non–solvent pair. The technique of using a solvent/non–solvent pair is nowadays exploited for QD purification and size selective precipitation.

However, the publication that truly ignited the research of nanocrystal ligand chemistry was the landmark paper by Murray et al. [2]. This work combined the use of organometallic precursors (dimethylcadmium) with long chain phosphine oxides (trioctylphosphine oxide (TOPO)) as capping agents and high temperature inert–atmosphere solution chemistry. Precursor solutions of dimethyl cadmium and trioctylphsphine chalcogenides (sulfur, selenium or tellurium) were combined and subsequently injected into a hot coordinating solvent (TOPO) to produce highly monodisperse NCs of CdS, CdSe and CdTe under lyophobic conditions.

Consequently, TOPO became the standard capping agent for organometallic type synthetic routes.

Owing to its highly volatile nature and toxicity, dimethyl cadmium is both difficult to work with and allows only for limited control of nucleation and growth kinetics. This issue was overcome, when Peng et al. [7] showed in 2001 that cadmium oxide (CdO) is a feasible alternative to dimethyl cadmium resulting in equal or superior quality nanocrystals. In this work strong binding hexylphosphonic acid (HPA) or tetradecylphosphonic acid (TDPA) was used as the metal complexing ligand. Following the cadmium source substitution, it was found that several cadmium salts with an anion of a weak acid form viable precursors for the synthesis of high quality CdSe nanocrystals, among which fatty acids were proven to be the most versatile ligand system [27].

Another major advance in nanocrystal reaction control was the transition from coordinating to non–coordinating solvents. The traditional use of TOPO prevented any ligand based control of the reaction kinetics and the final PSD was almost solely governed by the reaction time [7]. With the introduction of octadecene (ODE) as a suitable non–coordinating solvent by Yu et al. [28], tunable monomer reactivity through variation of the ligand concentration was demonstrated for the first time. ODE was chosen since it is liquid at room temperature with a high boiling point of about 320 $^{\circ}C$, while oleic acid, a natural surfactant, served as the ligand for the cationic precursor and NC stabilisation. This ligand system is to date one of the most ubiquitous and thoroughly studied frameworks for semiconductor nanocrystal synthesis. Figure 1.16 depicts the typical ligand classes used in current reaction schemes. Due to their long alkyl chains these ligands are non–polar and exhibit high boiling points.

The introduction of non–coordinating solvents enabled researchers for the first time to systematically investigate the effect of different precursors in the nucleation and growth of nanocrystals without hindrance or complication from a co–complexing solvent. This led to major advances towards the understanding and tunability of reaction kinetics [29], crystal structure [8] and shape control [4, 30–34] (Figure 1.17). In depth studies on ligand binding [35, 36] and precursor evolution [37–39] employing analytical methods like NMR spectroscopy, mass spectrometry and in–situ extended X–ray absorption fine structure (EXAFS) furthered the detailed understanding of reaction mechanisms. Classical molecular calculations [40] and ab initio calculations [41] were employed to investigate the ligand–surface bond on an atomistic level and have revealed the expected binding energies for various functional groups at nanoparticle interfaces.

Furthermore it was shown that impurities present in commercially available ligands have significant effects on the final synthetic result explaining the irreproducibility between different batches. For example, primary and secondary phosphine derivatives, which differently favour anisotropic growth, were identified as common impurities in TOPO [44]. In another account,

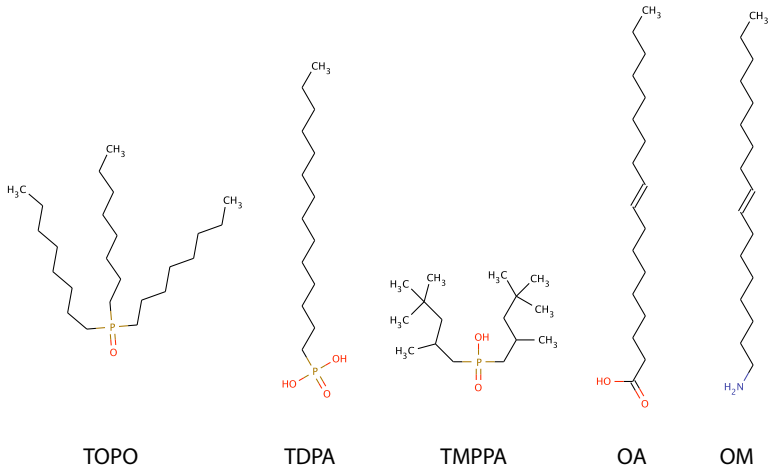

Figure 1.16 Representative molecules of common surfactant classes for colloidal semiconductor nanocrystal synthesis. From left to right: Trioctylphosphine oxide (TOPO), Tetradecylphosphonic acid (TDPA), Bis-(2,2,4-trimethylpentyl) phosphinic acid (TMPPA), Oleic acid (OA) and Oleylamine (OM).

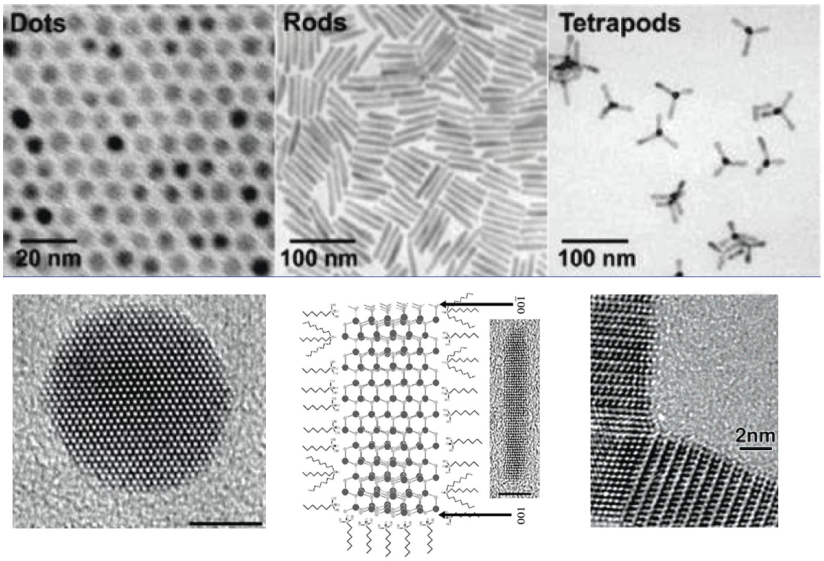

Figure 1.17 Top row: Transmission electron micrographs depicting CdSe dots, rods and tetrapods [42]. Bottom row: (left) Wurtzite CdSe nanocrystal dot in the $[000\bar{1}]$ orientation [42]. (centre) Model and HRTEM of a CdSe nanorod. (scale bars are 5 *nm*) According to the proposed growth mechanism the organic surfactants cannot coat one face of the nanocrystal, which raises the energy of this face, allowing it to grow quickly and form a rod shape [43]. (right) HRTEM image of a CdSe/CdS nanotetrapod fragment showing the interface between [111] planes of zincblende–CdSe seed and [001] planes of wurtzite–CdS arms [32].

Figure 1.18 Workstation for Automated Nanomaterials Discovery and Analysis (WANDA). Robotic deck featuring two liquid-dispensing robotic arms and an eight-element Low-Thermal Mass Reactor (LTMR) array for high-temperature nanocrystal synthesis [48].

a recent study suggested that secondary phosphines, which are impurities in trioctylphosphine (TOP), are actually responsible for the reactivity of the common chalcogenide precursor TOP–Se [37].

Due to those potential unknowns and the pursuit for non–toxic, cheap and stable surfactants a general trend towards simplification of ligand systems evolved. In recent years phosphine–free synthetic schemes, using ODE–Se [8, 9, 45] or SeO_2 [46] as chalcogenide precursors, were shown to produce high–quality NCs comparable to the traditional methods. Additionally to the environmental and cost advantages the reduction of ligand species involved in a reaction scheme generally facilitates the identification of the true effect of the remaining surfactants on NC nucleation and growth. On the other hand, current sophisticated synthetic methods demonstrate that the use of a binary ligand system can provide superior fine control of reaction kinetics [3].

Apart from the advances in ligand chemistry, technical evolution in synthetic techniques and automation led to high–throughput production and rapid parameter optimisation for NC synthesis. For instance, using micro reactors [47] and robotic platforms [48] (Figure 1.18), enabled combinatorial synthetic approaches to effectively investigate a multidimensional parameter space (photoluminescence (PL) wavelength, quantum yield (QY), PSD, product yield) in a fraction of time and with superior reproducibility compared to traditional manual methods.

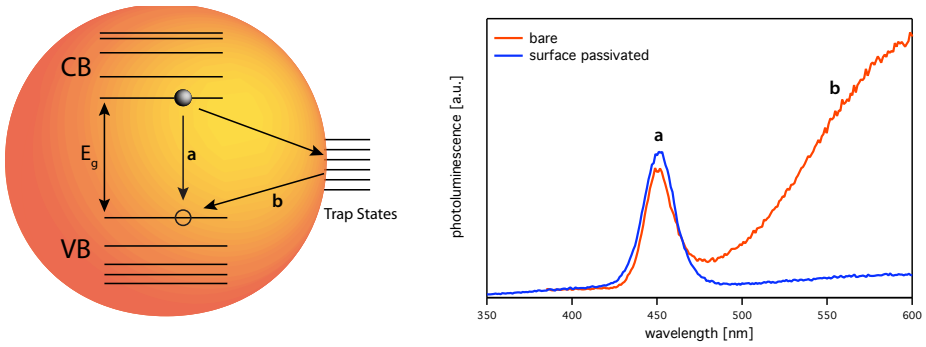

Figure 1.19 Left: Schematic of exciton recombination pathways in a typical semiconductor NC. Upon excitation of an electron into the conduction band (CB) radiative band gap recombination (**a**) competes with relaxation and recombination via surface trap states (**b**). Right: Emission spectra of CdS nanocrystals before (red) and after (blue) surface passivation. The significant trap emission arising form surface state recombination is almost completely suppressed once those pathways are blocked.

1.2.6 Optical Effects of Capping Ligands

So far the discussion of ligands was limited to their role during nanocrystal synthesis. However, it has been known for many years that ligands also have a major effect on the the optical properties of bare semiconductor nanocrystals [49]. At the surface, the orbitals of unpassivated atoms form trap states which cover a broad range of energies within the band gap, as depicted in Figure 1.19 (left). As discussed in section 1.1.4, the charge carriers have a finite probability to reach the NC surface, enabling surface trap states to provide multiple alternative pathways for radiative and non–radiative exciton recombination (**b**). These channels compete effectively with radiative band edge recombination (**a**) dependent on their relative energetic position. Therefore, the emission profile and quantum yield (QY) of quantum dots is directly related to the number and nature of available trap states. For instance, competing radiative recombination through a broad distribution of trap sites is reflected by a broad distribution of emissive states extending form the band edge emission to lower energies (deep–trap emission), see Figure 1.19 (right).

Adsorption of ligands to the NC surface has shown to either eliminate those surface states or facilitate photoinduced electron transfer (PET), where a charge carrier is extracted onto the ligand. Which one of those two processes is observed is strongly dependent on the energetic position of the conduction and valence band of the NC with respect to those of the molecular orbitals (MOs) of the ligands, as illustrated in Figure 1.20. Alkyl amine ligands have been shown to be efficient Lewis bases (electron donors) which bind to the cadmium surface atoms of CdSe nanocrystals. This binding raises the site energy of the surface state, effectively removing this recombination pathway, and increasing band–edge emission [49–51].

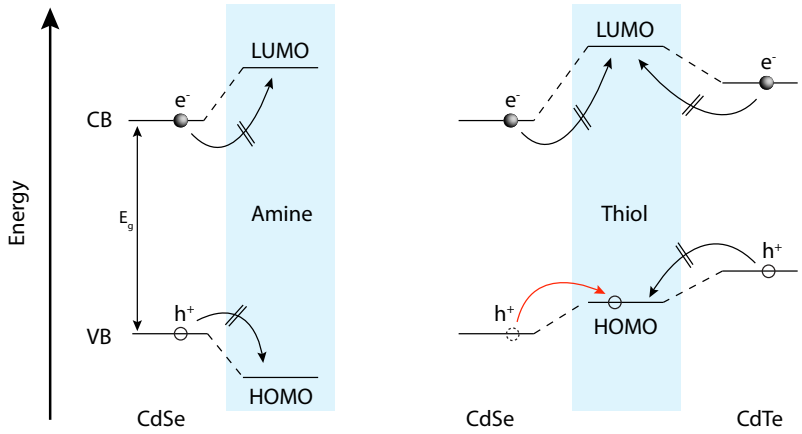

Figure 1.20 Schematic of Band gap configurations for surface passivation with amine (left) and thiol ligands (right). Binding of amine ligands to the surface of a CdSe QD results in a potential barrier at the surface site effectively blocking charge carrier trapping. The different effects of thiol ligand binding to CdSe and CdTe are a result of the different band gap offsets relative to the thiols highest occupied molecular orbital (HOMO). The photoluminescence quenching in CdSe is assumed to be due to a transfer of the photoexcited hole from the top of the NC valence band (VB) to the HOMO of the attached ligand (red arrow) [52].

The importance of the relative energetic alignment between the NC band gap and the ligand orbitals is highlighted by the adverse effects of thiol surfactants on CdSe and CdTe quantum dots. The same thiols that yield a high QY and single–exponential decay kinetics for CdTe QDs are observed to almost completely quench the luminescence of CdSe by inducing fast non–radiative decay processes [52]. Considering that the two semiconductors are chemically similar and have comparable band gap energies, the strong difference between thiol–capped CdSe and CdTe QDs is explained by the difference in the position of the valence band–edge relative to the redox level of the thiol capping molecule. As shown in Figure 1.20 (right), due to the energy difference of the CdSe and CdTe valence band ($\sim 0.5\ eV$), the thiol redox potential is situated above the valence band–edge for CdSe but below the CdTe valence band–edge. Efficient hole trapping in CdSe by thiol moieties culminates in a dramatic reduction of the band–edge QY. Conversely, a QY increase in the case of CdTe results from the elimination of surface trap state. A recent study [53] exploited the effect of relative energy alignments by employing a phenanthroline ligand, whose oxidation potential can be manipulated by ion complexation at the aza crown ether sites, leading ultimately to a suppression of hole scavenging. The accompanying change in photoluminescence intensity was proposed to be used for a metal ion sensing nanocrystal system.

While most studies on optical ligand effects are focused on the metal binding species [49, 51, 52, 54] few have investigated the role of chalcogenide surface sites. Jasieniak et al.

[55] demonstrated the importance of surface composition in regards to quantum efficiency by studying a series of CdSe nanocrystals with a tunable cadmium/selenium stoichiometry. In II–VI semiconductors, the conduction band levels are primarily made up from the metal s orbitals, whereas the valence band is mainly composed of the chalcogenide p orbitals. Since unpassivated cadmium and selenium sites act as potential electron and hole traps respectively, both species have to be taken into account when examining ligand passivation. It was found that alkyl amine ligands (metal binding) have a minor effect on the QY of Se–rich nanocrystals while the emission of Cd–rich particles was greatly increased. The opposite was true for trioctylphosphine (chalcogenide binding) as the passivant. This highlights the selectivity of metal and chalcogenide binding ligands and the critical dependence of NC luminescence on their surface stoichiometry. Following those considerations, specific passivation of CdSe with a binary ligand system recently demonstrated the reproducible formation of highly luminescent quantum dots [56].

While the general optical effect of ligands is governed by their relative energy level configurations, the magnitude of this effect is related to the degree of surface coverage. In this regard steric aspects have to be considered. Ligand packing on nanocrystal surfaces can be modelled employing simple geometric calculations. Katari et al. [57] used cone shapes to represent ligand molecules with their dimensions governed by the ligands swept–out radius r_{sweep} and extended molecule length l. As illustrated in Figure 1.21, the maximum number of ligand cones n_{cone} which can fit on a particle surface can be determined by:

$$n_{cone} = \frac{4\pi(r+l)^2}{\pi r_{sweep}^2} \times \frac{\pi}{3\sqrt{2}} \quad , \tag{1.48}$$

where the first term represents the surface area of a ligand coated nanocrystal divided by the area of one ligand cone base, and the second term accounts for the closest packing fraction of equally sized circles. Next, the number of surface atoms on a nanocrystal surface for a given radius r is determined through:

$$n_{SA} = \frac{4}{3}\pi r^3 - \frac{4}{3}\pi(r-c_l)^3 \frac{\rho N_A}{M} \quad , \tag{1.49}$$

where c_l is the thickness of an atomic monolayer (half the standard unit cell height), ρ is the material density, N_A is the Avogadro constant and M is the molar mass. Dividing the number of surface atoms by the maximum number of ligand cones one obtains the percent surface coverage. This percentage is plotted for a CdSe NC as a function of radius for a range of ligand swept–out radii in the bottom graph of Figure 1.21. Assuming a uniform distribution of cadmium and selenium surface atoms, a 50 % coverage means that every Cd atom is bound to one metal binding ligand molecule on average, with nothing bound to the surface of Se

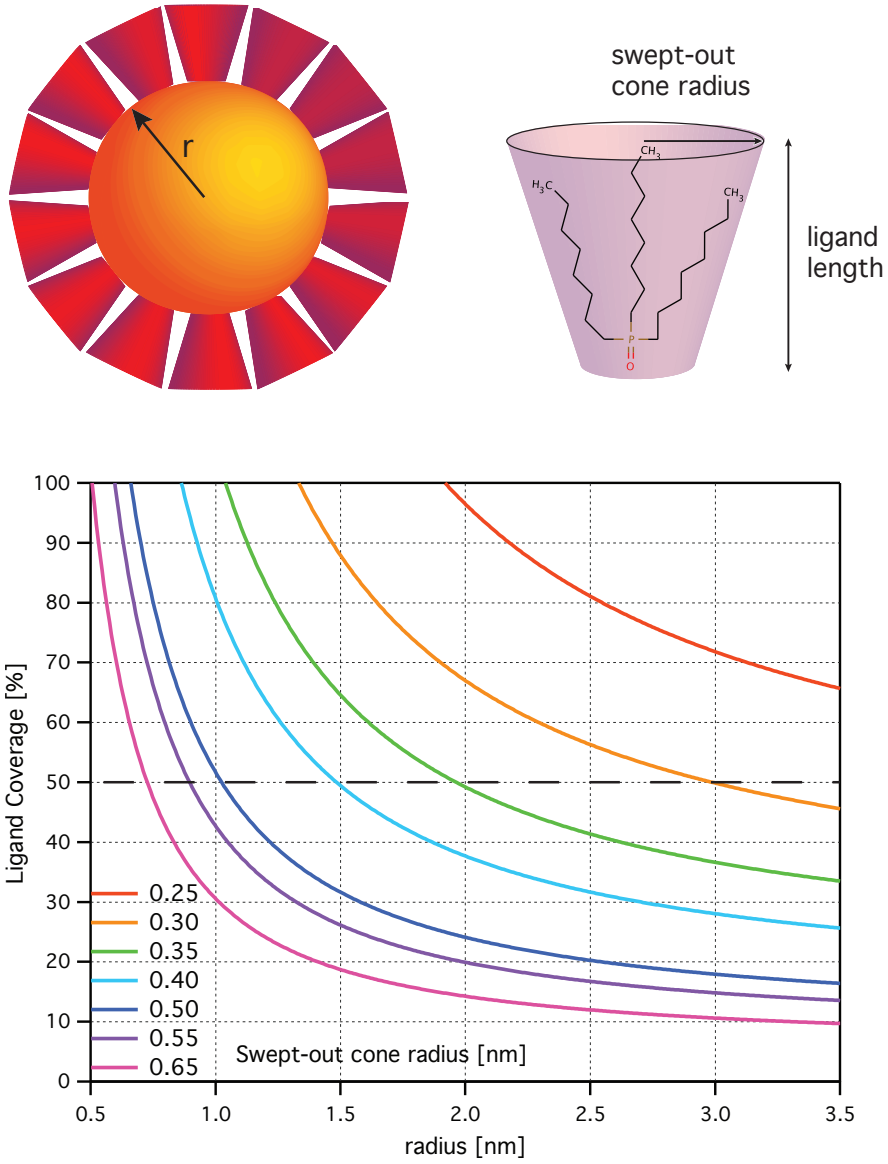

Figure 1.21 Model for ligand packing on nanocrystal surfaces [57]. TOP: Schematic of a spherical nanocrystal with radius r, capped with close packed ligands represented by cone shapes. The dimensions of the cone are determined trough the structural attributes of the ligand (here TOPO). BOTTOM: Calculated maximum coverage of ligand cones on CdSe nanocrystals for a ligand length of 9.9 Å(TOPO [58]).

atoms. Examining the graph, two general trends are observed: First, the increasing passivation percentage with decreasing particle radius can be explained via steric considerations. On a smaller nanocrystal, the curvature is greater than for a larger nanocrystal. Thus, larger nanocrystals cannot accommodate as close a packing of surface ligands as smaller ones, leading to a lower surface coverage. Second, for a given particle size, the surface coverage increases with decreasing swept–out radius, since less bulky ligands lead to less steric hindrance and a higher number of ligands can be fit onto the crystal surface. This trend can be observed experimentally given that the degree of surface passivation directly relates to an enhancement of emission intensity. By coating CdSe nanocrystals with primary, secondary and tertiary alkylamine ligands, Bullen et al. [51] demonstrated that luminescence enhancements clearly followed the trend: primary $\gg$ secondary $>$ tertiary amines. Furthermore, it was found that the alkyl chain lengths ranging from C_2 to C_{18} had no significant effect on the emission intensity.

As all capping ligands reversibly bind to the nanocrystal surface their adsorption/desorption is controlled primarily by their solubility in the given solvent [51] and the concentration of free ligand. This generally leads to a PL decline upon purification or dilution of nanocrystal solutions due to ligand desorption [50] and concomitant generation of surface site vacancies (traps states). As a result of the labile nature of surfactant binding and the previously discussed steric issues of surface coverage, ligand passivation is unsuitable for practical nanocrystal applications where a high QY, environmental robustness and long–term stability are important. These requirements can be met by growing an epitaxial inorganic shell of a suitable semiconductor material onto the NC cores, which not only passivates $\sim$100 % of surface sites but also enables band gap engineering through the combination of different semiconductor materials. An in–depth discussion of the synthesis and optical effects of epitaxial shells is presented in Chapters 3 to 5. At this stage, it is sufficient to state that epitaxial passivation (with an appropriate material) leads to the greatest reduction in the number of surface traps.

1.3 Blinking in Single Semiconductor Nanocrystals

Despite the substantial progress made in the control of colloidal nanocrystal synthesis it still results in an ensemble of size–distributed particles. As theoretically predicted (Section 1.1.5) and illustrated in Figure 1.22, quantum dots should exhibit discrete, atomic–like energy levels, and an absorption spectrum of ultra–narrow transitions. While the discrete nature of the absorption spectrum has been verified, the transition linewidths appear significantly broader than expected due to *homogeneous* broadening at room temperature and further

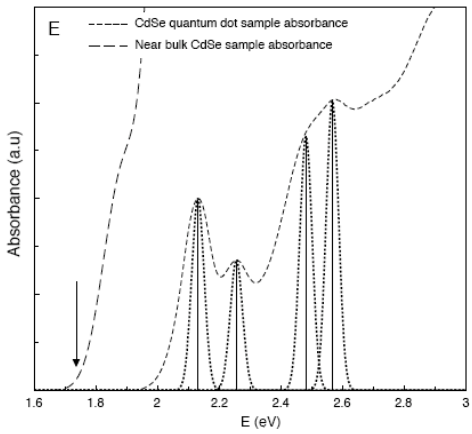

Figure 1.22 Plot of absorption spectra of near bulk CdSe crystals and CdSe quantum dots (dashed). The solid lines describe the hypothetical transitions of a single nanocrystal at zero Kelvin, while the dotted lines depict thermally broadened transitions [71].

inhomogeneous broadening due to the size distribution in ensembles*, leading to a loss of spectral information. As a consequence, single particle spectroscopy evolved as an important tool in order to overcome the effects of ensemble averaging [59]. The first spectroscopic photoluminescence studies on the single nanocrystal level revealed that the emission of an individual QD under continuous illumination switches intermittently between high (on) and low (off) intensity states [60, 61]. This phenomenon — commonly known as "blinking" — is universally observed in all types of fluorophores [62], including molecules [63], quantum dots of several materials [64–67], as well as nanorods [68] and even nanowires [69, 70].

1.3.1 Key Features of Fluorescence Intermittency

Following the assumption of *binary* blinking (on/off), it is customary to characterise the PL dynamics via binning the detected on– and off–times, which are discriminated by a suitable (but arbitrary) chosen intensity threshold. Unlike in the case of single molecules, histograms of the on– and off–times of single NCs exhibit highly non–exponential probability distributions. Employing the threshold analysis, these histograms were found to be best fitted by inverse power laws [66, 72, 73] of the type:

$$P(t_{on/off}) = At^{-m_{on/off}} \quad , \tag{1.50}$$

* It is worth noting that the full width half maximum of the band edge absorption is commonly utilised as a first indicator for the size distribution of a NC ensemble.

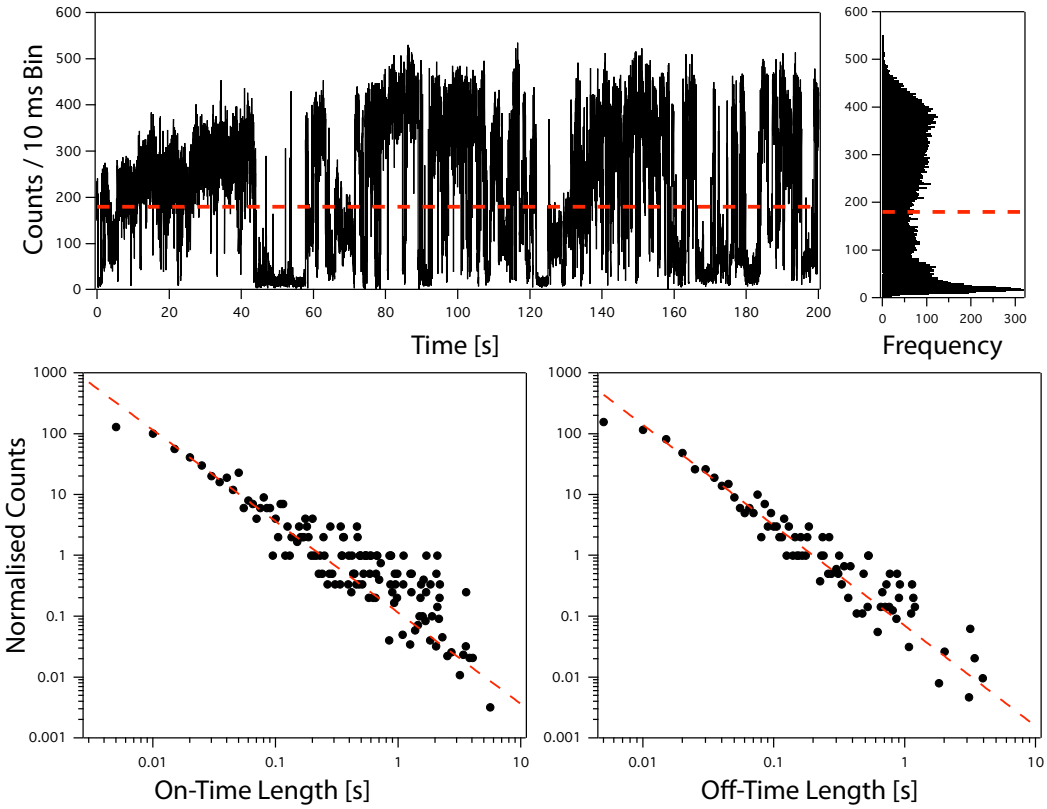

Figure 1.23 Top: PL trajectory of a single CdSe/CdS/CdZnS core/shell nanocrystal with corresponding intensity histogram. The red dashed line marks the chosen threshold to discriminate between the on– and off–state. Bottom: Log versus log plots of on– and off–length histograms compiled from the blinking trace. The data is fitted to an inverse power law (red dashed line) yielding an exponent m of 1.5 and 1.65 for on– and off–times respectively.

where $m_{on/off}$ is a dimensionless quantity that characterises the distribution function $P(t)$, and ranges from 1.2 to 2.0 [59]. For colloidal quantum dots, those power laws can extend over a wide range that spans up to nine orders of magnitude in probability density and five to six orders of magnitude in time, as shown in Figure 1.23. The appearance of such power law (scale–free) kinetics has important implications for the analysis of the temporal evolution of the PL intensity. Since the shortest and longest observed time scales for blinking events are currently set by experimental limitations (bin time, total observation time), those subjectively set parameters as well as the selected intensity thresholds will inevitably affect the resulting statistics [74]. Thus, very stringent experimental conditions are needed to accurately determine these probability distributions [75]. Furthermore, the lack of a characteristic time scale points to a wide distribution of rates, since any single rate process would lead to a single exponential distribution for both on– and off–times.

Studying the effects of temperature and excitation power it was found that the power law slopes for both on– and off–times are generally temperature independent between 10 and 400 K [66, 72, 73, 76] suggesting tunnelling or another temperature independent, light–driven mechanism to be responsible for photoluminescence intermittency. While the off–times were found to be insensitive to excitation power, on–times were observed to decrease linearly with increasing intensity [60, 76]. Additionally, a secondary, photoinduced process leads to a truncation of the on–time power law slope ('cutoffs') at long times, where the truncation time decreases with increasing intensity [66].

Several groups have investigated the effects of the environment on the blinking behaviour of QDs, however with partly conflicting results. Isaac et al. [77] reported a dependence of blinking statistics on the dielectric environment where an increase in matrix polarity led to longer off–times. In another study by Pelton et al. [78], the recorded power noise spectra of ensemble NC emission — which reflect the photoluminescence intermittency of individual dots — exhibited a power law of the form $p(f) \sim f^{-\alpha} (\alpha \sim 1)$. Comparing a dense film of nanocrystals deposited on glass with NCs dispersed in chloroform, they observed identical (within experimental error) values for the power law exponent, in sharp contrast with the results of Isaac et al. The insensitivity of QD blinking statistics to a change in the dielectric environment is further supported by the findings of Stefani et al. [79] which showed no difference when comparing nanocrystals placed on glass and (conductive) ITO substrates.

In another account, Koberling et al. [80] and Müller et al. [81] investigated the influence of the gaseous surroundings on the resultant power law distributions. Comparing the effect of argon and oxygen atmospheres, Koberling observed a shortening in on–times and a general decrease in count rates upon exposure to oxygen. In contrast, Müller et al. observed a dramatic enhancement of the photoluminescence intensity from single core/shell CdSe/ZnS nanocrystals upon sudden exposure to air from an evacuated surrounding. Both the number of particles contributing to emission as well as the average emission intensity from a single particle increased. The presence of air resulted in a shortening of off–times compared to vacuum whereas the statistics for the on–times remained unaffected. To gain further insight, the effect of each major constituent of air on the off–time statistics was tested. It was found that the simultaneous presence of water and oxygen was crucial for the observed emission enhancement.

The presented results illustrate the difficulty to unambiguously discern the role of environmental factors on the NC blinking behaviour. On the one hand, some trends might be obscured by differently chosen experimental parameters, affecting the obtained statistics. On the other hand, differences in the synthetic approach of the analysed quantum dots could be responsible for the seemingly contradicting observation. As discussed before, the optical

properties of NCs are highly sensitive to the synthetic route and state of surface passivation, precluding a direct comparison of those results.

The effect of surface passivation on the blinking statistics was examined by Hohng et al. [82] who could demonstrate almost complete blinking suppression by coating the surface of CdSe/ZnS nanocrystals with β–mercaptoethanol (BME) under bio–compatible conditions. This effect was reversible upon ligand removal and only modified the on–times leaving the off–time statistics unchanged. In another study, Gomez et al. [83] examined the effects of octylamine ligands and epitaxially grown CdS shells on the PL intermittency of CdSe nanocrystals. While their observation of on–time modification is consistent with the work of Hong et al. they also reported a change in the off–time probability distribution. Gomez et al. related those changes to the degree of surface passivation and established a clear trend of decreasing m_{on} times and increasing m_{off} times when going from bare CdSe NCs to octylamine–capped CdSe to CdSe/CdS core/shells. The effect of shelling CdSe nanocrystals with a wide band gap material was also reported by Shimizu et al. [66] where a claimed six monolayer ZnS shell led to a modification of the truncation time of the on–time histograms while the off–time statistics remained unchanged. These three independent reports are consistent in that — in spite of the somewhat different effects — surface passivation appears to play a distinct role in the blinking mechanism [84, 85].

An insight that was reached through the utilisation of time correlated single photon counting (TCSPC) is that the photoluminescence intermittency of single NCs does not actually follow a binary level behaviour but consists of multiple recombination channels. First demonstrated by Schlegel et al. [86], TCSPC measurements of single CdSe/ZnS quantum dots revealed that the photoluminescence decay time fluctuates during the measurement time leading to a multi exponential decay and implicating a manifold of recombination pathways. It was found that the PL intensity correlates positively with decay time, being consistent with a model of fluctuating non–radiative decay channels that lead to variable dynamic quenching processes of the excited state. This observation was later confirmed by Fisher et al. [87] who could additionally show that, by selecting only the photons near maximum intensity, a single exponential decay is obtained which was found to be consistent across different independently synthesized samples. In agreement with the study of Schlegel they assigned the variations in decay rates and emission intensity to fluctuations in non–radiative relaxation pathways.

Since the traditional threshold method is not suitable to reliably discriminate multiple intensity levels, Zhang et al. [88] employed a method derived from information theory, namely the changepoint method [89], to analyse emission trajectories of CdSe/ZnS core/shell NCs. Utilising this technique, a continuous distribution of emission states was found, consistent with the reports discussed previously. Furthermore, the limitations of the traditional threshold

method were highlighted by demonstrating how the intensity histogram can be obscured by the choice of bin time, whereas the changepoint method is statistically unbiased and systematic.

Very recently, Gomez et al. [90] reported on the emission trajectories of highly crystalline CdSe/CdS core/shells. They identified a well defined three level pattern where a low quantum yield intermediate state connects the commonly observed "on" and "off" states. The emission of the intermediate state is assigned to a positive trion state, which is supported by several recent observations [91–93], despite the long standing presumption that trions are responsible for the off–states in blinking trajectories [94]. In accordance with the findings by Fisher and Schlegel, the intensity levels were found to be strongly correlated to their respective lifetimes, with a single rate process connecting the high and intermediate state and a multi–exponential decay rate linking the intermediate and low intensity level. The blinking trajectories were analysed by extending the threshold method to two intensity thresholds in order to account for the third intensity level. This approach seemed suitable as the three states were narrow and well defined. However, it was pointed out that the changepoint method would have lead to a more robust identification of number and magnitude of intensity levels.

Furthermore, Gomez et al. examined the influence of the gaseous surrounding on those core/shell particles, changing the environment between dry and wet nitrogen. While a dry nitrogen atmosphere led to a loss of the three level emission pattern and generally low emission yield, the introduction of water into the nitrogen flow recovered the three–state structure. The authors assigned this behaviour to an enhanced passivation of surface states through oxygen and water molecules, in agreement with earlier studies [80, 81]. The observation of the three state system, in contrast to the traditional binary behaviour reported for CdSe/CdS core/shells [76, 83], was attributed to the superior synthetic methods employed [3, 95]. Earlier reports were based on samples synthesised by organometallic routes which offer inferior growth control and lead to a high degree of crystal defects.

1.3.2 Theoretical Models of Blinking

Having presented the key experimental findings made in the study of single nanocrystal fluorescence, we now proceed to discuss the current theoretical models used to describe the underlying mechanism of blinking. The first quantum dot blinking model was developed by Efros and Rosen [94], which is still one of the most widely used mechanisms in spite of its numerous shortcomings. Figure 1.24 illustrates the proposed mechanism in which the "off" periods are assigned to the times when the nanocrystal resides in an ionized state. In such a case the luminescence is quenched by non–radiative Auger recombination, which is mediated by enhanced Coulomb interactions between the electron and hole in the strong confinement regime. Upon strong laser illumination multiple excitons can be formed and

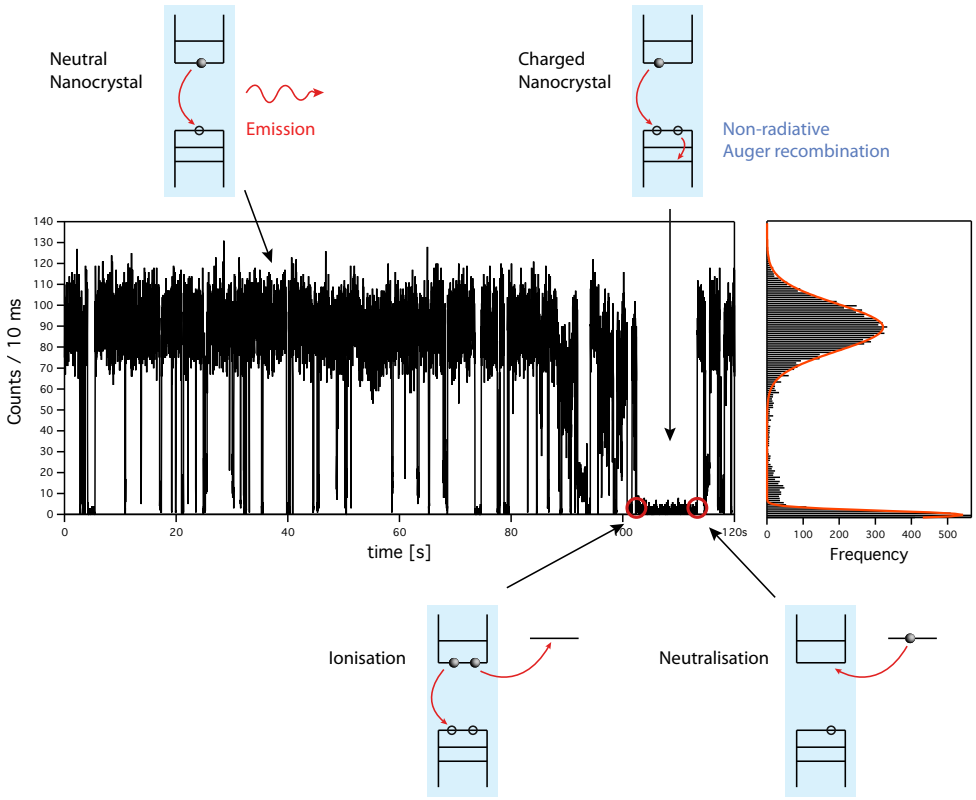

Figure 1.24 Blinking mechanism according to Efros and Rosen [94]. The photoluminescence trajectory of a single nanocrystal displays a binary pattern, manifesting in a characteristic histogram of two Gaussian distributions (right). In this model, the high intensity state is assigned to radiative exciton recombination from a charge neutral NC, while the dot is rendered dark when ionised.

the energy released from a single electron–hole recombination event facilitates the ejection of another charge carrier (typically an electron) into the surrounding matrix, leaving the particle in an ionised state. In this charged state, the screening of Coulomb interactions is diminished leading to a strong enhancement of Auger processes. Since Auger pathways are several orders of magnitude faster than radiative recombination, subsequently formed excitons experience rapid non–radiative relaxation via those channels, quenching any emission and thereby rendering the quantum dot dark. Once the ejected charge carrier returns to the NC (neutralising it) radiative recombination is recovered. This model provided the first intuitive picture to explain the blinking observations in NCs. However, a key issue of this theory is that it predicts characteristic on/off rates and corresponding exponential probability distributions, in sharp contrast with the experimentally found power–law statistics.

To overcome those limitations, a series of modified models utilizing the long–lived trap hypothesis have been suggested in the literature [66, 96, 97]. Verberk et al. [98] assigned the

ionisation process to electron tunnelling towards a uniform spatial distribution of traps in the surrounding matrix. Owing to a static distribution of trapping and de–trapping rates which are governed by a distance r of the trap state from the NC surface and trap depth ΔE, the rate of tunnelling k_{tunnel} is given by:

$$k_{tunnel} = k_0 exp\left(-\frac{2}{\hbar}\sqrt{2m_e r\Delta E}\right) \quad , \tag{1.51}$$

which, by following a statistical argument, predicts power law off–time distributions. Here k_0 represents the electron tunnelling attempt frequency. Following the assumption of a homogeneous trap state distribution, the trapping probability decays exponentially with distance r. The probability density function for a charge carrier to tunnel a distance r from the NC surface is therefore $p(r) = \alpha e^{-\alpha r}$. The recovery rate, describing the back–tunnelling rate of the trapped electron to the ionised NC also varies exponentially with distance r, which is of the from $e^{-\beta r}$, but with a different decay length. Further assuming that the recovery time t also shows an exponential decay behaviour with distance, power laws are obtained when calculating those neutralisation time distributions, $p(t)$, with their exponents depending on the barrier heights. Explicitly, the off–time exponent is given by:

$$m_{off} = 1 + \sqrt{\frac{\alpha}{\beta}} = 1 + \sqrt{\frac{\Delta E_{NC\rightarrow T}}{\Delta E_{T\rightarrow NC}}} \quad , \tag{1.52}$$

where the subscripts in ΔE indicate the tunnelling direction. In this framework, the barrier heights, and therefore the exponent values, are determined by the material dependent parameters of the nanocrystals and the trap states in a particular matrix. This would be consistent with the effects of a changing dielectric environment on the blinking behaviour as reported by Isaac et al.[77], however conflicting with the studies by Pelton et al. [78] and Stefani et al. [79] who could not observe matrix–related effects on the blinking statistics. Additionally, the model fails to account for the power law distributed on–times, but would readily explain the lack of temperature dependence [66, 72, 73, 76] for both histograms due to the tunnelling–based mechanism.

Frantsuzov and Marcus [99] postulated an alternative mechanism that is based on surface trapping without the need for a long–lived external trap (ionisation), contradicting the original charging model [94]. In this framework the QD always returns back to the neutral ground state after photoexcitation directly or via surface states. The on/off switching of the NC luminescence intensity is thought to be caused by large variations of the non–radiative relaxation rate via hole trap states at the surface. The hole trapping is assumed to be induced by an Auger–assisted mechanism. As depicted on Figure 1.25, the surface states are thought to form an energy band located within the band gap, close to the valence band. Upon exciton

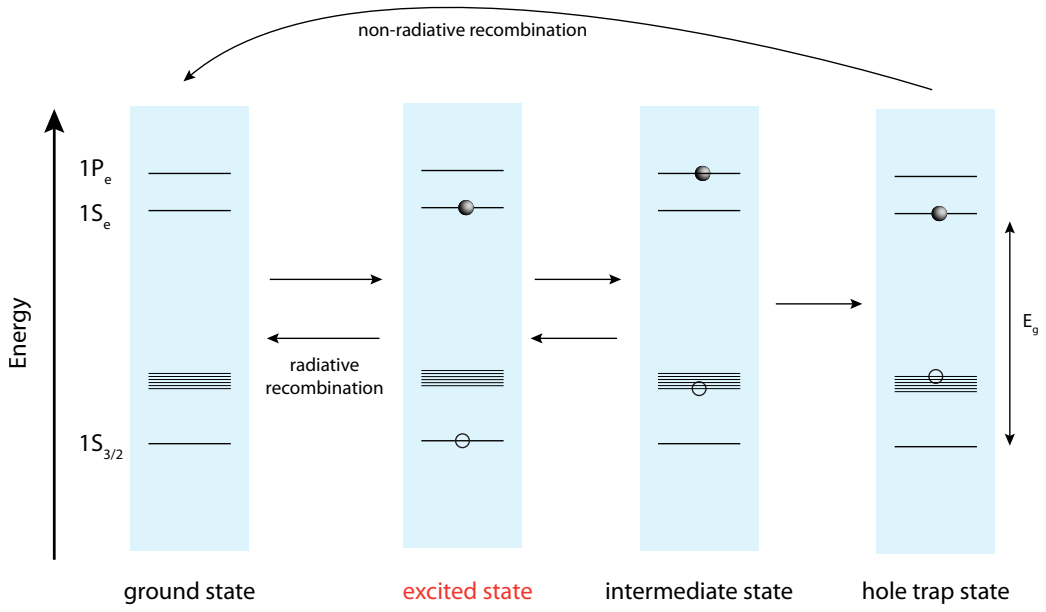

Figure 1.25 Blinking mechanism according to Frantsuzov and Marcus [99].

formation the hole can be trapped in the surface trap band. With the energy released form this trapping, the electron is subsequently promoted (via an Auger process) from the $1S_e$ to the $1P_e$ state (intermediate state). Following a phonon assisted relaxation of the charge carriers, the trap state ($1S_e$ + trapped hole) recombines non–radiatively to return back to the ground state. To explain the temporal evolution of blinking an additional assumption was made, namely that the energy difference, ε, between the $1S_e$ and the $1P_e$ state is subject to a light–driven diffusion process, which in turn strongly modifies the hole trapping rate. If ε is higher than a given value, the hole trapping rate becomes efficient, rendering the nanocrystal non–emissive. When the situation is reversed and ε is lower than the critical value, radiative recombination dominates the excitation dynamics and the NC switches to a bright state.

To recover the power law distribution of on– and off–times, the variation of ε was described by a diffusion equation with the diffusion coefficient proposed to be proportional to the excitation intensity and to depend only weakly on temperature. However it could depend on the environment and the QD preparation procedure. This model could successfully account for several experimentally found observations including the truncation of on–time distributions and its dependence on excitation intensity as well as the insensitivity of off–times regarding temperature and laser intensity changes. However, it predicts a constant power law exponent of $-3/2$ which cannot be altered. A model that overcomes this limitation was proposed by Tang and Marcus [100–102] which is based on a mechanism involving diffusion–controlled

electron transfer processes, similar to the considerations for the variable ε of Frantsuzov and Marcus.

It is important to bear in mind that in the theoretical models presented so far, the assumption of *binary* blinking is implicit. This is not consistent with the earlier discussed experimental observations of continuous emission intensity distributions [88] and three–level blinking [90], suggesting that photoluminescence intermittency *cannot* be described with any two–state model.

Following those experimental facts, a novel theoretical framework was recently reported [74]. Here, Fransuzov et al. attribute the fluctuations of emission intensity to atomic rearrangements in the QD surface layer. Based on the power noise studies on single NCs by Pelton et al. [78, 102], the model proposes an environment consisting of multiple stochastic two–level systems (TLS). As suggested before [99], non–radiative recombination is assumed to occur via hole trapping in any of the N quenching centres, which can switch dynamically between inactive and active conformations. Theses two conformational states (TLS) differ in their ability to trap holes ($k_{active} \ggg k_{inactive}$) and are postulated to be switched via light–induced jumps of surface atoms (e.g. ligand rearrangement) between two quasi–stable positions. Since surface atoms in a colloidal QD can be found in a variety of local crystal configurations, a wide distribution of switching rates can be expected. Thus, the non–radiative trapping rate in this model can be expressed as:

$$k_t(t) = \sum_{i=1}^{N} k_i \sigma_i(t) + k_0 \quad , \tag{1.53}$$

where the stochastic variable $\sigma_i(t)$ for each TLS randomly jumps between 0 (inactive) and 1 (active), k_i is the trapping rate in the active configuration and k_0 is the background non–radiative relaxation rate. This model is successful in describing several experimental facts including the truncated power law distributions, weak temperature dependence, and the power noise spectrum shape. Furthermore it accurately describes the strong dependence of power law distribution parameters and truncation times on the chosen intensity threshold, highlighting the bias introduced by this method of data analysis. Finally, it accounts for the continuous distribution of emission intensities as well as the correlations between subsequent blinking events [103, 104].

In summary it is evident that the detailed mechanism of blinking in single NCs is still not completely understood. However, substantial theoretical and experimental progress has been made: Firstly, strong evidence has emerged over the last decade indicating that the widely used charging model [94] is insufficient to describe fluorescence intermittence. This has led to a range of alternative models: Secondly, the traditional threshold method to analyse

on/off probability distributions was found not to be statistically robust, since it introduces artefacts dependent on the choice of threshold level [74, 75]. Additionally, since blinking was found *not* to be binary, it is not suitable for data analysis of multi–level intensity trajectories [88]; Finally, the non–radiative relaxation channels were found to be intimately related to particle *intrinsic* surface or defect states rather than external traps. The latter inspired several approaches aiming to minimise the number of those trap states, thus leading to suppressed blinking [82, 91, 105, 106][†].

1.4 Conclusion

The aim of this chapter is to provide the reader with a competent knowledge of the physical, chemical and optical properties of semiconductor nanocrystals, which forms the basis for the rest of this thesis. We presented the theoretical description of quantum confinement in those structures within the effective mass approximation employing a finite potential well model. Reviewing the aspects of semiconductor nanocrystal synthesis and their optical properties, particular attention was given to the role of the particle *surface* which was found to have a major impact on the physical properties of those materials. This surface dependence was reflected in the crucial role of capping ligands during synthesis and subsequent surface passivation. Discussing the phenomenon of fluorescence intermittency, observable on the single particle level, confirmed the strong relationship between the degree of surface passivation and the emission properties of NCs.

[†] A detailed discussion of this topic along with our experimental approach to blinking suppression will be presented in Chapter 4.

Bibliography

[1] L. E. Brus. The Journal of Chemical Physics **80**, 4403 (1984).

[2] C. B. Murray, D. J. Norris and M. G. Bawendi. Journal of the American Chemical Society **115**, 8706 (1993).

[3] J. van Embden and P. Mulvaney. Langmuir **21**, 10226 (2005).

[4] X. Peng, L. Manna, W. Yang, J. Wickham, E. Scher, A. Kadavanich and A. P. Alivisatos. Nature **404**, 59 (2000).

[5] M. A. Hines and P. Guyot-Sionnest. Journal of Physical Chemistry **100**, 468 (1996).

[6] J. J. Li, Y. A. Wang, W. Guo, J. C. Keay, T. D. Mishima, M. B. Johnson and X. Peng. Journal of the American Chemical Society **125**, 12567 (2003).

[7] Z. A. Peng and X. Peng. Journal of the American Chemical Society **123**, 183 (2001).

[8] J. Jasieniak, C. Bullen, J. van Embden and P. Mulvaney. J Phys Chem B Condens Matter Mater Surf Interfaces Biophys **109**, 20665 (2005).

[9] C. Bullen, J. van Embden, J. Jasieniak, J. E. Cosgriff, R. J. Mulder, E. Rizzardo, M. Gu and C. L. Raston. Chemistry of Materials **22**, 4135 (2010).

[10] J. H. Davies. *The physics of low-dimensional semiconductors: An introduction* (Cambridge University Press, 1998).

[11] J. J. Jasieniak. *Synthesis and Application of II–VI Semiconductor Quantom Dot*. Ph.D. thesis, The University of Melbourne, School of Chemistry (2008).

[12] S. Kim, B. Fisher, H. Eisler and M. Bawendi. J. Am. Chem. Soc **125**, 11466 (2003).

[13] L. Brus. Journal of Physical Chemistry **90**, 2555 (1986).

[14] L. Wang and A. Zunger. Physical Review B **53**, 9579 (1996).

[15] J. W. Mullin. *Crystallization*. 4 ed. (Butterworth-Heinemann, Boston, 2001).

[16] V. LaMer and R. Dinegar. Journal of the American Chemical Society **72**, 4847 (1950).

[17] J. van Embden, J. E. Sader, M. Davidson and P. Mulvaney. The Journal of Physical Chemistry C **113**, 16342 (2009).

[18] W. Ostwald. Zeitschrift für Physikalische Chemie **34**, 495 (1900).

[19] T. Sugimoto. Advances in Colloid and Interface Science **28**, 65 (1987).

[20] X. Peng, J. Wickham and A. Alivisatos. J. Am. Chem. Soc **120**, 5343 (1998).

[21] J. Thessing, J. Qian, H. Chen, N. Pradhan and X. Peng. Journal of the American Chemical Society **129**, 2736 (2007).

[22] Z. A. Peng and X. Peng. Journal of the American Chemical Society **124**, 3343 (2002).

[23] D. Talapin, A. Rogach, M. Haase and H. Weller. J. Phys. Chem. B **105**, 12278 (2001).

[24] J. Y. Rempel, M. G. Bawendi and K. F. Jensen. Journal of the American Chemical Society **131**, 4479 (2009).

[25] A. Fojtik, H. Weller, U. Koch and A. Henglein. Berichte der Bunsengesellschaft für physikalische Chemie **88**, 969 (1984).

[26] M. Steigerwald, A. Alivisatos, J. Gibson, T. Harris, R. Kortan, A. Muller, A. Thayer, T. Duncan, D. Douglass and L. Brus. Journal of the American Chemical Society **110**, 3046 (1988).

[27] L. Qu, Z. A. Peng and X. Peng. Nano Letters **1**, 333 (2001).

[28] W. W. Yu and X. Peng. Angewandte Chemie International Edition **41**, 2368 (2002).

[29] C. R. Bullen and P. Mulvaney. Nano Letters **4**, 2303 (2004).

[30] S. Deka, K. Miszta, D. Dorfs, A. Genovese, G. Bertoni and L. Manna. Nano Letters **10**, 3770 (2010).

[31] L. Carbone, C. Nobile, M. De Giorgi, F. D. Sala, G. Morello, P. Pompa, M. Hytch, E. Snoeck, A. Fiore, I. R. Franchini, M. Nadasan, A. F. Silvestre, L. Chiodo, S. Kudera, R. Cingolani, R. Krahne and L. Manna. Nano Letters **7**, 2942 (2007).

[32] D. V. Talapin, J. H. Nelson, E. V. Shevchenko, S. Aloni, B. Sadtler and A. P. Alivisatos. Nano Letters **7**, 2951 (2007).

[33] X. Peng. Advanced Materials **15**, 459 (2003).

[34] L. Manna, E. C. Scher and A. P. Alivisatos. Journal of the American Chemical Society **122**, 12700 (2000).

[35] A. Hassinen, I. Moreels, C. de Mello Donegá, J. Martins and Z. Hens. The Journal of Physical Chemistry Letters **1**, 2577 (2010).

[36] B. Fritzinger, R. K. Capek, K. Lambert, J. Martins and Z. Hens. Journal of the American Chemical Society **132**, 10195 (2010).

[37] C. M. Evans, M. E. Evans and T. D. Krauss. Journal of the American Chemical Society **132**, 10973 (2010).

[38] Z. H. Sun, H. Oyanagi, M. Uehara, H. Nakamura, K. Yamashita, A. Fukano and H. Maeda. The Journal of Physical Chemistry C **113**, 18608 (2009).

[39] H. Liu, J. S. Owen and A. P. Alivisatos. Journal of the American Chemical Society **129**, 305 (2006).

[40] P. Schapotschnikow, B. Hommersom and T. J. H. Vlugt. The Journal of Physical Chemistry C **113**, 12690 (2009).

[41] A. Puzder, A. J. Williamson, N. Zaitseva, G. Galli, L. Manna and A. P. Alivisatos. Nano Letters **4**, 2361 (2004).

[42] X. Peng. Accounts of Chemical Research **43**, 1387 (2010).

[43] E. Scher, L. Manna and A. Alivisatos. Philosophical Transactions of the Royal Society of London. Series A: Mathematical, Physical and Engineering Sciences **361**, 241 (2003).

[44] F. Wang, R. Tang and W. E. Buhro. Nano Letters **8**, 3521 (2008).

[45] M. Sun and X. Yang. The Journal of Physical Chemistry C **113**, 8701 (2009).

[46] O. Chen, X. Chen, Y. Yang, J. Lynch, H. Wu, J. Zhuang and Y. Cao. Angewandte Chemie International Edition **47**, 8638 (2008).

[47] A. Toyota, H. Nakamura, H. Ozono, K. Yamashita, M. Uehara and H. Maeda. The Journal of Physical Chemistry C **114**, 7527 (2010).

[48] E. M. Chan, C. Xu, A. W. Mao, G. Han, J. S. Owen, B. E. Cohen and D. J. Milliron. Nano Letters **10**, 1874 (2010).

[49] T. Dannhauser, M. O'Neil, K. Johansson, D. Whitten and G. McLendon. The Journal of Physical Chemistry **90**, 6074 (1986).

[50] G. Kalyuzhny and R. W. Murray. Journal of Physical Chemistry B **109**, 7012 (2005).

[51] C. Bullen and P. Mulvaney. Langmuir **22**, 3007 (2006).

[52] S. F. Wuister, C. de Mello Donegá and A. Meijerink. The Journal of Physical Chemistry B **108**, 17393 (2004).

[53] J. Völker, X. Zhou, X. Ma, S. Flessau, H. Lin, M. Schmittel and A. Mews. Angewandte Chemie International Edition **49**, 6865 (2010).

[54] C. Landes, C. Burda, M. Braun and M. A. El-Sayed. The Journal of Physical Chemistry B **105**, 2981 (2001).

[55] J. Jasieniak and P. Mulvaney. J Am Chem Soc **129**, 2841 (2007).

[56] W. Kim, S. J. Lim, S. Jung and S. K. Shin. The Journal of Physical Chemistry C **114**, 1539 (2010).

[57] J. E. B. Katari, V. L. Colvin and A. P. Alivisatos. The Journal of Physical Chemistry **98**, 4109 (1994).

[58] M. Marcus, W. Flood, M. Stiegerwald, L. Brus and M. Bawendi. The Journal of Physical Chemistry **95**, 1572 (1991).

[59] D. E. Gomez, M. Califano and P. Mulvaney. Phys Chem Chem Phys **8**, 4989 (2006).

[60] M. Nirmal, B. O. Dabbousi, M. G. Bawendi, J. J. Macklin, J. K. Trautman, T. D. Harris and L. E. Brus. Nature **383**, 802 (1996).

[61] S. A. Empedocles, D. J. Norris and M. G. Bawendi. Physical Review Letters **77**, 3873 (1996).

[62] P. Frantsuzov, M. Kuno, B. Janko and R. A. Marcus. Nat Phys **4**, 519 (2008).

[63] J. N. Clifford, T. D. M. Bell, P. Tinnefeld, M. Heilemann, S. M. Melnikov, J.-i. Hotta, M. Sliwa, P. Dedecker, M. Sauer, J. Hofkens and E. K. L. Yeow. The Journal of Physical Chemistry B **111**, 6987 (2007).

[64] J. Tittel, W. Gohde, F. Koberling, T. Basche, A. Kornowski, H. Weller and A. Eychmuller. Journal of Physical Chemistry B **101**, 3013 (1997).

[65] F. Koberling, A. Mews and T. Basché. Physical Review B **60**, 1921 (1999).

[66] K. T. Shimizu, R. G. Neuhauser, C. A. Leatherdale, S. A. Empedocles, W. K. Woo and M. G. Bawendi. Physical Review B **63**, 205316 (2001).

[67] M. Kuno, D. P. Fromm, A. Gallagher, D. J. Nesbitt, O. I. Micic and A. J. Nozik. Nano Letters **1**, 557 (2001).

[68] S. Wang, C. Querner, T. Emmons, M. Drndic and C. H. Crouch. Journal of Physical Chemistry B **110**, 23221 (2006).

[69] J. J. Glennon, W. E. Buhro and R. A. Loomis. The Journal of Physical Chemistry C **112**, 4813 (2008).

[70] J. J. Glennon, R. Tang, W. E. Buhro and R. A. Loomis. Nano Letters **7**, 3290 (2007).

[71] J. van Embden. *Synthesis and Optical Proeperties of CdSe Core and Core/Shell Nanocrystals*. Ph.D. thesis, The University of Melbourne, School of Chemistry (2008).

[72] M. Kuno, D. P. Fromm, H. F. Hamann, A. Gallagher and D. J. Nesbitt. The Journal of Chemical Physics **112**, 3117 (2000).

[73] M. Kuno, D. P. Fromm, H. F. Hamann, A. Gallagher and D. J. Nesbitt. The Journal of Chemical Physics **115**, 1028 (2001).

[74] P. A. Frantsuzov, S. Volkan-Kacso and B. Janko. Physical Review Letters **103**, 207402 (2009).

[75] C. H. Crouch, O. Sauter, X. Wu, R. Purcell, C. Querner, M. Drndic and M. Pelton. Nano Letters **10**, 1692 (2010).

[76] U. Banin, M. Bruchez, A. P. Alivisatos, T. Ha, S. Weiss and D. S. Chemla. The Journal of Chemical Physics **110**, 1195 (1999).

[77] A. Issac, C. von Borczyskowski and F. Cichos. Physical Review B **71**, 161302 (2005).

[78] M. Pelton, D. G. Grier and P. Guyot-Sionnest. Applied Physics Letters **85**, 819 (2004).

[79] F. D. Stefani, W. Knoll, M. Kreiter, X. Zhong and M. Y. Han. Physical Review B **72**, 125304 (2005).

[80] F. Koberling, A. Mews and T. Basche. Advanced Materials **13**, 672 (2001).

[81] J. Muller, J. M. Lupton, A. L. Rogach, J. Feldmann, D. V. Talapin and H. Weller. Applied Physics Letters **85**, 381 (2004).

[82] S. Hohng and T. Ha. Journal of the American Chemical Society **126**, 1324 (2004).

[83] D. E. Gomez, J. van Embden, J. Jasieniak, T. A. Smith and P. Mulvaney. Small **2**, 204 (2006).

[84] M. Jones, S. S. Lo and G. D. Scholes. Proceedings of the National Academy of Sciences **106**, 3011 (2009).

[85] V. Fomenko and D. J. Nesbitt. Nano Letters **8**, 287 (2008).

[86] G. Schlegel, J. Bohnenberger, I. Potapova and A. Mews. Physical Review Letters **88**, 137401 (2002).

[87] B. R. Fisher, H.-J. Eisler, N. E. Stott and M. G. Bawendi. The Journal of Physical Chemistry B **108**, 143 (2003).

[88] K. Zhang, H. Chang, A. Fu, A. P. Alivisatos and H. Yang. Nano Letters **6**, 843 (2006).

[89] L. P. Watkins and H. Yang. The Journal of Physical Chemistry B **109**, 617 (2004).

[90] D. E. Gómez, J. van Embden, P. Mulvaney, M. J. Fernée and H. Rubinsztein-Dunlop. ACS Nano **3**, 2281 (2009).

[91] X. Wang, X. Ren, K. Kahen, M. A. Hahn, M. Rajeswaran, S. Maccagnano-Zacher, J. Silcox, G. E. Cragg, A. L. Efros and T. D. Krauss. Nature **459**, 686 (2009).

[92] M. J. Fernée, B. N. Littleton and H. Rubinsztein-Dunlop. ACS Nano **3**, 3762 (2009).

[93] P. P. Jha and P. Guyot-Sionnest. ACS Nano **3**, 1011 (2009).

[94] A. L. Efros and M. Rosen. Physical Review Letters **78**, 1110 (1997).

[95] J. van Embden, J. Jasieniak, D. Gomez, P. Mulvaney and M. Giersig. Australian Journal of Chemistry **60**, 457 (2007).

[96] M. Kuno, D. P. Fromm, S. T. Johnson, A. Gallagher and D. J. Nesbitt. Physical Review B **67**, 125304 (2003).

[97] G. Margolin and E. Barkai. The Journal of Chemical Physics **121**, 1566 (2004).

[98] R. Verberk, A. M. van Oijen and M. Orrit. Physical Review B **66**, 233202 (2002).

[99] P. A. Frantsuzov and R. A. Marcus. Physical Review B **72**, 155321 (2005).

[100] J. Tang and R. A. Marcus. Physical Review Letters **95**, 107401 (2005).

[101] J. Tang and R. A. Marcus. The Journal of Chemical Physics **123**, 054704 (2005).

[102] M. Pelton, G. Smith, N. F. Scherer and R. A. Marcus. Proceedings of the National Academy of Sciences **104**, 14249 (2007).

[103] S. Volkán-Kacsó, P. A. Frantsuzov and B. Jankó. Nano Letters **10**, 2761 (2010).

[104] F. D. Stefani. New Journal of Physics **7**, 197 (2005).

[105] B. Mahler, P. Spinicelli, S. Buil, X. Quelin, J.-P. Hermier and B. Dubertret. Nat Mater **7**, 659 (2008).

[106] Y. Chen, J. Vela, H. Htoon, J. L. Casson, D. J. Werder, D. A. Bussian, V. I. Klimov and J. A. Hollingsworth. Journal of the American Chemical Society **130**, 5026 (2008).

2 Experimental Methods and Instrumentation

The purpose of this chapter is to provide the reader with a concise resource describing the generic experimental protocols and associated characterisation techniques employed throughout this thesis. Additionally, detailed discussions of electron microscopy and single particle spectroscopy, and their utilisation for nanocrystal characterisation will be presented. Specific details concerning particular experiments will be included within the respective chapters.

2.1 Chemicals and Solvents

2.1.1 Solvents

Methanol, ethanol, and acetone were purchased from Univar. Toluene and hexane were purchased from Chem–Supply. Chloroform and nonane were purchased form Merck and Fluka respectively. 2–methyl–tetrahydrofuran was obtained from Aldrich. All solvents were of analytical grade and used directly without any further purification unless otherwise stated.

2.1.2 Chemicals for Nanocrystal Synthesis

Cadmium oxide (CdO, Aldrich, 99.99 %), zinc acetate dihydrate (Aldrich, 99.8 %), selenium powder (Aldrich, 99.5 %, 100 mesh), sulfur (Aldrich, 99.99 %), 1–octadecene (ODE, Aldrich, 90 %), oleic acid (OA, Aldrich, 90 %), bis–(2,2,4–trimethylpentyl)phosphinic acid (TMPPA, Cytec Specialty Chemicals), trioctylphosphine (TOP, Aldrich, 90 %), tributylphosphine (TBP, Capot, 95 %), tributyl phosphite (TBPh, Aldrich, 90 %), oleylamine (OM, Pfaltz & Bauer, 97 %) and octadecylamine (ODA, Merck, 90 %) were used in the synthetic protocols described in the following.

2.2 Nanocrystal Synthesis and Washing

2.2.1 Reaction Setup

All quantum dot preparations within this thesis were performed using the hot–injection method [1] under inert atmosphere. A typical reaction setup, shown in Figure 2.1, consisted of a 3–necked round bottom flask sealed with SubaSeal rubber septa and connected to a

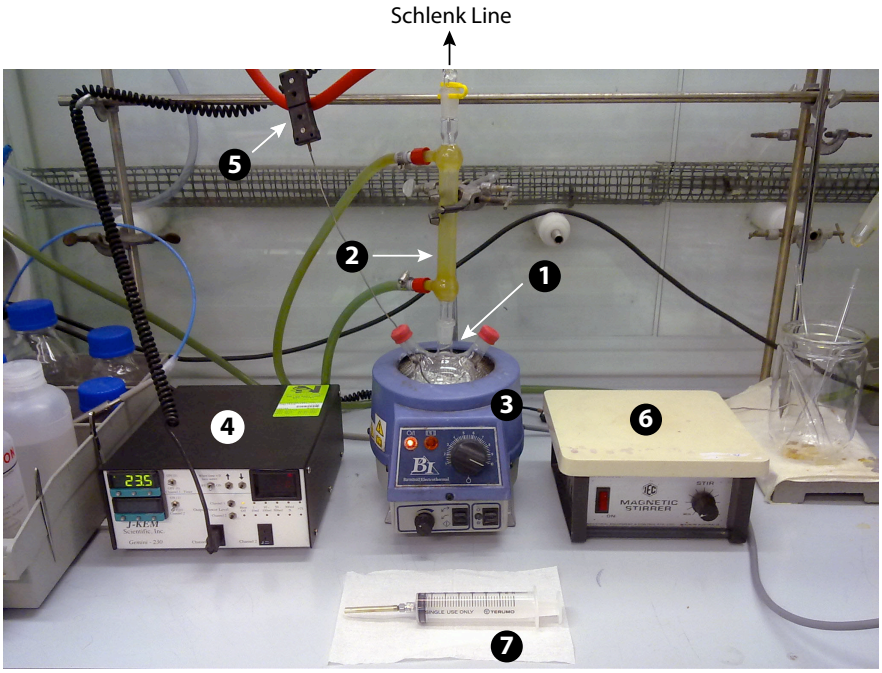

Figure 2.1 Photograph of a typical reaction setup for nanocrystal synthesis. (1) 3–necked round bottom flask sealed with SubaSeal rubber septa, (2) condenser, (3) EMA heating & stirring mantle, (4) J–KEM Gemini precision temperature controller, (5) thermal couple, (6) stirring plate, (7) 30 mL luer lock syringe, Schlenk line (not shown).

Schlenk line via a Graham or Liebig condenser. This configuration permitted degassing and performing reactions under inert atmospheres while simultaneously providing access for temperature control and precursor injection. The heating mantle was controlled by a precision temperature controller which monitored the solution temperature through a thermal couple. The temperature controller could be calibrated to specific reaction requirements and enables the monitoring and recording of the temporal evolution of the reaction temperature.

2.2.2 CdSe Core Synthesis

Following methods adapted from those reported by van Embden et al. [2], size tunable high quality CdSe nanocrystals were prepared. Careful adjustments of precursor reactivity via ligand chemistry and reaction conditions provided tight control over the nucleation and growth stages resulting in highly monodisperse, reproducible NC samples of sizes covering the entire visible spectrum. Optimized reaction parameters for various sizes are described in Table 2.1.

Figure 2.2 depicts the temperature profile and absorbance spectra for a typical CdSe quantum dot synthesis. CdO, ODE and TMPPA were mixed in a 250 mL 3–necked flask and

	Mother Solution				Injection Solution					Reaction Parameters		
1^{st} Abs Peak	ODE	CdO	TMPPA	Oleic Acid	Se	TOP	TMPPA	Oleyl Amine	ODE	Injection Temp	Growth Temp	Growth Time
$[nm]$	$[g]$	$[g]$	$[g]$	$[g]$	$[g]$	$[g]$	$[g]$	$[g]$	$[g]$	$[°C]$	$[°C]$	$[min]$
519	50	0.18	6.0	0.00	0.40	6.0	0	0	14	315	220*	60
524	60	0.18	6.4	0.00	0.26	2.8	0	0	22	300	260	20
550	50	0.20	6.0	0.00	0.22	2.5	0	2	11	305	230	50
575	60	0.30	0.0	3.50	0.30	3.0	4	2	7	300	220	40
585	60	0.30	0.0	4.00	0.45	4.0	3	2	7	300	220	20
600	60	0.44	0.0	5.62	0.65	4.5	3	2.8	3.4	305	235	60
617	60	0.44	0.0	6.00	0.653	5.0	3	3	5	305	235	60

Table 2.1 Optimized reaction parameters for size tunable CdSe nanocrystals through binary ligand control of TMPPA and oleic acid [2]. * For the smallest NCs, the temperature is allowed to drop to 200 $°C$ at which point 4 mL oleylamine are added before heating to 220 $°C$ for growth.

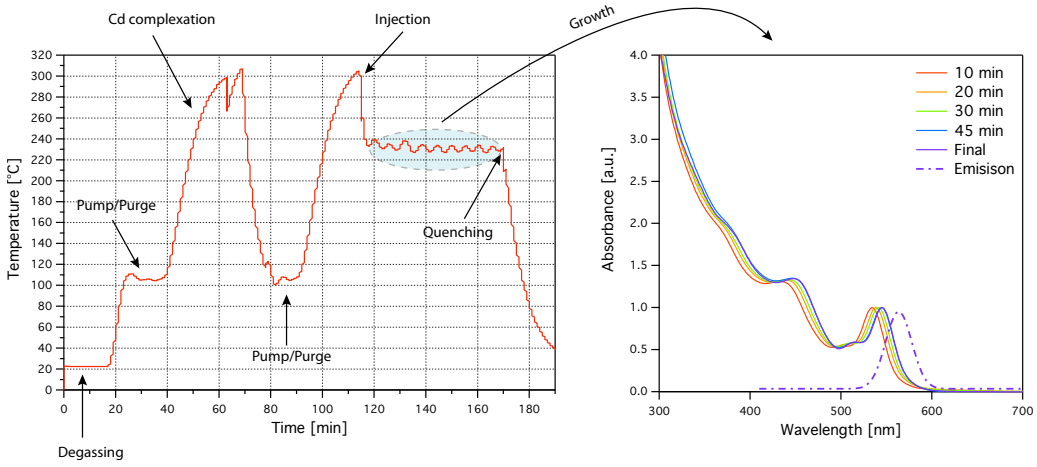

Figure 2.2 Left: Recorded temperature profile illustrating the various stages of a NC synthesis. Right: Normalised absorbance spectra from aliquots collected at regular growth times and final emission spectrum. The absorption red–shift reflects the particle growth.

Figure 2.3 Series of CdSe quantum dots dispersed in chloroform illuminated under low power UV–light. Emission wavelengths spanning the entire visible spectrum are realised through size–tunable synthetic schemes. Image courtesy of T.-L. Nguyen.

degassed at room temperature for $\sim$ 15 minutes. After heating the mother solution to 100 $^{\circ}C$ under nitrogen atmosphere three degas/nitrogen purge cycles were performed to remove any present water. The solution was then heated to 300 $^{\circ}C$ for $\sim$ 10 min to form a clear Cd–TMPPA complex. An optional step of cooling (to 100 $^{\circ}C$), three pump/purge cycles and reheating ensured the absence of any water formed during metal complexation.

The injection solution was freshly prepared by dissolving selenium in trioctylphosphine (TOP) on a Vortex mixer while heating and further sonication for $\sim$ 3 min to produce an optically clear solution. This was subsequently combined with oleylamine and ODE. After reheating the mother solution to slightly above ($\sim$ 5 $^{\circ}C$) the desired injection temperature, the heating mantle was replaced by a stirring plate and the temperature was left to drop.

A *rapid* injection of the selenium precursor through a suba seal at the *exact* injection temperature initialised the particle growth while causing a steep temperature drop of 40–50 $^{\circ}C$. The flask was reinserted into the heating mantle once the temperature dropped to 10 $^{\circ}C$ above the desired growth temperature. The particle growth was monitored by taking needle tip aliquots at regular time intervals which were immediately dispersed in chloroform to quench any further growth. Absorption and emission spectra of such samples were recorded to track the nanocrystal ensemble evolution. Once the desired particle size was reached, the reaction was quenched by a 5 mL ODE injection and further cooling to room temperature. The size–tunable fluorescence properties of such CdSe nanocrystals are depicted in Figure 2.3.

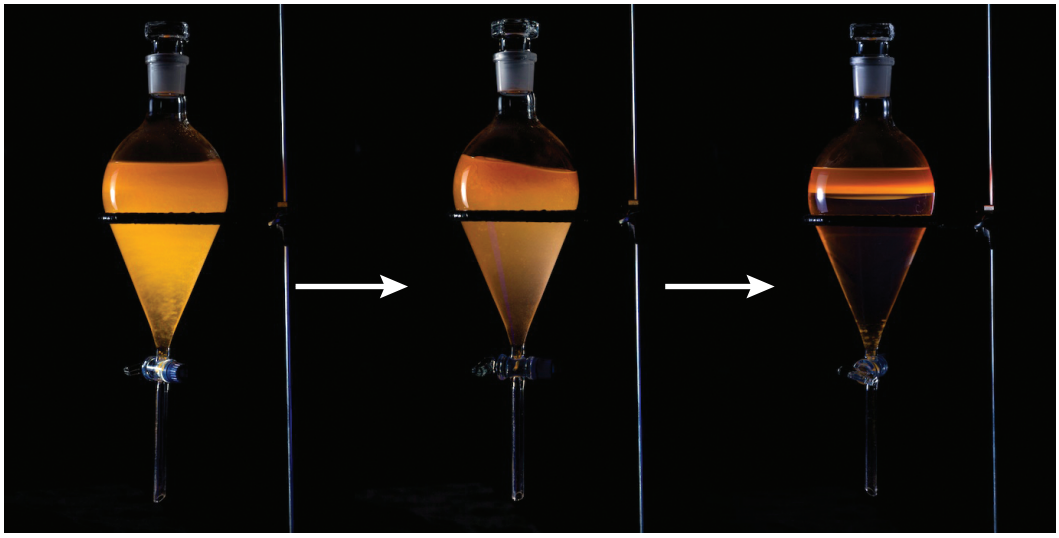

Figure 2.4 Photographs of CdSe nanocrystals during extraction in a separation funnel illuminated under low power UV light. The series illustrates the gradual phase separation holding the fluorescent NCs in the top, non–polar layer while reaction by–products and excess ligands are extracted into the bottom layer.

2.2.3 Post Preparative Washing and Storage of Nanocrystals

Post synthesis, the nanocrystals were washed in order to remove excess ligands and reaction by–products. The method followed the principles first outlined by Yu et al. [3] utilising an extraction rather than precipitation route. This proved to be a less invasive way to purify the nanocrystals preventing particle aggregation. The protocol is highly suitable for NCs dispersed in long chain non–polar solvents with impurities including oleic acid, oleylamine, TOP, TMPPA, etc.

The raw reaction solution was placed in a separation funnel and diluted with an equivalent volume of chloroform. Methanol was gradually added under swirling until two distinct phases were established, as shown in Figure 2.4. The nanocrystals typically assembled in the non–polar ODE/chloroform phase (top layer), while residual salts were drawn into the methanol/chloroform phase (bottom layer). To increase the solubility of excess ligands (oleic acid, TOP) in the methanol phase, small quantities of ethanol were added. Subsequently the lower phase was decanted into a waste container and the extraction was typically repeated two to three times to remove most of the unreacted monomer and excess ligands. It should be noted that the addition of too much chloroform or ethanol prevented phase separation but could be remedied through the addition of fresh ODE along with each extraction. To concentrate the NCs, the ODE phase was reduced by adding small amounts of acetone, and subsequently placed in a round bottom flask to remove any residual solvents utilizing a rotary

evaporator. Such processed quantum dots were stored in sealed vials in the dark ready to use for further experiments.

2.3 Absorption and Photoluminescence Spectroscopy

Absorbance spectra in solution were collected either with a Cary 5 UV–vis–NIR or an Agilent 8453 UV–vis spectrophotometer. Photoluminescence and Photoluminescence excitation (PLE) solution spectra were recorded with a Hiroba Jobin Yvon Fluorolog–3. Nanocrystal samples for PL studies were adjusted to an absorption of $\lesssim 0.1$ at the respective excitation wavelength to avoid large re–absorption effects. Excitation was typically at 400 nm employing excitation and emission slit widths of 1 nm and a 0.1 s integration time.

Quantum dot fluorescence lifetimes were established on the Hiroba Jobin Yvon Fluorolog–3 equipped with a TCPC (time correlated photon counting) card and a 403 nm picosecond pulsed NanoLED. For those measurements, a 5–7 nm bandpass at the band edge emission peak wavelength was usually chosen.

2.4 Cryogenic Photoluminescence Excitation Spectroscopy

While the oscillator strength of the first exited state is generally strong and well resolved, higher order states are increasingly difficult to identify due to their increasing weakness. This problem is exacerbated by the inhomogeneous broadening in ensemble measurements, effectively concealing transitions. Photoluminescence excitation spectroscopy (PLE) is a common technique to improve the spectral resolution, since only a subset of the sample distribution is probed. By monitoring a narrow spectral region of the PL band while scanning the excitation energy, PLE reveals absorption features with inhomogeneous broadening greatly reduced. Conducting these measurements at cryogenic temperatures further improves the resolution due to the weakened effect of homogeneous (thermal) broadening.

To form a glass at cryogenic temperatures (80 K), 2–methyl–tetrahydrofuran was chosen as the solvent, since it disperses as–prepared NCs without the need of ligand exchange. In order to generate an optically clear glass, it was essential to completely remove any water from the solvent. Consequently, the solvent was refluxed over sodium/benzophenone for 24 h prior to use. In a typical preparation a sample of highly purified NCs was dispersed into an aliquot of freshly distilled solvent (to an absorbance of $\sim$0.1 at the band edge transition) and subsequently transferred into a custom–made cryogenic quartz cuvette. The sample was then loaded into an optical spectroscopy cryostat (Oxford Instruments OptistatDN) and cooled to 80 K with liquid nitrogen. The sample was left for at least 15 min prior to performing any optical measurements to ensure thermal equilibrium was established. Integrated into the

Hiroba Jobin Yvon Fluorolog–3 spectrometer, PLE measurements were performed using the following parameters: Excitation slit width: 1 nm, emission slit width: 2 nm, integration time: 0.9 s, step size: 0.5 nm. The excitation wavelength for each sample was set to $\sim$2 nm to the blue of the PL emission peak.

2.5 Extinction Coefficients and Particle Sizing

Accurate determination of particle concentration and size is a central prerequisite for almost any application or study involving further processing of nanocrystals. Several groups [3–6] have established calibration curves quantifying the relationships between the band edge absorption and the particle size and molar extinction coefficient ε of NCs. The latter provides, in combination with the Lambert–Beer law, a convenient means to determine the NC concentration in solution. Yu et al. [3] were the first to report such calibration curves for CdSe, CdTe and CdS quantum dots, followed by other groups covering further materials like PbS [6] and PbSe [5]. Recently Jasieniak et al. [4] re–examined the calibration data for CdSe by combining transmission electron microscopy (TEM) with inductive couple plasma–optical emission spectroscopy (ICP–OES) and UV–vis absorption spectroscopy. Furthermore they demonstrated good agreement between their experimental results and a state–of–the–art atomistic semi–empirical pseudopotential model. Following their data, the relationship between particle diameter D $[nm]$ and the band edge absorption maximum obeys:

$$D = 59.60816 - 0.54736\lambda + 1.8873 \times 10^{-3}\lambda^2 - 2.85743 \times 10^{-6}\lambda^3 + 1.62974 \times 10^{-9}\lambda^4 \quad , \quad (2.1)$$

where λ is the wavelength in nm of the $1S(e) - 1S_{3/2}(h)$ absorption maximum. The molar extinction coefficient $\varepsilon_{1S}(M^{-1}cm^{-1})$ at λ was found to follow an exponential function of the form:

$$\varepsilon_{1S} = 155507 + 6.67054 \times 10^{13} exp\left(-\frac{E_{1S}}{0.10551}\right) \quad , \quad (2.2)$$

with E_{1S} being the energy at the band–edge absorption maximum in eV. The concentration of an ensemble of CdSe QDs is obtained via the Lambert–Beer law:

$$[CdSe](M) = \frac{Abs}{l(cm)\varepsilon_{1S}(M^{-1}cm^{-1})} \times \frac{\Delta E_{1S,\mathrm{HWHM}}(eV)}{0.06} \quad , \quad (2.3)$$

where $\Delta E_{1S,\mathrm{HWHM}}$ is the half–width–half–maximum of the first absorption peak on the low energy side. The second term presents a normalisation factor to account for variations in the PSD between samples. Figure 2.5 illustrated the sizing and ε_{1S} relationships along with the analytical method to extract $\Delta E_{1S,\mathrm{HWHM}}$ from an absorbance spectrum.

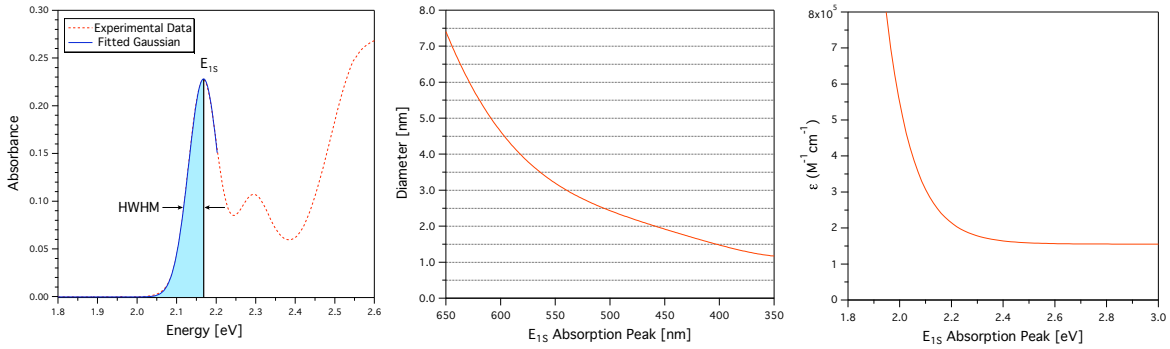

Figure 2.5 Left: Gaussian fit to the low energy side of the band edge absorption peak. Middle: Variation of CdSe nanocrystal diameter with the first absorption maximum. Right: Molar extinction coefficients of CdSe nanocrystals as a function of band gap energy [eV].

2.6 Single Nanocrystal Spectroscopy

In this section the fluorescence detection of individual nanocrystals, using confocal microscopy, is described. Furthermore the the concept of Time Correlated Single Photon Counting (TCSPC) for fluorescence lifetime measurements is addressed. To detect the emission from a single nanocrystal, there are two basic requirements that have to be met [7]: Firstly, it must be confirmed that only one nanocrystal at a time is probed while cancelling out other signals coming from proximate objects. Secondly, the signal from the probed quantum dot must be detected with an appreciable signal–to–background ratio (SBR).

The first requirement can be met by decreasing the probed volume to a minimum utilising a high numerical aperture (NA) objective, which is capable of focusing the probe beam into a diffraction limited spot. Furthermore one should prepare samples with an ultralow concentration of nanocrystals in an ultrapure host matrix to ensure a sufficient distance between single emitters. A concentration of one particle per square micrometre has been shown to be adequate to address the optical response from a single particle.

The second requirement, a high SBR, demands maximising the collection efficiency of the signal of interest while minimizing any background signal. To obtain a high collection efficiency, the first step is to maximise the fluorescence emission rate of the probed particle. Therefore the nanocrystal must be pumped with a high probability given by σ_p/A, where σ_p is the absorption cross section of a nanocrystal and A is the cross–sectional area of the focused laser beam. Thus, it is crucial to work with the smallest possible probe volume and to maximise σ_p. The latter can be achieved by the choice of an appropriate excitation wavelength as σ_p^{max} values are energy dependent through the strength of the allowed electric dipole transitions.

Another important parameter to account for is the absorption saturation of the particle. When a system is promoted to an exited state by an incident photon it takes a certain amount of time to decay back to its ground state, as given by the mean excited state lifetime. As the incident laser flux increases, more and more photons are absorbed per time which leads to a higher emission rate as long as the decay rate of the excited state is faster than the absorption rate. Once the absorption rate of incident photons exceeds the average emission rate, the particle experiences saturation and the ability to absorb further photons decreases. Therefore, σ_p decreases and any further rise in laser intensity results in more background photons rather than signal photons. On the other hand, at low beam intensities laser pulse noise becomes significant. Although the strength of this noise increases with intensity, the magnitude of the average signal grows more rapidly. As such, pulse generated noise is only a problem in the range of very low beam power.

To lower the background level, the detection of unwanted impurity fluorescence and residual excitation signals must be minimised. As background levels generally scale linearly with laser intensity, there is an optimum SBR. A common strategy, giving consideration to both the saturation intensity and the problem of pulse noise, is to operate the laser at a higher power and attenuate the beam afterwards by a neutral density filter. In addition, one should use optical elements that do not auto–fluoresce: This includes the microscope objective, filters, mirrors and oils. Furthermore the sample must be dispersed in ultrapure solvents and matrices, and the substrates must contain a low amount of unwanted fluorescent impurities. Due to the fact that the emitted photons from a single particle are red–shifted with respect to the absorbed laser photons, the two signals can be easily separated by dichroic mirrors and appropriate filters to prevent detection of the pump beam. It is also important to bear in mind that residual fluorescence increases with the energy of the pump which must be given careful consideration when working in the blue part of the spectrum. Finally, the detection system must have a high response over the wavelength range of the emitted photons and must possess a low dark count level.

2.6.1 Sample Preparation

Samples for single particle spectroscopy consisted of a dilute nanocrystal solution dispersed in toluene which was spin–coated onto a clean glass coverslip to give a homogeneous spatial distribution. The coverslips ($22\times22\ mm$) had a nominal thickness of $\sim 170\ \mu m$ and were cleaned via successive sonication for 20 minutes in each of the following solvents: dichloromethane, acetone, 10 % NaOH and Milli–Q water (twice). Subsequently they were stored in fresh Milli–Q water, and — prior to use — dried under a stream of dry nitrogen. Washed nanocrystals were diluted to a concentration of $\sim 10^{-8}M$ in spectroscopic grade toluene (Aldrich, ACS

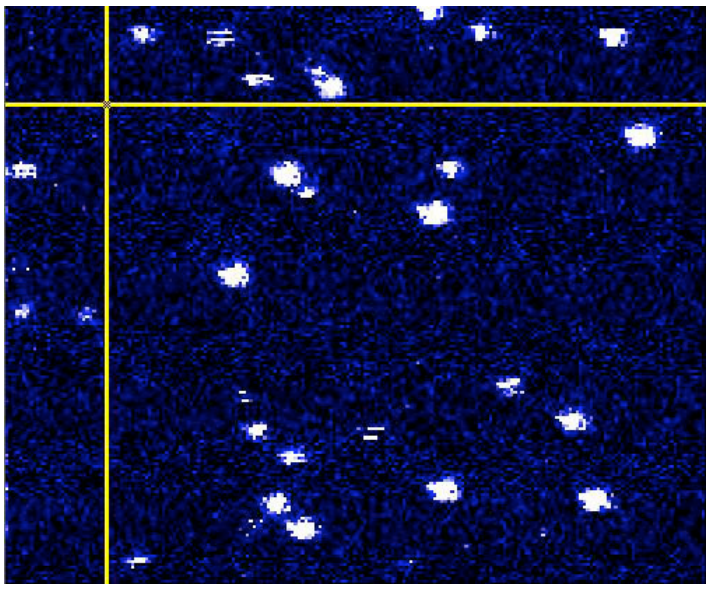

Figure 2.6 Confocal scan image of single CdSe/CdS/ZnS nanocrystals. The streaks found in some of the particles indicate blinking.

spectrophotometric grade, $\geq$ 99.5 %) of which 20 μL were spin cast onto a clean coverslip. The spin–coating process involved a six second ramping phase from standstill to 3000 rpm followed by a six second phase at constant speed and a further six second deceleration phase to halt (Specialty Coating Systems Model P6700). Following this protocol homogeneous films of spatially resolvable individual nanocrystals, as shown in Figure 2.6, were reproducibly obtained.

2.6.2 Confocal Setup

The custom–built system for single nanocrystal detection consisted of a pulsed laser diode excitation system, an inverted microscope equipped with a raster scanning piezoelectric sample stage and an avalanche photodiode (APD) detection system. All optical elements (mirrors, pinholes, filters, etc.) were purchased from Thorlabs. A simplified schematic of its configuration is outlined in Figure 2.7.

The excitation system consisted of a pulsed light source (λ= 466 nm, 10 MHz repetition rate, PicoQuant, LDH-P-C-470) that was controlled by a laser driver (PicoQuant, PDL 800–B) producing light pulses with a FWHM of 70 ps. To ensure homogeneous illumination, the multi–mode beam was focused through a tube lens and a pinhole aperture (10μm). This treatment spatially removed all out of plane beam modes while leaving a collimated laser beam with a Gaussian intensity profile. By passing the light through a neutral density filter wheel, the excitation intensity could be continuously adjusted from 50 nW up to 1.5 μW.

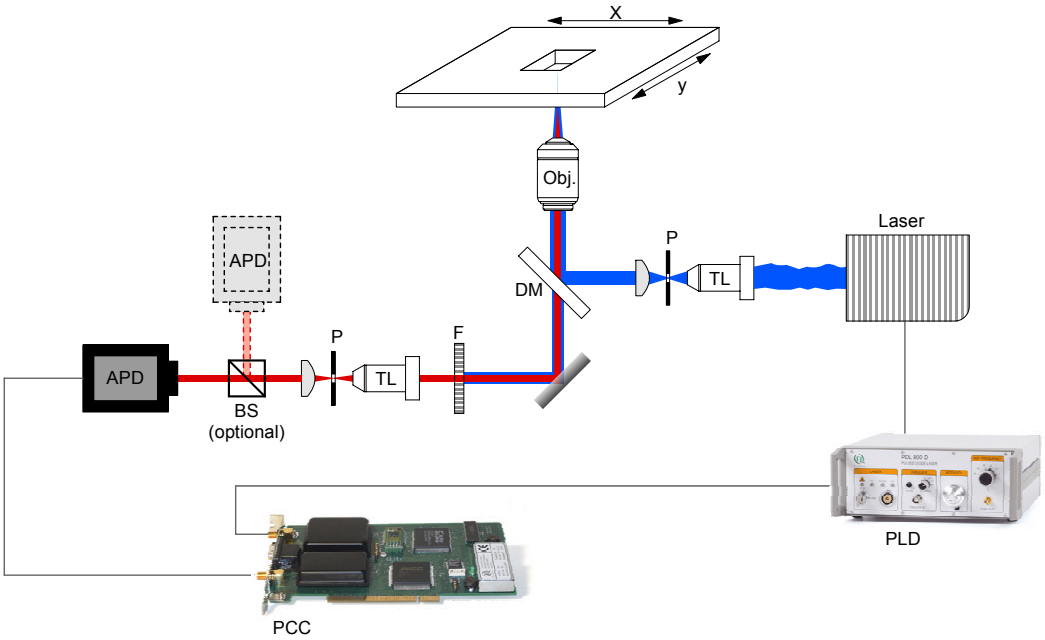

Figure 2.7 Schematic of a confocal setup for single particle spectroscopy. Pulsed laser driver (PLD), laser, tube lens (TL), pinhole (P), dichroic mirror (DM), microscope objective (Obj.), cut–off filter (F), beam splitter (BS), avalanche photo diode (APD) and PCC represents the photon counting card.

Subsequently the beam was directed into an inverted microscope (Olympus IX71) where it was deflected off a dichroic mirror into the back aperture of an infinity–corrected 100x 1.4 NA oil–immersion objective (Olympus UPlanSApo).

The excitation light was then focused into a diffraction–limited spot at the focal plane. As the light passes through the lens, it interferes with itself creating a ring-shaped diffraction pattern, known as an Airy pattern. The innermost spot in the pattern defines the maximum resolution R and is given by the Rayleigh criterion:

$$R = \frac{0.61\lambda}{n \sin\theta} \quad . \tag{2.4}$$

Here θ is the collection angle of the lens, which depends on the width of objective lens and its focal distance from the specimen. n is the refractive index of the medium surrounding the objective and sample, while λ represents the illumination wavelength. The quantity '$n \sin\theta$' is also known as the numerical aperture. Therefore, with the employed setup (λ= 466 nm, 1.4 NA) a maximum lateral resolution of 203 nm was attained leading to the requirement that two particles must be separated by at least that distance to be identified as single emitters.

Emitted fluorescence and backscattered excitation light was then collected and re–collimated by the same objective and passed back through the dichroic mirror, which transmits the emission signal ($\lambda > 500\ nm$) whilst reflecting the excitation light. The emission was further filtered by a combination of two long–pass filters and refocused through a pinhole that was located at the microscope image plane. This caused the spatial rejection of most out–of–focal–plane signals giving improved axial resolution, known as the confocal advantage [7]. To reject as much out–of–focal–plane signals as possible while keeping attenuation of the particle signal minimised, the pinhole size was closely matched to the size of the excitation spot multiplied by the magnification of the microscope. Following the pinhole, the signal of interest was sent to a Hanbury–Brown and Twiss interferometer [8] comprising a non–polarising 50/50 beamsplitter (optional) and two avalanche photodiodes (PerkinElmer, SPCM–AQR–15, dark count rate $< 50\ s^{-1}$) which were connected to a photon counting card (PicoQuant, TimeHarp 200).

A confocal image was created utilising a computer–controlled piezoelectric stage (PI, P-517.2CL, linear travel range $100\times100\ \mu m$) raster–scanning the sample across the fixed laser spot. A step size of $0.2\ \mu m$ was chosen to match the maximum setup resolution to one pixel. The acquired image was built up of an array of pixels with a contrast representing the respective detected emission intensity (Figure 2.6). Single nanocrystal analysis was then achieved by positioning a particle in the excitation/detection spot.

Photoluminescence decay times of individual NCs were obtained by connecting the pulsed laser driver to the start channel of the photon counting card enabling time–tagged time–resolved (TTTR) measurements. Furthermore blinking time trajectories were extracted from this TTTR data by applying a chosen bin time. For anti–bunching measurements [9], the outputs of both APDs were connected to the start and stop channels of the photon counting card which, after the introduction of an electronic delay (about $80\ ns$) in one of the detector outputs, allowed for the measurement of photon inter–arrival times.

2.6.3 Time–Correlated Single Photon Counting (TCSPC)

As discussed previously, fluorescence lifetime is a unique quantity that gives insight into the electronic structure of nanocrystals. Time–Correlated Single Photon Counting (TCSPC) allows one to extract this information by recording the times between excitation and photon (emission) arrival. The technique utilizes the quantum–mechanical nature of fluorescence, i.e. an individual particle may emit only one photon at a time. As illustrated in Figure 2.8, by extending the data collection over multiple excitation/emission cycles, one can reconstruct the lifetime profile by binning single photon events collected over many cycles.

The method is based on the decoupling of the generation time and the arrival time of single photons. The reference for the measurement *start* is the excitation pulse which is triggered

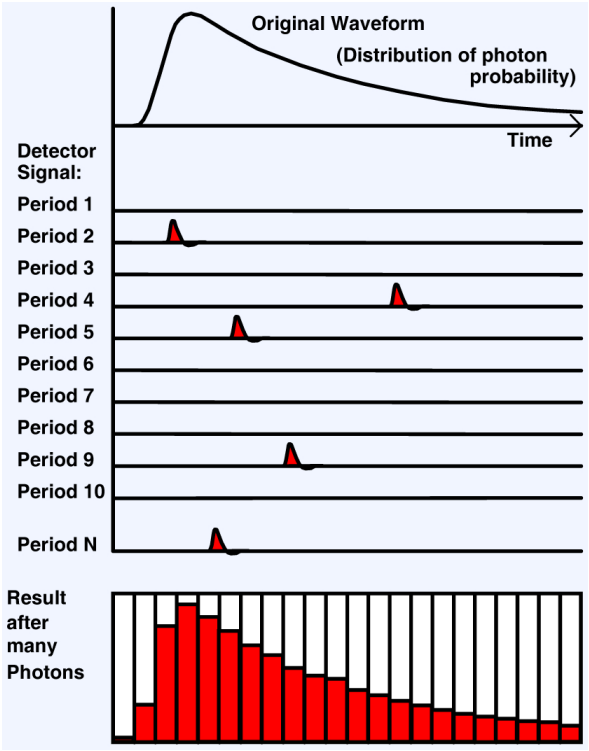

Figure 2.8 Illustration of lifetime reconstruction through a histogram of single photon events [10].

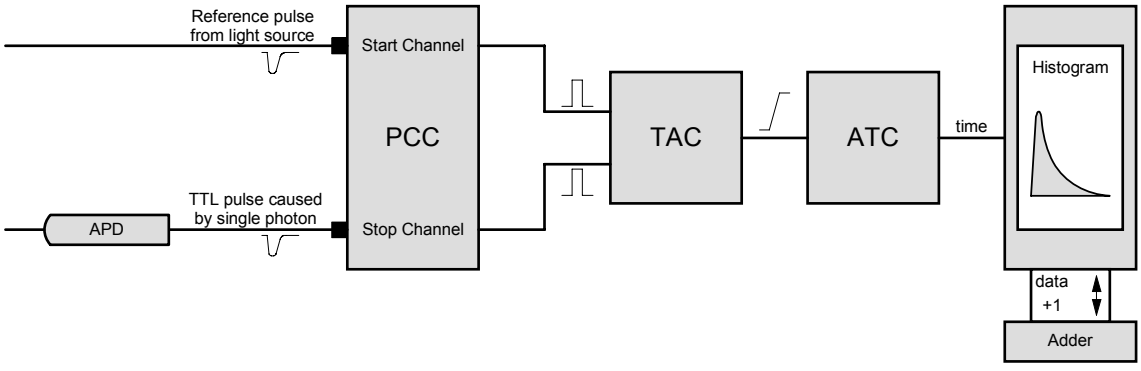

Figure 2.9 Schematic of data acquisition in TCSPC experiments.

by the laser driver PLD and synchronised to the photon counting card (PCC) to activate a time–to–amplitude converter (TAC) circuit. Upon photon detection at the APD the *stop* signal is triggered, converting the TAC into a time and the event is recorded into a histogram of times since excitation (see Figure 2.9). As this system saves the arrival time of each photon detection separately, it is commonly referred to as the Time–Tagged–Time–Resolved (TTTR) mode, which provides maximum flexibility in off–line data analysis. Provided the condition of registering no more than one photon per cycle is true, the histogram of photon arrivals per time bin represents the time decay one would have obtained from a single shot time–resolved analogue recording. Upon collecting multiple arrival times to gather the full range of delays between excitation and emission of a photon, the fluorescence decay profile of the probed nanocrystal can be reconstructed.

2.6.4 Anti–Bunching — Evidence of Single Nanocrystal Probing

The fact that a single particle can emit only one photon per excitation can be exploited to unambiguously demonstrate that the spots in Figure 2.6 represent individual NCs. As mentioned previously, the Hanbury–Brown and Twiss setup can be used to measure inter–arrival times between consecutive photon pairs. The investigated emission signal is split by the 50/50 beamsplitter, and fed into the two APDs. One detector delivers the start pulse, while the other triggers the stop pulse at the photon counting card. Recording of several inter–arrival times of consecutive photons results in a histogram of the time differences between the photons at both detectors. For an anti–bunching experiment with pulsed excitation [11], the histogram becomes a train of correlation peaks spaced by the laser pulse interval (100 ns/ 10 MHz repetition rate). Since the laser pulse width is much shorter than the fluorescence lifetime, it is highly unlikely that a single emitter will be excited several times within one laser pulse. Consequently, the chance of the detection of a photon pair from a single particle becomes extremely small. The ratio of the height of the central coincidence peak to the adjacent peaks is therefore an indicator of the number of emitters in the excited volume. Thus, the missing peak at 120 ns in Figure 2.10 is a strong indicator that the fluorescence signal originates from a single nanocrystal. Anti-bunching was the standard method throughout this work to assert that the data collected by single particle spectroscopy derived from individual quantum dots.

2.6.5 Fluorescence Intermittency Analysis

As discussed in Section 1.3, the traditional method to extract blinking statistics from single particle fluorescence trajectories involves integration of the measured intensity (number of detected photons) over time bins of fixed width. Subsequently an intensity threshold is applied to assign the photons to 'on' and 'off' levels. This method is inherently problematic since

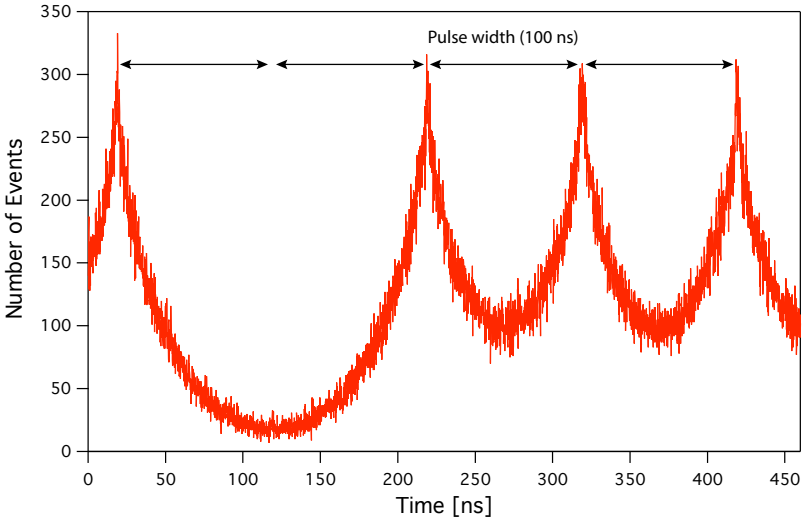

Figure 2.10 Antibunching in the emission of a single CdSe/CdS/ZnS core/shell nanocrystal with pulsed laser excitation. The distance of the correlation peaks reproduces the excitation pulse interval time.

it introduces an artificial time scale [12]. If a NC blinks during a single binning time, these separate, short blinking periods will be mistaken for one, longer period. The issue can be mitigated by reducing the bin width, however, this increases the effect of shot noise and instrumental noise, eventually making it impossible to choose a sensible threshold as photons emitted from the NC and background light become indistinguishable.

A recent study by Crouch et al. [13] investigated the effects of bin width and intensity threshold on the on–time probability distribution. They found that both truncation time and power–law exponent are significantly affected by the chosen parameters. Their analysis shows an increase of truncation time by a factor of four when changing the bin width from 1 ms to 10 ms. In the case of a 1 ms bin width, a threshold cannot be confidently set due to an overlap between background and signal leading to a distorted truncation time value. Furthermore the on–time exponent m_{on} was found to decrease steadily with increasing bin width. Testing the robustness of the chosen intensity threshold, the results were stable for intensity histogram exhibiting well resolved and separated background and signal peaks, and the threshold fell in the flat region in between. On the other hand, significant distortions in the on–time distributions occurred if the threshold fell outside this range.

To circumvent these shortcomings, a novel changepoint method based on an Bayesian approach [14] was employed to analyse the time resolved fluorescence trajectories of single NCs*. This method yields a quantitative and statistically robust analysis and is not limited

* The author acknowledges D. L. Ensign (author of Reference [14]) for the provision of the Python code to implement the Bayesian algorithm.

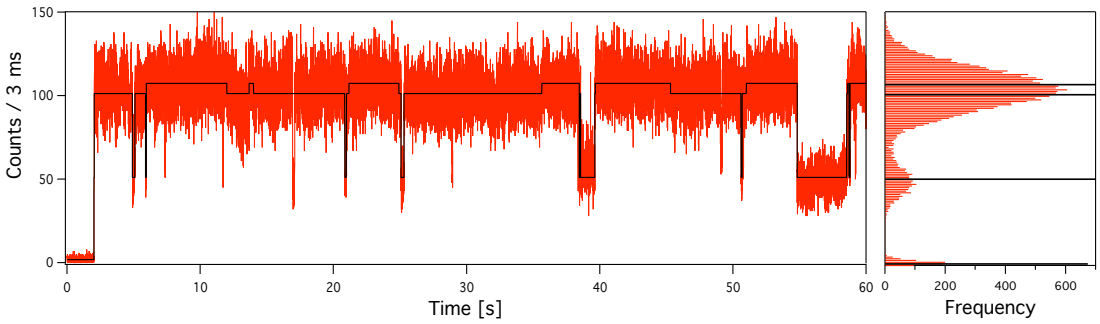

Figure 2.11 Plot of a single nanocrystal fluorescence trajectory (3 *ms* bin time) and intensity histogram (red). The black trace represents the Bayesian fit identifying changepoints and intensity levels.

to two state blinking. In contrast to other changepoint methods based upon maximum likelihood estimates [12], the Bayesian method allows for a more systematic means not only to changepoint detection but also to cluster the data into intensity states.

Changepoints in the intensity trajectory are located by calculating the "odds" of a change occurring using Bayesian statistics. The algorithm for multiple changepoint detection initially calculates the Bayes factor for a whole blinking trajectory. If the factor is larger than the set threshold value the trajectory is split into two sub–trajectories for which separate Bayes factors are computed. If a calculated Bayes factor falls below the cut–off, the segment is assumed to contain no changepoint and the algorithm stops at that sub–trajectory. The splitting and subsequent calculation is repeated until all Bayes factors are less than the threshold (i.e., until no further changepoints can be detected), resulting in a set of trajectory segments. To test whether those segments can be grouped into states of common intensity levels, a mean count level for each segment is calculated. Subsequently the Bayesian approach is applied in a similar manner as for changepoint detection. Instead of evaluating the existence of a changepoint, a Bayes factor is calculated indicating whether two segments with similar mean intensity are better described by one or two states.

Figure 2.11 depicts the trajectory fit for a single nanocrystal fluorescence trace. The calculated trajectory is in good agreement with the experimental data, detecting 35 changepoints and four intensity levels. As is apparent from the histogram, the two highest levels are likely to belong to the same state. This can be verified by comparing the fluorescence decay profiles constructed from the respective photon arrival times since photons from the same recombination state show identical kinetics. It is important to note that the algorithm employed in this these is aimed at Poisson distributed data and therefore binning is required. The author of reference [14] provides equations for a binomial Bayes factor which does not require binning and is suitable for experiments where photon arrival time information is available.

However, implementation of these equations into the source code was not successful and therefore fluorescence data was binned into 10 ms intervals.

2.7 Electron Microscopy

In this section the structural characterisation of nanocrystals via electron microscopy is described. Furthermore the various operation modes along with their respective attainable information is discussed. In order to characterize materials on a scale down to single atoms, transmission electron microscopy (TEM) has become arguably the most efficient and versatile tool. This technique exploits de Broglie's ideas of wave–particle duality which correlates the wavelength of electrons (λ_e) to their energy (E), and can be approximated as

$$\lambda_e \sim \frac{h}{\sqrt{2m_0E}} \quad . \tag{2.5}$$

In this equation h is Planck's constant, m_0 is the electron mass, E is in electron volts and λ_e in nm. Hence a 100 keV electron, for instance, has a wavelength of ~ 4 pm, which is much smaller than the diameter of an atom. At such high energies the velocity of electrons becomes greater than half the speed of light, and therefore relativistic effects must be considered which modifies equation 2.5 to

$$\lambda = \frac{h}{\sqrt{2m_0E\left(\frac{1+E}{2m_0c^2}\right)}} \quad , \tag{2.6}$$

further decreasing the wavelength. However the practical resolution of TEMs is nowhere near that wavelength limit of resolution due to the lack of perfect electron lenses [15].

Apart from a substantially increased resolution compared to optical microscopy, another advantage of electrons is their "ionizing" nature, meaning that they are capable of removing tightly bound inner–shell electrons from the attractive field of the atomic nucleus. This leads to a wide range of secondary signals (see Figure 2.12) which can be recorded by suitable detectors, giving additional information aside from the physical image of the specimen. Despite the wide range of information the TEM is capable of providing, an inherent drawback is that it forms two dimensional images of three dimensional specimens. All obtained images, diffraction patterns (DP) and spectra are therefore *averaged* through the specimen thickness, and accurate image *interpretation* becomes crucial. As will be discussed shortly, images formed in Z-STEM mode allow for a more intuitive interpretation [16–18] which contributes to the increasing popularity of this technique.

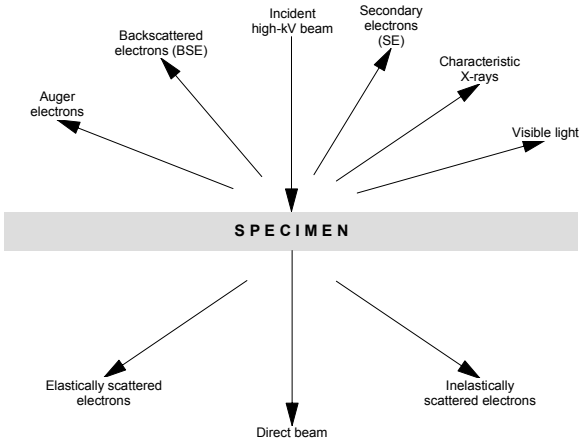

Figure 2.12 Signals generated when a high–energy beam of electrons interacts with a thin specimen.

2.7.1 TEM Grid Preparation

Assuming an optimal alignment of the instrument, the quality of nanocrystal TEM images is largely dependent the purity of the sample and the thickness of the support film. Apart from the potential risk of contamination of the microscope chamber, any organic impurities typically lead to carbon build–up on the sample film under the intense electron beam (especially in STEM mode). This results in a reduction of image contrast precluding high (atomic) resolution imaging, as shown in Figure 2.13. Therefore the general aim of sample preparation is to reduce organic compounds (ligands, impurities) to a minimum, while preserving the dispersibility of NCs in solution.

Throughout this thesis the following protocol was employed: As–prepared NCs were washed as outlined in section 2.2.3. Subsequently $\sim 1\ mL$ of sample solution was placed in a 10 mL centrifuge tube and diluted with 2 mL of hexane. The tube was filled with acetone to dissolve ODE and the cloudy dispersion was centrifuged at 4400 rpm for 3 min. If residual ODE was still present (oily instead of dry plug) the hexane/acetone treatment was repeated. To liberate the NCs from excess ligands, the precipitate was re–dispersed in hexane and the quantum dots were destabilised by successively adding small quantities of 2–propanol. This approach led to the precipitation of NCs while free ligands remained in solution. The particles were subsequently separated by centrifugation as described previously. Successful washing typically led to the deposition of a homogeneous QD film on the inner wall of the centrifuge tube after solvent decanting.

The precipitate was dried under nitrogen flow and then dissolved in a mixture of spectroscopic grade cyclo hexane and octane (4:1 ratio) to give an optical density of ~ 0.1 at the band–edge absorption peak. This solution was ultra–sonicated for several seconds and one drop was

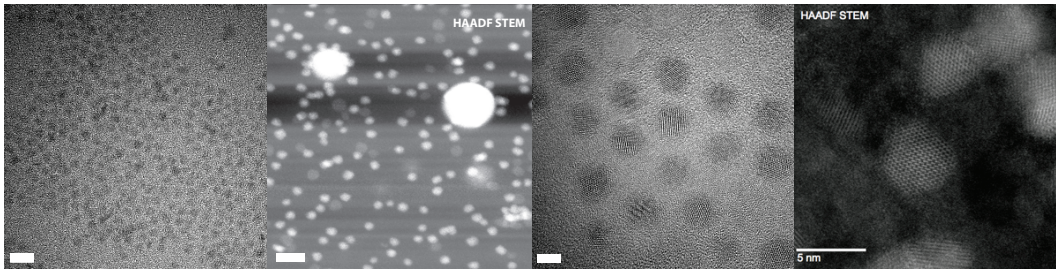

Figure 2.13 Brightfield TEM and HAADF STEM images illustrating effects of sample preparation. From left to right: TEM image (scale bar 10 nm) with reduced contrast due to a thick support film and insufficient particle washing; HAADF image (scale bar 10 nm) with carbon build–up under the electron beam due to organic impurities; HRTEM and HAADF images (both scale bar 5)nm demonstrating atomic resolution due to a thin support film and successful sample washing.

deposited on a "free–standing" TEM grid. Upon evaporation of the solvent, the sample was placed on a fresh filter paper and allowed to dry for several minutes under ambient conditions before transferred into a storage box. Specimen for TEM analysis were usually prepared at least one day in advance to ensure complete solvent evaporation.

The employed TEM substrates were either carbon ($\sim$ 5 nm film thickness) coated copper grids with Formvar backing (ProSciTech, GSCU300C-50, 300 mesh) or ultra–thin carbon ($>$ 3 nm film thickness) over holey carbon coated copper grids (TedPella, 400 mesh). While the former substrates were suitable for particle sizing, their thick support film led to reduced contrast preventing ultra high resolution imaging (especially in STEM mode) for which the TedPella grids were utilised. The TEM sample holder was subject to a 10–15 min plasma clean (Fischione, Model 1020) to remove any potential contaminations from previous samples. Before STEM imaging, a 10–12 sec plasma clean of the samples slightly improved the stability against carbon build–up, however some films appeared to become brittle under the electron beam after this treatment.

2.7.2 The FEI Tecnai F20 Electron Microscope

TEM and STEM imaging was accomplished on a FEI Tecnai F20 electron microscope operated at 200 keV and equipped with a HAADF (STEM) detector. The general construction of a TEM can be divided up into the following sections from top to bottom: The illumination system which comprises the electron source and the condenser system forming the electron beam; The subsequent specimen stage is followed by the objective system which is the most important part in a TEM; All optics afterwards are integrated into the imaging system, where the first lens is important to diffraction imaging. The remaining optics can be more or less neglected, as even though they provide a huge amount of magnification, they have virtually

no influence on the scientific results. The image is then projected onto a phosphor viewing screen or recorded through projection onto the image sensor of a CCD camera (Gatan Inc.).

In TEMs two kinds of electron sources are usually employed: The first one is called a thermionic source, which produces electrons when heated. The second type, which is operating in the F20, is a field–emission gun (FEG), which produces monochromatic electrons when an intense electric field is applied. Field emission is based on the principle of increasing electric field strength E at sharp points given by:

$$E = \frac{V}{r} \quad . \tag{2.7}$$

Therefore if a 1 kV potential is applied to a tungsten wire with a tip radius of $\sim$0.1 μm, then E is 10^6 V/m which lowers the work function barrier sufficiently for electrons to tunnel out of the tungsten. To operate with field emission, the wire surface must be pristine, which can be achieved by working under UHV conditions ($<10^{-11}$Torr). As the electron source is operated at ambient temperature, this process is also called "cold field emission". FEGs produce an electron source about three orders of magnitude smaller than their thermionic analogues. This enables a FEG–TEM to form an extremely fine beam probe allowing one to operate the microscope also in scanning mode with high spatial resolution.

The condenser system contains two lenses, called $C1$ and $C2$, two sets of shift–and–tilt coils and an aperture. Its main function is to form the specimen illuminating probe from the electron source and to align the beam with the optic axis of the microscope, which is the central concern in order to obtain a high performance.

Electron lenses are the magnetic equivalent of glass lenses in an optical microscope and, to a large extent, the same principles apply. They consist of electronic coils generating a magnetic field, which bends electron beams in approximately the same way as a convex glass lens bends monochromatic light. However, in contrast to a *fixed* focal length in glass lenses, this parameter is *adjustable* in electric lenses by varying the magnetic field strength.

In order to understand how the beam probe is formed some fundamental properties of convex lenses must be addressed. There are two ways to control rays coming through the lens, illustrated in Figure 2.14. First, it produces a magnified image of an object in the image plane. Second, it focuses incident parallel beams to a point in the back focal plane of the lens. These correlations are describe by Newton's lens equation

$$\frac{1}{u} + \frac{1}{v} = \frac{1}{f} \quad , \tag{2.8}$$

where magnification and demagnification can be defined by $M = \frac{v}{u}$ and M^{-1} respectively. Hence, for a fixed object distance, an increase in magnetic field strength leads to a shorter focal

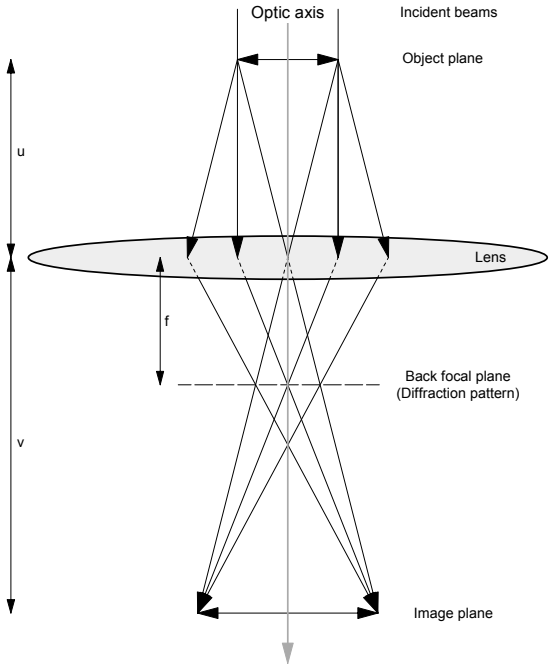

Figure 2.14 Ray diagram for an object, symmetrically positioned around the optic axis.

length which in turn lowers the image magnification. In the condenser system, these principles are employed to control the beam cross–overs which will determine the final probe shape. The two lenses are coupled since the image plane of $C1$ acts as the object plane for $C2$ and they produce either a parallel beam for TEM imaging and diffraction, or a convergent beam for the finest possible probe on the sample (STEM mode, micro–diffraction). An additional variable is the $C2$ aperture which improves the beam coherence, by removing higher angle electrons but at the expense of illumination intensity.

After passing the specimen, the scattered electrons are collected by the objective lens, sitting just below the sample stage. It is often considered as the "heart" of the microscope, since here all beam–specimen interactions take place, images and diffraction patterns are formed, and hence its quality ultimately limits the obtainable resolution of the microscope.

As already mentioned, electron lenses are imperfect compared to their optical analogues, which leads to three major defects one has to deal with. First, *spherical aberration* caused by the inhomogeneous acting of the lens field on off–axis rays, meaning that higher angle electrons are more strongly bent towards the axis. As a result, a point object is imaged as a disk of finite size, limiting the ability to magnify detail. The degree of this defect for a particular lens is expressed in the spherical aberration coefficient C_s which is approximately equal to the focal length. The second major defect is *chromatic aberration*, meaning that low energy

electrons are more strongly bent than high energy electrons. This issue is not a problem for the condenser system, as the FEG produces highly monochromatic electrons. However, as the beam passes the specimen, inelastic scattering leads to a significant broadening of energies. As inelastic scattering increases with sample thickness, the thinnest possible film is desirable to minimize this effect. Finally, astigmatism, arising from non–perfectly symmetrical magnetic fields in electron lenses and non–centred apertures inserted into the field, must be corrected. However, the latter can be rectified via stigmators, which introduce compensating fields to balance the inhomogeneities.

Assuming that astigmatism can be completely corrected and the specimen is sufficiently thin to neglect chromatic aberration, the practical attainable resolution limit $r(\beta)$ is given by

$$r(\beta) = \sqrt{\left(0.61\frac{\lambda}{\beta}\right) + (C_s\beta^3)^2} \quad , \tag{2.9}$$

where the first term relates to the theoretical resolution given by the Rayleigh criterion and the second accounts for the contribution of spherical aberration, while β is the aperture collection semiangle. An important implication of equation 2.9 is the existence of an optimum (compromise) value for β, given by

$$\beta_{opt} = 0.77\frac{\lambda^{\frac{1}{4}}}{C_s^{\frac{1}{4}}} \quad . \tag{2.10}$$

Substituting equation 2.10 into equation 2.9, the practical resolution is given by

$$r_{min} = 0.91(C_s\lambda^3)^{\frac{1}{4}} \quad . \tag{2.11}$$

With a C_s value of 1.2 mm for the FEI Tecnai F20, a high point-to-point resolution r_{min} of $\sim$0.15 nm is attainable. Since the human eye can resolve a distance of $\sim$ 0.2 mm, the maximum useful magnification is therefore in the order of 10^6. Above this magnification, no more detail will be revealed. Additionally, it becomes apparent that choosing the right objective aperture size (limits β) becomes crucial to obtain maximum resolution.

Apart from the quality of a lens, measured by its C_s value, there is a particular field strength at which it operates at maximum performance. Therefore it is common practice to keep the objective lens excitation unchanged while moving the specimen into the respective object plane, the so–called *eucentric* plane, to bring the image in focus. The eucentric plane is normal to the optic axis and contains the axis of the specimen holder rod. Therefore the sample does not move laterally when tilting the holder axis. All planes in the imaging system, which correlate with the objective lens, are defined with reference to the eucentric plane. This is

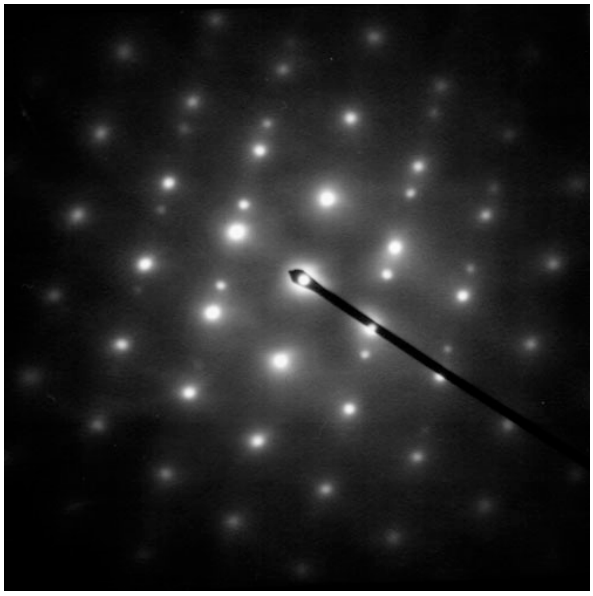

Figure 2.15 Selected are diffraction (SAD) pattern of a single austenite crystal in a piece of steel.

important to note as varying the objective lens field strength affects its magnification and consequently the magnification of the whole microscope.

2.7.3 Diffraction vs. Image Mode

The imaging system constitutes the link between images and diffraction patterns (DP), formed by the objective lens, and the final observable projection on the viewing screen. The DP represents the *angular* scattering distribution of a specimen and is formed in the back focal plane of the objective lens. As mentioned before, electron lenses focus *parallel* incident beams into a spot in the back focal plane, and therefore *every spot* in the diffraction pattern accounts for parallel rays diffracted by the specimen in a *certain angle* (see Figure 2.15). On the other hand, the *spatial* scattering distribution gives rise to the contrast formed in the objective lens image plane. Therefore to focus a DP on the viewing screen, the object plane for the subsequent projector system must be shifted from the objective lens's image plane to its back focal plane. This is controlled by the field strength of the intermediate lens, representing the first lens of the imaging system (see Figure 2.16).

As it is sometimes desirable to select just a certain region of the specimen to contribute to the diffraction pattern, a so–called Selected–Area Diffraction (SAD) aperture, sitting in the image plane of the objective lens, can be inserted. Furthermore, in image mode, bright–field or dark–field images are formed dependent on whether direct or scattered electrons are chosen to contribute to the image. This is the second task of the objective aperture, sitting in the

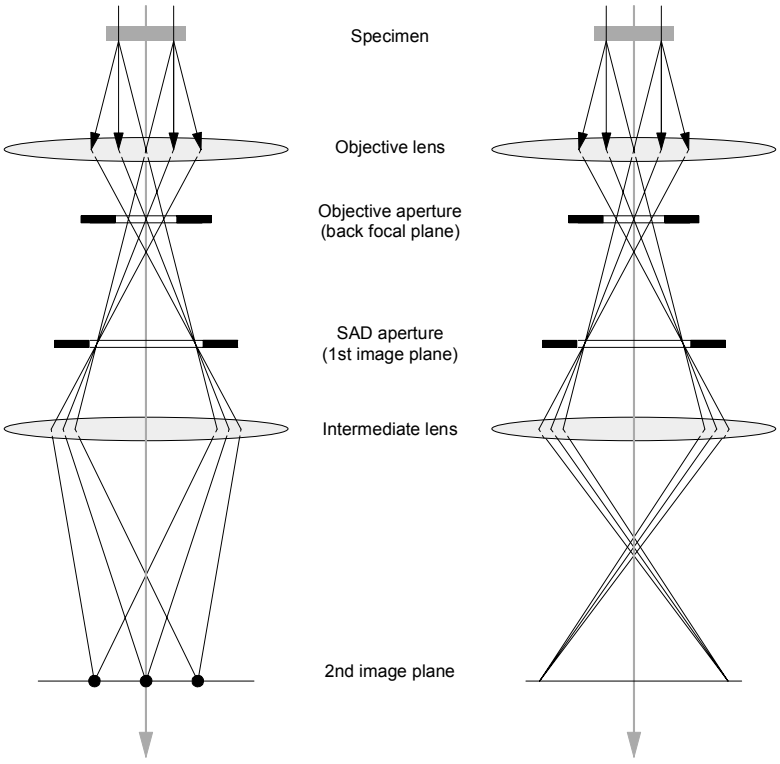

Figure 2.16 The two basic operation modes of a TEM. The intermediate lens selects either the back focal plane (left) or the first image plane (right) as its object by changing its field strength. Therefore either the diffraction pattern or an image is formed in the second image plane respectively, which is subsequently magnified onto the viewing screen.

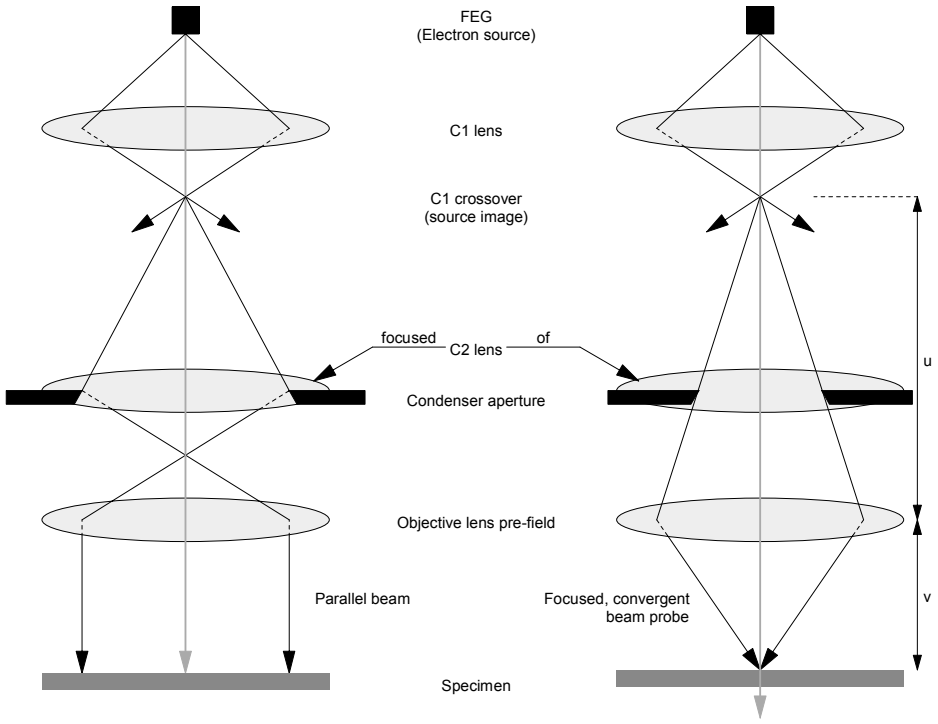

Figure 2.17 Schematic of the condenser system forming parallel illumination (left) or a convergent beam probe (right) for TEM and STEM operation respectively.

objectives back focal plane. It is therefore the most important aperture in the TEM, since its size directly affects the obtainable resolution whilst its position selects whether the direct or a specific diffracted beam forms the observed image.

2.7.4 Scanning Mode (STEM)

For high–resolution TEM (HRTEM) imaging and diffraction, parallel illumination is essential to attain sharp patterns as well as best image contrast. Therefore $C2$ is focused to produce an image of the source at the front focal plane of the objective lens pre–field sitting just above the specimen. In exactly the reverse manner of a focal plane, a broad parallel beam of electrons incident is then generated for parallel illumination of the specimen (see Figure 2.17 left).

In contrast, STEM operates by forming a convergent beam to the smallest possible probe which is raster–scanned over the specimen and the signals from various detectors can be plotted as a function of probe position to built up an image. Due to the serial image formation, compared to the "one–shot" acquisition of TEM mode, interferences from the surrounding environment become crucial and stringent conditions are necessary to achieve atomic resolution [19, 20]. To form a convergent beam, the objective lens pre–field acts now as a third condenser

lens $C3$, while $C2$ is strongly weakened or even switched off (see Figure 2.17 right). This is necessary to maximise the demagnification of the $C1$ crossover (source image), as given by

$$M^{-1} = \frac{u}{v} \quad , \tag{2.12}$$

where u and v are the object and image distances for $C3$, respectively. Since v is kept constant in order to form the probe in the specimen plane, a maximum value of u is sought by shifting the cross–over of $C1$ (first source image) up. Hence, the role of $C1$ is fundamentally different in STEM mode as opposed to TEM mode. It is used directly to form the probe and its maximum field strength dictates the minimum attainable beam size, since $C3$ is kept constant to assure its image plane coincides with the specimen plane. Apart from a minimum probe size, it is essential to keep the beam scanning *parallel* to the optic axis at all times so that it mimics the parallel beam in a TEM even though it is scanning. This is provided by double deflection scan coils sitting in the front focal plane of $C3$ and controlling the beam scanning over the specimen.

It is evident that the principle of image formation in STEM mode is fundamentally different from TEM. Using TEM, a certain angular range of scattered electrons is selected and projected via lenses onto the viewing screen. In contrast, STEM follows the same principles as confocal microscopy where an image is build up in a serial manner as an array of pixels with a contrast representing the respective signal intensity recorded by a detector. A substantial advantage of forming images this way is that there are no imaging lenses necessary, and hence no lens defects compromising the resolution. The latter is only governed by the interaction volume of the probe interrogating the specimen.

To switch between brightfield and darkfield mode in conventional TEM, the objective aperture selects either direct or scattered electrons to form the image. In STEM, this selection is provided by electron detectors sitting in a conjugate plane of the diffraction pattern. Therefore a discoidal bright field (BF) detector placed into the direct beam of the DP only records unscattered electrons from wherever the probe is scanning on the specimen, while all scattered electrons fall onto an annular detector (which surrounds the BF detector) to form a darkfield image (see Figure 2.18). The latter is therefore called annular darkfield (ADF) imaging and it can be performed *simultaneously* with BF imaging in STEM mode.

2.7.5 Atomic Number Contrast STEM (Z–STEM)

To appreciate the importance of different illumination types in terms of image and DP formation, some fundamentals of electron scattering must be addressed. The interactions of an incident electron beam with a crystal lattice can be generally divided into *elastic* (no energy loss) and *inelastic* (energy loss) scattering. While the effects of *inelastic* scattering

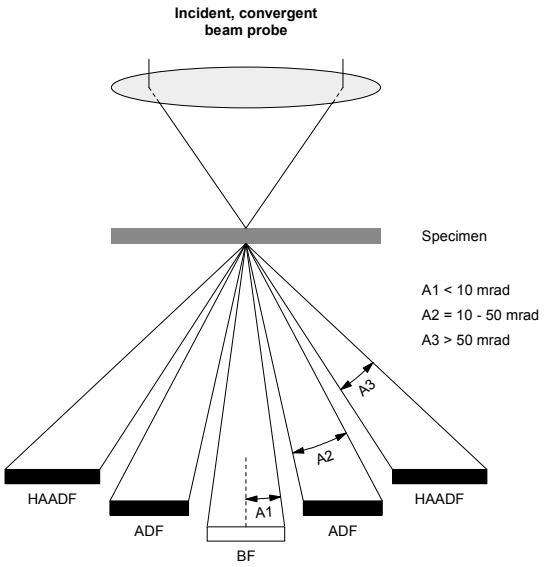

Figure 2.18 Schematic of a STEM imaging detector set–up along with the range of electron scattering angles gathered by each detector.(BF=Bright Field; ADF=Annular Dark Field; HAADF=High Angle Annular Dark Field)

are exploited in analytical methods such as electron energy–loss spectrometry (EELS) or EDAX, image and DP formation arises almost exclusively from *elastic* scattered electrons. What is observable in an image and how the contained information must be interpreted is dependent on the type of *contrast* from which it arises. When incident electrons are elastically scattered by the specimen, the electron wave can change both its amplitude and its phase. Thus a fundamental distinction is made between *amplitude contrast* and *phase contrast*. In the majority of cases both types contribute to an image, although, typically one will tend to dominate.

Due to the wave–particle duality of electrons, amplitude contrast must be further differentiated by considering either the wave or the particle nature of the electrons. The concept that actually applies is determined by the angle through which electrons are scattered when propagating through a specimen. As they are charged particles, Coulomb interactions play a significant role. When attracted to the positive nuclei of the specimen, they are strongly scattered through large angles up to 180° (complete backscattering). This is described by Rutherford–type scattering and interpreted in terms of particle–particle interactions. The extent of high–angle scattering is dependent on the density and thickness of the specimen, hence this type of contrast is termed *mass–thickness* contrast. Conversely, the wave concept is utilised when incident electrons interact with the negatively charged electron cloud of the sample, resulting in a small angular deviation. In this case, *coherency* effects become dominant

which increase for lower scattering angles. High–angle Rutherford–scattered electrons are therefore regarded as *incoherent* (phases of electron waves are not related). By treating electrons as waves, the interaction with the specimen is then termed diffraction and therefore the observed contrast is called *diffraction* contrast, which is highly sensitive to the lattice structure and orientation of the specimen.

It becomes apparent that, depending on which information is of interest one has to choose a certain contrast and therefore set up the TEM to the respective conditions. As the photophysics of nanocrystals, and especially nanocrystal heterostructures, are substantially governed by their size, shape and elemental composition, mass–thickness contrast is most useful [21–23]. Z–contrast represents the detection limit of mass–thickness contrast and is, due to a FEG source, possible to be performed at atomic resolution.

As mentioned before, mass–thickness contrast originates from high–angle scattered electrons and it is therefore reasonable to describe them as particles. Since unscattered electrons do not contribute to image formation, the scattering probability of an electron upon passing through a specimen is an essential factor and related to the total interaction cross section of a single atom, given by

$$\sigma_T = \sigma_{\text{elastic}} + \sigma_{\text{inelastic}} \quad , \tag{2.13}$$

with σ defined in terms of the effective radius of the scattering centre, r, that

$$\sigma = \pi r^2 \quad . \tag{2.14}$$

The expression for r may become highly complicated, depending on how accurately the scattering process in a real specimen is approximated. Apart from the effective radius, σ is furthermore governed by the angular distribution of scattering from an atom, which is considered by the *differential* cross section $d\sigma(\theta)/d\Omega$, where Ω is the solid angle into which electrons are scattered through an angle θ with

$$d\Omega = 2\pi(1 - \cos\theta) \quad . \tag{2.15}$$

High–angle elastic scattering on nuclei was first observed by Geiger and Rutherford (1911), who derived the following expression for the differential cross section of a single atom

$$\frac{d\sigma(\theta)}{d\Omega} = \frac{e^4 Z^2}{16\,(E_0)^2\, sin^4\frac{\theta}{2}} \quad . \tag{2.16}$$

In this equation, E_0 is the incident beam energy, e is the electron charge, and Z is the atomic number of the scattering nucleus. Integration of equation 2.16 from 0 to π leads to the total

elastic nuclear cross section of

$$\sigma_{\text{nucleus}} = 1.62 \times 10^{-24} \left(\frac{Z}{E_0}\right)^2 \cot^2 \frac{\theta}{2} \quad , \tag{2.17}$$

revealing that the probability of electron scattering by a nucleus is dependent on the beam energy (E_0), the deviation angle (θ) and the atomic number (Z). The angle dependence can be directly observed when looking at a diffraction pattern, where the spot intensity is related to the scattering angle (see Figure 2.15).

To account for the scattering of a specimen with thickness t and density ρ, the total cross section is given by

$$Q_T(t) = \left(\frac{N_0(\rho t)}{A}\right) \sigma_{\text{nucleus}} = 1.62 \times 10^{-24} \left(\frac{N_0(\rho t)}{A}\right) \left(\frac{Z}{E_0}\right)^2 \cot^2 \frac{\theta}{2} \quad , \tag{2.18}$$

where N_0 is Avogadro's number (in units of cm^{-3} or m^{-3}) and A is the atomic weight of the specimen atoms. The term (ρt) is called the "mass–thickness" of the specimen giving the contrast its name. Therefore images, just formed by electrons scattered into a particular angular range, have a contrast which is linearly dependent on *thickness* as well as on the square of the *atomic number* (Z^2). To obtain a more accurate differential cross section, screening of the surrounding electron cloud as well as relativistic effects have to be considered. By including the screening parameter θ_0 and the relativistic corrected wavelength λ_R, the so–called screened relativistic Rutherford cross section is

$$\frac{d\sigma(\theta)}{d\Omega} = \frac{\lambda_R^4 Z^2}{64\pi^4 (a_0)^2 \left[\sin^2 \frac{\theta}{2} + \left(\frac{\theta_0}{2}\right)^2\right]^2} \quad , \tag{2.19}$$

where a_0 is the Bohr radius of the scattering atom. This is the most widely used cross section for TEM calculations, although it cannot describe σ exactly as it ignores the wave nature of the electron beam and a full treatment would involve wave mechanics. However, as stated before, the wave properties of electrons must be considered only for low angle scattered beams, as the extent of interference of spatially separated scatterers (coherence) is inversely proportional to its deviation angle. Therefore, as long as the observed image originates just from high angle scatter, where the primary electrons are incoherent, equation 2.19 describes the cross section accurately.

This high angle condition is provided in Z contrast microscopy [24–26] by utilizing an ADF detector with a very large inner collection angle (typically tens of millirads), a so–called high angle annular darkfield (HAADF) detector and has several beneficial implications concerning

image interpretation compared to diffraction contrast and phase contrast (used in HRTEM). Due to scattering from nuclei, the scattering centres are highly localized with virtually no overlap between adjacent columns and are considered as contributing independently to the image intensity. These images are very intuitively interpretable, as the intensity distribution originates from a convolution of the incident probe with the appropriate cross-sections, providing atomic resolution with elemental contrast. The major strength of HAADF imaging is, that by suppressing interference in image formation, *dynamical diffraction* effects are prevented which dominate in images formed by diffraction or phase contrast. These imaging methods are highly sensitive to sample thickness and objective lens defocus as well as lattice structure and sample orientation. This can lead to effects such as contrast reversals complicating accurate image interpretation. Conversely, HAADF contrast is generally unaffected by small changes in objective defocus or specimen thickness and does not 'encrypt' specimen information. This ensures that reliable structural information can be extracted from the raw image without having to compare the experimental results with time–consuming and delicate simulations, as is the case in standard phase–contrast HRTEM [27].

2.7.6 Image Analysis

TEM analysis within this thesis was performed on nanocrystal samples to obtain structural information such as size distribution, shape and crystal structure. As mentioned previously, colloidal synthesis of NCs leads always to a defined size distribution with its FWHM giving direct insight into the quality of the method. Size distributions from TEM/STEM images were determined using the freeware program FIJI, which is based on ImageJ, by either manual or software–assisted measurement of the diameters of at least 100 particles. As illustrated in Figure 2.19, the recorded sizes were then binned into 0.1 nm intervals and the resultant histograms fitted to Gaussian distributions. From those fits the mean size and FWHM of the size distribution were estimated.

The limited contrast between particles and background is one of the major difficulties in accurately assessing the particle size distribution. Image processing such as background correction and contrast enhancement can facilitate the analysis to some degree. However, the key factors to obtain images suitable for size analysis are the appropriate choice of grids, sample preparation and deposition techniques as well as imaging conditions [28, 29].

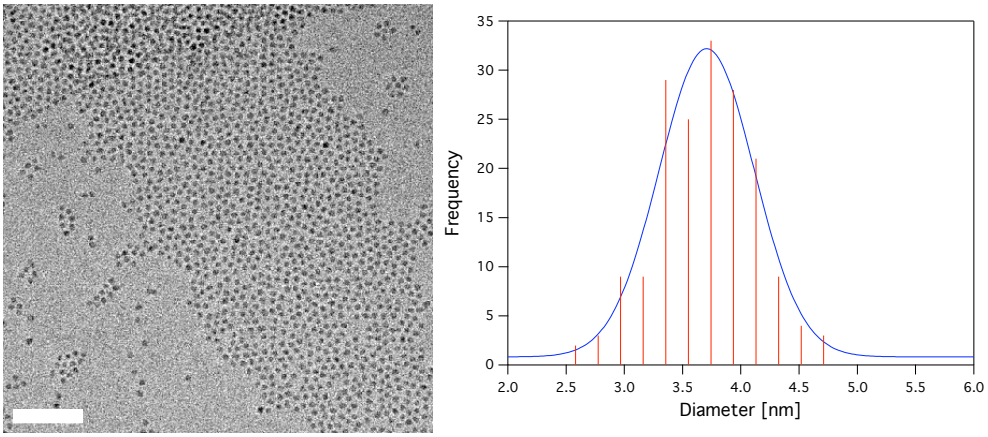

Figure 2.19 Brightfield TEM image (50 nm scale bar) and corresponding size–distribution histogram. The binned data is fitted to a Gaussian distribution resulting in a mean diameter of 3.71 nm which is in excellent agreement with the predicted value of 3.81 nm from absorption spectroscopy (first absorption peak at 576 nm).

Bibliography

[1] C. B. Murray, D. J. Norris and M. G. Bawendi. Journal of the American Chemical Society **115**, 8706 (1993).

[2] J. van Embden and P. Mulvaney. Langmuir **21**, 10226 (2005).

[3] W. W. Yu, L. Qu, W. Guo and X. Peng. Chemistry of Materials **15**, 2854 (2003).

[4] J. Jasieniak, L. Smith, J. v. Embden, P. Mulvaney and M. Califano. The Journal of Physical Chemistry C **113**, 19468 (2009).

[5] I. Moreels, K. Lambert, D. De Muynck, F. Vanhaecke, D. Poelman, J. Martins, G. Allan and Z. Hens. Chemistry of Materials **19**, 6101 (2007).

[6] L. Cademartiri, E. Montanari, G. Calestani, A. Migliori, A. Guagliardi and G. Ozin. Journal of the American Chemical Society **128**, 10337 (2006).

[7] W. E. Moerner and D. P. Fromm. Review of Scientific Instruments **74**, 3597 (2003).

[8] R. Hanbury-Brown and R. Q. Twiss. Nature **177**, 27 (1956).

[9] T. Basche, W. E. Moerner, M. Orrit and H. Talon. Physical Review Letters **69**, 1516 (1992).

[10] W. Becker. *Advanced Time–Correlated Single Photon Counting Techniques* (Springer, 2005).

[11] K. D. Weston, M. Dyck, P. Tinnefeld, C. Müller, D. P. Herten and M. Sauer. Analytical Chemistry **74**, 5342 (2002).

[12] L. P. Watkins and H. Yang. The Journal of Physical Chemistry B **109**, 617 (2004).

[13] C. H. Crouch, O. Sauter, X. Wu, R. Purcell, C. Querner, M. Drndic and M. Pelton. Nano Letters **10**, 1692 (2010).

[14] D. L. Ensign and V. S. Pande. The Journal of Physical Chemistry B **114**, 280 (2009).

[15] D. B. Williams and C. B. Carter. *Transmission Electron Microscopy: A Textbook for Science* (Plenum Press, New York, 1996).

[16] P. D. Nellist and S. J. Pennycook. Ultramicroscopy **78**, 111 (1999).

[17] E. M. James and N. D. Browning. Ultramicroscopy **78**, 125 (1999).

[18] E. M. James, N. D. Browning, A. W. Nicholls, M. Kawasaki, Y. Xin and S. Stemmer. Journal of Electron Microscopy **47**, 561 (1998).

[19] D. A. Muller, E. J. Kirkland, M. G. Thomas, J. L. Grazul, L. Fitting and M. Weyland. Ultramicroscopy **106**, 1033 (2006).

[20] A. Muller and J. Grazul. Journal of Electron Microscopy **50**, 219 (2001).

[21] van SchooneveldMatti M., A. Gloter, O. Stephan, L. F. Zagonel, R. Koole, A. Meijerink, M. J. M. and de GrootFrank M. F. Nat Nano **5**, 538 (2010).

[22] J. R. McBride, T. C. Kippeny, S. J. Pennycook and S. J. Rosenthal. Nano Letters **4**, 1279 (2004).

[23] A. V. Kadavanich, T. C. Kippeny, M. M. Erwin, S. J. Pennycook and S. J. Rosenthal. Journal of Physical Chemistry B **105**, 361 (2001).

[24] O. L. Krivanek, M. F. Chisholm, V. Nicolosi, T. J. Pennycook, G. J. Corbin, N. Dellby, M. F. Murfitt, C. S. Own, Z. S. Szilagyi, M. P. Oxley, S. T. Pantelides and S. J. Pennycook. Nature **464**, 571 (2010).

[25] L. J. Allen. Nat Nano **3**, 255 (2008).

[26] K. W. Urban. Science **321**, 506 (2008).

[27] V. Grillo, E. Carlino and F. Glas. Physical Review B (Condensed Matter and Materials Physics) **77**, 054103 (2008).

[28] W. D. Pyrz and D. J. Buttrey. Langmuir **24**, 11350 (2008).

[29] G. H. Woehrle, J. E. Hutchison, S. Özkar and R. G. Finke. Turkish Journal of Chemistry **30**, 1 (2006).

3 Synthesis and Optical Properties of II-VI Core/Shell Nanocrystal Heterostructures

3.1 Introduction

Semiconductor quantum dots are increasingly considered the future building blocks for a plethora of applications ranging from opto–electronic devices, such as LEDs [1–4], solar cells [5–7] and lasers [8–11], to medical techniques for drug delivery or as fluorescent bio–markers [12, 13]. Since as–prepared nanocrystals have to be functionalised and processed to suit these applications, common prerequisites are sufficient robustness of their properties against post–synthetic treatments and long–term stability. In Chapter 1 we have introduced the concept of surface states and their major influence on the optical properties of NCs. It was shown that appropriate ligands are able to passivate such trap states, however the labile nature of the ligand–surface bond leads to a PL decline upon purification or dilution of nanocrystal solutions [14] making this route of surface passivation unsuitable for practical applications. Furthermore steric hindrance between capping molecules prevents the passivation of all surface sites.

As a result, the preparation of core/shell nanocrystal heterostructures with the growth of an epitaxial inorganic shell of a suitable semiconductor material onto the NC cores (see Figure 3.1) has become the standard for surface passivation today. Because of the strong covalent bonds at the material interface and the inorganic nature of the passivating shell, this method provides superior robustness against post–synthetic treatment and is theoretically able to passivate 100 % of surface sites. Another major advantage of core/shell particles is the possibility of band gap engineering through the combination of different semiconductor materials which extends the control over charge carrier confinement beyond the size dependency of bare cores.

Figure 3.1 illustrates the two major confinement scenarios in core/shell structures. A band gap alignment in which the valence and conduction band of one material is encased within the band gap of the other leads to the formation of a Type–I heterostructure in which both charge carriers are confined in the small–band gap region of the particle. If the wider band gap material constitutes the shell, the core is buried in a potential energy well, concentrating the charge carriers into the core, away from the surface. Therefore, surface trap sites will have a diminished impact on the fluorescence efficiency and fewer environmental factors will influence the emission intensity and quantum yield. These systems, based on CdSe/CdS and

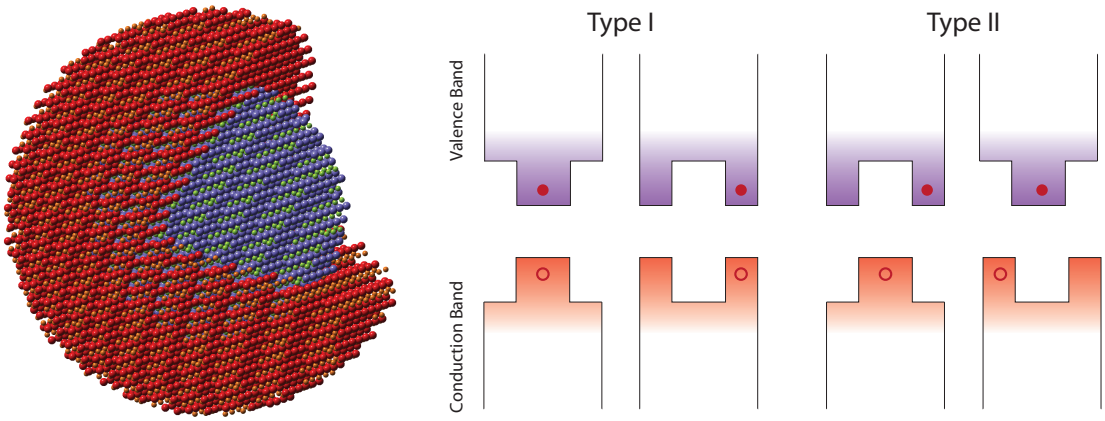

Figure 3.1 Right: Space filling cut–out model of a core/shell nanocrystal. Left: Schematic illustrating the various band gap alignments in Type–I and Type–II NC heterostructures. The red filled and empty circles indicate the electron and hole localisation respectively. In Type–I systems, both the electron and hole are confined into the same region (either core or shell). In Type–II structures charge carrier separation is facilitated confining electron and hole into opposite domains of the core/shell heterostructure.

CdSe/ZnS material combinations, have been shown to produce efficient and stable fluorescence with extremely high quantum yields close to unity [15–18]. Another advantage of sulphur containing shells is the much more positive oxidation potential of S^{2-} compared to Se^{2-}, resulting in a higher threshold to photo–oxidative degradation and surface defect formation. Conversely, heterostructures in which the band alignment is inverted and the wider band gap material comprises the core, lead to confinement of the exciton within the shell region. This system is termed a Quantum Dot Quantum Well (QDQW) [19, 20] and enables the study of two dimensional confinement in nanocrystals which is controlled by the shell thickness.*

Another confinement scenario is established when the electron and hole are confined into different regions of the heterostructure forming a Type–II system [21–25]. This is achieved when the combination of two semiconductor materials produces a staggered band gap alignment, as depicted on the right side of Figure 3.1. The spatial separation of the charge carriers leads to fundamentally different optical properties compared to Type–I structures and is generally desirable for applications involving fast charge separation such as photovoltaic devices.

The work presented in this chapter is focused on the investigation of Type–I core/shell heterostructures of the type CdSe/CdS and CdSe/ZnS. The aim was to investigate the evolution of the electronic spectra as a function of shell growth. For the first time, the development of higher order transitions in CdSe/CdS was quantified as a function of shell

* An in–depth study of a core/shell heterostructure containing such a quantum well will be presented in Chapter 5.

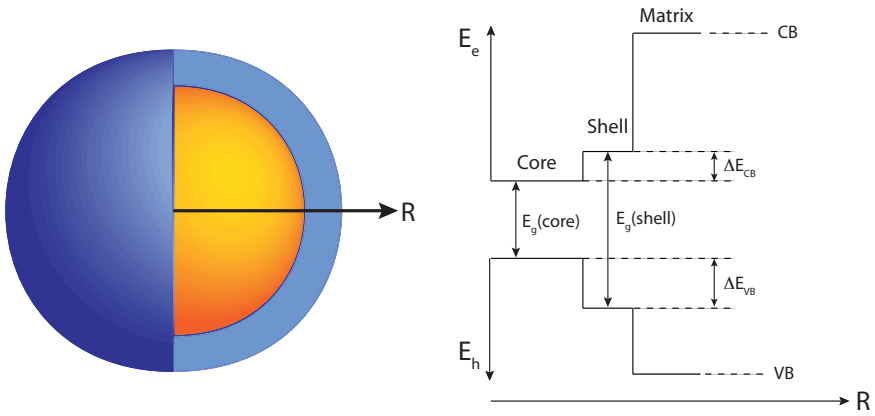

Figure 3.2 A schematic of a core/shell NC along with the corresponding radial energy diagram (not to scale). $E_g(core)$ ($E_g(shell)$) is the band gap of the core (shell) and ΔE_{VB} (ΔE_{CB}) is the potential offset of the valence band (conduction band) between core and shell.

thickness and core size. We begin by examining the Type–I system theoretically by extending the finite potential well model introduced in Chapter 1 for concentric core/shell structures. Subsequently, we present the experimental details pertaining to the successful synthesis and shell thickness control in such heterostructures, followed by their structural and optical analysis. The contents of this chapter will also be relevant in later chapters, which address the synthesis and characterisation of more complex core/multi–shell nanocrystals.

3.2 Finite Potential Well Model for a Type-I Core/Shell Nanocrystal

In Chapter 1, it was shown that the energy levels of core semiconductor nanocrystals can be qualitatively described by a finite spherical potential well model. Following the approach by Schooss et al. [26], this model can be extended for spherical core/shell heterostructures assuming the electron and hole wave functions as non–interacting particles and a uniform shell thickness with no alloying at the material interface, as depicted in Figure 3.2. Since the objective of these calculations is to understand the trends in red shifts in absorbance with increasing shell thickness and the difference in red shifts between ZnS and CdS overcoats, we limit our discussion to the lowest excited state, $S1$. By analogy to the finite potential model for core NCs, the eigenfunction can be expressed as a product of radial and angular components as

$$\psi_{n,l,m}(r,\theta,\phi) = R_{n,l}(r)Y_{l,m}(\theta,\phi) \quad , \tag{3.1}$$

Material	Band gap E_g $[eV]$	Electron effective mass m_e^*	Hole effective mass m_h^*	CB Offset with CdSe $[eV]$	VB Offset with CdSe $[eV]$	Mono-layer thickness $[nm]$
CdSe	1.74	0.13	0.45	0.00	0.00	0.351
CdS	2.45	0.18	0.60	0.29	0.42	0.337
ZnS	3.62	0.20	0.80	0.68	1.20	0.312
Matrix	15.74	1.00	1.00	4.00	10.00	—

Table 3.1 Bulk parameters employed in the modelling of CdSe/CdS and CdSe/ZnS core/shell heterostructures. [28, 29]

where $R_{n,l}(r)$ is a linear combination of spherical Bessel and Neumann functions, and $Y_{l,m}(\theta, \phi)$ are spherical harmonics.

In order to determine the exact form of the wavefunctions, the spatially dependent potentials within the core/shell structure must be determined. In this model a reference potential of 0 eV for the electron and hole is assumed at the lowest conduction band and highest valence band in the heterostructure. As illustrated in Figure 3.2, the potential offsets ΔE_{CB} and ΔE_{VB} are applied within the shell region and a finite matrix potential offset is assigned outside the particle. The particular potential values and other structural parameters employed in these calculations are given in Table 3.1. However it is important to bear in mind that these values are taken to be known with $\sim$10 meV accuracy and scatter widely throughout the literature [27].

Depending on the spatial location of a carrier, its wavenumber is given by:

$$k = \begin{cases} \sqrt{\dfrac{2m^* E^a}{\hbar^2}} & \text{if } r < a \\ \sqrt{\dfrac{2m^*(E^a - \Delta E_X^a)}{\hbar^2}} & \text{if } r \geq a \end{cases} \tag{3.2}$$

where a marks the radial position of the material interface, E^a is the carrier's relative energy in the $1S$ state and ΔE_X^a is the potential offset applied for the shell (X=CB or VB) and outer matrix (X=m).

Furthermore, the radial component $R_{n,l}(r)$ of the eigenfunctions must satisfy the continuity relations for both the wavefunction (Equation 3.3) and the corresponding probability currents (Equation 3.4) at the core/shell interface as well as at the shell/matrix interface, given by:

$$R_{n,l_c}(r)\big|_{r=a} = R_{n,l_m}(r)\big|_{r=a} \tag{3.3}$$

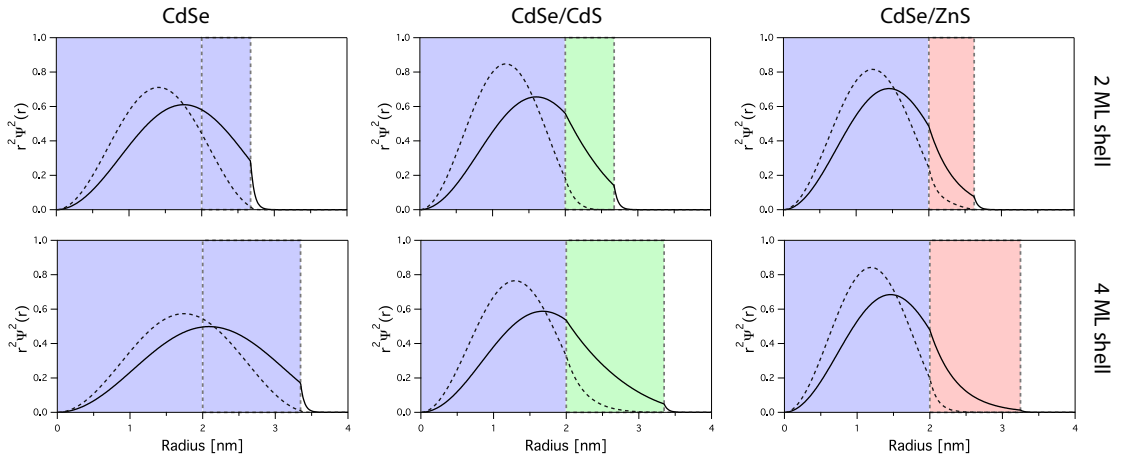

Figure 3.3 Radial probability distributions of the lowest state electron (solid line) and hole (dashed line) wavefunctions for pure CdSe, CdSe/CdS and CdSe/ZnS core/shell heterostructures with a core radius of 2 nm and a shell thickness of 2 (top) and 4 (bottom) semiconductor monolayers.

$$\frac{1}{m_c^*}\frac{dR_{n,l_c}(r)}{dr}\bigg|_{r=a} = \frac{1}{m_m^*}\frac{dR_{n,l_m}(r)}{dr}\bigg|_{r=a} \quad . \tag{3.4}$$

Finally, analogous to the core model, the solutions must be regular at the origin and vanish sufficiently quickly within the matrix[†].

Figure 3.3 displays the radial probability distributions for the $1S$ electron and hole states in pure CdSe nanocrystals, as well as CdSe/CdS and CdSe/ZnS core shell structures. All systems are based on a 2 nm core radius, and shell thicknesses of two (top) and four (bottom) monolayers are compared. First inspection of the plots reveals that the electron is generally more delocalised compared to the hole which can be attributed to its lower effective mass and thus higher kinetic energy. Consequently the probability function of the electron is more likely to be found at the surface than the hole. In the bare dots the wavefunction of the lighter electron spreads over the entire particle and can tunnel slightly into the surrounding matrix whereas the heavier hole has a higher probability at the centre of the dot and does not extend beyond the particle surface. Growth of a CdS shell onto the core surface leads to a distinct change in charge carrier confinement. With a VB offset of $\sim$0.4 eV and a larger effective mass in the CdS shell, the hole has a relatively low probability of penetrating the CdS shell. In contrast, due to the small conduction band offset between CdSe and CdS the electron is able to tunnel deep into the surrounding CdS shell and has still a significant probability of reaching the particle surface for shell thicknesses below two monolayers ($\sim$ 0.6 nm). In the case of a ZnS shell, both charge carriers are well localised within the CdSe core, due to the larger

[†] The author acknowledges the assistance of D. Gómez with the calculations.

tunnelling barrier at both the conduction and valence band edges. The electron wavefunction still penetrates the ZnS shell, however the probability decays rapidly within the ZnS region. From the calculations it is evident that a ZnS shell thickness of about four semiconductor monolayers ($\sim 1.2\ nm$) is sufficient to diminish the probability of either charge carrier reaching the surface, leading to a substantially weakened surface sensitivity compared to bare CdSe cores and CdS overcoated core/shells NCs. In general, the increased delocalisation of the electron lowers its confinement energy and consequently the overall energy of the excited state. The extent of this energy loss can be experimentally observed as a red shift of the first excited state transition in the absorbance spectrum and is a useful tool for monitoring shell growth.

From these discussions it is evident that the choice of shell material has a significant impact on the final band gap of the heterostructure. For chemically robust particles with a minimum of red shift it is generally best to choose the shell material with the largest potential barriers for both charge carriers, such as ZnS. However, in some cases it is desirable to actively shift the exciton energy towards lower energies, and in this case a lower potential offset is beneficial. Furthermore, the aspect of lattice mismatch between the core and shell material has to be taken into account for epitaxial shell deposition which will be discussed shortly.

3.3 Preparation of Type-I Core/Shell Nanocrystals

The first studies on core/shell heterostructures were reported as early as 1987 [30], when Henglein et al. demonstrated that samples of aqueous CdS/$Cd(OH)_2$ could reach a quantum yield of 50 % at room temperature and show substantially higher resistance against photoanodic corrosion compared to bare CdS particles. In close succession Brus et al. [31] and White et al. [32] were the first to report on the growth of a ZnS and ZnSe shell respectively onto CdSe cores, observing quantum yield gains up to one order of magnitude upon annealing. However, those early methods suffered poor control over shell growth resulting in very thin shells and poor size distributions.

These difficulties were overcome with the introduction of the hot–injection method by Murray et al. [33] opening up new approaches to shell synthesis. In 1996, Hines and Guyot–Sionnest [34] were the first to demonstrate CdSe/ZnS core shell particles with both a high QY and a narrow size distribution utilising the hot–injection method with organometallic precursors in a one–pot reaction. A 0.6 nm ZnS shell was deposited onto $\sim 3\ nm$ CdSe cores resulting in an astounding 50 % QY at room temperature. More detailed studies followed shortly on CdSe/ZnS [28] and CdSe/CdS [35] heterostructures, which revealed that the strain between the two materials at the core/shell interface is a crucial factor limiting the epitaxy of the final particles.

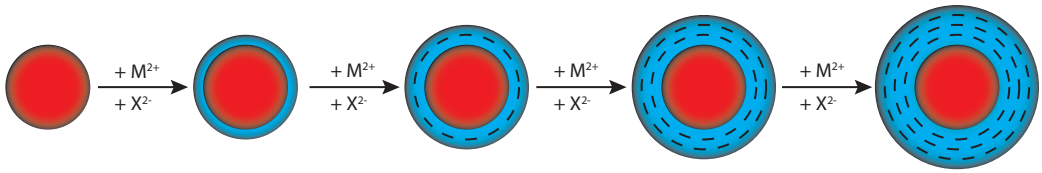

Figure 3.4 A schematic illustrating the layer–by–layer SILAR protocol for shell growth onto spherical Nanocrystals. The shells are grown one atomic monolayer at a time through the sequential addition of the respective chalcogenide anions (X^{2-}) and metal cations (M^{2+}) up to the desired shell thickness.

With the move towards 'greener' synthetic methods for nanocrystal preparation Reiss et al. [18] was the first to report on the deposition of ZnSe shells onto CdSe cores without the need of any pyrophoric organometallic precursors, using zinc stearate as the zinc source. The resulting particles were reported to possesses room temperature photoluminescence efficiencies of 60–85 % in organic solvents as well as in water after functionalisation with mercapto–undecanoic acid.

To prevent homogeneous nucleation of the shelling material, the protocols up to this point relied on drop–wise addition of the mixed metal and chalcogenide precursors [36]. Through the gradual introduction of the precursor, the supersaturation was kept below the critical nucleation level while maintaining it high enough for sufficient growth rates. Another approach to prevent homogeneous nucleation was introduced in 2003 with the seminal paper by Li et al. [37].

Atomic–layer–epitaxy (ALE) is a molecular beam technique in which the cationic and anionic species is introduced in an alternating pattern into the growth chamber. In this way, only one half of a monolayer will grow in each period, and because the two species do not coexist in the chamber, homogeneous nucleation is avoided. Therefore, a thin film grows in a well–controlled manner. The same principle was extended for thin film deposition onto solid substrates from solution baths, using the successive–ionic–layer–adsorption–and–reaction (SILAR) deposition method [38].

Li et al. adapted the SILAR technique for the growth of CdS shells onto CdSe nanocrystals demonstrating highly epitaxial deposition with almost monolayer control over shell thickness (see Figure 3.4). By using air–stable and inexpensive cadmium oleate and 1–octadecene–sulphur as metal and chalcogenide precursors, it was shown that the SILAR protocol was highly reproducible and capable of large scale preparation. Furthermore, due to the generic protocol of layer–by–layer deposition, a wide range of core/shell or multi–shell combinations [15, 17, 21, 25, 39–41] were prepared and studied using this technique.

Through the course of this thesis, all core/shell heterostructures were prepared utilising the SILAR protocol. In the following, we present the experimental details and synthetic considerations for the successful preparation CdSe/CdS and CdSe/ZnS structures.

3.3.1 Experimental Details

3.3.1.1 Injection Solutions

The shelling precursor stock solutions were all prepared at a concentration of 0.1 M. The cadmium and zinc solutions were prepared by dissolving either 0.01 mol CdO (1.2841 g) or 0.01 mol zinc acetate dihydrate (2.195 g) in 0.04 mol TMPPA (11.6168 g) and enough 1–octadecene (ODE) to yield a total volume of 100 mL. The solutions were degassed at room temperature for one hour and slowly heated to 100 $°C$ for a further 30 min under vacuum at which point three pump/purge cycles were performed. Under nitrogen, the solutions were heated to 300 $°C$ for two hours and subsequently cooled to 80 $°C$. At this point the solution appeared optically clear. To remove residual water released during the complexation process, the solutions were degassed for another 10 min before allowing to cool to room temperature. The sulphur stock solution was prepared by dissolving 0.01 mol sulphur (0.3207 g) in 100 mL ODE (78.8 g). The preparation protocol was analogous to the metal precursors, except for the complexation taking place at 120 $°C$ for two hours. Prior to use, all stock solutions were heated to 60 $°C$.

3.3.1.2 Core/Shell Synthesis

Core/shell heterostructures were prepared through adapted synthetic protocols by Li et al. [37] and van Embden et. al. [42]. In a typical synthesis, thoroughly washed NCs dispersed in chloroform were added to a three–neck round–bottom flask along with a mixture of ODE/octadecylamine (ODA) in a 2.5:1 ratio by weight to produce a 40 μM dispersion of nanocrystals in solution. The mixture was carefully degassed at room temperature before being heated to 80 $°C$ at which point three pump/purge cycles were performed. The reaction was then flooded with nitrogen and slowly heated to the appropriate temperature for the deposition of the first shell layer. In all reactions an initial metal layer (M–rich) was deposited to create a metal rich surface. Subsequent shell growth was performed by introducing first the chalcogenide precursor (X1) followed by the metal source (M1) and so forth. The quantities of such injections to deposit one atomic monolayer at a time were calculated on a volume basis (see Section 3.3.2). Typically each layer was allowed to grow for 15 min and the reaction was always finished on a metal layer. To ensure complete shell growth under those reaction conditions, the introduction of a 30 % excess of metal precursor (for each metal injection) was found to be necessary. Following the growth of the final layer, the nanocrystals were annealed

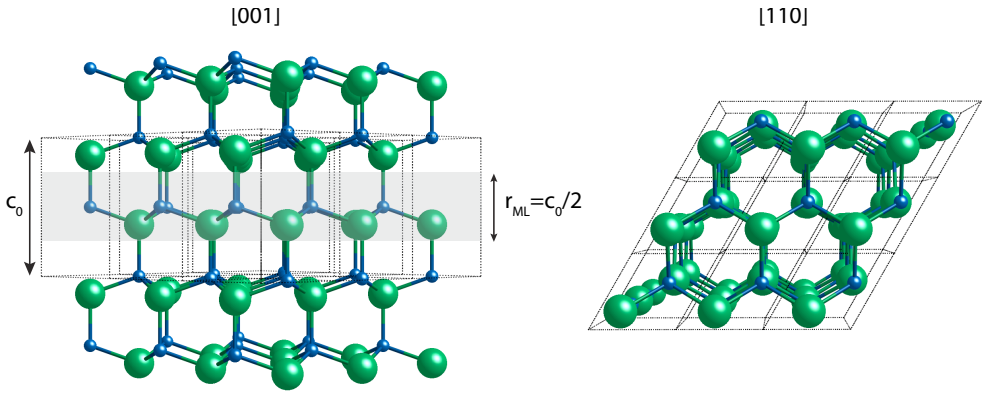

Figure 3.5 Schematics of a wurtzite crystal lattice along different Miller indices with the dotted lines identifying the unit cells. The radial increase of a spherical wurtzite nanocrystal per semiconductor monolayer r_{ML} is defined as half the c–lattice parameter $c_0/2$ throughout this thesis.

Material	Lattice parameter a_0 $[nm]$	Lattice parameter c_0 $[nm]$	Molar mass M $[g/mol]$	Density ρ $[g/cm^3]$
CdSe	0.430	0.702	191.37	5.816
CdS	0.4135	0.6749	144.46	4.82
ZnSe	0.398	0.653	144.35	5.27
ZnS	0.3811	0.6234	97.474	4.090

Table 3.2 Material parameters employed for SILAR shelling monolayer calculations [43].

at 200 $°C$ for one hour and further stirred at 70 $°C$ for another 12 hours before being purified as outlined in Chapter 2.

3.3.2 Monolayer Calculations

To achieve monolayer control over shell growth one has to firstly define a semiconductor monolayer and secondly be able to precisely calculate the amount of precursors required to produce such a shell thickness. The nanocrystals prepared throughout this thesis were found to exhibit the anisotropic wurtzite crystal structure for which the definition of monolayer thickness is dependent on which direction of the hexagonal unit cell is considered. For the calculations in this work we chose the projection along the c–axis with the thickness of a single semiconductor monolayer r_{ML} defined by half the c_0 lattice parameter, as illustrated in Figure 3.5.

To determine the amount of precursor required to generate such a monolayer, the concentric shell model (CSM) is employed which is based on the volumetric increase of a spherical particle upon shell growth. With r_{ML} considered as the radial increase upon deposition, it can be shown that for a given concentration of core nanocrystals $[NC]$, of a mean diameter D, the total number of moles of each precursor that need to be added is:

$$n_{precursor} = \frac{4}{3}\pi \left[(D + r_{ML})^3 - D^3 \right] \frac{\rho[NC]}{M} \quad , \tag{3.5}$$

where ρ (g/m^3) and M (g/mol) are the density and molecular weight of the shelling material, respectively. $[NC]$ and D for CdSe nanocrystals were accurately determined utilising the expressions outlined in Section 2.5 [44] and the parameters for the shelling materials are given in Table 3.2. It is important to note, that for the full growth of a semiconductor monolayer equimolar amounts of *both* atom types are needed. Thus, to grow a four monolayer thick shell, eight atomic monolayer injections are required. All calculations for shell growth were combined into a single spreadsheet with an example given in Appendix A.

3.3.3 Growth Temperature

Given their small volume and high surface energy, the growth rate of a nanocrystal is sensitive to small changes in reaction temperature. As such, the choice of temperature at which the shells are grown is critical. On the one hand higher temperatures increase the reactivity of both the particles and the shell precursors (monomers), which favours shell growth and prevents the build up of monomer in solution — a condition leading to homogeneous nucleation of the shell material. On the other hand too high temperatures can induce Ostwald ripening of the nanocrystals. Given that ripening depends strongly on particle size [45], the temperature for shell deposition must be adjusted accordingly, with the smallest particles requiring the lowest temperature. Generally, one should aim for the highest possible temperature to impart appreciable shell growth rates and maximum crystallinity through annealing while avoiding particle ripening. Table 3.3 lists the reaction temperatures applied for the growth of CdSe/CdS nanocrystals with various initial CdSe core sizes [42]. For the growth of CdSe/ZnS heterostructures a continuous temperature ramping protocol was utilised with the temperatures given in Table 3.4.

3.3.4 Ligand chemistry

Next to the reaction temperature, the choice of complexing agents is another vital consideration as they control the various equilibria of precursor solubility, monomer release and shell growth [46]. The SILAR protocols developed at the University of Melbourne employ the phosphinic

Size Range $[nm]$	Band Edge Absorbance λ_{max} $[nm]$	Temperature 1 $[°C]$	Temperature 2 $[°C]$
2.7 - 3.5	530 - 570	230	240
3.5 - 4.6	570 - 600	235	240
4.6 - 6.2	600 - 630	235	245

Table 3.3 Reaction temperatures utilised for the growth of CdSe/CdS core/shell structures with various CdSe cores sizes. Temperature 1 was required for the growth of the first two semiconductor monolayers while Temperature 2 was applied for the growth of all subsequent shells [42].

Layer	M–rich	X1	M1	X2	M2	X3	M3	X4	M4	X5	M5
Growth Temp. $[°C]$	220	230	235	240	240	240	240	245	245	250	250

Table 3.4 Reaction temperatures utilised for the growth of individual atomic metal (M) and chalcogenide (X) monolayers to prepare CdSe/ZnS core/shell structures with CdSe cores of a 3 nm diameter and larger.

acid TMPPA as the metal complexing ligand, which is in contrast to the more commonly used oleic acid (OA) [25, 37]. It was shown that TMPPA can successfully stabilise NCs by decreasing their surface tension and increasing the supersaturation of the system while OA accelerates Ostwald ripening [47]. The stabilisation effect of TMPPA is particular beneficial for the shelling of smaller nanocrystals which have a higher tendency to dissolve. However, the growth of CdS shells onto CdSe cores using pure Cd–TMPPA and ODE–S results reproducibly in homogeneous nucleation of the shelling material and smaller than predicted shell thicknesses due to the strong binding of TMPPA to the particle surface [42]. To remedy this issue, oleic acid was substituted into the growth medium in a mole ratio of 20:1 (OA:Cd-injected) immediately after any cadmium layer injection. On the one hand, oleic acid complexes cadmium monomer to controllably lower the supersaturation, while on the other side, it facilitates TMPPA displacement at the particle surface, increasing its reactivity. Using this binary ligand approach, uniform CdS shell growth in the absence of homogeneous nucleation was achieved.

For the growth of ZnS shells, supplementation of the Zn–TMPPA precursor with OA was not suitable, since oleic acid complexes zinc cations too strongly, preventing their effective release. Consequently the sulphur precursor was targeted to control the supersaturation. It is known that TOP can efficiently complex sulphur dissolved in ODE and reduce supersaturation. However TOP binds too strongly to sulphur to allow for good quality ZnS shell growth [46]. Thus tributylphosphite (TBPh) was chosen to control the supersaturation since it binds more weakly to sulphur (the oxygen groups intermediate between the phosphorus and the alkyl

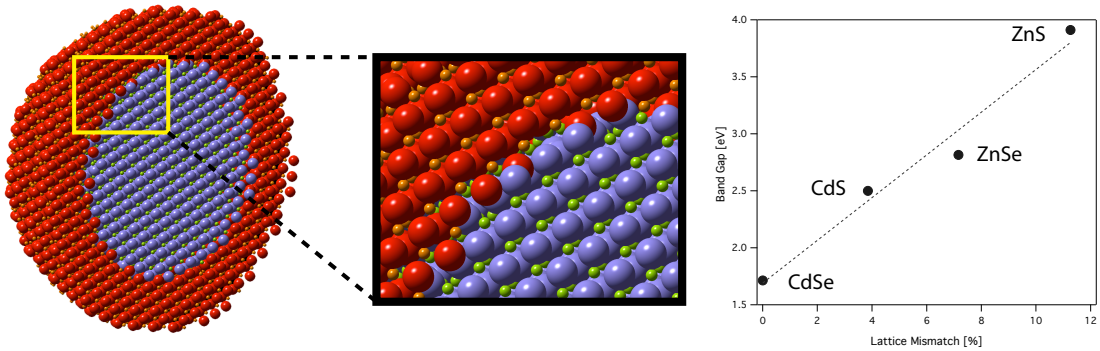

Figure 3.6 Left: Cut–away model and zoom–in of an ideal core/shell nanocrystal heterostructure with no lattice distortions at the materials interface. Right: Band gap energy as a function of the percent lattice mismatch between bulk CdSe and the other semiconductor shell materials.

chains withdraw electron density from the phosphorus moiety making it less nucleophilic [48]). A supplementation of TBPh with a 0.5:1 mole ratio to sulphur was found to successfully suppress homogeneous nucleation (HN) while allowing for good ZnS shell growth.

3.3.5 The Effects of Lattice Strain

From the charge carrier distribution calculations presented previously, it is clear that ZnS is a superior shell material compared to CdS for CdSe based Type–I structures. Due to its larger conduction and valence band offsets, a ZnS shell is able to effectively confine both the electron and hole in the core region away from the surface, leading to an increased QY and chemical stability. However, those calculations assume an ideal, defect–free crystal structure (see Figure 3.6) and do not take lattice strain at the interfaces into account.

In real structures, even if the core and shell material posses the same crystal structure, lattice mismatch will always be present due to the differences in their material specific bond lengths (see Table 3.2). The plot on the right in Figure 3.6 depicts the relative lattice mismatch of CdS, ZnSe and ZnS relative to CdSe as a function of their respective band gap. There is a discernible trend in which higher band gap materials possess smaller lattice parameters; thus there is always a trade–off between lattice mismatch and the degree of charge carrier confinement.

Depending on the extent of lattice mismatch it can considerably affect the final QY. To maintain epitaxial growth, the bond lengths of core and shell material have to approach each other leading to compression of the larger lattice parameter material and tension of the smaller parameter material at the interface. However shell deposition on a substrate with different bond lengths can only proceed to a critical thickness before a lattice defect (misfit dislocation)

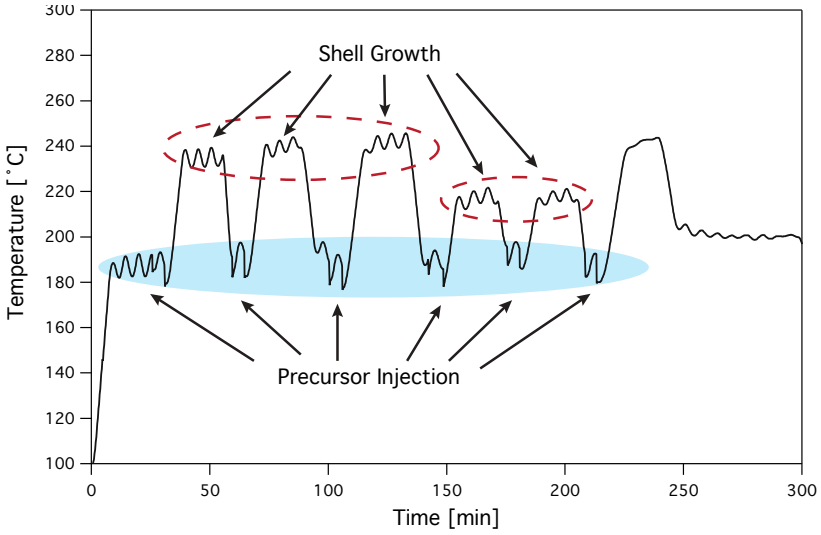

Figure 3.7 Temperature profile of a SILAR shelling reaction combined with Thermal Cycling. Precursors were introduced at a lower injection temperature which was followed by an immediate temperature increase for shell growth.

will arise near the interface to ease the strain, allowing the materials to relax to their native bond lengths. These defects introduce a new source for non–radiative recombination centres, effectively reducing the QY of the particle.[‡] Thus, it is commonly observed, that the emission QY of core shell particles is highly dependent on the width of the shell. The maximum is typically observed at a lower coverage in CdSe/ZnS nanocrystals ($\sim 0.4\ nm$) compared to CdSe/CdS particles ($\sim 0.74\ nm$) due to the larger lattice mismatch relative to CdSe [35]. However, it is important to bear in mind that even if core/shell structures with a thin shell exhibit higher QYs, they also show a substantially lower resistance against post–synthetic treatments.

Apart from its influence on optical properties, lattice strain also manifests itself by altering the kinetics and uniformity of shell deposition. In contrast to core growth, where there is no lattice mismatch, shell deposition actually increases the surface energy by introducing lattice strain to the crystal. As the particles will always strive to minimise their overall free energy, this energy increase acts as an additional barrier to shell deposition, making it exceedingly difficult to grow thick shells of large–mismatch materials.

Similarly, the morphology of the growing NC is affected by the strain. As the various crystal faces exhibit different surface energies, their respective growth rates vary as well. The strain induced during shell growth amplifies those differences, leading to larger variations in those growth rates. This manifests itself in the formation of non–spherical heterostructures and

[‡] The optical effects of internal crystals defects and their prevention are subject of Chapter 4.

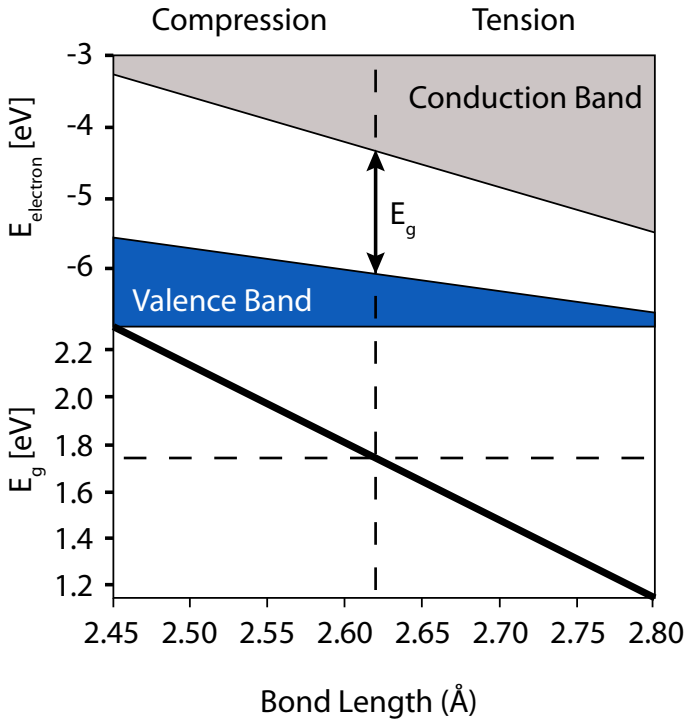

Figure 3.8 A schematic illustrating how the valence band edge, the conduction band edge and the band gap change as a function of CdSe bond length [50]. The equilibrium bond length (2.62 Å) and band gap (1.74 eV) are denoted by the dashed lines.

distinct size distribution broadening commonly observed for CdSe/ZnS particles with thick shells. To maintain the spherical morphology of core/shell structures despite a large lattice mismatch a modification to the SILAR approach, called Thermal Cycling (TC) [17, 21, 49], was recently reported. In this method the shelling precursors for the growth of one semiconductor monolayer are introduced at a relatively low temperature, to allow for uniform distribution into the bulk solution and partial adsorption onto the particle surface. Subsequently the temperature is rapidly increased to induce the shell growth onto the existing NCs. To deposit multiple layers, this temperature change is repeatedly cycled as depicted in Figure 3.7. Using this concept, Blackman et al. could demonstrate the synthesis of spherically shaped CdSe/CdTe and CdS/CdSe/CdTe [49] as well as CdSe/CdTe/ZnSe core/shell heterostructures [21] which traditionally exhibit elongated shapes.

Other recent studies aimed at the exploitation of lattice strain as a means to systematically tune the band gap of the heterostructure [51, 52]. Smith et al. [52] demonstrated dramatic changes in conduction and valence band energies of core and shell after overcoating a CdTe core with ZnS, ZnSe, ZnTe, CdS, or CdSe. The smaller lattice parameters of the shell material relative to CdTe led to a compressive effect on the core crystal structure. Keeping the shell

below the critical thickness for surface defect formation, the distortions upon shell growth forced the materials to adopt unnatural bond lengths. This led to changes in CB and VB energies since they are derived from the crystal bonds, altering the electronic band gap. The change is described by a negative deformation potential α, given by

$$\alpha = \frac{\delta E_g}{\delta \left(lnV\right)} \quad , \tag{3.6}$$

where E_g is the band gap and $\delta(lnV)$ is the fractional volume change. For II–VI and III-V materials, this potential is negative ($\alpha_{CdSe} = -2.9$), meaning that compression of the crystal widens the band gap [53]. Figure 3.8 illustrates the changes in CB, VB and band gap as a function of bond length deformation for CdSe. These studies are important to bear in mind when interpreting theoretical calculations that neglect the effect of lattice strain, as they generally overestimate the degree of confinement in core/shell structures. Rather than a sudden potential step function at the materials interface, a reduced gradual transition is more realistic due to the deformation potential.

3.4 Electron Microscopy

In order to correctly assign the effects of core size and shell thickness to the observed optical properties, tight size control must be achieved. In ensemble measurements the position and sharpness of the spectral features are directly related to the particle size distribution (PSD) of the examined sample and, as such, must be accurately determined. Figure 3.9 depicts the TEM data and PSDs of CdSe core nanocrystals and their subsequent CdSe/CdS and CdSe/ZnS core/shell structures. To achieve epitaxial growth and accurate shell thicknesses, the initial PSD of the core sample needs to be as narrow as possible and the particles of a uniform shape. The CdSe cores, prepared as outlined in Chapter 2, exhibited highly spherical shapes and a standard deviation of about 10 %. Utilising the SILAR protocol as described previously, the growth of a CdS shell is shown to retain the spherical shape of the cores indicating uniform shell deposition on all crystal facets. Based on the monolayer calculations, the final particle size of the core/shell structures was predicted to be 7.6 nm, which is in close accord with the experimentally determined mean size of 7.4 nm, demonstrating near monolayer precision. Furthermore a narrowing of the size distribution to $\sim$ 8.2 % was observed. This effect can be explained through size focussing due to the introduction of excess monomer (and the consequential supersaturation increase), as discussed in Chapter 1.

The growth of CdSe/ZnS core/shell particles did not yield the same degree of growth control, which can be attributed to the large interfacial lattice strain between the CdSe core and the ZnS shell, effectively restricting homogeneous growth. The heterostructures largely

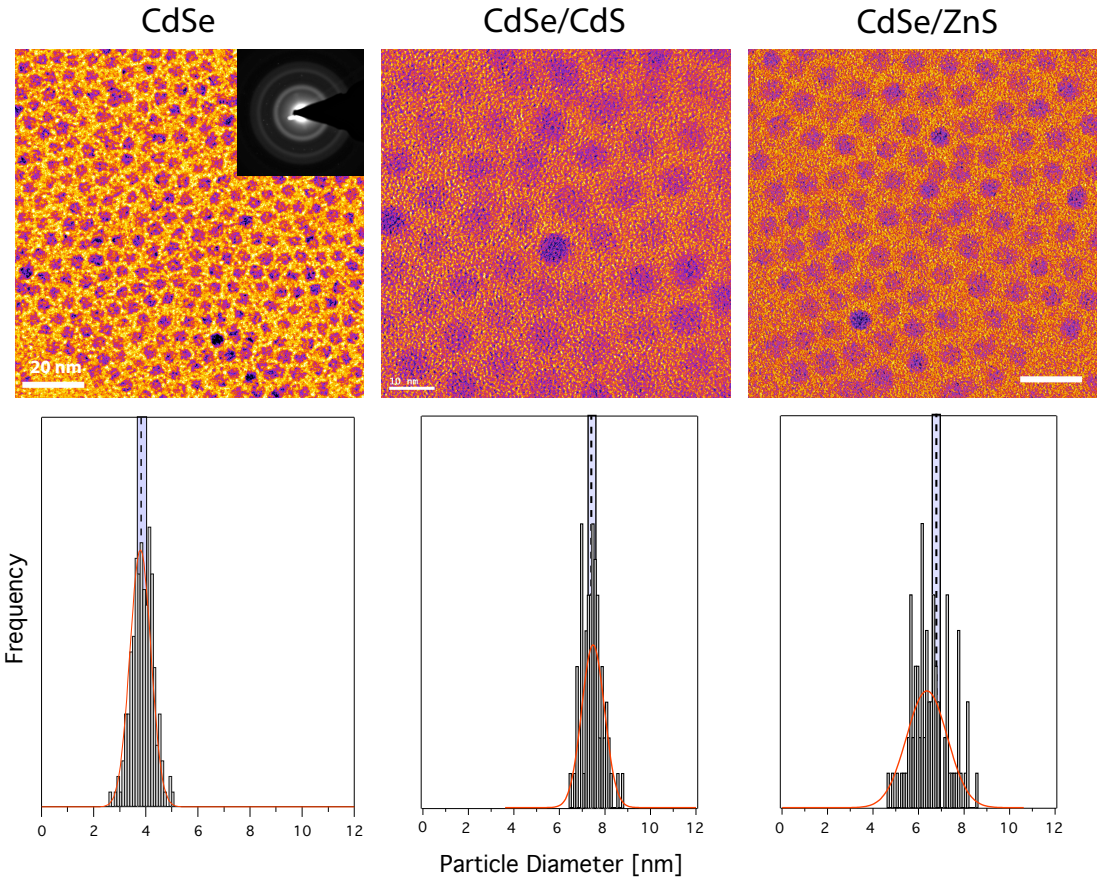

Figure 3.9 Top: Bright field TEM images of CdSe nanocrystals with a 3.9 *nm* diameter (left), and derived CdSe/CdS (centre) and CdSe/ZnS (right) core/shell heterostructures with a shell thickness of 1.8 *nm* and 1.25 *nm* respectively. Bottom: Corresponding histograms of the measured particle sizes. The dashed lines indicate the expected size of the nanocrystals, with the grey box outlining the associated error of ± 0.175 *nm* (one c–lattice plane of CdSe). Gaussian distributions were fitted to the histograms to obtain the mean diameter and PSD. Scale bars: CdSe and CdSe/ZnS (20 *nm*), CdSe/CdS (10 *nm*).

maintained their spherical morphology, however not to the extent observed for CdSe/CdS. Furthermore, inspection of the PSD histogram reveals a broadening in size distribution to 13.1 % standard deviation. The experimentally determined mean size of 6.4 nm, however, is still in good agreement with the predicted diameter of 6.8 nm. The results obtained from TEM analysis demonstrate, that accurate control over shell growth can be achieved when adhering to the protocols described in the experimental section. Generally superior control was achieved for CdSe/CdS NCs compared to CdSe/ZnS particles due to the smaller lattice mismatch. Nevertheless, the size and shape of the ZnS coated heterostructures were still in good agreement with the predicted final diameters for most core sizes.

3.5 Electronic State Evolution

Nanocrystals with their feature–rich absorption spectra are unique systems to identify and study the electronic transition states at ambient conditions, normally not accessible with the bulk material. One of the fundamental and basic experimental questions about quantum dots is how their electronic spectra evolve with size in the strong confinement regime. While this questions was extensively addressed for CdSe NCs [54, 55], only few studies investigated the spectral evolution in core/shell systems [42, 56, 57]. Indeed, the first comprehensive study [42] on the evolution of the first excited state in CdSe/CdS core/shell heterostructures over a wide range of core sizes and shell thicknesses was reported just recently. In this section, we begin by comparing the general evolution of the optical spectra as well as the band edge transition for CdSe/CdS and CdSe/ZnS core/shell structures. Subsequently, we focus on the detailed examination of the CdSe/CdS system, extending the analysis of van Embden et al. [42]. Additional to the first excited state, the development of higher order transition is comprehensively analysed for multiple core sizes and shell thicknesses. Furthermore the effect of temperature on charge carrier confinement over the same parameter space was examined.

3.5.1 Band Edge Transitions in CdSe/CdS and CdSe/ZnS Nanocrystals

As the optical properties of nanocrystalline systems are directly related to the degree of exciton confinement, absorption and emission measurements became standard methods to gain insight into the electronic state configuration of NCs. Figure 3.10 depicts the evolution of the normalised absorbance (**A** and **B**) and emission (**C** and **D**) spectra for CdS and ZnS shell growth respectively, onto CdSe core NCs with a cadmium rich surface. As indicated by the arrows in the insets of **A** and **B**, the first excited state generally shifts to larger wavelengths upon shell growth. A first distinct shift is generally observed after deposition of the first monolayer, regardless of the shelling material. However, subsequent growth of a ZnS shell

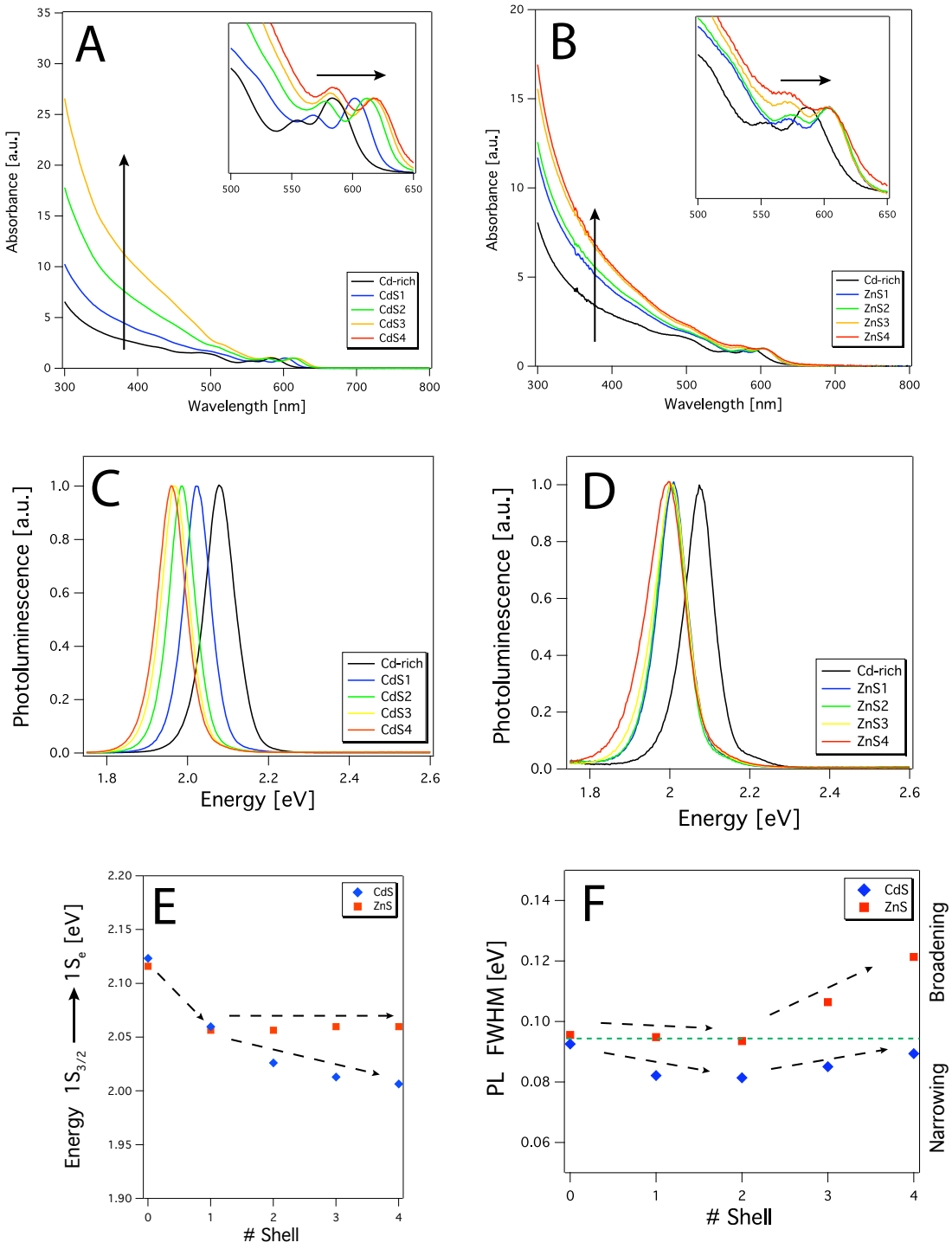

Figure 3.10 Normalised absorption (**A** & **B**) and emission (**C** & **D**) spectra of CdSe/CdS (left) and CdSe/ZnS (right) core/shell nanocrystals taken after deposition of individual semiconductor monolayers onto 4.06 *nm* and 4.13 *nm* CdSe cores respectively. The different magnifications highlight the main spectral changes that occur upon shell deposition. Panel **E** illustrates the energy decay of the first excited state as a function of CdS (blue) and ZnS (red) shell thickness. The layer number '0' assigns the CdSe core with a metal enriched surface (Cd–rich). Panel **F** depicts the FWHM evolution of the PL peak during shell deposition of CdS (blue) and ZnS (red). The green dashed line indicates the FWHM of the initial core sample.

leads only to minute changes in band edge absorbance position, whereas a continuous, albeit weakened, shift towards lower energies is observed with increasing CdS shell thickness (see Figure 3.10 **E**).

These divergent trends are reflected in the emission spectra and are in agreement with the theoretically predicted trends of charge carrier localisation within the different core/shell structures. The confining potential of a higher band gap material is generally not fully established with the growth of the first monolayer. Therefore, the exciton is able to deeply penetrate this region, effectively reducing the confinement and the concomitant red–shift is observed. In the case of ZnS, subsequent deposition leads to strong confinement of both charge carriers into the particle centre due to the large conduction and valence band offsets and no further shifts are detected. In contrast, the continuous red shift upon CdS shelling can be attributed to the small conduction band offset between CdSe and CdS, enabling the electron to extensively delocalise into the CdS region [37], as theoretically predicted. As the shell becomes thicker, the tunnelling probability of the electron decreases leading to the observed weakened red shifts.

Focussing on the high energy part (below 500 nm) of the absorbance spectra, it can be seen that there is an increase relative to the band edge absorption for both systems upon shell growth. With each additional monolayer this higher energy absorbance is systematically strengthened, which may be attributed to the enlarged absorption cross–section of the resultant nanostructure. The enormity of this increase in the CdSe/CdS case arises most likely from a combination of the increased cross–section, the high shell–to–core volume ratio and the high extinction coefficient of CdS compared to CdSe.

Figure 3.10 **F** illustrates the evolution of the full width at half maximum (FWHM) of the band edge emission peak as a function of shell growth for both systems. The FWHM is a common indicator to monitor changes in size distribution of the particle ensemble during growth. In general focusing of the PSD is observed for the deposition of the first two semiconductor monolayers and broadening with every subsequent layer growth. However, the extent of narrowing was found to be more pronounced for CdS compared to ZnS, while the opposite was true for the size broadening past two monolayers. Thus, it was often observed in the case of CdSe/CdS, that the final core/shell structures exhibited a narrower emission band than the initial cores, whereas the PL peak of CdSe/ZnS was mostly broadened. This can be related to the differences in lattice mismatch between core and shell material and is consistent with the PSD results gained from TEM analysis. Due to these observations and the more detailed spectral data of CdSe/CdS heterostructures, further analysis was limited to this system in order to gain more accuracy in the quantification of spectral shifts during shell growth.

	Shell/Core Volume Ratio					
Core radius [nm]	CdS1	CdS2	CdS3	CdS4	CdS5	CdS6
1.45	0.87	2.14	3.89	6.19	9.11	12.73
1.74	0.70	1.67	2.95	4.59	6.63	9.11
2.045	0.58	1.35	2.34	3.57	5.07	6.87
2.395	0.48	1.10	1.88	2.82	3.94	5.27

Table 3.5 Calculated volume ratios for the CdSe/CdS core/shell samples analysed in Figure 3.11.

3.5.2 The Effect of Core Size

Figure 3.11 illustrates the effect of the initial CdSe core size on CdS shell growth. The normalised absorbance spectra (eV scale) in **A**, **B**, **C** and **D** are taken from samples with initial core sizes of 2.90 nm, 3.48 nm, 4.09 nm and 4.79 nm respectively and CdS shell thickness ranging from 1–6 monolayers. From these plots, two clear trends are discernible. Firstly, examining the absorbance at the high energy part of the spectra, it is revealed that its relative magnitude compared to the band edge absorbance generally increases with smaller core sizes. Apart from the higher extinction coefficient of CdS compared to CdSe, this trend reflects the shell–to–core volume ratio V_{shell}/V_{core}. The total volume of the core and outer well can be approximated by

$$V_{core} = \frac{4}{3}\pi r_{CdSe}^3 \quad \text{and} \tag{3.7}$$

$$V_{shell} = \frac{4}{3}\pi r_{CdSe/CdS}^3 - \frac{4}{3}\pi r_{CdSe}^3 \quad , \tag{3.8}$$

respectively. Thus the volume ratio of shell and core can be expressed as:

$$V_{shell}/V_{core} = \frac{r_{shell}^3 - r_{CdSe}^3}{r_{CdSe}^3} \quad . \tag{3.9}$$

From the calculated ratio values in Table 3.5, it is clear that the increase in high energy absorbance correlates with an increase in the volume ratio due to smaller core radii and thicker CdS shells.

The second trend can be deduced by drawing attention to the figure insets, where it is revealed that the relative extent of red–shift upon shell growth increases towards smaller core diameters. This can be explained by the stronger confinement in smaller cores and thus a higher kinetic energy of the charge carriers, enabling deeper tunnelling into the shell. For a clearer demonstration of this effect, Figure 3.12 (left) depicts the energy loss of the first excited

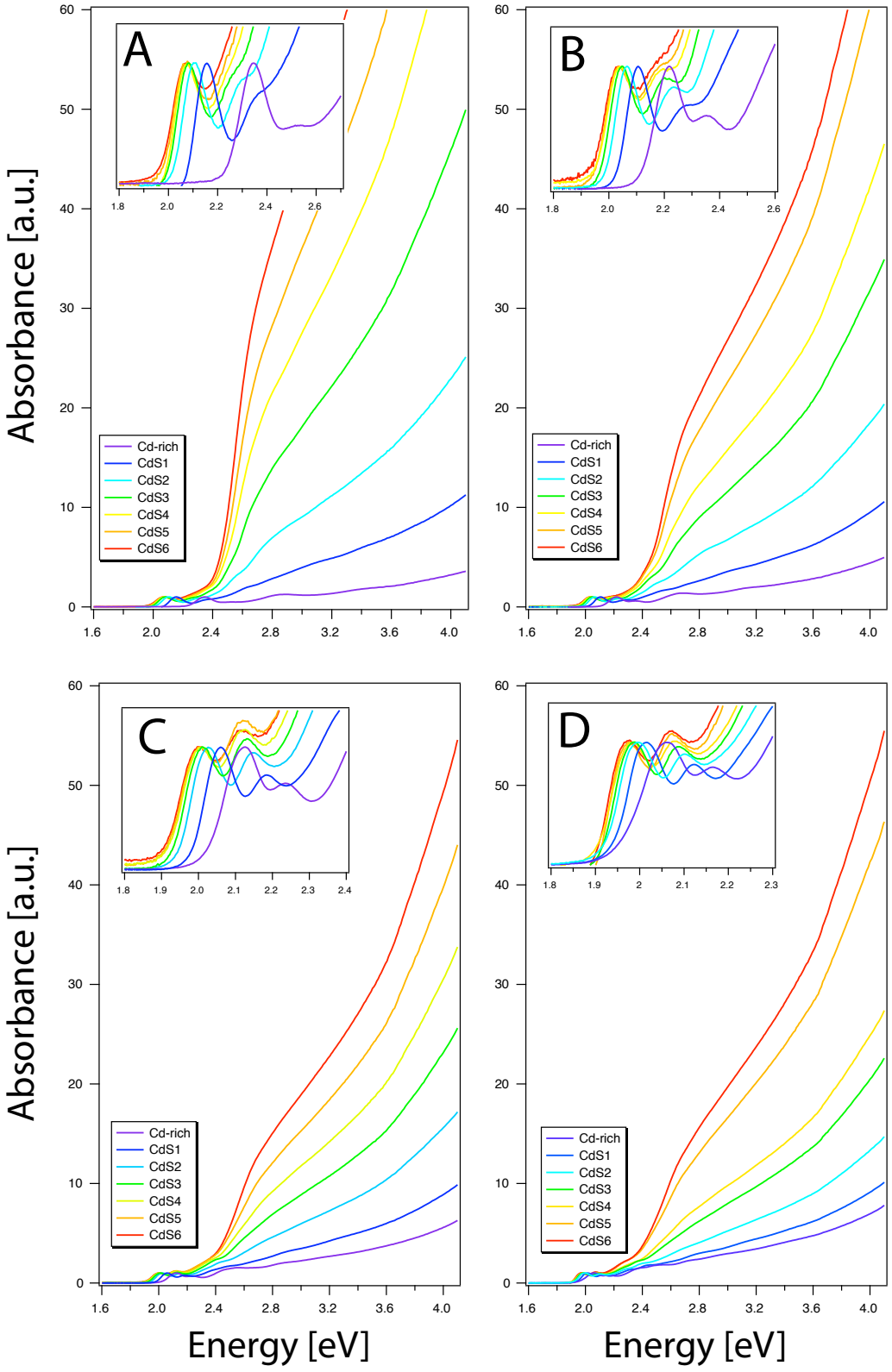

Figure 3.11 Plots **A**–**D** present the normalised absorbance spectra taken after each CdS monolayer shell growth onto CdSe cores of 2.90 nm, 3.48 nm, 4.09 nm and 4.79 nm diameter, respectively.The inset magnifications highlight the spectral changes that occur close to the first excited state transition.

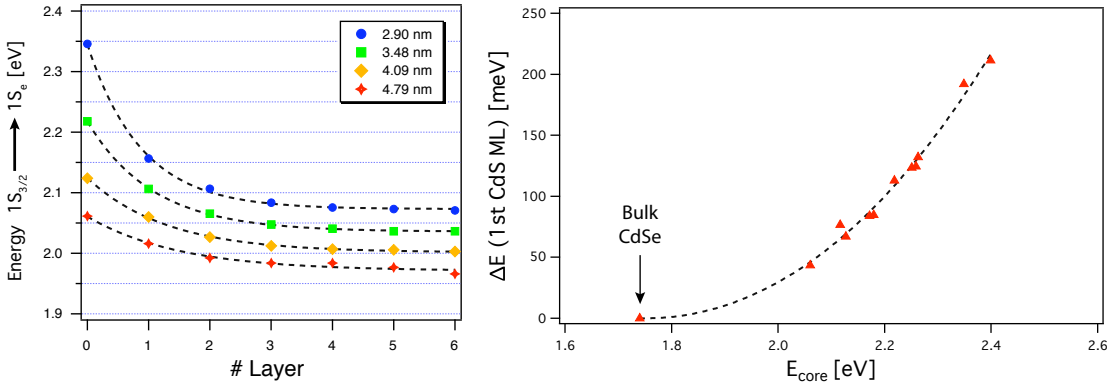

Figure 3.12 Left: Band edge energy decays as a function of CdS shell thickness for the 4 samples under investigation. Right: Energy loss of the first excited state after growth of one CdS monolayer as a function of the initial CdSe core energy.

stated as a function of shell growth for the four samples under investigation. Apart from a global red-shift of the energies with increasing core size, the band edge transition energy for all four samples experiences an exponential decay. This decrease is pronounced for the growth of the first three CdS monolayers and eventually plateaus with further shell deposition. Due to the steeper decay with decreasing core size, the initial energy span of the band edge transition of $\sim$285 meV condenses to a range of only $\sim$105 meV. Thus, preservation of emission colour on CdSe/CdS core/shell nanocrystals is impossible to attain.

To highlight the increasing red—shift for smaller core radii, the plot on the right of Figure 3.12 depicts the energy decay after deposition of one CdS monolayer as a function of initial core energy. The data points were gathered from multiple shelling reactions with shell thickness verification either by HRTEM or spectrally [42]. As a reference, the energy of the bulk band gap of CdSe (1.74 eV) is also plotted at $\Delta E = 0$ to aid the fitting of the data. This point is reliable given that no further changes in absorbance are expected once the bulk size is reached.

3.5.3 The Effect of Temperature on the Band Edge Transition

Figure 3.13 illustrates the effect of temperature on the PL properties of CdSe/CdS core/shell quantum dots. The spectra shown were taken from the sample with a core size of 2.90 nm. Comparison of the spectral bands at room temperature (left) and 80 K (centre) reveals two effects. The peak energy of the initial core PL spectra is blue–shifted by $\sim$40 meV and the FWHM over the course of shell growth is on average $\sim$ 25 meV narrower at low temperature (see plot on the right), which is in qualitative agreement with other results [58, 59].

The blue–shift can be explained by the temperature dependence of the band gap energy in bulk semiconductors which was also reported for nanocrystals [58]. Since the band gap reflects

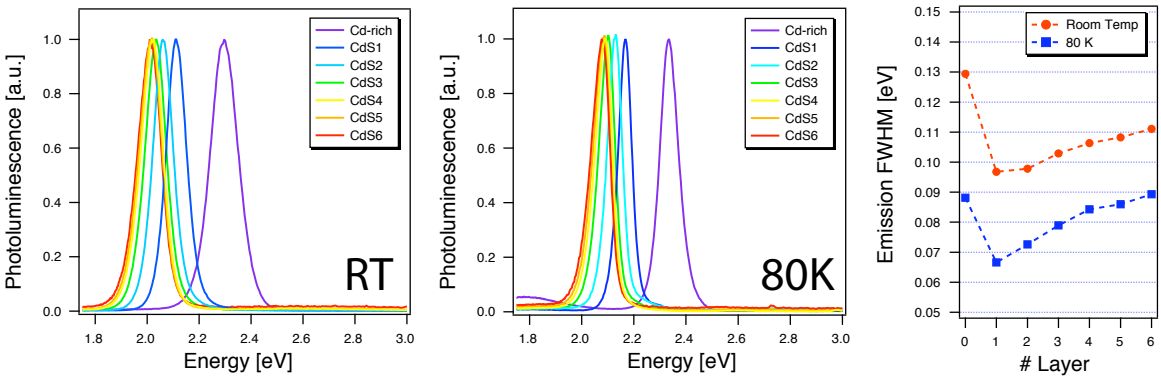

Figure 3.13 Normalised PL spectra of CdSe/CdS NCs with a core size of 2.90 nm taken at room temperature (left) and 80 K (centre) after growth of individual CdS monolayers. Right: Comparison of the emission band FWHM at room temperature (red) and 80 K (blue) as a function of CdS shell thickness.

the bond energies of the underlying crystal lattice, temperature dependent phonon changes and electron–phonon interactions result in an alteration of the band edge transition. The relationship between band gap energy and temperature can be described, following O'Donnell et al. [60], by:

$$E_g(T) = E_g(0) - S\langle\hbar\omega\rangle \left[coth\left(\frac{\langle\hbar\omega\rangle}{2k_BT}\right) - 1\right] \quad , \tag{3.10}$$

where $E_g(0)$ is the band gap at 0 K, S is a dimensionless coupling constant, k_B is the Boltzmann constant and $\langle\hbar\omega\rangle$ is an average phonon energy. According to this equation, the band gap energy is expected to decrease with increasing temperature in agreement with experimental observations. This demonstrates, that the energy shift with temperature arises from temperature dependent band gap shrinkage, while the actual confinement energies for the charge carriers are temperature *independent* [59].

To explain the narrowing of the FWHM, it is important to bear in mind, that theoretically the spectrum of QDs should exhibit discrete ultra–narrow transitions. However the linewidth of those transitions is significantly widened through homogeneous and inhomogeneous broadening, as illustrated previously in Figure 1.22. While inhomogeneous broadening results from the structural disparity in the ensemble, homogeneous broadening arises from temperature dependent carrier–phonon scattering. The temperature dependence of the excitonic peak broadening can be described by:

$$\Gamma(T) = \Gamma_{inh} + \sigma T + \Gamma_{LO}\left(e^{E_{LO}/k_BT} - 1\right)^{-1} \quad , \tag{3.11}$$

where Γ_{inh} is the inhomogeneous broadening, which is temperature independent, and the last two terms represent the homogeneous broadening due to exciton–phonon interactions [59]. σ

is the exciton–acoustic–phonon coupling coefficient, Γ_{LO} represents the exciton–LO–phonon coupling coefficient and E_{LO} is the LO–phonon energy. Thus the observed FWHM narrowing occurs due to a reduction in homogeneous broadening based on diminished carrier–phonon interactions at lower temperatures.

Figure 3.14 reports on the energy loss of the band edge emission as a function of shell growth at room temperature (**A**) and 80 K (**B**). Direct comparison of the two graphs reveals the low temperature induced blue–shift discussed previously. Additionally, close examination reveals that the extent of energy decay with CdS shell growth is reduced for all four samples at low temperatures. To highlight this effect, the decays at room temperature and 80 K for each sample were normalised to their initial core energy and plotted in sub–figures **C**–**F** for direct comparison. The accompanying insets depict the relative energy difference ΔE between the two decays as a function of shell thickness, showing an increase in ΔE with CdS shell growth.

This discovery was somewhat unexpected and is not fully understood yet. However a possible explanation could be derived from the different temperature dependence of the CdSe and the CdS band gap. Since S and $\langle\hbar\omega\rangle$ from Equation 3.10 are material specific parameters [60], it is reasonable to assume that the band gap widening in the CdS shell occurs to a different (larger) extent than in the CdSe core. Thus, an increase to the relative offsets of the valence and conduction bands between the two materials would lead to a higher potential barrier at the core/shell interface, naturally explaining the observed reduction in energy loss at low temperatures.

3.5.4 Higher Order Transitions in CdSe/CdS Nanocrystals

After investigating the evolution of the first excited state in core/shell nanocrystals, the data presented in this section provides further inside into the spectral evolution of such heterostructures by analysing their higher order transitions. While the oscillator strength of the first exited state is generally strong and well resolved, higher order states are increasingly difficult to identify due to their increasing weakness. This problem is exacerbated by the inhomogeneous broadening in ensemble measurements, effectively concealing transitions. To improve the spectral resolution, photoluminescence excitation spectroscopy (PLE) was employed which only probes a subset of the sample distribution. By monitoring a narrow spectral region of the PL band while scanning the excitation energy, PLE reveals absorption features where inhomogeneous broadening is greatly reduced. As demonstrated in Figure 3.15 (left), transitions that are obscured in the absorption spectrum (black trace) can be resolved by PLE (green trace). Further improvements can be achieved through low temperature measurements (red trace) due to the reduced homogeneous broadening. The middle graph shows the PLE spectra for the initial CdSe core samples after enriching the surface with

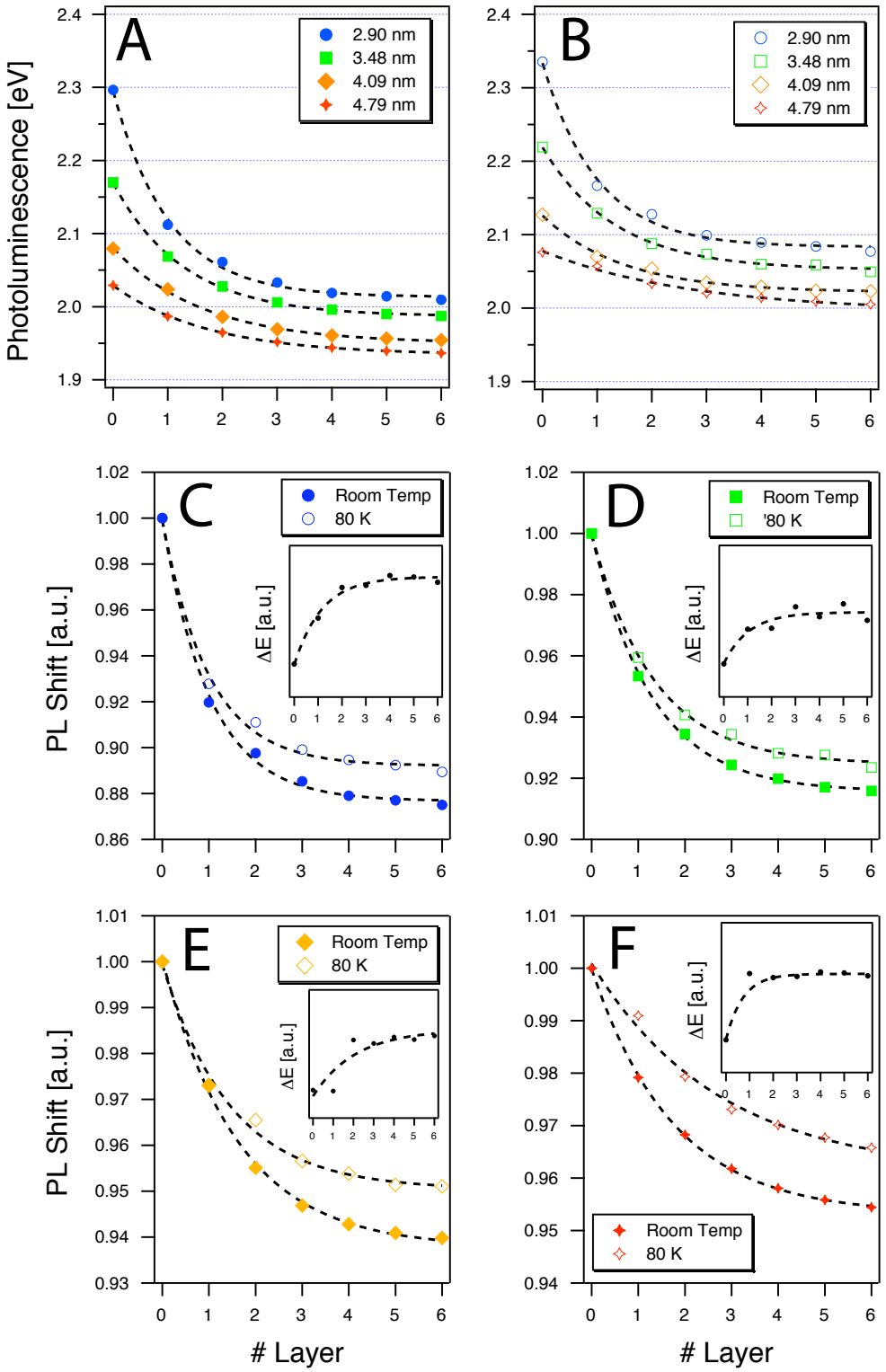

Figure 3.14 Band edge emission energy as a function of CdS shell thickness for the 4 samples under investigation at room temperature (**A**) and 80 K (**B**). Graphs **C**–**F** depict the energy decays at room temperature and 80 K normalised to their initial core energy for the samples with 2.90 nm, 3.48 nm, 4.09 nm and 4.79 nm CdSe core size, respectively. The accompanying insets show the relative energy difference ΔE between the two decays as a function of CdS shell thickness.

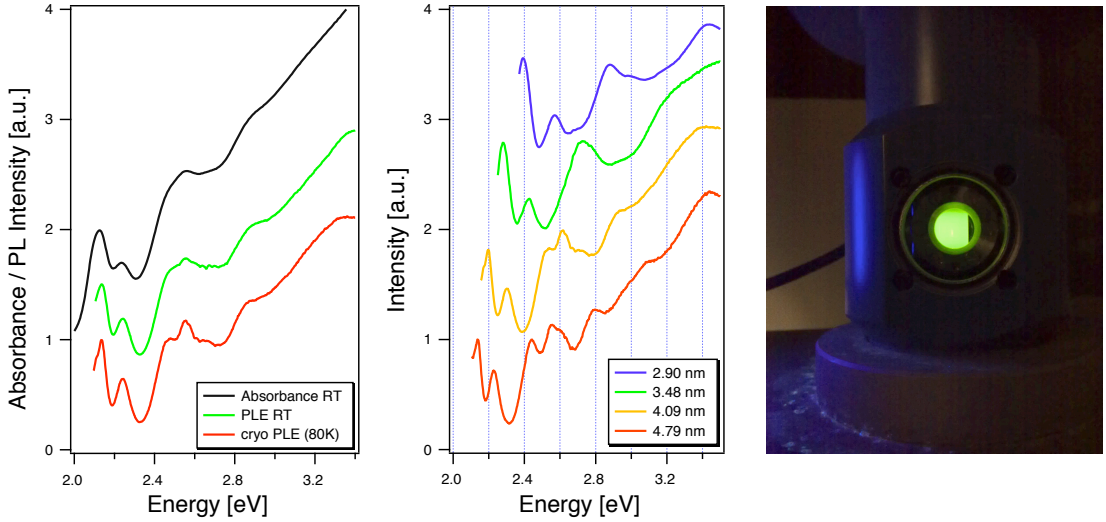

Figure 3.15 Left: Normalised absorbance and PLE spectra of 4.09 *nm* CdSe cores demonstrating the improved resolution of low temperature PLE measurements. Centre: Normalised PLE scans for the 4 different size QD samples. Size increases from top to bottom. Right: Photograph of 4.09 *nm* CdSe nanocrystals in the cryostat at 80 *K* under UV irradiation.

cadmium. The spectra are arranged in order of increasing dot size (top to bottom), where the decreasing confinement clearly shifts the transitions towards lower energies. In addition, a greater number of transitions is observable for larger cores due to the increased density of states (DOS) close to the band edge. The photograph on the right of Figure 3.15 shows the 4.09 *nm* CdSe core sample in the cryostat chamber under UV irradiation, highlighting the intense luminescence at low temperatures. The sample preparation for cryogenic measurements was outlined in Chapter 2.

To obtain PLE data for each sample the band edge emission was measured first. Since features are most efficiently resolved in PLE when the emission is monitored on the blue edge of the PL peak, a wavelength 5 *nm* to the blue side of the emission maximum was selected, as denoted by the downward pointing arrow in Panel **A** of Figure 3.16. The discrete nature of the optical transitions observed in the absorbance spectra of panel **A** highlights the monodispersity of the sample (4.09 *nm* CdSe cores) and rules out the possibility of aggregation within the glass at low temperatures. Panel **D** shows a low temperature PLE spectrum obtained from the sample of CdSe cores outlined in Panel **A** (solid line) and the fitted spectrum (dotted line). Extraction of the transition peak positions was accomplished by fitting a combination of a cubic background and Gaussian functions (see Panel **E**) following the method reported by Norris et al. [54]. The cubic background accounts for the continuum–like nature of underlying transitions that are not resolved. From analysis of Panel **D** we can see that the empirical

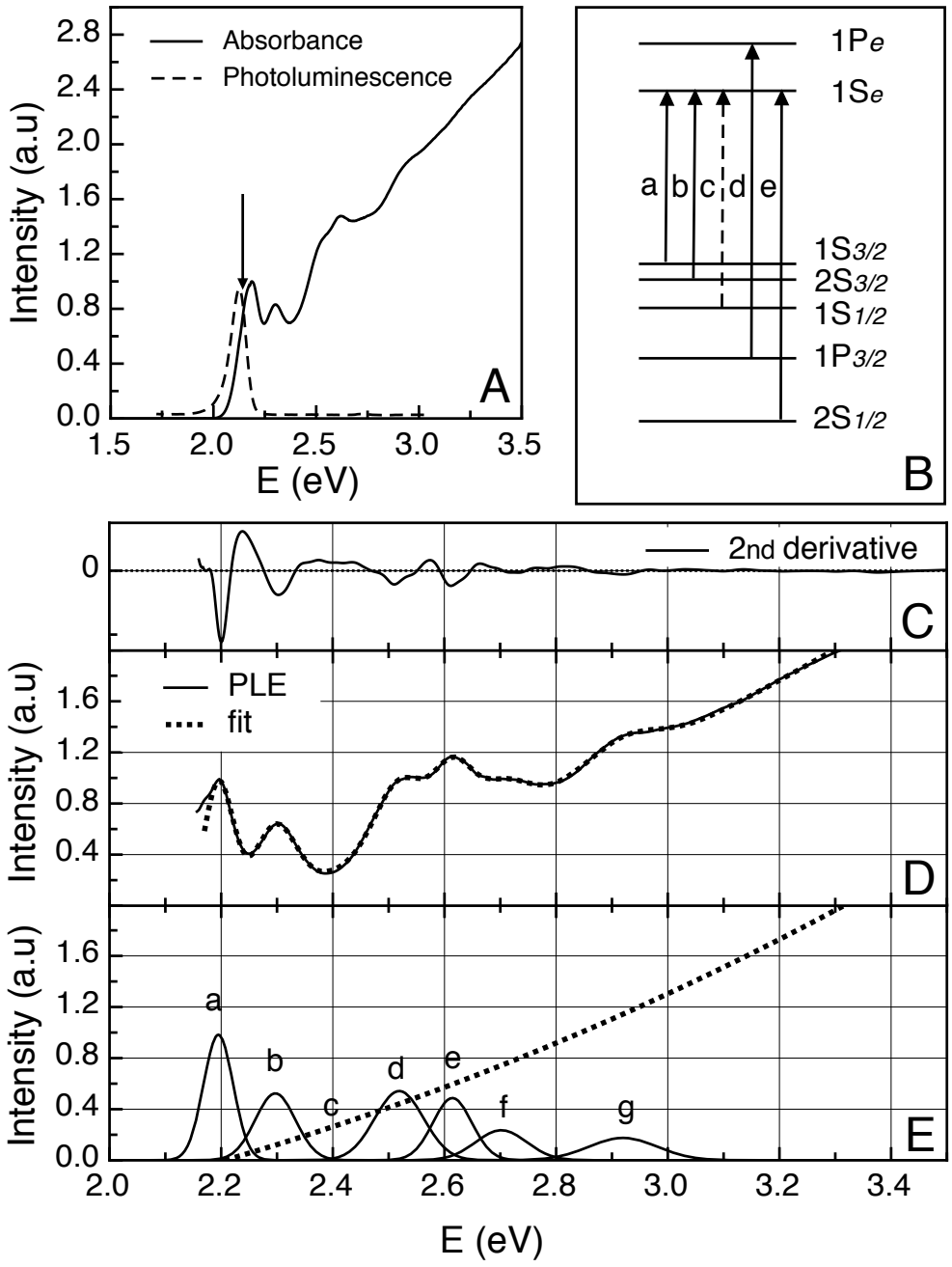

Figure 3.16 **A** Absorbance (solid line) and PL (dashed line) of 4.09 *nm* CdSe cores at 80 *K*. The arrow marks the emission energy at which the PLE was scanned. **B** Schematic of the first five transition states in CdSe nanocrystals. **C** Second derivative of the PLE spectrum shown in Panel **D**. **D** 80 *K* PLE spectrum of 4.09 *nm* CdSe cores (solid line) and the corresponding fit (dotted line). **E** Fitting procedure showing the Gaussian transitions as well as the cubic background employed during the fitting procedure.

fit agrees well with the observed data and allows for confident assignment of the optical transitions from the Gaussian functions. The first seven transitions (a)–(g) are labelled in Panel **E**. Notably transition (c) ($1S_{1/2} - 1S_e$) was assigned minimal oscillator strength as this transition is known to be weak in CdSe cores [54]. Consistent with previous reports we also observe that the optical transitions tend to become broader with increasing energy [54]. For reference and in order to further confirm assignment of the optical transitions a 2^{nd} derivative analysis was also performed on the PLE spectrum. The results of this analysis are presented in Panel **C**. Importantly, the transition energies obtained using both methods of analysis ceded almost identical results.

Due to the high quality of CdSe NCs as many as seven absorption features could be resolved in a single spectrum. However, only the first five transitions could be confidently assigned for the core/shell samples due to the large absorbance of the CdS shell, which obscures the highest energy optical transitions. We also observed additional structure on the first absorption peak. In some spectra a narrow line with LO phonon replicas is observed on top of a much broader feature, which is consistent with band edge exciton fine structure [55]. Thus an additional weak Gaussian was added to fit the first transition where fine structure was observed. For analysis of the transition energy the broad component, which carried most of the oscillator strength, was used. For reference Panel **B** shows a schematic of the first five optical transitions in CdSe nanocrystals [54]. The weaker $1S_{1/2} - 1S_e$ transition labelled (c) is denoted by a dashed line arrow.

Figure 3.17 shows all PLE traces recorded for analysis. The general red–shift with increasing CdS shell thickness and large intensity rise at higher energies is clearly observable and follows the trend of the absorbance measurements previously discussed. The features assigned to transitions (a), (b) and (d) dominate the spectra while the feature of transitions (c) is generally weak. The highest monitored state (e) is readily observable for larger core sizes (Panel C and D) but difficult to determine for the smaller ones (Panel A and B).

The final results of the fitting procedure of the entire data set is presented in Figure 3.18. Following the illustration of previous reports [54, 56], all transition energies were normalised to the first excited state energy. Thus the effect of CdS shell deposition on higher order transitions may be more readily observed. Over the whole data set, the first five transitions ($1S_{3/2}1S_e$, $2S_{3/2}1S_e$, $1S_{1/2}1S_e$, $1P_{3/2}1P_e$ and $2S_{1/2}1S_e$) were monitored and labelled (a–e), as assigned in Panel **E** of Figure 3.16. While transitions (a), (b) and (d) were successfully tracked for all core sizes, transitions (e) and (c) could not be confidently extracted for the 3.45 *nm* and 4.09 *nm* core size, respectively. To confidently assign the transitions to extracted PLE features, we compared the energies obtained from the core traces with experimental and calculated values reported in the literature, observing good agreement [54].

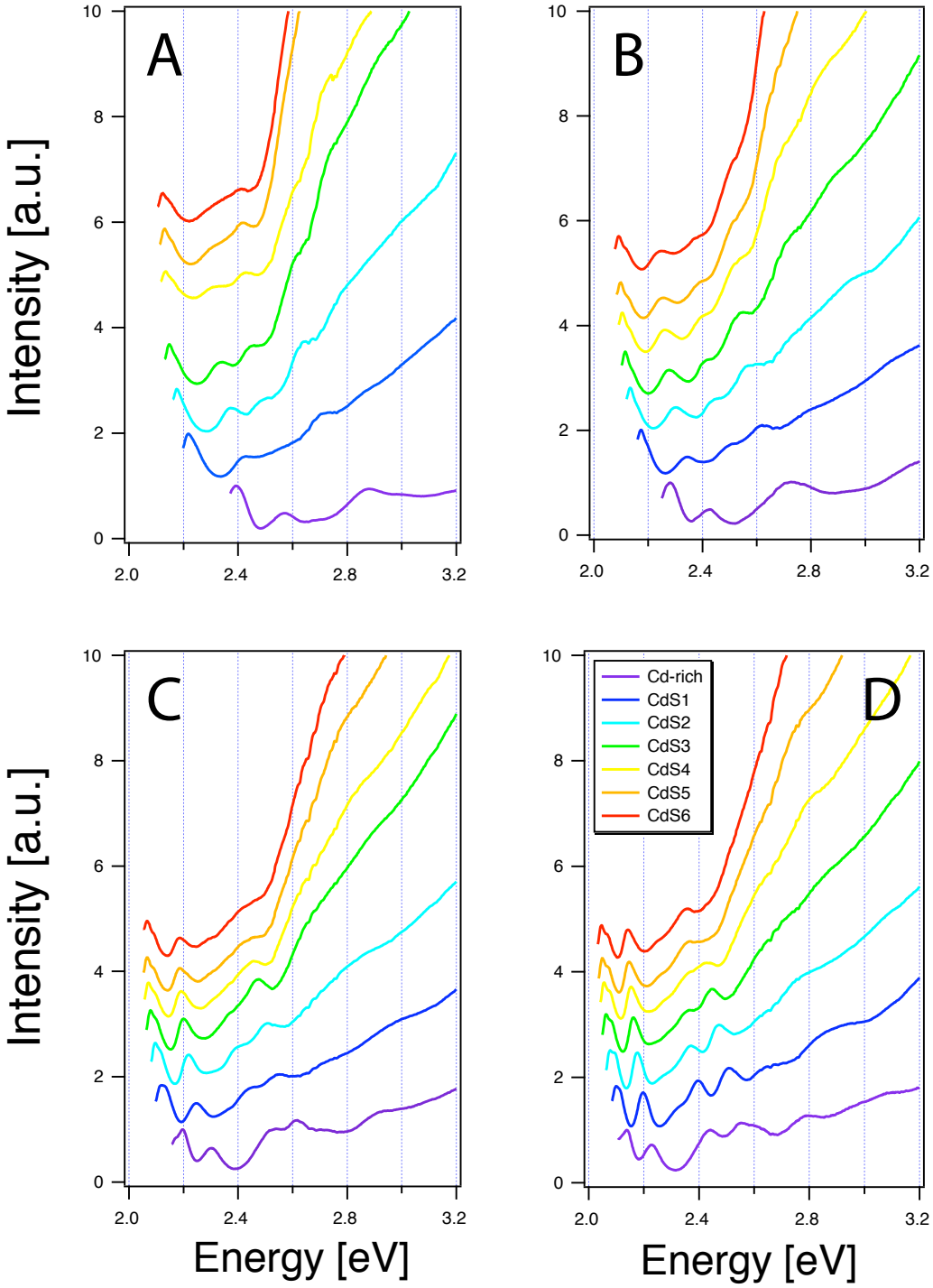

Figure 3.17 Normalised PLE scans of CdSe/CdS core/shell NCs at 80 K taken after each deposition of 1–6 CdS monolayers. The shell thickness increases from bottom to top. **A**=2.90 nm; **B**=3.45 nm; **C**=4.09 nm; **D**=4.79 nm CdSe core size.

The extent of relative energy loss caused by CdS shell growth was generally larger with decreasing core size in all transitions, except for transition (e) in the sample with 4.79 nm core size. In this case, a blue shift of ∼140 meV was observed, effectively merging into the feature of transition (d). Pandey et al. [57] reported negligible relative shifts of the transitions, $2S_{3/2}1S_e$ and $2S_{1/2}1S_e$ with CdS shell growth, while the energy loss of the $1P_{3/2}1P_e$ was found to be distinctively greater than the loss in confinement energy of the S states. These observations were related to the relative band gap offsets of CdS. As the S states are assigned to hole states, their insensitivity to shell growth suggests that the valence band offset to CdS is larger than the energy of these states. The P transition however is related to the electron state, and as such is not confined by the small conduction band offset between CdSe and CdS.

Our data sets do not completely reproduce these trends. Rather than distinct differences between S and P transition evolution, we see small to moderate red shifts for all monitored transitions with build–up of CdS. It is important to note, that the trends reported by Pandey et al. [57] were extracted from room temperature absorbance spectra, making it difficult to accurately assign transition energies due to homogeneous and inhomogeneous broadening. Over the range of all investigated core sizes, the higher energy transitions $1P_{3/2}1P_e$ (d) and $2S_{1/2}1S_e$ (e) exhibit a stronger relative energy loss (25–140 meV) compared to the second excited state $2S_{1/2}1S_e$ (b) (1-32 meV), suggesting that these states are confined by the CdS band gap only to a minor extent. Transition (b) showed a moderate red shift upon shell growth of around 32 meV towards the band edge transition in the smallest core sample. For all other core sizes the relative shift was negligible, in agreement with Ref. [57]. The weak $1S_{1/2}1S_e$ (c) exhibited a moderate relative shift ranging from ∼18 meV to ∼54 meV.

Investigating the effect of core size on the transition evolution, it was revealed that the highest transitions (d) and (e) showed the strongest condensation towards the band edge transition of 168 meV and 184 meV from 2.90 nm to 4.79 nm cores, respectively. This is 2–3 times the energy loss compare to the second and third excited state (b) and (c) shifting 76 meV and 60 meV towards the first excited state respectively.

Overall the combined condensation effects of increasing core size and CdS shell thickness led to a shrinkage of the transition energy range from ∼610 meV to ∼285 meV, approximately halving it. However no distinct correlation between the extent of energy loss as a function of shell thickness and core size could be established. To obtain a more detailed insight into the evolution of the higher order transitions, *ab initio* calculations would be extremely helpful to predict the energy levels as a function of core diameter and shell thickness.

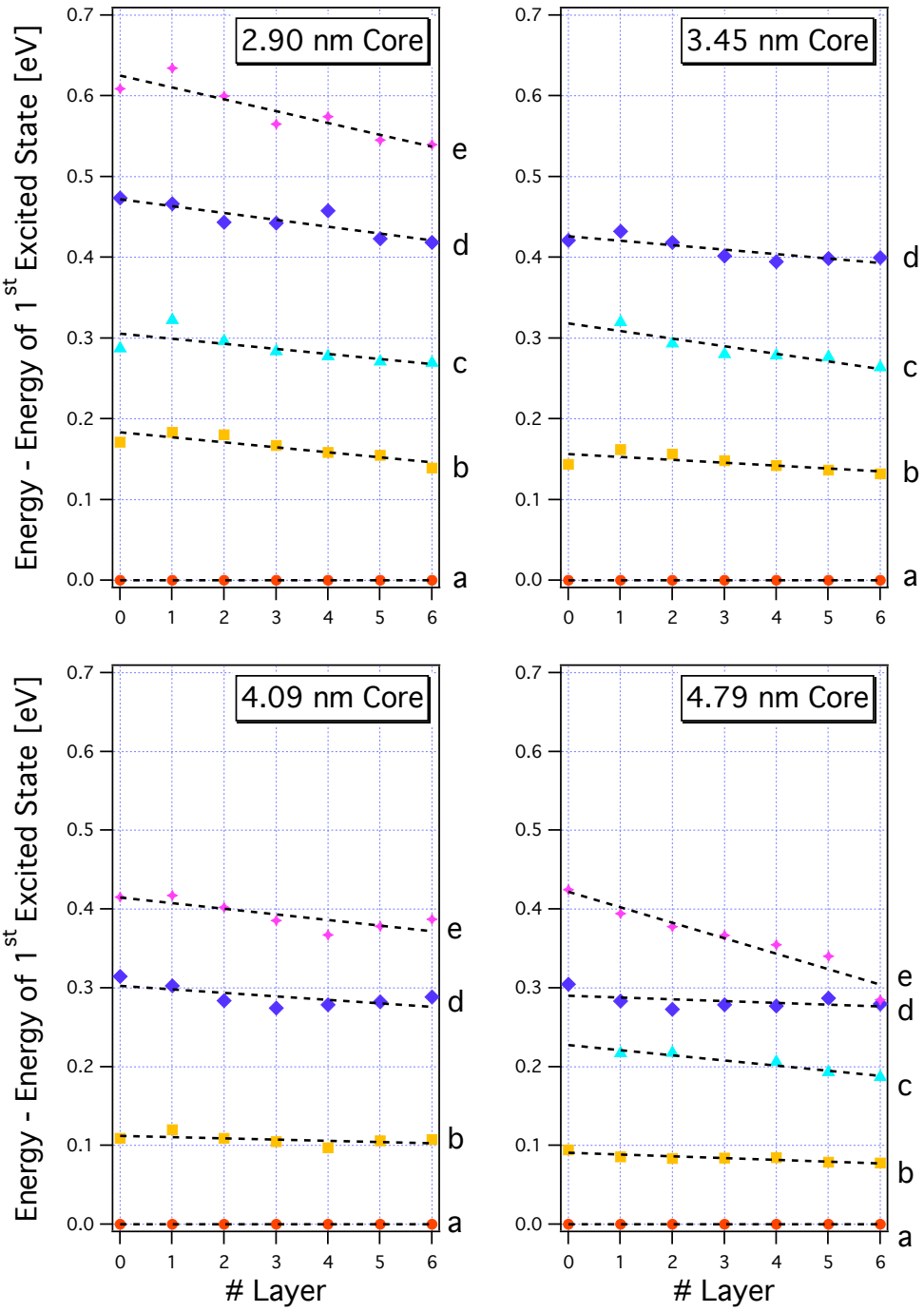

Figure 3.18 Transitions energies relative to the first excited state as a function of CdS shell thickness for the four CdSe core sizes under investigation. The peak positions were extracted from PLE data as described in the text and shown in Figure 3.16. The transitions are labelled a–e as assigned in Panel **E** of Figure 3.16. The dashed lines serve as visual guide for the transition evolution.

3.6 Conclusion

The work presented in this chapter provides an in–depth discussion of the effect of shell deposition in Type–I core/shell heterostructures. The theoretical exciton confinement description in the framework of the effective mass approximation has been presented. The details involved in the successful preparation of CdSe/CdS and CdSe/ZnS core/shell heterostructures have been discussed and monolayer control of shell thickness demonstrated. Optical analysis of the prepared heterostructures by means of absorbance and emission spectroscopy revealed good agreement with the theoretically predicted trends of exciton confinement and lattice strain. Temperature dependent PL measurements revealed that at low temperatures the confinement in CdSe/CdS heterostructures was increased and became more pronounced with increasing shell thickness. The low temperature PLE analysis of four CdSe/CdS samples with core sizes ranging from 2.90 nm to 4.79 nm with CdS shells of 1–6 monolayers, provides the first comprehensive report on the evolution of the first five transition states as a function of shell thickness and core size. The general principles of core/shell synthesis and confinement effects in Type–I structures will be highly relevant for the following chapters, focusing on more complex core/multishell systems.

Bibliography

[1] B. S. Mashford, T. L. Nguyen, G. J. Wilson and P. Mulvaney. Journal of Materials Chemistry **20**, 167 (2010).

[2] A. L. Rogach, N. Gaponik, J. M. Lupton, C. Bertoni, D. E. Gallardo, S. Dunn, N. Li Pira, M. Paderi, P. Repetto, S. G. Romanov, C. O'Dwyer, C. M. Sotomayor Torres and A. Eychmüller. Angewandte Chemie International Edition **47**, 6538 (2008).

[3] J. M. Caruge, J. E. Halpert, V. Wood, V. Bulovic and M. G. Bawendi. Nat Photon **2**, 247 (2008).

[4] H. Huang, A. Dorn, V. Bulovic and M. G. Bawendi. Applied Physics Letters **90**, 023110 (2007).

[5] P. V. Kamat. Journal of Physical Chemistry C **112**, 18737 (2008).

[6] I. Gur, N. A. Fromer, M. L. Geier and A. P. Alivisatos. Science **310**, 462 (2005).

[7] W. U. Huynh, J. J. Dittmer and A. P. Alivisatos. Science **295**, 2425 (2002).

[8] Y. Chan, J. S. Steckel, P. T. Snee, J. M. Caruge, J. M. Hodgkiss, D. G. Nocera and M. G. Bawendi. Applied Physics Letters **86**, 073102 (2005).

[9] J. J. Jasieniak, I. Fortunati, S. Gardin, R. Signorini, R. Bozio, A. Martucci and P. Mulvaney. Advanced Materials **20**, 69 (2008).

[10] V. I. Klimov, A. A. Mikhailovsky, D. W. McBranch, C. A. Leatherdale and M. G. Bawendi. Science **287**, 1011 (2000).

[11] V. I. Klimov, A. A. Mikhailovsky, S. Xu, A. Malko, J. A. Hollingsworth, C. A. Leatherdale, H. J. Eisler and M. G. Bawendi. Science **290**, 314 (2000).

[12] W. C. W. Chan and S. Nie. Science **281**, 2016 (1998).

[13] X. Gao, Y. Cui, R. M. Levenson, L. W. K. Chung and S. Nie. Nature Biotechnology **22**, 969 (2004).

[14] G. Kalyuzhny and R. W. Murray. Journal of Physical Chemistry B **109**, 7012 (2005).

[15] R. Xie, U. Kolb, J. Li, T. Basche and A. Mews. Journal of the American Chemical Society **127**, 7480 (2005).

[16] J. McBride, J. Treadway, L. C. Feldman, S. J. Pennycook and S. J. Rosenthal. Nano Letters **6**, 1496 (2006).

[17] D. Chen, F. Zhao, H. Qi, M. Rutherford and X. Peng. Chemistry of Materials **22**, 1437 (2010).

[18] P. Reiss, J. Bleuse and A. Pron. Nano Letters **2**, 781 (2002).

[19] A. Mews, A. Eychmueller, M. Giersig, D. Schooss and H. Weller. Journal of Physical Chemistry **98**, 934 (1994).

[20] A. Eychmüller, A. Mews and H. Weller. Chemical Physics Letters **208**, 59 (1993).

[21] B. Blackman, D. Battaglia and X. Peng. Chemistry of Materials **20**, 4847 (2008).

[22] M. Jones, S. Kumar, S. S. Lo and G. D. Scholes. Journal of Physical Chemistry C **112**, 5423 (2008).

[23] S. A. Ivanov, A. Piryatinski, J. Nanda, S. Tretiak, K. R. Zavadil, W. O. Wallace, D. Werder and V. I. Klimov. Journal of the American Chemical Society **129**, 11708 (2007).

[24] J. E. Halpert, V. J. Porter, J. P. Zimmer and M. G. Bawendi. Journal of the American Chemical Society **128**, 12590 (2006).

[25] R. Xie, X. Zhong and T. BaschÈ. Advanced Materials **17**, 2741 (2005).

[26] D. Schooss, A. Mews, A. Eychmüller and H. Weller. Physical Review B **49**, 17072 (1994).

[27] J. Muller, J. M. Lupton, P. G. Lagoudakis, F. Schindler, R. Koeppe, A. L. Rogach, J. Feldmann, D. V. Talapin and H. Weller. Nano Lett **5**, 2044 (2005).

[28] B. O. Dabbousi, J. Rodriguez-Viejo, F. V. Mikulec, J. R. Heine, H. Mattoussi, R. Ober, K. F. Jensen and M. G. Bawendi. Journal of Physical Chemistry B **101**, 9463 (1997).

[29] S.-H. Wei and A. Zunger. Applied Physics Letters **72**, 2011 (1998).

[30] L. Spanhel, M. Haase, H. Weller and A. Henglein. Journal of the American Chemical Society **109**, 5649 (1987).

[31] A. R. Kortan, R. Hull, R. L. Opila, M. G. Bawendi, M. L. Steigerwald, P. J. Carroll and L. E. Brus. Journal of the American Chemical Society **112**, 1327 (1990).

[32] C. F. Hoener, K. A. Allan, A. J. Bard, A. Campion, M. A. Fox, T. E. Mallouk, S. E. Webber and J. M. White. The Journal of Physical Chemistry **96**, 3812 (1992).

[33] C. B. Murray, D. J. Norris and M. G. Bawendi. Journal of the American Chemical Society **115**, 8706 (1993).

[34] M. A. Hines and P. Guyot-Sionnest. Journal of Physical Chemistry **100**, 468 (1996).

[35] X. Peng, M. C. Schlamp, A. V. Kadavanich and A. P. Alivisatos. Journal of the American Chemical Society **119**, 7019 (1997).

[36] D. V. Talapin, A. L. Rogach, A. Kornowski, M. Haase and H. Weller. Nano Letters **1**, 207 (2001).

[37] J. J. Li, Y. A. Wang, W. Guo, J. C. Keay, T. D. Mishima, M. B. Johnson and X. Peng. Journal of the American Chemical Society **125**, 12567 (2003).

[38] S. Park, B. L. Clark, D. A. Keszler, J. P. Bender, J. F. Wager, T. A. Reynolds and G. S. Herman. Science **297**, 65 (2002).

[39] D. Battaglia, B. Blackman and X. Peng. Journal of the American Chemical Society **127**, 10889 (2005).

[40] D. Battaglia, J. J. Li, Y. Wang and X. Peng. Angewandte Chemie International Edition **42**, 5035 (2003).

[41] D. V. Talapin, I. Mekis, S. Gotzinger, A. Kornowski, O. Benson and H. Weller. The Journal of Physical Chemistry B **108**, 18826 (2004).

[42] J. van Embden, J. Jasieniak and P. Mulvaney. Journal of the American Chemical Society **131**, 14299 (2009).

[43] R. W. G. Wyckoff. *Crystal Structures* (WILEY-VCH, 1969).

[44] J. Jasieniak, L. Smith, J. v. Embden, P. Mulvaney and M. Califano. The Journal of Physical Chemistry C **113**, 19468 (2009).

[45] D. Talapin, A. Rogach, M. Haase and H. Weller. J. Phys. Chem. B **105**, 12278 (2001).

[46] J. van Embden, J. Jasieniak, D. Gomez, P. Mulvaney and M. Giersig. Australian Journal of Chemistry **60**, 457 (2007).

[47] J. van Embden and P. Mulvaney. Langmuir **21**, 10226 (2005).

[48] J. van Embden. *Synthesis and Optical Proeperties of CdSe Core and Core/Shell Nanocrystals*. Ph.D. thesis, The University of Melbourne, School of Chemistry (2008).

[49] B. Blackman, D. M. Battaglia, T. D. Mishima, M. B. Johnson and X. Peng. Chemistry of Materials **19**, 3815 (2007).

[50] A. M. Smith and S. Nie. Accounts of Chemical Research **43**, 190 (2010).

[51] S. Yang, D. Prendergast and J. B. Neaton. Nano Letters **10**, 3156 (2010).

[52] A. M. Smith, A. M. Mohs and S. Nie. Nature Nanotechnology **4**, 56 (2009).

[53] S. H. Tolbert and A. P. Alivisatos. Annual Review of Physical Chemistry **46**, 595 (1995).

[54] D. Norris and M. G. Bawendi. Physical Review B **53**, 16338 (1996).

[55] D. J. Norris, A. L. Efros, M. Rosen and M. G. Bawendi. Physical Review B **53**, 16347 (1996).

[56] A. D. Lad and S. Mahamuni. Physical Review B **78**, 125421 (2008).

[57] A. Pandey and P. Guyot-Sionnest. The Journal of Chemical Physics **127**, 104710 (2007).

[58] G. W. Walker, V. C. Sundar, C. M. Rudzinski, A. W. Wun, M. G. Bawendi and D. G. Nocera. Applied Physics Letters **83**, 3555 (2003).

[59] D. Valerini, A. Cretí, M. Lomascolo, L. Manna, R. Cingolani and M. Anni. Physical Review B **71**, 235409 (2005).

[60] K. P. O'Donnell and X. Chen. Applied Physics Letters **58**, 2924 (1991).

4 Trap State Reduction in Core/Shell Semiconductor Nanocrystals

4.1 Introduction

Fluorescence intermittency of semiconductor nanocrystals [1] is one of the main inconveniences of these bright emitters for practical applications requiring constant and reliable luminescence. However, at the same time it is one of their most intriguing properties. To understand the mechanism of QD blinking in order to control — and ultimately suppress — this behaviour fuelled a field of intense research over the past decade [2–14]. In Section 1.3, we reviewed the key observations and theoretical models related to the phenomenon of blinking. It was concluded that the detailed mechanism of blinking in single NCs is still not completely understood. However it is widely accepted that intermittency is intimately linked to the degree of available trap states intrinsic to the particle, and involves Auger processes which facilitate non–radiative exciton recombination.

Following these considerations, two approaches to blinking suppression developed in recent years. The first aims to minimise the number of trap states available to the charge carriers [15–17]. These arise from unpassivated dangling bonds present at internal crystal defects and surface atoms, as illustrated in Figure 4.1. The second approach tackles the efficiency of Auger recombination itself [18]. Specific band gap engineering is thought to efficiently suppress Auger recombination, thus rendering the NC emissive even during charge carrier trapping.

4.1.1 Elimination of Surface Traps

One of the first reports to highlight the link between passivation of surface states and blinking suppression was published in 2004 by Hohng and Ha [17]. Commercially available CdSe/ZnS NCs were tethered to a glass surface, and blinking could be greatly reduced by flushing aqueous solutions of β–mercaptoethanol (BME) over the particles. This effect was demonstrated to be reversible as removal of BME, by flushing in a buffer solution, recovered the traditionally observed blinking behaviour for those particles. By studying the blinking suppression properties of BME and several other chemicals, the authors established two characteristics of effective anti–blinking reagents. First, successful reagents contained a thiol moiety, and second, they had to be sterically 'small'. On the basis of these results, a 'state–filling' model was proposed, in which the thiol moiety of BME reduces a surface trap state, rendering it inaccessible to

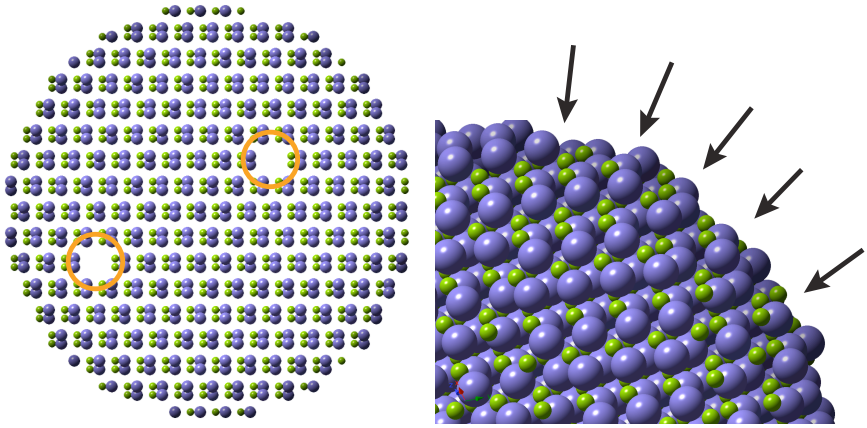

Figure 4.1 Model of a CdSe Nanocrystal depicting structural sources of potential trap states. Unpassivated atomic bonds at internal crystal defects (left) and surface atoms (right) are highlighted by orange circles and black arrows respectively.

electrons from the NC core. Due to the small size of BME, a high degree of passivation of such surface traps was attainable. Another recent report by Fomenko et al. [7] showed similar results by introducing a propyl gallate to the QD surrounding, leading to dramatic suppression of blinking behaviour. Additionally, they reported a substantial shortening of fluorescence lifetime from 21 ns to 4 ns while the quantum yield (QY) remained constant. As suppressed blinking is generally explained by a reduction of available trap states (i.e. fast non–radiative recombination channels) one would expect an increase of the average lifetime. The observed opposite behaviour was therefore attributed to a concomitant increase of the radiative rate k_{rad}, since the QY is defined by:

$$QY = \frac{k_{rad}}{k_{rad} + k_{nonrad}} = \tau_{FL} \times k_{rad} \quad , \tag{4.1}$$

which was found to remain constant.

Although the addition of such ligand molecules to QD suspensions remarkably suppresses blinking, it requires the QDs to be constantly immersed in the ligand solution due to their labile surface bond. This imposes significant limitations on the kind of experiment and applications feasible with these particles. A complementary approach to ligand passivation is the growth of Type–I core/shell heterostructures with extremely thick shells aiming to fully isolate the exciton from the particle surface (see Figure 4.2 left). Recently two groups [15, 16] reported the synthesis of such structures consisting of a CdSe core overcoated with a thick shell of CdS displaying considerably reduced blinking without the need for extra surface passivation steps. Chen and Klimov [16] overcoated cores of a 3–4 nm diameter with CdS to reach a final size of 15–20 nm. In these samples, ∼20 % of particles were found to be non-blinking (200

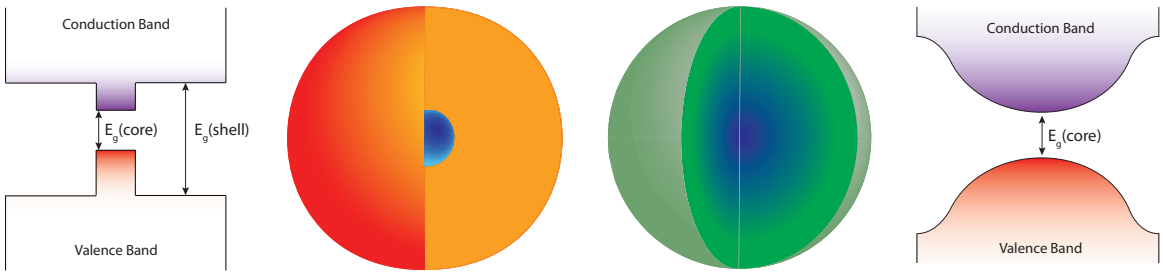

Figure 4.2 Left: 3D schematic of the thick shell CdSe/CdS heterostructure [15, 16] with corresponding band gap alignment (not to scale). Right: 3D model of an alloyed CdZnSe/ZnSe heterostructure [18]. The interface between core and shell material transitions smoothly from a Cd–rich centre to a Zn–rich shell material at the outer NC edge as indicated by the colour gradient from blue to green. This gradual transition is thought to result in a 'soft' confinement situation as depicted in the corresponding band structure schematic.

ms time resolution) under continuous illumination. Due to the small conduction band offset between CdSe and CdS the electron delocalises extensively into the shell and consequently, a substantial red–shift is observed. Owing to the thick shell, the PL of those particles was found to be stable against repeated precipitation and re–dispersion as well as transfer into water by ligand exchange. This insensitivity to surface treatment supports the claim of complete isolation of the exciton away from any surface trap states. However, the relatively low QY of ∼40 % was attributed to internal crystal defects forming in such thick shells.

The report by Mahler et al. [15], published simultaneously, describes similar observations. CdSe/CdS core/shells with a core size of 2.5 *nm* and a shell thickness of ∼5 *nm* exhibited the same extensive red–shift upon shell growth. However, 68 % of non–blinking dots (30 *ms* time resolution) and a QY of 70 % was stated which was attributed to the small lattice mismatch between CdSe and CdS and the highly epitaxial shell growth under the employed reaction conditions. Furthermore, analysing the fluorescence intermittency as a function of shell growth, an inverse correlation between shell thickness and blinking frequency was established.

4.1.2 Band Gap Engineering for Blinking Suppression

An alternative strategy to eliminate blinking behaviour, focusing on the efficiency of Auger recombination in NCs, was reported by Wang et al. [18]. They synthesised a ternary CdZnSe alloy core capped with a shell of ZnSe and observed continuous fluorescence with no fluctuations from single particles on timescales from milliseconds to hours. The nanocrystals presented an atypical fluorescence spectrum, with a broad main line, red–shifted side bands and a shortened lifetime of about 7 *ns*, instead of about 20 *ns* or longer commonly observed for core/shell QDs. To explain these unusual features, Wang et al. postulated that the non–blinking emission arose

from a positively charged trion (an exciton plus a hole). This would account for the observed lifetime which is significantly shorter than the long decay of typical NCs which originates from the lowest excited state having a forbidden optical transition dipole (dark state) [19]. The red–shifted side bands found in the PL spectrum were assigned to so–called 'shake–up lines', observed previously from charged exciton recombination in self-assembled InAs quantum dots [20].

In typical core/shell QDs, charged exciton states are thought to relax very quickly through fast Auger processes, leading to the general view that trion states are non–emissive. The model by Wang et al. is based on the premise, that the Auger decay rate is linked to the steepness of the interfacial confinement potential in core/shells. Considerable suppression of Auger recombination is assigned to the 'soft' exciton confinement which could result from a graded alloy core/shell NC, such as the CdZnSe/ZnSe structure, where the interface between core and shell material smoothly transitions from a Cd–rich core to a Zn–rich shell material at the outer NC edge (see Figure 4.2 right).

Efficient Auger recombination requires breaking strict momentum conservation, such as in typical core/shell NCs where the change from one material to another is extremely abrupt, causing the potential to resemble a series of sharp steps [18]. It is at these sharp interfaces, where charge carriers acquire sufficient momentum to undergo Auger processes, and by introducing a smooth core/shell interface, these Auger rates are predicted to be suppressed by several orders of magnitude [21]. However, there have been no systematic experimental studies directly relating the softness of the confinement potential to the Auger rate or to fluorescence blinking. Furthermore, the gradual material transition in the particles, analysed by Wang et al., has yet to be experimentally confirmed [22].

Apart from the soft confinement potential in this type of core/shell NCs another structural feature, potentially reducing blinking, is the continuous grading of lattice parameters between the core and shell region. As discussed in Chapter 3, lattice strain at the interface of core/shell NCs is a potential source of internal crystal defects. The gradual transition in CdZnSe/ZnSe alloyed particles would minimise this strain to a great extent potentially resulting in defect–free crystals.

Following the report by Wang et al. and their data interpretation, Spinicelli et al. [23] investigated the reduction of Auger recombination efficiency in the thick shell CdSe/CdS system. Close analysis of single particle PL traces revealed fluctuations between a high and intermediate intensity emitting state, of which the high state was assigned to radiative monoexcitonic recombination and the lower one to recombination of a trion. The observation of a bright trion state in such heterostructures is related to the strong localisation of the hole in the core combined with the extensive delocalisation of the electron across the whole particle. In this picture, Coulomb interactions between the charge carriers are greatly reduced, inducing

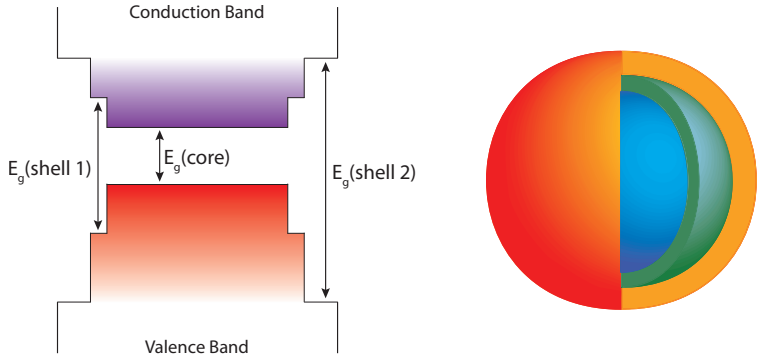

Figure 4.3 3D model of a CdSe/CdS/ZnS core/shell/shell heterostructure along with the corresponding band gap alignment. The CdSe, CdS and ZnS regions are colour coded in blue, green and orange respectively.The function of the intermediate CdS layer is twofold. On the one hand, it mediates the lattice strain between the CdSe core and the outer ZnS shell. On the other side it introduces an intermediate potential step at the band offsets between CdSe and ZnS, effectively 'softening' the confinement.

an increase of Auger lifetime (eventually making it less efficient than radiative recombination). As mentioned previously in Section 1.3, a similar low emitting state was observed by Gomez et al. [4] in CdSe/CdS core/shells, however with significantly thinner CdS shells. They also assigned the emission of the intermediate state to a positive trion state in agreement with Spinicelli et al. Both studies observed the lifetime of the trion emission to be shorter than the decay of the high intensity state, in agreement with the results of Wang et al. [18]. However, additional features in the PL spectrum due to trion emission, were not reported.

Further evidence, supporting strongly reduced Auger recombination in such particles, was provided by amplified stimulated emission (ASE) experiments [24] which revealed an extraordinarily large bandwidth of optical gain ($>500\ meV$) and extremely low excitation thresholds. Additionally, multiexcitonic emission, which is normally inhibited by Auger processes, was clearly observable and found to be efficient in these systems [25].

While these recent reports demonstrate impressive progress towards non–blinking QDs, the fundamental mechanism of fluorescence blinking in semiconductor NCs is still far from understood. However, several trends can be derived. On the one hand, blinking suppression seems to be not only a matter of exciton isolation away from surface trap states but is also likely to be linked to the mitigation of Auger processes. Furthermore, the strategy to prepare nanocrystals with reduced blinking clearly points towards the elimination of crystal defects.

Following these considerations, the work presented in this chapter investigates the structural requirements to combine efficient exciton confinement with the minimisation of crystal defects. Our approach follows the ideas of Talapin et al. [26] and Xie et al. [27], and involves preparing a core/shell/shell Type–I structure based on a CdSe/CdS/ZnS material combination. The

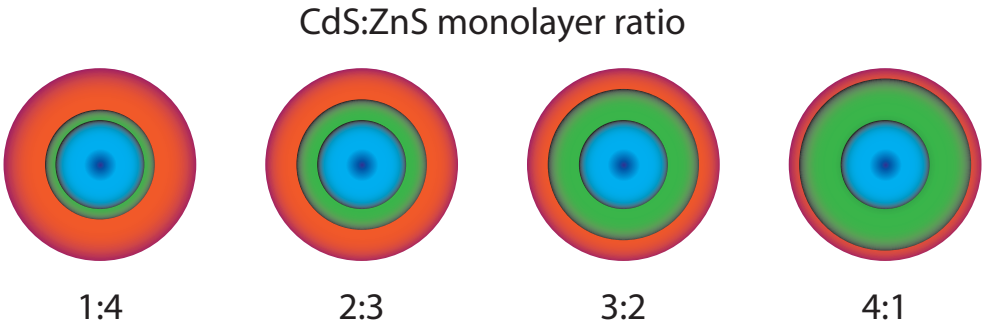

Figure 4.4 Illustration of the graded core/shell/shell samples under investigation. CdSe, CdS and ZnS are colour coded with blue, green and orange respectively. While the CdSe core size remained constant, CdS/ZnS shell thickness combinations were analysed ranging from a monolayer ratio of 1:4 through to 4:1.

intermediate CdS shell should mitigate the lattice strain between CdSe and ZnS by acting as a 'buffer' layer with its lattice parameters located in between those of the other two materials. This should facilitate the epitaxial growth of thicker ZnS shells and minimise the formation of interface defects. Considering the idea of a soft potential by Wang et al., the CdS layer also acts as an intermediate potential step, grading the confinement between the CB and VB offsets of CdSe and ZnS, as depicted in Figure 4.3.

The aim is to investigate and optimise reaction conditions as well as the relative thicknesses of the CdS and ZnS shells, in order to maximise radiative exciton recombination in such materials. By varying the ratio between CdS and ZnS monolayers from 1:4 to 4:1 (see Figure 4.4), we analyse the effects of lattice strain and total confinement potential on the optical properties of the resulting QDs. We begin by examining the core/shell/shell system theoretically by adapting the finite potential well model for concentric core/shell structures presented in Chapter 3. Subsequently, we present the experimental details pertaining to the successful synthesis of such heterostructures, followed by their structural and optical analysis.

4.2 Finite Potential Well Model for a Graded Type–I Core/Shell/Shell Nanocrystal

To describe the graded core/shell/shell structure within the effective mass approximation, the model for core/shell systems, presented in Chapter 3, is still valid. As this approach is extendible to multiple shells [28], an additional potential was introduced to account for the second shell. To obtain valid solutions it was furthermore required, that the radial component of the eigenfunctions is continuous at all interfaces and vanishes sufficiently quickly within the matrix. The plot on the right hand side of Figure 4.5 depicts the radial energy diagram

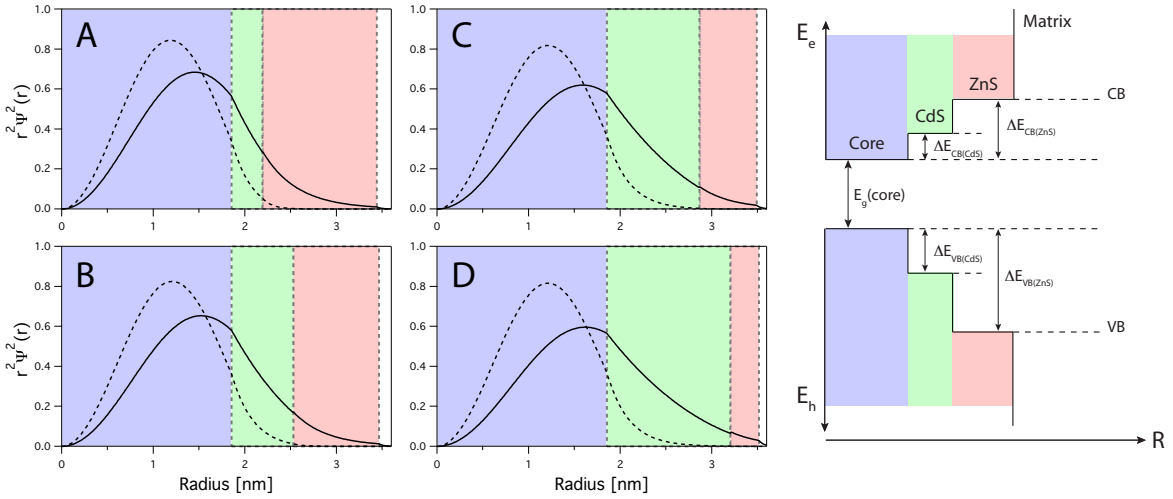

Figure 4.5 Radial probability distributions of the lowest state electron (solid line) and hole (dashed line) wavefunctions for core/shell/shell nanocrystals based on the material parameters for CdSe/CdS/ZnS particles. The panels A–D represent the CdS–to–ZnS monolayer ratios from 1:4 to 4:1, respectively, with a common CdSe core radius of 1.85 nm. CdSe, CdS and ZnS regions are colour coded in blue, green and red respectively. The plot on the right depicts the radial energy diagram (not to scale). $E_g(core)$ is the band gap of the core and ΔE_{VB} (ΔE_{CB}) is the potential offset of the valence band (conduction band) between core and the respective shell.

on which the calculations were based. The material parameters and band gap offsets ΔE between the core and shell materials were taken from Table 3.1. The panels A–D display the calculated radial probability distributions of the $1S$ electron (solid line) and hole (dashed line) wavefunctions for the four heterostructures depicted in Figure 4.4 with a CdS–to–ZnS monolayer ratio ranging from 1:4 to 4:1, respectively. For simplicity we refer in the following to these as samples A–D.

As observed previously, the electron is generally more delocalised compared to the hole due to its lower effective mass and smaller potential barriers at the conduction band compared to those at the valence band. All four configurations show a strong localisation of the hole in the core with a rapid decline in the shell region. The hole distribution in sample A exhibits a slightly stronger confinement which can be attributed to the 'early' onset of the deep valence band potential of ZnS at a radius of $\sim$2.2 nm. However, the decline of the hole distribution in all structures indicates sufficient confinement to prevent the charge carrier reaching the particle surface.

Examining the trend of increasing CdS shell thickness and narrowing ZnS shell from panel A to D, a distinct extension of the electron distribution into the shell domain can be observed. While the decay is appreciably steep in structure A, it continuously flattens as the onset of the ZnS conduction band potential is pushed back with increasing width of the intermediate

CdS shell. This extension can be attributed to the small conduction band offset between CdSe and CdS which does not provide a significant potential barrier for the electron, enabling it to deeply penetrate into the shell region. Thus, considering the reduction of available trap states, the sample with maximum ZnS shell thickness (panel A) should provide the best results as it provides the largest potential well against the exciton reaching possible surface traps. For the same reason, this configuration should also yield the smallest red–shift upon shell growth due to the strongest confinement out of these four heterostructures. However, it is important to recall that these calculations can not account for the effects of lattice strain at the material interfaces, which is (to a certain degree) shell thickness dependent [29, 30]. We know already that this strain can lead to internal crystal defects, and thus is another potential source of trap state formation. In the following, we describe the synthetic details and experimental characterisation of the four core/shell/shell samples to study the concerted effects of confinement potential and lattice strain on their optical properties.

4.3 Preparation of Graded Seal CdSe/CdS/ZnS Core/Shell/Shell Nanocrystals

The CdSe/CdS/ZnS core/shell/shell heterostructures were prepared following the protocols described in Chapter 3. For this work, CdSe cores of 3.2 nm and 3.7 nm diameter were synthesised, as outlined in Chapter 2. After rendering the CdSe core surface cadmium rich, shell growth was performed by adding calculated amounts of the metal and chalcogenide injection solutions in an alternating manner. The reaction temperature for the growth of individual semiconductor monolayers was set to the values stated in Table 3.4. The high temperatures ensured good crystallinity during shell growth and facilitated the reduction of defects through annealing. The temperature increase towards thicker shells was found to be necessary to counteract the declining surface reactivity with increasing particle size, thus maintaining adequate growth rates. As discussed previously, the Cd–rich and all CdS shell depositions were substituted with oleic acid in a 20:1 mole ratio (OA:Cd), while ZnS semiconductor monolayers were supplemented with a 0.5:1 (TBPh:S) mole ratio of TBPh. This binary ligand protocol enabled tight control over shell deposition, while minimising the occurrence of homogeneous nucleation. Following the completion of shell growth the solution was annealed at 200 $^{\circ}C$ for 1 h and subsequently stirred at 70 $^{\circ}C$ for another 12 hrs to further reduce the number of crystal defects.

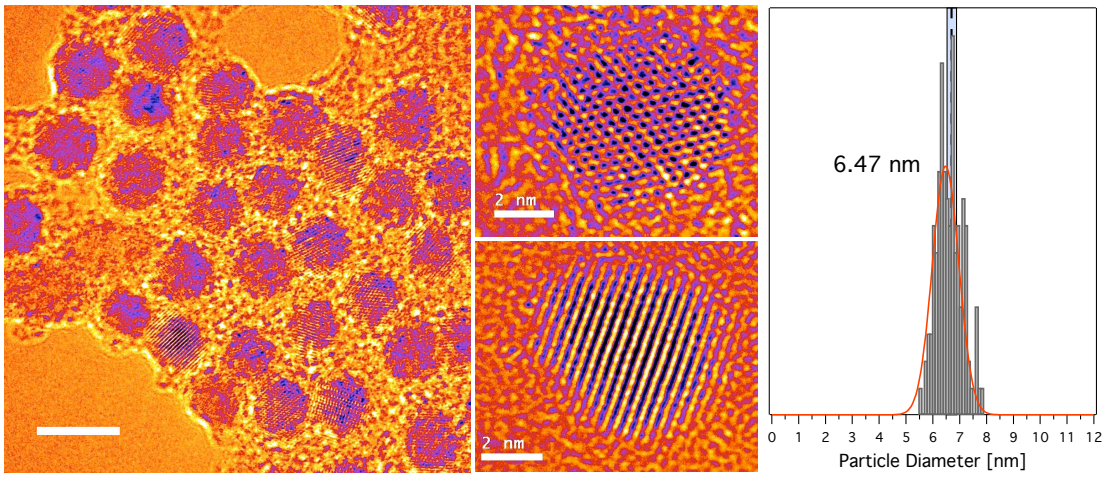

Figure 4.6 Left: Bright Field HRTEM images of CdSe/CdS/ZnS core/shell/shell nanocrystals with a core size of 3.2 *nm* and a CdS:ZnS shell thickness ratio of 1:4 monolayers. The scale bars on the left and centre are 10 *nm* and 2 *nm* respectively. Right: Corresponding particle size distribution with a mean diameter of 6.47 *nm*. The black dashed line with the light blue box represent the predicted size of 6.8 *nm* with its associated error.

4.4 Electron Microscopy

To confirm successful and quantitative shell growth, the core/multishell samples were subject to structural analysis via TEM. Figure 4.6 presents TEM images and the corresponding particle size distribution (PSD) for CdSe/CdS/ZnS nanocrystals with a core size of 3.2 *nm* and a CdS:ZnS shell thickness ratio of 1:4 monolayers. From the PSD it is readily observed, that the measured mean particle size of 6.47 *nm* closely matches the theoretically predicted diameter of 6.8 *nm* (indicated by the dashed black line). This deviation is less than the thickness of one monolayer (∼0.6–0.7 *nm*), implying quantitative shell growth. Inspection of the TEM images reveals an almost spherical shape, with occasional slight elongations. This deformation is commonly observed upon growth of ZnS shells and is likely a result of lattice strain, as discussed in Chapter 3. The atomic resolution images of single nanocrystals in the centre of Figure 4.6 support the highly epitaxial shell growth with no stacking faults or other internal crystal defects visible. The top image clearly exhibits the hexagonal symmetry of the wurtzite crystal structure on the atomic scale. Similar results were observed for the other three samples under investigation. Comparison of the PSD with that of CdSe/ZnS particles (see Figure 3.9) reveals improved monodispersity and a closer match to the predicted particle diameter. This improvement can be directly related to the effect of the intermediate CdS layer, efficiently reducing interface lattice strain and thus facilitating epitaxial shell growth.

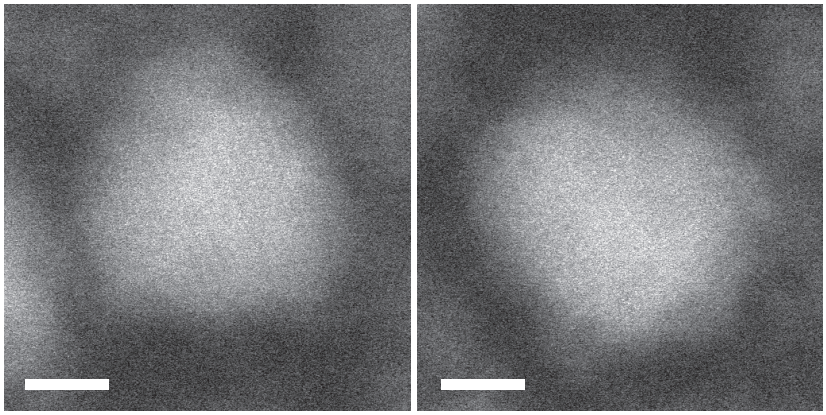

Figure 4.7 HAADF STEM images of CdSe/CdS/ZnS core/shell/shell nanocrystals with a core size of 3.2 nm and a CdS: ZnS shell thickness ratio of 1:4 monolayers. Lattice structure is only faintly visible due to environmental interferences limiting the attainable resolution. The scale bars are 2 nm.

A drawback of bright field TEM is the lack of elemental contrast, thus precluding the possibility to investigate the uniformity of shell material distribution or the occurrence of potential atom diffusion (alloying). To overcome this limitation, high angle annular dark field (HAADF) STEM can be employed, as introduced in Chapter 2. This technique yields a contrast which is directly related to the atomic number, thus letting heavier elements appear brighter in the image [31, 32]. However, attempts to discern core from shell material using this technique failed due to insufficient resolution (see Figure 4.7) of the microscope, arising from the environmental conditions at hand [33]. Thus the optical properties discussed in the following, are assigned to the postulated *ratios* of CdS to ZnS shell thickness, which can be derived from the incremental particle size increase upon shell deposition. Therefore effects related to potential alloying within the particles are only speculative.

4.5 Optical Properties of graded Core/Shell/Shell Nanocrystals

4.5.1 Absorbance and Emission

Figure 4.8 displays the normalised absorbance spectra taken after the deposition of each semiconductor monolayer (ML) of the CdSe/CdS/ZnS heterostructure with 1 ML of CdS and 4 ML of ZnS (sample A). As seen on the right, the deposition of the first CdS shell results in a large red–shift of $\sim$77 meV and a strong increase in absorbance at energies above 2.5 eV. The spectral shift arises from the electron delocalisation into the shell region due to the low CB offset between CdSe and CdS, as previously discussed in Chapter 3. It was generally observed, that the majority of the spectral shifts within each monolayer occurred after the deposition

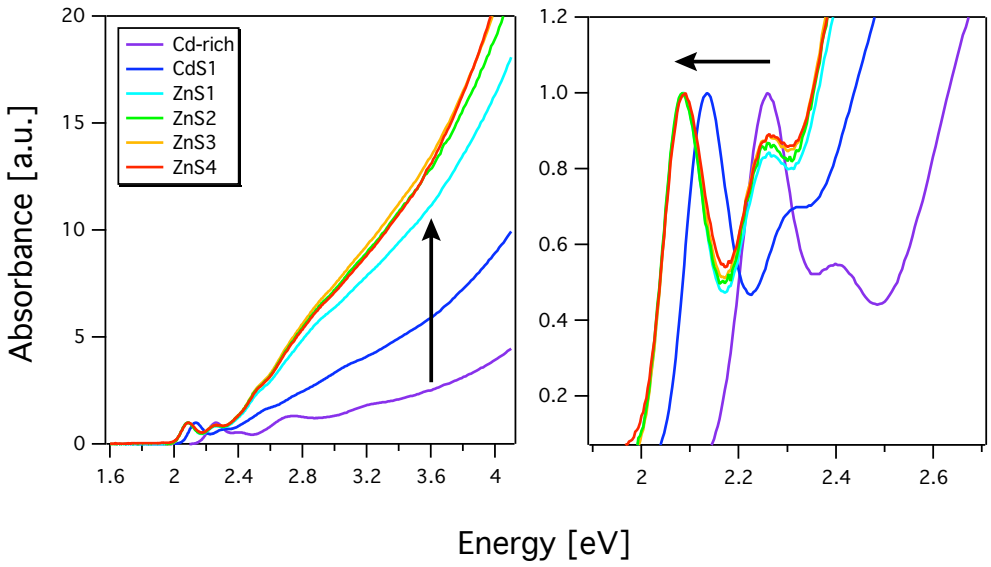

Figure 4.8 Normalised absorbance spectra taken after the deposition of each semiconductor monolayer (ML) of the CdSe/CdS/ZnS heterostructure with a CdSe core size of 3.7 nm, 1 ML of CdS and 4 ML of ZnS (sample A). The main trends in spectral evolution during shell growth are indicated by the black arrows.

of the chalcogenide layer, while the extent was dependent on the shelling material. Thus, following the sulphur injection for the first ZnS layer, we detected an additional spectral shift along with another absorbance increase at higher energies due to the preceding cadmium layer. However, the energy of the band edge transition red–shifted only $\sim$43 meV with completion of the first ZnS monolayer as a result of the large CB offset between CdS and ZnS. Following this point, little change was observed in the spectral features for the remaining three ZnS monolayers, suggesting effective exciton confinement is reached in such structures. From the magnified plot on the right, it can be seen that the first transition peak remains narrow throughout the shelling process, indicative of favourable growth conditions and reflecting the sample monodispersity confirmed via TEM.

In Figure 4.9 we analyse the evolution of the photoluminescence spectrum during shell growth and investigate the effect of the four different CdS:ZnS shell ratios. The graphs from top to bottom represent the samples A–D based on a CdSe core size of 3.7 nm with CdS:ZnS shell monolayer ratios varying from 1:4 to 4:1 respectively. The plots on the right side show the changes in FWHM (blue circles) and peak position energy (red squares) as a function of shell growth with the corresponding traces on the left. The green and red shading in the right hand side plots indicates CdS and ZnS shell regions respectively.

Inspection of the band edge emission shifts for all four samples reveals, spectral red–shifts occurring generally up to the completion of the first ZnS layer, reproducing the trend observed

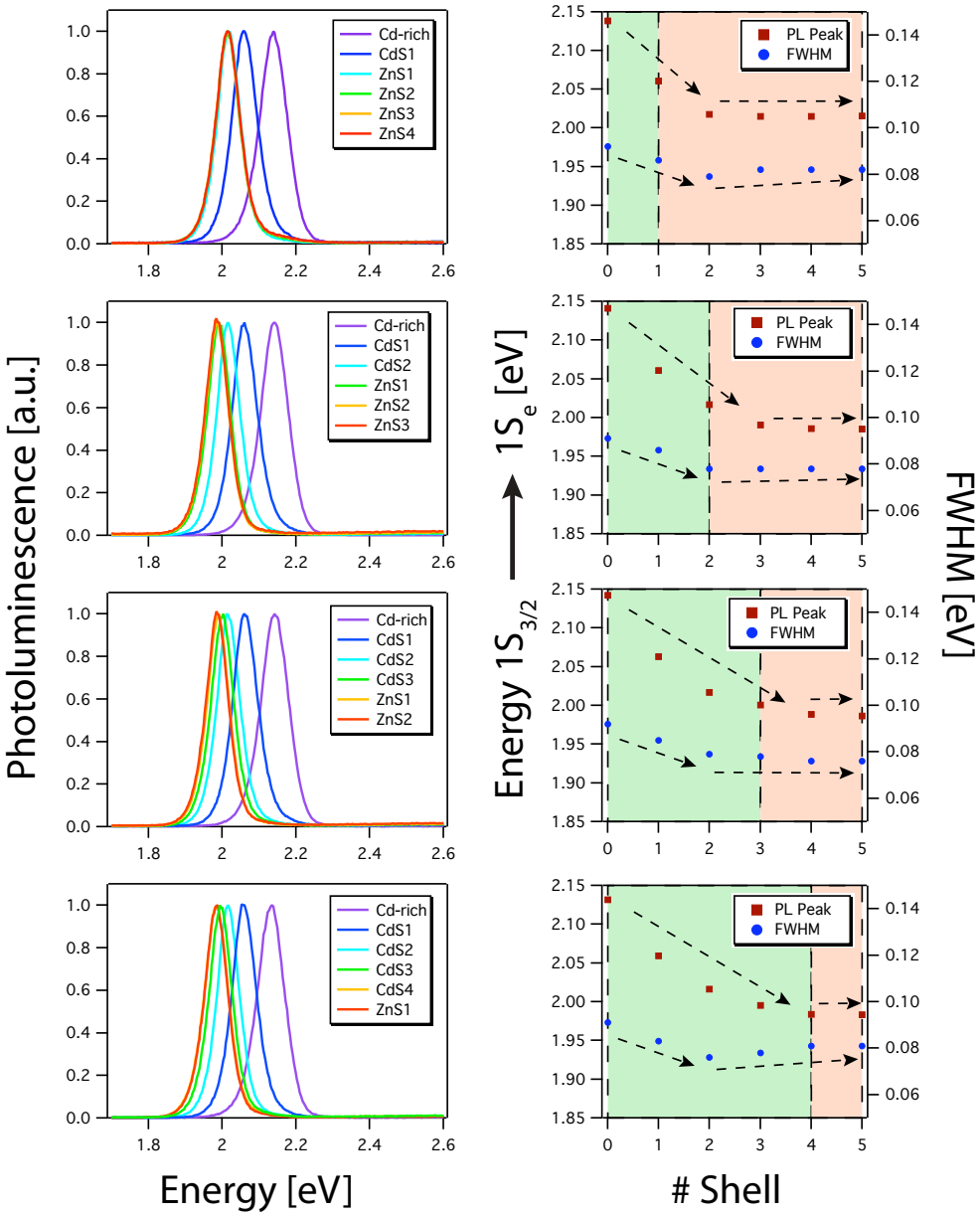

Figure 4.9 Photoluminescence traces (left) and corresponding plots of PL peak energy and FWHM (right) of CdSe/CdS/ZnS core/multishell samples with a common CdSe core size of 3.7 *nm*. From top to bottom, the CdS:ZnS monolayer ratio varies from 1:4 to 4:1, as indicated by the green and red shading in the right hand side plots. The black arrows are a guide to the eye highlighting the various trends during shell deposition.

in absorbance shifts. Thus an early change from CdS to ZnS shell material, as in sample A, leads to an overall stronger confinement of the charge carriers, which manifests itself in a total red–shift of $\sim$123 meV — 30 meV less compared to the other three samples ($\sim$153 meV). This is consistent with the trend of exciton expansion due to increasing CdS shell thickness, predicted by the model calculations. We already know that the extent of energy decay is strongest for the first layers and weakens continuously with further shell deposition. Therefore the restricting effect on energy loss upon growth of the first ZnS layer is not as significant in samples B–D, since the energy decay is already considerably weakened by the growth of the preceding CdS layers.

Inspecting the evolution of the full width at half maximum (FWHM), we observe focussing of the size distribution up to the deposition of the second monolayer for all four samples. Upon growth of subsequent layers, the FWHM is found to either stay virtually constant (sample C) or broaden slightly (sample A, B, D). This is consistent with the trends presented previously in Chapter 3, however the extent of broadening with the deposition of ZnS layers is significantly reduced when compared to the growth of pure ZnS shells in Figure 3.10 **F**. This reflects the improved PSD in such core/shell/shell heterostructures found by TEM analysis and can be related to the strain mediating effect of the intermediate CdS shell.

In the light of practical applications, requiring the retention of emission energy, the shell ratio used in sample A is the most suitable due to the fact it exhibits the smallest red–shift of all for samples. Furthermore, from the evolution of the FWHM the data suggests that an intermediate CdS shell of only one monolayer already significantly improves the epitaxy of the following material deposition.

4.5.2 Fluorescence Lifetime

To gain further insight into the optical effects of strain mediation and carrier confinement we studied the fluorescence lifetime evolution of samples A–D upon shell growth. Lifetimes were measured as outlined in Chapter 2 and fitted to stretched exponentials of the form

$$y = y_0 + A \times exp\left[-\left(\frac{t}{\tau}\right)^{\beta}\right] \quad , \tag{4.2}$$

which yield the average lifetime τ, and a β parameter ranging between 0 and 1. A β value of 1 corresponds to a single exponential decay process, with decreasing values indicative of a broader distribution of recombination pathways [11]. Figure 4.10 displays an example of such a fit for CdSe/CdS core/shell nanocrystals dispersed in chloroform, yielding an average lifetime of 16.4 ns and a β–value of 0.76. It is important to bear in mind that β is also influenced by the PSD in ensemble measurements, as particles with slightly different structural

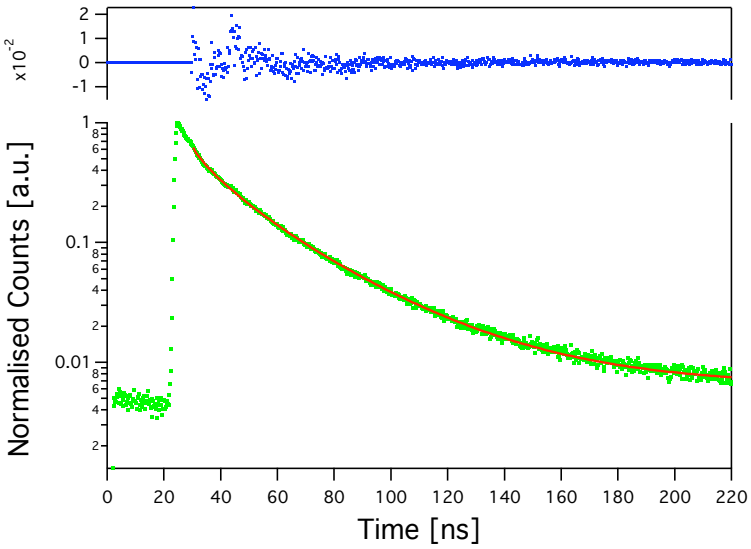

Figure 4.10 Semi–log plot of the fluorescence decay time of CdSe/CdS core/shell nanocrystals with a core size of 3.7 nm and shell thickness of three monolayers. The sample was excited at a wavelength of 403 nm. The lifetime and β–value were extracted by fitting the data with a stretched exponential decay (red curve) yielding $\tau = 16.4\ ns$ and $\beta = 0.76$ (fitting residual shown above).

features will exhibit different lifetimes. However, the polydispersity of the four samples under investigation was fairly similar. Therefore, the net effect of changes in β is postulated to arise from differences in the number of available recombination channels.

The observed quantum yield is a result of combined radiative and non–radiative recombination rates, and similarly, the mean lifetime Γ_{tot} is a sum of the individual decay times of such channels:

$$\Gamma_{tot} = \Gamma_{rad} + \Gamma_{nonrad} \quad . \tag{4.3}$$

Changes in radiative decay time Γ_{rad} are related to the confinement situation of charge carriers, leading to changes in the strength of Coulomb interactions. For example, the growth of CdS shells facilitates charge separation, as the hole is strongly localised in the core region while the electron can extend over the whole core/shell structure. Thus, Coulomb interactions are diminished and a lengthening of the observed lifetime is expected. ZnS shells, on the other hand, strongly confine both charge carriers in the core, effectively enhancing their wave function overlap, which should lead to a shortened radiative lifetime. Non–radiative decay via trap states is known to be several orders of magnitude faster than radiative recombination [7]. Thus, its impact on the observed mean lifetime can be significant and correlates directly with the number of such traps. Therefore, a distinct shortening of Γ_{tot} (concomitant with a decrease in QY) is commonly assigned to the formation of trap states.

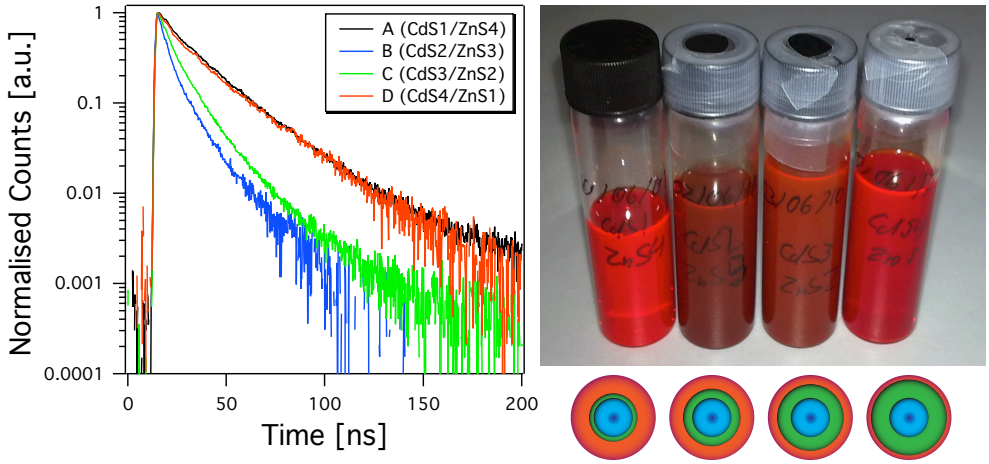

Figure 4.11 Fluorescence lifetime decays of samples A–D (left) and photograph of the corresponding samples dispersed in chloroform under ambient light (right). Stretched exponential fits recovered mean decay times of 18.2 *ns*, 6.3 *ns*, 8 *ns* and 14.5 *ns* for samples A–D respectively. The photograph qualitatively demonstrates the higher brightness of samples A and D compared to samples B and C.

Figure 4.11 presents the recorded lifetime decays (left) of the final samples A–D along with a photograph of the NCs dispersed in chloroform (right). Fitting the traces to stretched exponentials yielded mean decay times of 18.2 *ns*, 6.3 *ns*, 8 *ns* and 14.5 *ns* for samples A–D respectively. As a single exponential decay appears as a straight line when plotted on a logarithmic scale, it is immediately observed that samples A and D exhibit fluorescence decays which are highly mono exponential, while the traces of samples C and D indicate a larger number of recombination channels. From the photograph taken under ambient light, it is readily observed, that this difference correlates with brightness of the particles which is significantly higher for samples A and D compared to the central samples B and C. This supports the postulated relation between lifetime shortening and the availability of non–radiative decay channels.

These results were somewhat unexpected, as they suggest a facilitation of non–radiative recombination in shell ratios of 2:3 compared to a 1:4 ratio. In the light of confinement softening, this appears counter–intuitive, as a more equal shell ratio should reduce the overall steepness of the confinement potential. Considering the effect of lattice strain mediation, one could argue that a more equal shell ratio (2:3, 3:2) would also distribute the strain more equally over the whole structure, thus reducing the chance of interface defect formation. On the other hand, it was shown that lattice strain increases with shell thickness, as the material lattice becomes more rigid [34]. Following this hypothesis, the smaller number of available trap states in samples A and D could be attributed to the higher flexibility of the one monolayer

thick shell component, thus reducing the probability of crystal defect formation upon shell deposition.

To deepen our understanding of these phenomena, the recombination dynamics of the four samples were studied as a function of shell growth. The plots on the left hand side of Figure 4.12 show a series of lifetime decay curves taken after each subsequent layer of CdS or ZnS shell growth for samples A–D (top to bottom). The panels on the right present τ (blue circles) and β values (red squares) extracted from stretched exponential fits of the corresponding trace. The green and red shadings indicate CdS and ZnS shell regions respectively, analogous to Figure 4.9.

Focussing on the trends for sample A, both β and τ decreased after deposition of the initial CdS layer onto the Cd–rich cores. This is indicative of an increase in non–radiative recombination which is unexpected, since shell deposition of one ML CdS should be highly epitaxial and decrease the number of surface trap states. The reasons for this behaviour are not clear at present, however this trend was witnessed consistently for all four samples. Upon deposition of two subsequent ZnS layers, β increased continuously which can be attributed to epitaxial growth and the efficient isolation of the charge carriers in the particle centre, effectively blocking the access to surface trap states. With the deposition of the final two ZnS layers, only minor changes in β were detected yielding a final value of 0.84. Similarly the lifetime stayed virtually constant at $\sim$ 18 ns after the deposition of the first CdS layer.

Looking at the trends for sample B, a very different evolution was noticed. Upon growth of the second CdS layer, both lifetime and β stayed constant (within experimental error) at 17–18 ns and 0.77 respectively. However, in contrast to the trend in sample A, a significant decline of both parameters is observed following the deposition of one ZnS layer, which continues to the growth of ZnS–2. The decay time shortening from 17 ns to 6.5 ns along with the decrease of β from 0.77 to 0.70 suggests substantial formation of trap states upon ZnS shell growth. Since the confinement potential of the three ZnS layers is comparable to that of sample A, the increase in non–radiative recombination was attributed to the formation of interface defects at the CdS–ZnS shell interface. This suggests that an intermediate CdS shell, thicker than one ML becomes too rigid to allow for epitaxial ZnS growth. This is confirmed in samples C and D where a distinct lifetime shortening upon ZnS shell deposition was consistently observed.

The trends of sample C, are consistent with the observations made for sample B, as τ stays generally constant with CdS shell growth and decreases upon ZnS deposition. The β values do not closely follow this progression but an overall decline is clearly detectable. In the case of sample D, both lifetime and β remain constant (except for CdS–3) at $\sim$17 ns and 0.78 throughout CdS shell growth. Deposition of one ML ZnS leads to a minor decrease of β to 0.72 and a lifetime shortening to 14.5 ns. However this effect is not as pronounced, compared

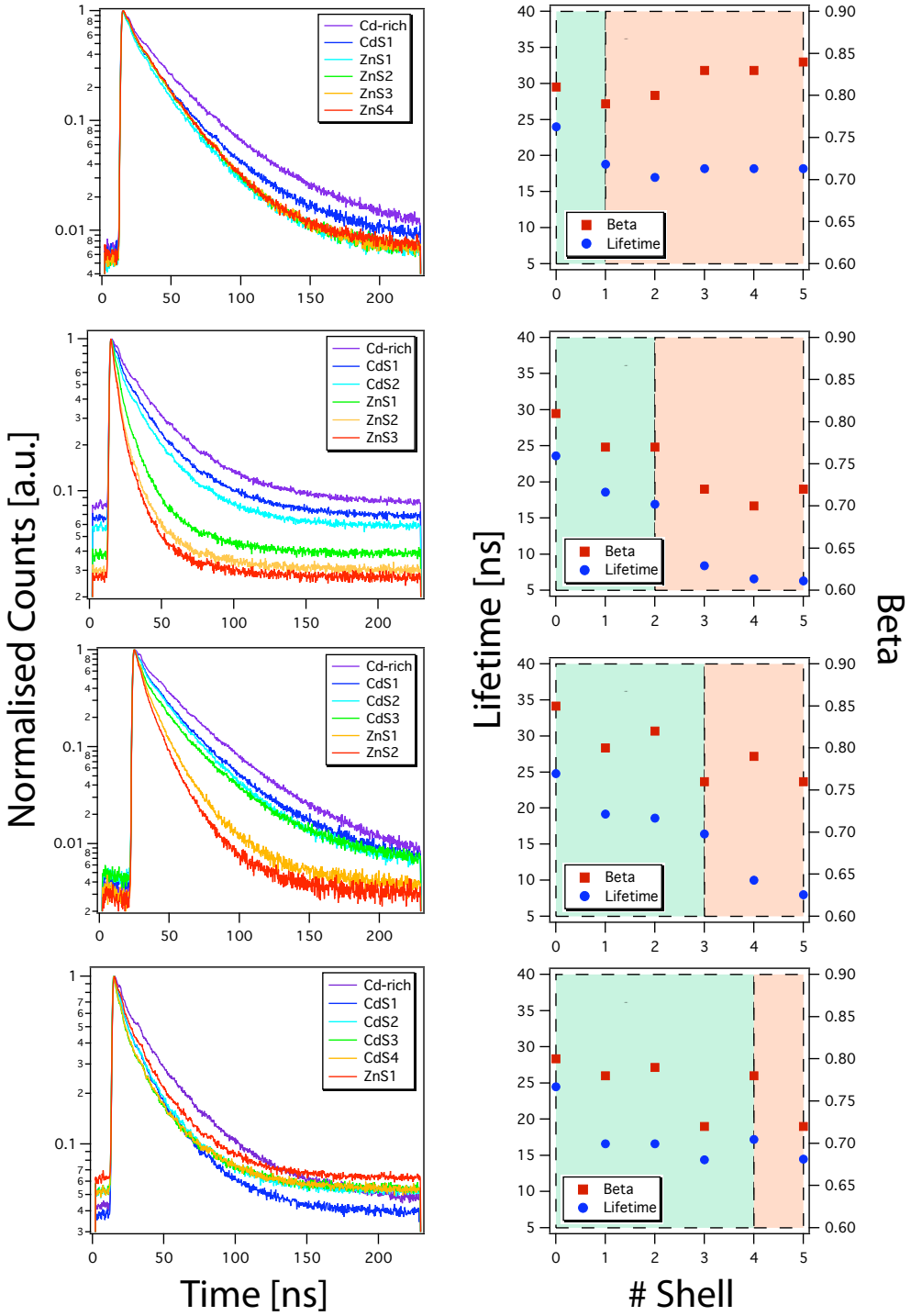

Figure 4.12 Lifetime traces as a function of shell growth (left) along with the corresponding τ (blue circles) and β (red squares) values obtained from stretched exponential fits (right). The data from top to bottom was collected from samples A–D respectively.

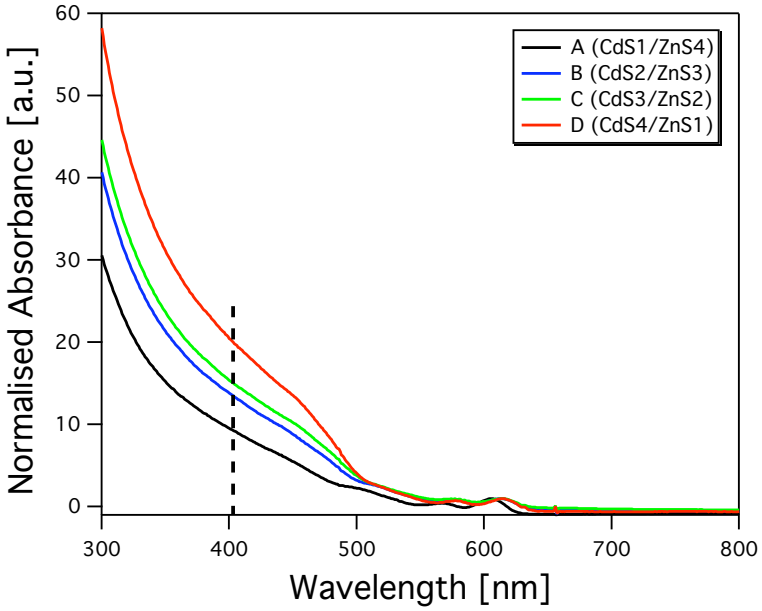

Figure 4.13 Absorption spectra of samples A–D normalised to the band edge transition. The dashed line indicates the excitation wavelength (403 nm) of the pulsed laser utilised for lifetime measurements.

to samples B and C. This diminished influence is attributed to the, at this point, appreciable exciton confinement of a four ML thick CdS shell.

It is important to note that for a truly quantitative comparison of the lifetime trends between samples, the differences in absorption at the excitation wavelength (403 nm) must be considered. Although great care was taken to conduct all measurements at similar concentrations and the particle diameters of the four samples are comparable, differences in material composition still affect their absorbance (especially) at higher energies. Figure 4.13 displays the absorption spectra of the final samples A–D normalised to the band edge transition. A trend of increasing absorption below 500 nm with increasing CdS content is readily observed. This effect was attributed to the high extinction coefficient of CdS as discussed previously in Chapter 3. Since the excitation wavelength of the pulsed laser falls within this spectral region, it is reasonable to question whether the conducted lifetime measurements are sensitive to this difference. However, the investigation of this effect was beyond the scope of this study and was therefore not accounted for.

In conclusion, our analysis of photoluminescence and lifetime ensemble data indicates that the combination of a one monolayer intermediate CdS shell and a four monolayer outer ZnS shell yields the best results in terms of trap state reduction and exciton confinement. Deposition of one monolayer of CdS significantly enhances the retention of a narrow PSD while being flexible enough to allow for epitaxial growth of a thick outer ZnS shell. This

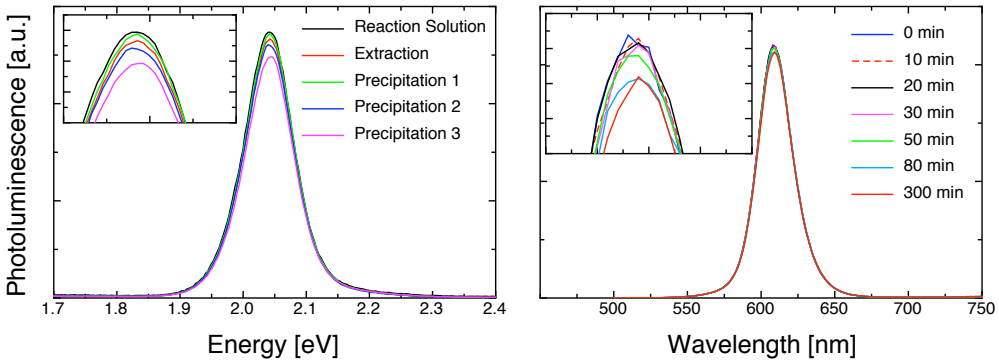

Figure 4.14 Photoluminescence spectra of sample A (CdS:ZnS monolayer ratio 1:4) taken after a series of purification steps (left) and extended irradiation (right). The particle washing involved and extraction with a methanol/chloroform mixture and three successive precipitation/re–dissolution steps using acetone and chloroform (see Chapter 2 for detailed protocol). Photostability was tested by irradiating NCs dispersed in toluene in a sealed quartz cuvette with a 250 W lamp at a wavelength of 480 nm.

resulted in highly luminescent particles exhibiting a β value of 0.84 which was found to be higher than the initial core value, in contrast to the trend of the other samples. Therefore the studies presented in the following were solely conducted on sample A.

4.5.3 Environmental Robustness

To test the degree of exciton isolation from the particle surrounding, stability tests against post–synthetic treatment were performed on sample A. Figure 4.14 displays emission spectra taken after several washing steps (left) and intense sample irradiation over an extended period of time (right). Particle purification leads commonly to a decline in QY due to the removal of surface passivating ligands [35]. Any detected drop in PL upon NC washing is therefore a direct consequence of charge carriers reaching the crystal surface. As such the extent of quenching directly reflects the efficiency of exciton confinement in the core/shell/shell structure. Multiple sample purification steps were performed as outlined in Chapter 2. After each the band edge absorbance was adjusted to similar values and the emission spectra was recorded. Normalising the spectra to the recorded absorbance value at the excitation energy, resulted in the graph presented on the left hand side of Figure 4.14. The minute decline of PL (highlighted in the inset) demonstrates excellent robustness and efficient exciton confinement in those materials.

Furthermore the resistance against photo–bleaching was tested by intense irradiation of the particles. After placing the nanocrystals dispersed in toluene in a sealed quartz cuvette and illuminating them with a 250 W lamp at a wavelength of 480 nm, PL spectra were recorded at certain time intervals to monitor any change due to photo–bleaching. Similar to

the observations upon sample purification, only a minor drop was detected over an irradiation time up to 300 *min*. This supports further the high robustness of these NC heterostructures.

4.6 Single Particle Fluorescence Analysis

To investigate the optical properties of individual QDs and to analyse their blinking behaviour, sample A was subject to single particle fluorescence spectroscopy. The details of sample preparation and the microscopy setup were covered in Chapter 2. Measurement of single particle photoluminescence trajectories under ambient conditions revealed complete blinking suppression over an observation time of 2 *min* for ∼25 % of the investigated particles. To confirm that the photoluminescence was indeed from a single emitter, photon anti–bunching measurements were performed as described in Chapter 2. Figure 4.15 displays typical PL trajectories recorded from the particles exhibiting blinking suppression under various excitation powers. The detected count rate of those NCs was found to be well defined and constant with rare fluctuations.

The collection of PL trajectories in TCSPC (time correlated single photon counting) mode [36] enabled us furthermore to reconstruct the fluorescence decay time of these stable emitters. Employing the Bayesian changepoint algorithm [37], the photons were first assigned to states of different intensities (where appropriate) as illustrated in the upper graph of Figure 4.16. The close match of the calculated mean intensities (blue lines) of these states to the trajectory histogram maxima (right panel) supports the accuracy of this method. Subsequently, the fluorescence decay of the intensity state of interest was reconstructed from the respective photon arrival times* which was successfully fitted to a single exponential function of the form:

$$y = y_0 + A \times exp\left(-\frac{t}{\tau}\right) \quad . \tag{4.4}$$

The observation of a single exponential decay when selecting only photons from the maximum intensity state within a PL trajectory was reported previously [11], and was assigned to the radiative recombination channel. Thus, it enables the quantitative measurement of the single–exponential radiative lifetime of CdSe/CdS/ZnS core/shell structures at room temperature. Furthermore, the single exponential signature is another feature supporting a single NC as the photon source, since the PL trajectory of a QD cluster would yield a multi–exponential decay profile arising from the various radiative recombination channels of the individual particles within the aggregate [38].

* The author acknowledges Gary Beane for the provision of a customised IgorPro script to extract fluorescence decay histograms from time–tagged data files.

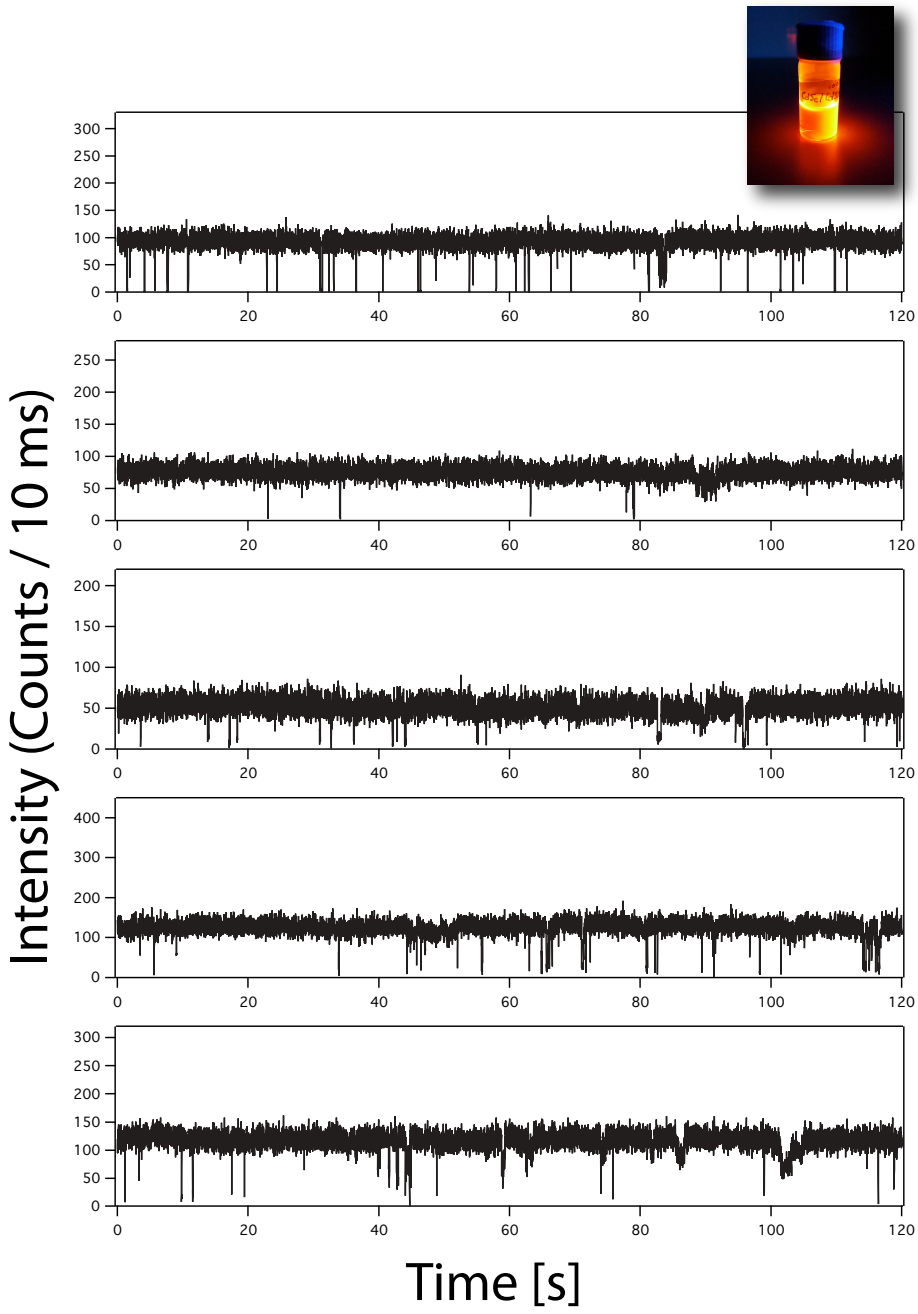

Figure 4.15 Photoluminescence trajectories collected from individual nanocrystals of sample A (CdS:ZnS monolayer ratio 1:4) exhibiting strong blinking suppression. The particles were excited at 466 nm with a power of 300 nW, 300 nW, 300 nW, 400 nW and 600 nW respectively. The photograph on the top right corner shows the particles dispersed in chloroform illuminated under low power UV–light.

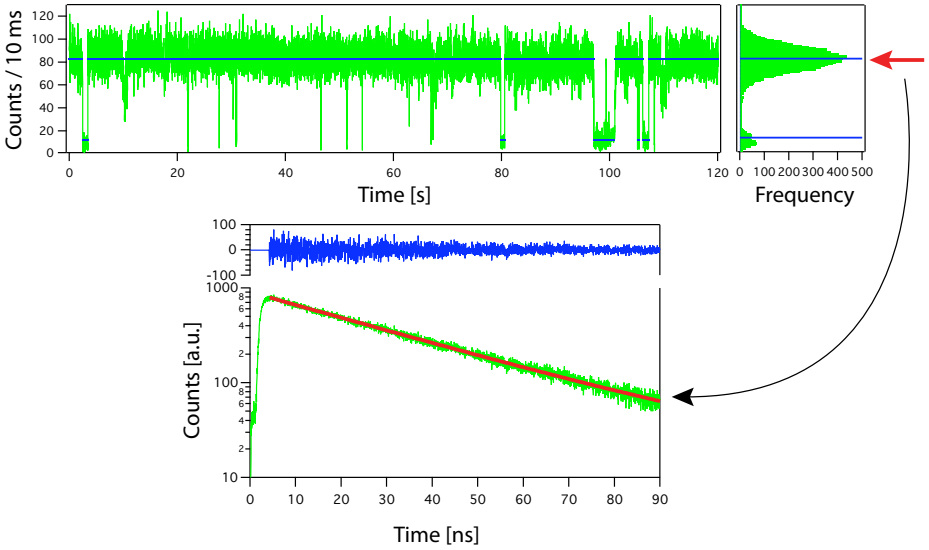

Figure 4.16 Top: Photoluminescence time trajectory of a single CdSe/CdS/ZnS core/shell nanocrystal (Sample A) with corresponding intensity histogram (left panel). The blue lines represent the intensity states extracted by the Bayesian changepoint detection algorithm. Bottom: Semi–log plot of photon arrival times (time tagged data) representing the decay time of the high intensity state. The lifetime was extracted by fitting the data with a single exponential decay yielding a value of 31 ns for this particular NC (fitting residual shown above).

The exceptional long term stability of these nanocrystals against continuous irradiation enabled us furthermore to study their excitation intensity dependence. Panel A of Figure 4.17 presents eight PL trajectories of the same single CdSe/CdS/ZnS heterostructure (sample A) with individual observation times of 2 min. The traces from top to bottom were successively collected while increasing the excitation power in 100 nW increments with each measurement from 100 nW to 800 nW, utilising a neutral density filter wheel. The laser power was measured just before entering the microscope. The recorded series reveals excellent emission stability over all excitation powers and the appearance of an intermediate state at 800 nW excitation power. Since these traces were successively recorded during continuous illumination, Panel A represents a total observation time of 16 min (plus time for excitation power adjustments). The intensity histograms of the respective trajectories plotted in Panel B reveal a direct relationship between excitation power and mean emission intensity level. Increasing the laser power from 100 nW to 800 nW led to a continuous increase of the mean emission intensity level from 30 to 190 counts per 10 ms bin, as illustrated in Panel D (blue squares). This continuous increase indicates that the absorption saturation for these particles is not reached within the range of probed excitation power and an increase in excitation flux directly translates into a higher photon emission rate. To support this interpretation, we estimated the number of

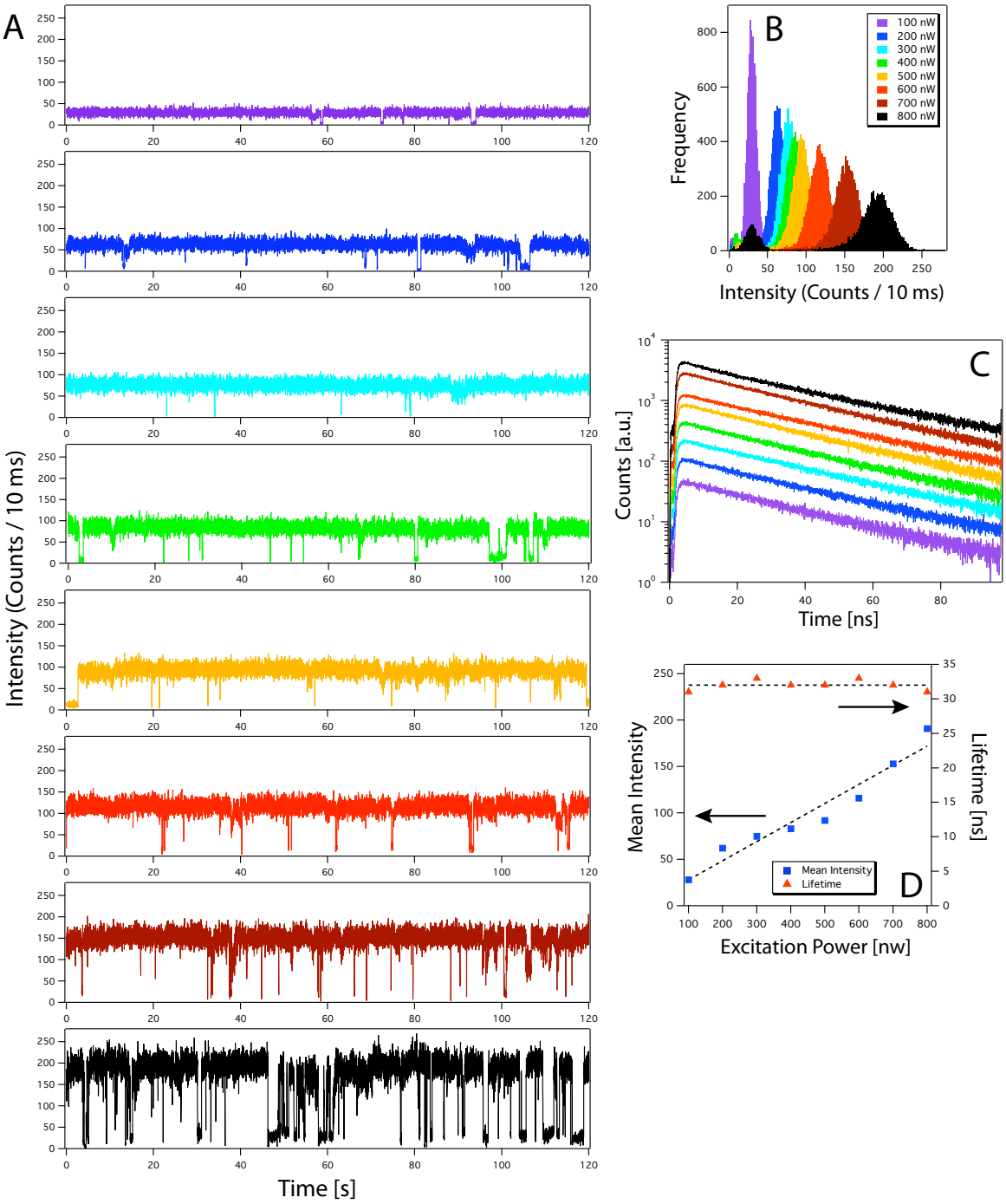

Figure 4.17 Collected photoluminescence time trajectories from the same single CdSe/CdS/ZnS nanocrystal at different excitation powers. The traces from top to bottom were successively recorded with increasing excitation power from 100 nW to 800 nW in 100 nW steps ($\lambda_{exc} = 466\ nm$).

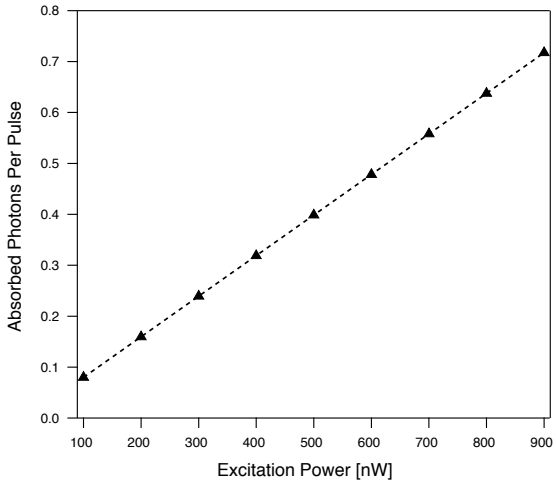

Figure 4.18 Calculated average number of absorbed photons per pulse as a function of laser power following Equation 4.5.

photons per pulse that are absorbed by a single quantum dot, given by

$$N_{abs}(pulse) = \frac{P_{exc}}{R} \times \frac{C_{abs}}{A} \times \frac{\lambda}{hc} \quad . \tag{4.5}$$

Here P_{exc} (W) is the measured excitation power, R is the repetition rate of the pulsed light source (10 MHz), C_{abs} (cm^2) represents the absorption cross section of an individual nanocrystal, A (cm^2) is the illuminated area produced by the confocal setup, and the last term represents the inverse of the energy of a single photon with h and c being the Planck constant and the speed of light respectively.

As discussed in Chapter 2, the employed confocal setup with an excitation wavelength of 466 nm and an objective with a NA of 1.4 yields a diffraction–limited spot of $\sim$200 nm radius, equating to an excitation area of $\sim 1.3 \times 10^{-9} cm^2$. Furthermore, the absorption cross section C_{abs} of an individual core/shell nanocrystal can be approximated to $\sim 4.4 \times 10^{-15} cm^2$ [39]. Figure 4.18 depicts the calculated number of absorbed photons per pulse as a function of laser power following Equation 4.5. The linear increase of the average photon number per pulse from $\sim$0.1–0.7 with increasing laser power correlates with the experimentally observed linear trend of detected photon counts from the nanocrystal. However, even at the highest employed excitation power the average number of absorbed photons does not surpass one, therefore making it highly unlikely to reach the threshold of absorption saturation within this power range, even without accounting for any losses due to scattering of optical elements.

Studying the excitation power effect on fluorescence lifetime, we limited the analysis to the maximum intensity state. The appearance of intermediate state fluorescence was too

sparse to reconstruct meaningful decay time histograms and was not observable in all intensity trajectories. Comparing the lifetime traces in Panel C of Figure 4.17, it is clear that the fluorescence lifetimes appeared to be virtually independent of excitation power, in contrast to the mean intensity. Fitting the decays to single exponential functions consistently yielded a decay time of $\sim$32 ns for this particular nanocrystal, as depicted in Panel D (red triangles). Earlier studies [40, 41] reported lifetime shortening due to the emergence of a fast component with increasing excitation intensity. This was attributed to an increased formation of multi–excitons which possess faster radiative decay channels due to the involved non–radiative Auger processes. Considering the intensity range under investigation it is likely that biexcitons are formed at the highest laser powers [40]. However the biexciton lifetime is in the range of a few 100 ps and has low quantum yield [42], making it difficult to detect due to the slow time resolution of the employed setup. This could explain the intensity independent lifetime behaviour observed in our experiments.

It is important to note, that the analysis of other particles exhibited different lifetimes and a varying extent of response regarding the emission intensity. This can be assigned to structural differences between individual NCs or variations in orientation relative to the excitation beam [43]. However, all probed particles showed the same trends of a direct relation ship between emission intensity and excitation power, and an independent, constant lifetime. The PL trajectories and their analysis of four other dots can be found in Appendix B.

4.7 Conclusion

This chapter gives a comprehensive account on the structural requirements for trap state reduction in core/shell heterostructures. We reviewed the current literature and experimental advances towards non–blinking QDs which indicate an intimate link between blinking and the number of available trap states present in the nanocrystal. Following these considerations, a structural model based on a CdSe/CdS/ZnS core/shell/shell system was proposed with the intermediate CdS shell serving as a 'buffer' layer to mediate lattice strain, while the outer ZnS shell provides efficient exciton confinement. Investigating a parameter space of four CdS–to–ZnS shell ratios, theoretical and experimental analysis revealed a 1:4 semiconductor monolayer ratio to yield the best performance in terms of exciton confinement combined with a minimum of available trap states. TEM and PL measurements confirmed the high crystallinity and narrow PSD of those heterostructures. The NCs were found to be highly robust against post–synthetic treatment such as extensive purification and intense irradiation (Figure 4.14) , making them potential candidates for practical applications. Finally single nanocrystal fluorescence spectroscopy revealed strong blinking suppression with $\sim$25 % of analysed CdSe/CdS/ZnS particles exhibiting continuous non–blinking comparable to the

results reported on CdSe/CdS particles with extremely thick shells [16]. However, our NCs showed a much smaller red–shift due to the stronger exciton confinement of ZnS compared to CdS. Furthermore the preparation can be accomplished within several hours compared to several days required for thick CdS shell growth [16]. Investigating the effect of excitation power on individual QDs, we observed a direct correlation between excitation flux and mean emission intensity, while the fluorescence lifetime — which was single exponential — appeared to be independent and constant. These observations suggest that the absorption saturation of those QDs is not reached within the utilised excitation power range, which was confirmed by the calculated theoretical absorption rate under the experimental conditions.

The results presented in this chapter pose further evidence, that the degree of blinking is intimately linked to the number of trap states available to the charge carriers, and that carefully optimised reaction conditions and material combinations can lead to highly epitaxial heterostructures exhibiting efficient blinking suppression.

Bibliography

[1] M. Nirmal, B. O. Dabbousi, M. G. Bawendi, J. J. Macklin, J. K. Trautman, T. D. Harris and L. E. Brus. Nature **383**, 802 (1996).

[2] J. Zhao, G. Nair, B. R. Fisher and M. G. Bawendi. Physical Review Letters **104**, 157403 (2010).

[3] S. Rosen, O. Schwartz and D. Oron. Physical Review Letters **104**, 157404 (2010).

[4] D. E. Gómez, J. van Embden, P. Mulvaney, M. J. Fernée and H. Rubinsztein-Dunlop. ACS Nano **3**, 2281 (2009).

[5] P. A. Frantsuzov, S. Volkan-Kacso and B. Janko. Physical Review Letters **103**, 207402 (2009).

[6] P. Frantsuzov, M. Kuno, B. Janko and R. A. Marcus. Nat Phys **4**, 519 (2008).

[7] V. Fomenko and D. J. Nesbitt. Nano Letters **8**, 287 (2008).

[8] D. E. Gomez, J. van Embden, J. Jasieniak, T. A. Smith and P. Mulvaney. Small **2**, 204 (2006).

[9] P. A. Frantsuzov and R. A. Marcus. Physical Review B **72**, 155321 (2005).

[10] J. Muller, J. M. Lupton, A. L. Rogach, J. Feldmann, D. V. Talapin and H. Weller. Applied Physics Letters **85**, 381 (2004).

[11] B. R. Fisher, H.-J. Eisler, N. E. Stott and M. G. Bawendi. The Journal of Physical Chemistry B **108**, 143 (2003).

[12] M. Kuno, D. P. Fromm, H. F. Hamann, A. Gallagher and D. J. Nesbitt. The Journal of Chemical Physics **115**, 1028 (2001).

[13] K. T. Shimizu, R. G. Neuhauser, C. A. Leatherdale, S. A. Empedocles, W. K. Woo and M. G. Bawendi. Physical Review B **63**, 205316 (2001).

[14] S. A. Empedocles, D. J. Norris and M. G. Bawendi. Physical Review Letters **77**, 3873 (1996).

[15] B. Mahler, P. Spinicelli, S. Buil, X. Quelin, J.-P. Hermier and B. Dubertret. Nat Mater **7**, 659 (2008).

[16] Y. Chen, J. Vela, H. Htoon, J. L. Casson, D. J. Werder, D. A. Bussian, V. I. Klimov and J. A. Hollingsworth. Journal of the American Chemical Society **130**, 5026 (2008).

[17] S. Hohng and T. Ha. Journal of the American Chemical Society **126**, 1324 (2004).

[18] X. Wang, X. Ren, K. Kahen, M. A. Hahn, M. Rajeswaran, S. Maccagnano-Zacher, J. Silcox, G. E. Cragg, A. L. Efros and T. D. Krauss. Nature **459**, 686 (2009).

[19] M. Nirmal, D. J. Norris, M. Kuno, M. G. Bawendi, A. L. Efros and M. Rosen. Physical Review Letters **75**, 3728 (1995).

[20] P. P. Paskov, P. O. Holtz, S. Wongmanerod, B. Monemar, J. M. Garcia, W. V. Schoenfeld and P. M. Petroff. Physica E: Low-dimensional Systems and Nanostructures **6**, 440 (2000).

[21] G. E. Cragg and A. L. Efros. Nano Letters **10**, 313 (2009).

[22] D. D. Sarma, A. Nag, P. K. Santra, A. Kumar, S. Sapra and P. Mahadevan. The Journal of Physical Chemistry Letters **1**, 2149 (2010).

[23] P. Spinicelli, S. Buil, X. Quelin, B. Mahler, B. Dubertret and J. P. Hermier. Physical Review Letters **102**, 136801 (2009).

[24] F. García-Santamaría, Y. Chen, J. Vela, R. D. Schaller, J. A. Hollingsworth and V. I. Klimov. Nano Letters **9**, 3482 (2009).

[25] H. Htoon, A. V. Malko, D. Bussian, J. Vela, Y. Chen, J. A. Hollingsworth and V. I. Klimov. Nano Letters **10**, 2401 (2010).

[26] D. V. Talapin, I. Mekis, S. Gotzinger, A. Kornowski, O. Benson and H. Weller. The Journal of Physical Chemistry B **108**, 18826 (2004).

[27] R. Xie, U. Kolb, J. Li, T. Basche and A. Mews. Journal of the American Chemical Society **127**, 7480 (2005).

[28] D. Schooss, A. Mews, A. Eychmüller and H. Weller. Physical Review B **49**, 17072 (1994).

[29] S. Yang, D. Prendergast and J. B. Neaton. Nano Letters **10**, 3156 (2010).

[30] A. M. Smith, A. M. Mohs and S. Nie. Nature Nanotechnology **4**, 56 (2009).

[31] O. L. Krivanek, M. F. Chisholm, V. Nicolosi, T. J. Pennycook, G. J. Corbin, N. Dellby, M. F. Murfitt, C. S. Own, Z. S. Szilagyi, M. P. Oxley, S. T. Pantelides and S. J. Pennycook. Nature **464**, 571 (2010).

[32] N. D. Browning, M. F. Chisholm and S. J. Pennycook. Nature **366**, 143 (1993).

[33] D. A. Muller, E. J. Kirkland, M. G. Thomas, J. L. Grazul, L. Fitting and M. Weyland. Ultramicroscopy **106**, 1033 (2006).

[34] X. Peng, M. C. Schlamp, A. V. Kadavanich and A. P. Alivisatos. Journal of the American Chemical Society **119**, 7019 (1997).

[35] G. Kalyuzhny and R. W. Murray. Journal of Physical Chemistry B **109**, 7012 (2005).

[36] W. E. Moerner and D. P. Fromm. Review of Scientific Instruments **74**, 3597 (2003).

[37] D. L. Ensign and V. S. Pande. The Journal of Physical Chemistry B **114**, 280 (2009).

[38] D. P. Shepherd, K. J. Whitcomb, K. K. Milligan, P. M. Goodwin, M. P. Gelfand and A. Van Orden. The Journal of Physical Chemistry C **114**, 14831 (2010).

[39] C. A. Leatherdale, W. K. Woo, F. V. Mikulec and M. G. Bawendi. The Journal of Physical Chemistry B **106**, 7619 (2002).

[40] B. Fisher, J. M. Caruge, D. Zehnder and M. Bawendi. Physical Review Letters **94**, 087403 (2005).

[41] D.-H. Lee, C.-T. Yuan, M. Tachiya and J. Tang. Applied Physics Letters **95**, 163101 (2009).

[42] V. I. Klimov, A. A. Mikhailovsky, D. W. McBranch, C. A. Leatherdale and M. G. Bawendi. Science **287**, 1011 (2000).

[43] R. Schuster, M. Barth, A. Gruber and F. Cichos. Chemical Physics Letters **413**, 280 (2005).

5 Synthesis and Optical properties of a CdSe/ZnS/CdSe Dual Quantum System

5.1 Introduction

Through band gap engineering, core shell nanocrystal heterostructures offer the possibility to control the spatial localisation of charge carriers within the particle. As discussed in the previous chapter, Type–I systems, like the CdSe/CdS/ZnS graded seal structures, provide excellent confinement of the exciton into the core, drastically reducing the influence of surface defects on the optical properties of the system.

Another Type–I system is the so–called Quantum Dot Quantum well (QDQW) in which a layer of low–bandgap material shell is deposited onto a core with a higher band gap. In this case, both charge carriers are localised within the shell and exciton confinement in the radial direction becomes pseudo two dimensional. First synthetic attempts of this system were reported almost two decades ago [1, 2] where a monolayer of HgS was formed on a CdS core via surface ion exchange and subsequently overcoated by several layers of CdS. This report inspired several groups to characterise the QDQW system experimentally [3–7] as well as theoretically [8–11]. However due to the underdeveloped synthetic routes for core growth and shelling reactions, the samples were of low quality and did not exhibit the predicted 2D confinement properties. This was overcome by the introduction of the SILAR protocol and synthetic advances [12–14] in NC heterostructure synthesis which enabled Battaglia et al. [15] to build a highly epitaxial CdS/CdSe/CdS QDQW with monolayer (ML) control over the different shells.

When combining the QDQW with a traditional Type–I system in one core/shell heterostructure, a so-called Dual Quantum System (DQS) [16] is formed, in which a core and outer well region of a low–bandgap material are spatially and electronically separated by a high–bandgap material barrier, as illustrated in Figure 5.1. Since this system hosts two potential regions for radiative exciton recombination, the corresponding PL spectrum should exhibit two emission peaks *if* the recombination centres are sufficiently separated. Apart from potential applications of those dual–emitting particles in optical devices [17–19], the spatial and electronic configuration of the two confinement regions in a single nanocrystal structure comprises a unique system to study quantum coupling and charge carrier localisation in complex NC heterostructures.

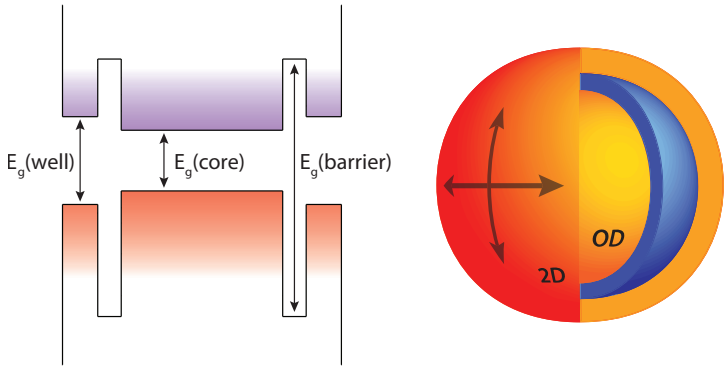

Figure 5.1 Left: Bandstructure schematic for a Dual Quantum System. Excitons can form either in the core or the well region. Right: 3D model of the DQS illustrating the quasi–2D confinement in the outer well and 0D core confinement.

The aim of the work presented in this chapter was to investigate the requirements for a DQS system of the type core/barrier/well to exhibit two well–resolved spectral peaks in the steady state PL spectrum. These two peaks originate from radiative recombination in two separate regions of the DQS, namely the core wherein the confinement is in all three directions (0D exciton) and the outer well region where the carrier confinement (both electron and hole) occurs only in two directions (2D exciton). First, we theoretically examine the electronic states of core/barrier/well NCs within the EMA, and establish the structural requirements to successfully demonstrate a dual–emitting DQS. This is followed by the experimental details pertaining to the successful synthesis of such a nano-crystalline system. Finally, the results from optical and structural characterisation of the core/barrier/well system are discussed and compared to the theoretically predicted trends.

5.2 Finite Potential Well Model for a Dual Quantum System

To describe the DQS system theoretically, the model presented in Chapter 4 was adapted. While the boundary conditions are identical, the material parameters were adjusted to describe the CdSe/ZnS/CdSe heterostructure (see Table 5.1). The utilised geometry to describe the DQS model consists of four regions and three interfaces, as schematically shown in Figure 5.2. To find bounded solutions, the structure is isolated by an infinitely thick ZnS barrier following the model by Nizamoglu et al. [20].

The shortcomings of the effective–mass approximation have been mentioned previously [23]. First–principle calculations on QDQW systems [24] employing the charge patching method [25], have shown that the EMA overestimates the charge carrier localisation in few monolayer wells. This arises, among other factors, most likely form the neglect of geometric distortions

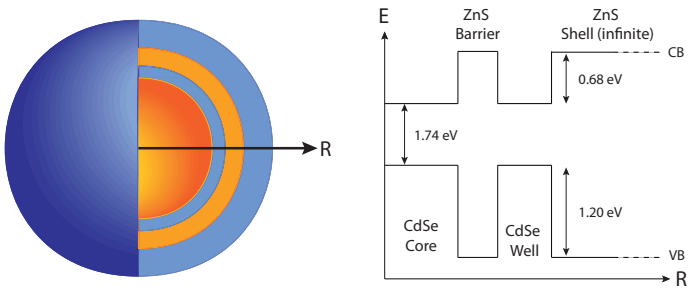

Figure 5.2 Schematic of a CdSe/ZnS/CdSe/ZnS heterostructure NC along with the corresponding radial energy diagram (not to scale). The orange and blue regions represent CdSe and ZnS respectively.

	Band gap E_g $[eV]$	Electron effective mass m_e^*	Hole effective mass m_h^*	CB Offset with CdSe $[eV]$	VB Offset with CdSe $[eV]$	Monolayer thickness $[nm]$
CdSe	1.74	0.13	0.45	0.00	0.00	0.351
ZnS	3.62	0.20	0.80	0.68	1.20	0.312

Table 5.1 Bulk parameters employed in the modelling of CdSe/ZnS/CdSe DQS heterostructures. [21, 22]

(i.e. lattice strain) that occur at the interface of two adjacent materials. This strain leads to a reduction of the band offsets and therefore to a decreased confinement potential [26, 27]. Considering a few monolayer region that is in addition curved around a spherical particle, this strain contribution can have a significant effect on the well potential. Therefore, the calculations presented do not attempt to reproduce accurate exciton energies. Nevertheless the model is useful to study the general trends of spatial charge carrier localisation within DQS systems.

5.3 Analysis of the Electronic Structure in a DQS

The adjustable structural features in the Dual Quantum System are core size, barrier width and well thickness. To investigate how those parameters affect the optical properties, the following parameter space was explored: CdSe core diameters of 3, 4, 5, 6 and 6.9 nm; ZnS barrier widths from 2 to 5 monolayers (0.312 – 1.56 nm); CdSe wells thicknesses from 1 to 4 monolayers (0.351 – 1.4 nm).

Independent studies [20, 28] have assigned the core and shell PL peaks to radiative recombination of $1S_e - 1S_h$ and $2S_e - 2S_h$ excitons respectively. The assignment of the shell emission to the $2S$ exciton was based on $k \bullet p$ calculations [28] which predict this state to

be the energetically lowest, located in the well region. Thus the analysis presented in the following is limited to the solutions of $1S$ and $2S$ excitons. For each of the 80 structural combinations, normalised radial probability densities $r^2\Psi^2(r)$ of electron and hole as well as the wave function overlap have been calculated. For simplicity, the radial probability densities of the first and second excited state will be expressed by $d(1S)$ and $d(2S)$, respectively.

It is important to note, that the assignment of well emission to the $2S$ exciton is only valid if the charge carriers can not relax into the $1S$ state before radiative recombination. This is not the case in traditional NCs where charge carriers excited into higher states are observed to thermalise to the band edge, and emission is only observed from the $1S$ transition. Therefore the proposed model holds only on the assumption, that exciton relaxation from the $2S$ into the $1S$ state is prevented due to their sufficient spatial separation into different regions of the heterostructure. To prove the validity of this assumption is beyond the scope of this study.

5.3.1 The Effect of Barrier Width

As discussed in previous chapter, the hole (1S and 2S) shows a stronger localisation when compared to the electron, arising from its larger effective mass and larger valence band offset between CdSe and ZnS. Confined either to the core or well region, the hole probability density decayed rapidly within the ZnS barrier and tunnelled into the other domain only to a negligible extent regardless of barrier thickness. In contrast, the electron distribution $r^2\Psi_e^2(r)$ is appreciably sensitive to a change in barrier width. Figure 5.3 depicts the evolution of charge carrier localisation as a function of barrier size. Here, the calculations for the $1S$ exciton are presented but identical behaviour was observed for the $2S$ case.

An increase in barrier width results generally in stronger localisation and promotes the spatial confinement towards the 'favoured' region. Depending on the configuration of the DQS at hand, this can lead either to an increase or decrease in wave function overlap (see insets). On the left hand side, the evolution of charge carrier localisation for a heterostructure with a 2 nm core radius and 4 ML outer well is presented. $r^2\Psi_e^2(r)$ extends over the core and well range but predominantly remains in the well region. With increasing well thickness this tendency becomes more pronounced, effectively separating the electron from the hole and resulting in a pseudo Type–II situation. On the right hand side, a system with same core size but a slightly thinner well (3 ML) is depicted. In this case, the electron confinement is biased towards the core region and likewise an increase in barrier width facilitates this trend, enhancing the exciton overlap. These two examples not only demonstrate the effect of barrier width as a kind of 'amplifier' for charge localisation but also highlight the sensitivity towards the outer well thickness.

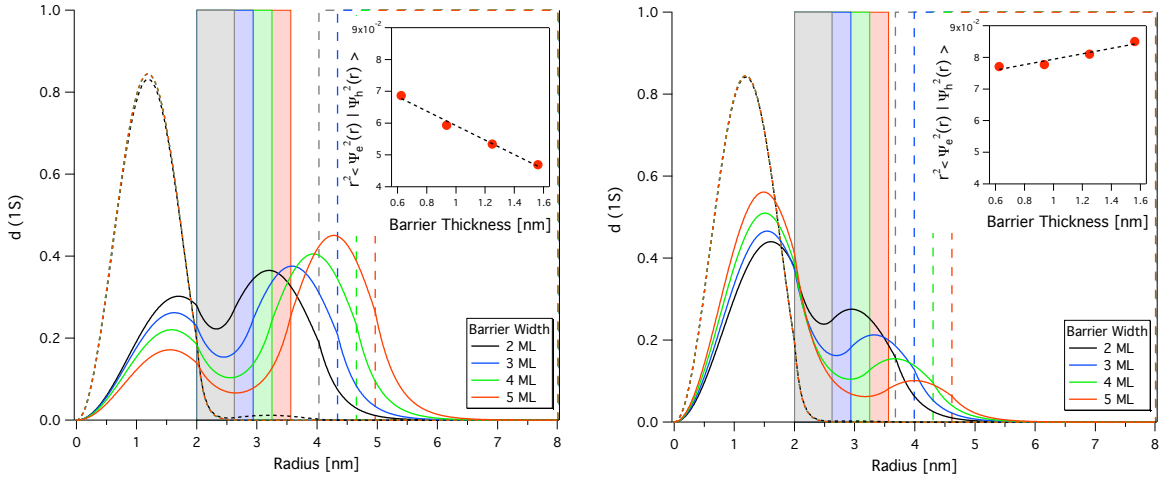

Figure 5.3 Calculated radial probability densities for the $1S$ electron (solid lines) and hole (dashed lines) as a function of barrier thickness. The filled and dashed rectangles mark the onsets of the ZnS barrier and outer infinite ZnS shell respectively. Left: DQS with a CdSe core of 2 nm radius and a 1.4 nm CdSe outer well (4 ML). Right: DQS with same core size and a 1.05 nm outer well (3 ML). The insets depict the electron and hole wave function overlap as a function of barrier thickness.

5.3.2 The Effect of Core Size and Well Thickness

The influence of the CdSe well is somewhat more intricate as it is correlated to the core size. Furthermore it has an unexpected significant effect on the $1S$ exciton for smaller cores. Figure 5.4 compares the $1S$ charge carrier distribution as a function of well thickness for structures with core radii of 2 nm (A) and 3 nm (B). In both cases the hole (dashed line) is well confined in the core domain and unaffected by the outer well. In contrast, the spatial distribution of the electron (solid line) of the small core structure extends significantly into the shell region with increasing well thickness which leads to a drastic decrease in wave function overlap (inset). The same effect is observable for the heterostructure with a larger core, however only to a minor extend, as $r^2\Psi_e^2(r)$ decays sufficiently within the ZnS barrier due to the reduced confinement in larger cores. As mentioned previously a thicker barrier would counteract this trend as long as the spatial probability is dominant in the core region. Otherwise it would even further promote the charge carrier separation.

The decreasing exciton overlap upon CdSe well growth was also experimentally observed as shown in Figure 5.4 (C) and (D). Both plots show photoluminescence spectra of DQS particles in solution at the stages before and after CdSe well layering. The structures of (C) and (D) are based on cores with a $\sim$ 2 nm and $\sim$ 2.9 nm radius respectively closely resembling the theoretical model. For the structure with the smaller core a substantial PL loss is observed upon growth of one CdSe monolayer. This decrease progresses further with deposition of a

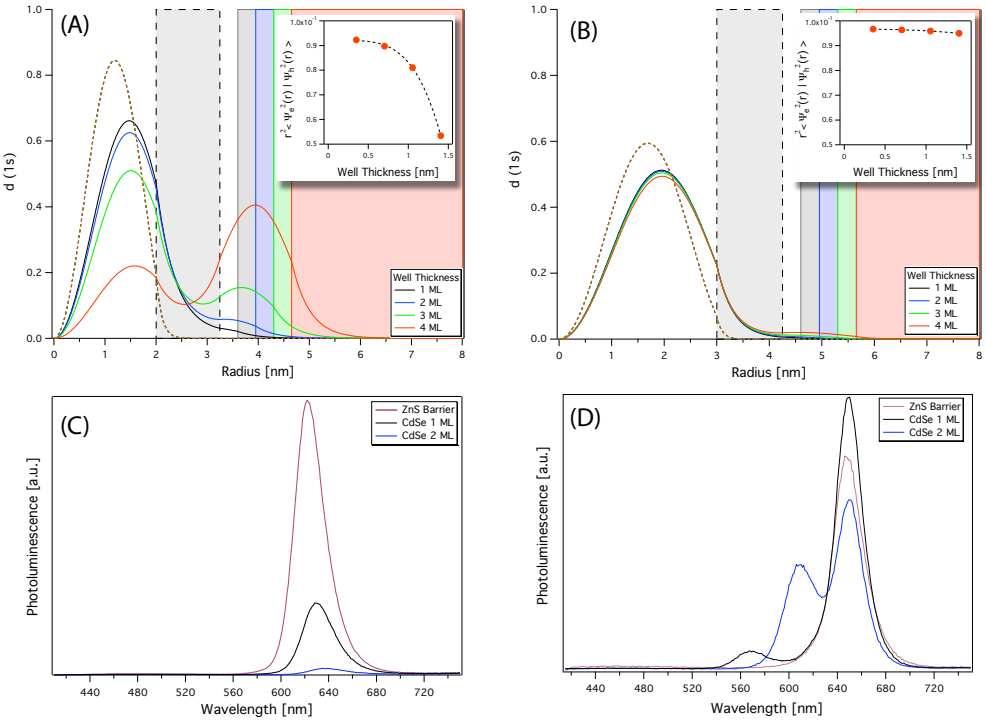

Figure 5.4 Top: Calculated radial probability densities for the $1S$ electron (solid lines) and hole (dashed lines) as a function of CdSe well thickness. The modelled structures are based on cores with a 2 nm (A) and 3 nm (B) radius along with a 1.25 nm ZnS barrier (4 ML). Bottom: Photoluminescence spectra of CdSe/ZnS/CdSe DQS particles in solution before and after growth of the outer CdSe well. The heterostructures were grown from cores with $\sim$ 2 nm (C) and $\sim$ 2.9 nm (D) radii.

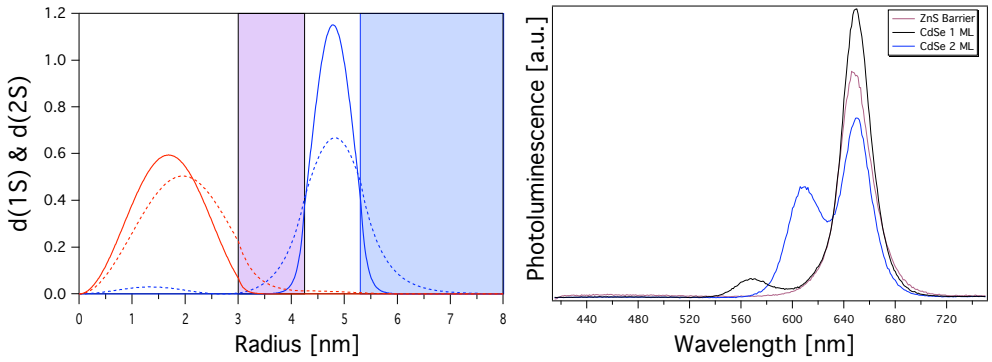

Figure 5.5 Left: Calculated radial probability densities for the $1S$ (red) and $2S$ (blue) exciton based on a core with 3 nm (B) radius and a 1.25 nm ZnS barrier (4 ML). Right: Reproduction of Panel (D) of Figure 5.4 for direct comparison with the theoretical model.

second layer and was attributed to the reduced charge carrier overlap as suggested by the calculations. On the other hand, for the large core structure no PL reduction is detected. In contrast, a significant PL increase along with the emergence of the second emission peak is recorded following the growth of the first CdSe layer. The enhancement is in accordance with the observations by Battaglia et al. [16] for large core systems, however the reasons for this effect are not clear at present. A plausible explanation could be a better passivation of a CdSe surface (compared to a ZnS surface) by the ligand system at hand (amines) [29]. After coating with a second CdSe layer the core emission drops then back to slightly under the initial value before well growth. The emergence of the second PL feature is attributed to the appreciable separation of $1S$ and $2S$ excitons as theoretically predicted for these structural parameters (see Figure 5.5).

The effect of well thickness on the $2S$ exciton is illustrated in Figure 5.6. Here structures with core radii ranging from 2 nm to 3.45 nm with a barrier width of 4 ML were examined. For all core sizes and a one monolayer CdSe outer well, the $2S$ hole was found to be localised in the core region. Upon further increase in well thickness, the hole probability density switched then to the well domain. By comparing the four models, a clear trend could be deduced. The transition of the hole localisation from core to outer well occurred with a two monolayer well for the smallest cores, while the DQS models with 2.5 and 3 nm core radii needed a 3 ML outer well. Finally, for the largest studied core size the shift was not observed for CdSe wells smaller than 4 ML. This behaviour was found to be correlated to the relative volume ratio V_{well}/V_{core} between CdSe core and well. The total volume of the core and outer well can be approximated by

$$V_{core} = \frac{4}{3}\pi r_{core}^3 \quad \text{and} \tag{5.1}$$

$$V_{well} = \frac{4}{3}\pi r_{well}^3 - \frac{4}{3}\pi r_{CdSe/ZnS}^3 \tag{5.2}$$

respectively. Thus the volume ratio of well and core can be expressed as:

$$V_{well}/V_{core} = \frac{r_{well}^3 - r_{CdSe/ZnS}^3}{r_{core}^3} \quad . \tag{5.3}$$

Depending on the ratio, the $2S$ hole localised either in the central or outer domain. Empirically it was found that a ratio of around 2-3 marks the threshold to the transition from core to well confinement. If the ratio was below that value the hole was found to be sitting in the core region and vice versa for volume ratios above that threshold.

The $2S$ electron did not show a similarly clear trend, however a distinct dependence on the volume ratio was observed likewise. As noted previously the spatial probability is generally

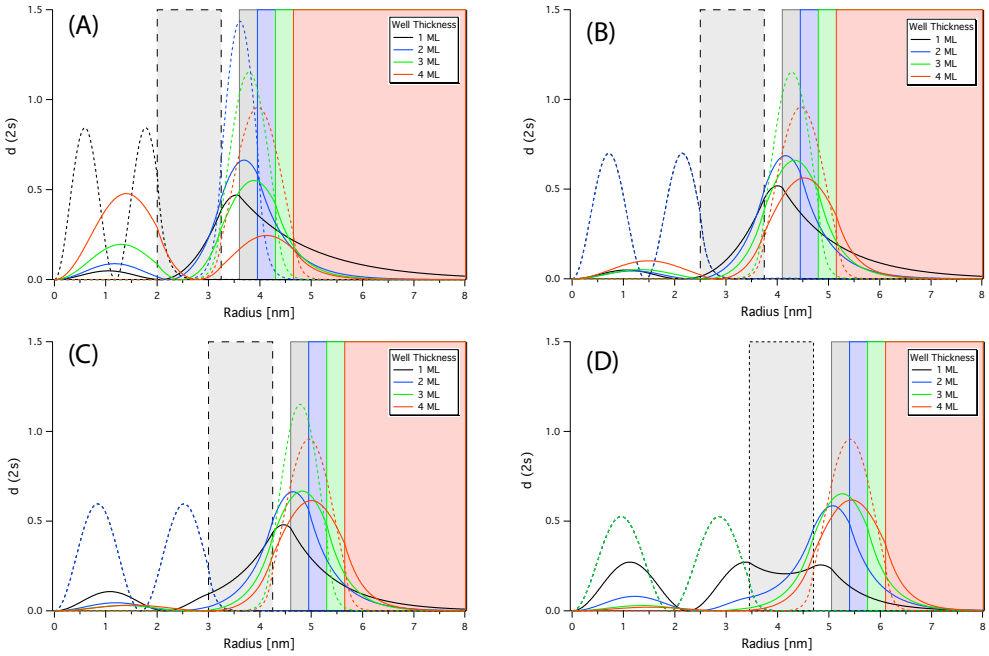

Figure 5.6 Calculated radial probability densities for the $2S$ electron (solid lines) and hole (dashed lines) as a function of CdSe well thickness. DQS models with core radii of 2, 2.5, 3 and 3.45 nm (A–D) along with a 4ML ZnS barrier are depicted.

harder to confine and more delocalised over the entire heterostructure compared to the hole. In most cases, the probability distribution was found to be dominant in the outer well region except for the heterostructures with a 2 nm core radius/4 ML well and a 3.45 nm core radius/1 ML well which hosted the $2S$ electron mainly in the core domain. Overall the electron seemed to have a tendency to be localised in the well section, even for thin wells of just one monolayer. Depending on core size this bias was then either supported (C, D) or diminished (A, B) with increasing well thickness.

So far no results for the modelled DQS with a 1.5 nm core radius have been discussed. This system behaved differently compared to the bigger core models, which was attributed to the extremely large V_{well}/V_{core} ratio. Figure 5.7 shows the $1S$ (left) and $2S$ (right) probability distributions for this core size with a barrier width of 4 ML as a function of well thickness. The volume ratio was calculated to range from 3.3 up to ∼18 dependent on the number of CdSe well monolayers. Due to this large ratio the localisation trends for the $1S$ and $2S$ charge carriers reversed to a certain degree. The $1S$ hole was initially confined in the core region as expected but shifted into the well section for CdSe wells past 3 ML. This trend was observed likewise for the $1S$ electron which transitioned gradually from predominantly residing in the core domain to the outer well with increasing well thickness. The plot on the right side demonstrates the analogue behaviour for the $2S$ exciton but with a transition from the

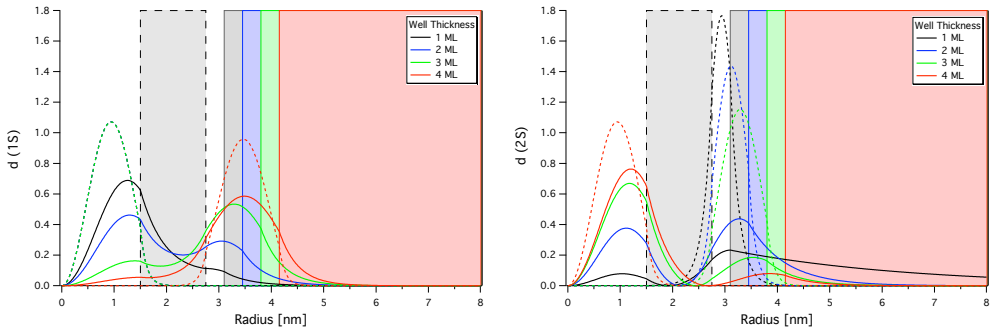

Figure 5.7 Calculated radial probability densities for the $1S$ (left) and $2S$ (right) excitons for the small core (1.5 nm radius) model with a 4ML ZnS barrier. The plots display the trends with increasing CdSe well thickness.

well region towards the core. These reversed trends can be explained by the reversed extent of local confinement in core and outer well. For all configurations discussed previously the core presumably provided a weaker confinement environment compared to the few monolayer well domain. In contrast, considering a DQS with a small core of just 1.5 nm radius and a CdSe well of 4 ML thickness (1.4 nm) the large well/core volume ratio of ∼18 reverses this confinement situation, making the well the weaker confinement domain.

5.3.3 Conclusion

Bearing in mind that for practical applications of the DQS system dual emission must be observable, the effects and trends presented above suggest that there is just a narrow margin of parameter space that has to be well balanced in order to provide for the emergence of the second PL feature. Dual emission is assigned to the separate recombination of $1S$ and $2S$ excitons within the core and outer well region respectively. Considering the $1S$ exciton, a larger core combined with a thick ZnS barrier and thin outer CdSe well is favourable since it facilitates the efficient electron confinement into the core and maximises e–h wave function overlap. However, as demonstrated in Figure 5.6, heterostructures with larger cores require a thicker outer CdSe well to efficiently localise the $2S$ charge carriers in this domain, which in turn can diminish the $1S$ e–h wave function overlap, as shown in Figure 5.4. Even if this effect is insignificant for systems with large cores, the energy change of the well emission with increasing well thickness must be considered. As noted previously, the EMA model employed in this work is not accurate enough to calculate accurate transition energies. However experimental studies have shown [16] that a red shift towards smaller energies is observed with increasing well thickness, which was assigned to the decreasing confinement in this domain. Thus, an increasingly thick outer well would lead to the 'fusion' of the two emission features annihilating the dual color effect.

To sum up, the separate tunability of core and well emission wavelength, as desirable for practical applications, appears to be not just an issue of adjusting their respective dimensions and separating them with a sufficiently thick barrier. Rather a sensitive balance between the two confinement regions must be established which dictates the attainable emission energy combinations. Moreover, synthetic aspects like lattice strain and particle surface energy further reduce the range of feasible, epitaxially grown DQS particles. After having established the theoretical requirements for a dual–emitting core/barrier/well system, the focus of the following section is now turned towards the synthetic implications and realisation of such a heterostructure.

5.4 Preparation of DQS core/shell Nanocrystals

For the successful synthesis of a colloidal Dual Quantum System several hurdles had to be overcome. To prepare a high quality core/shell heterostructure, epitaxial growth between two materials and good control over growth kinetics is essential. As discussed in the previous chapter, lattice strain can have a significant impact on the optical properties of NCs. Thus, to prevent crystal defects at the interface and minimise lattice distortions, a DQS based on a CdSe/CdS/CdSe material combination would be sensible. However, due to the small conduction band offset between the two materials, the electron can easily extend through the CdS region resulting in a significant red shift [30]. As suggested by the calculations presented in the previous section, a large barrier potential is vital to facilitate exciton localisation within the core and well region. Therefore ZnS with its wide band gap offset relative to CdSe was chosen as the barrier material. However, the large lattice mismatch (∼13 %) between ZnS and CdSe makes the epitaxial and controllable growth of a ZnS barrier with substantial thickness quite difficult.

The second major aspect to be considered is the size dependence of surface energy. As the NCs grow the curvature decreases steadily which reduces the overall reactivity at the surface. Therefore it becomes increasingly difficult to maintain sufficient shell growth for large particles. However, to allow for the study of the $1S$ and $2S$ exciton recombination dynamics by means of optical analysis, the core and well emission energies have to be sufficiently separated in order to avoid crosstalk [31]. As the control over the well emission energy is very limited and not well understood yet, the separation must be achieved through the utilisation of big CdSe cores (4.7–6.7 nm diameter) to shift the core emission energy into the red part of the spectrum. Furthermore the usage of large cores facilitates the efficient confinement of the $1S$ exciton according to the previous EMA calculations. To overcome these synthetic challenges, the choice of reaction conditions like ligand chemistry and growth temperature were found to be crucial in order to achieve adequate precursor and particle surface reactivity.

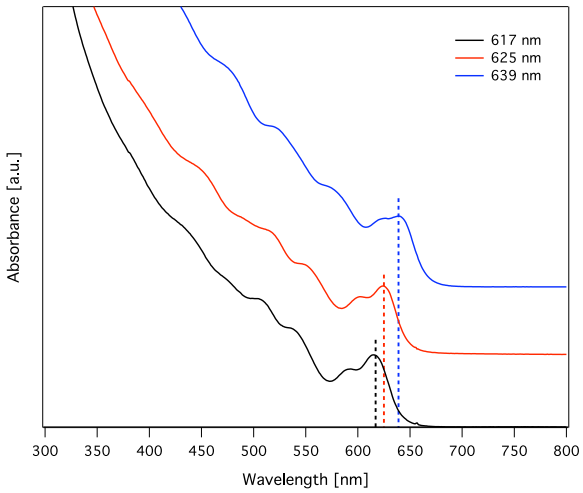

Figure 5.8 Absorption spectra of CdSe cores prepared using the protocols outlined in Chapter 2. The core samples utilised for the DQS synthesis exhibit a band edge absorbance of 617 nm (black), 625 nm (red) and 539 nm (blue).

5.4.1 Experimental Details

The metal shelling precursors (0.1 M) were prepared by dissolving CdO or zinc acetate dihydrate in oleic acid (1:10 molar ratio) and ODE. Each solution was degassed at room temperature for up to one hour. After increasing the temperature to 80 $°C$, three pump–purge cycles were performed. Subsequently the precursors were flooded with nitrogen and further heated to 240 $°C$ until the the solutions turned optically clear. Upon cooling to 80 $°C$ the solutions were once again degassed for 10 min to remove residual water released during the complexation process. The selenium precursor (0.1 M) was made by dissolving pure Se powder in tributylphosphine (TBP) (1:16 molar ratio) and ODE. Selenium was successfully complexed after through stirring and ultra sonication for 10 min without the need of heating. Subsequently the solution was degassed for 15 min and kept under nitrogen atmosphere for further use. The sulphur precursor (0.1 M) was prepared by adding pure suffer in ODE and then treating the solution analogue to the metal precursors, except the dissolution temperature was set to 130 $°C$ for 60 min. While the chalcogenide precursors were long–term stable ($\sim$1 month) and remained liquid at room temperature, the metal oleate solutions (especially Zn–oleate) had to be kept at elevated temperatures (80$°C$) to prevent solidification. Moreover the metal precursors needed to be used within two weeks, as longer ageing resulted in considerable variations in reactivity.

CdSe core nanocrystals of various sizes were synthesised following the protocols outlined in Chapter 2. Very large cores with the band edge absorption peak at 625 nm (5.8 nm diameter) and 639 nm (6.6 nm diameter) were prepared following the method for NCs with a band

Layer	Cd–rich	S1	Zn1	S2	Zn2	S3	Zn3	S4	Zn4	S5	Zn5
Growth Temp. [$^{\circ}C$]	225	230	235	240	240	240	240	240	240	245	245

Table 5.2 Reaction temperatures utilised for the growth of ZnS monolayers.

edge absorption at 617 nm. The growth time was then extended to 120 min at which point the optical density of the reaction solution was measured to determine the actual particle concentration. Utilising the SILAR approach [14, 32], as outlined in Chapter 3, the quantities of cadmium and selenium precursors were calculated to enlarge the particles in one–monolayer steps to the desired diameter. As precursor sources 0.1 M solutions of Cd–TMPPA [30] and ODE–Se [33] were employed. The growth temperature was raised to 240 $^{\circ}C$ and Cd and Se were allowed to react for up to 40 min while monitoring the particle growth via absorption spectroscopy (Figure 5.8). After cooling the reaction solution to room temperature the CdSe cores were washed and stored as described previously.

The ZnS barrier was grown following modified protocols reported by Battaglia et al. [16] and van Embden et al. [34]. In a typical synthesis, washed CdSe quantum dots were dispersed in a mixture of ODE and oleylamine with a mass ratio of 1:1 to give a final particle concentration of 4 μM. In contrast to the original protocol by Battaglia et al. [16], ODA was substituted with oleylamine (OM) as it exhibits similar reactivity but is liquid at room temperature which facilitated the post–synthetic washing and dispersibility of the final nanocrystals. The solution was thoroughly degassed at room temperature before being heated to 100 $^{\circ}C$. At this point up to three pump–purge cycles were performed followed by further heating under nitrogen to the desired reaction temperature, as outlined in Table 5.2. Bearing in mind the large lattice mismatch between CdSe and ZnS, and that the DQS at hand is based on quite large cores – both circumstances that oppose shell growth – reaction temperatures $\geq$ 240 $^{\circ}C$ were found to be necessary in order to achieve appreciable ZnS shell deposition.

Similar to the shelling reactions described previously, an initial metal layer was deposited to create a metal rich surface. To prevent homogeneous nucleation of the shelling material, 0.4 x $n(S)_{final}$ of tributylphosphite were added to the reaction mixture following the growth of the initial cadmium enriching layer. Subsequent shells were grown by alternating injections of chalcogenide and metal precursor solutions with individual reaction times of 15 min per layer. Analogous to the preparation of Type–I core/shell structures, a 30 % excess of metal precursor was introduced with each metal layer to ensure complete shell formation. Furthermore it was found that the addition of OM in a 1:1 molar ratio relative to the introduced oleic acid with each metal precursor injection promoted the ZnS shell formation. Following the growth of the final zinc layer, the nanocrystals were annealed at 210 $^{\circ}C$ for one hour to ensure complete shell growth and minimisation of crystal defects before the outer well system was added.

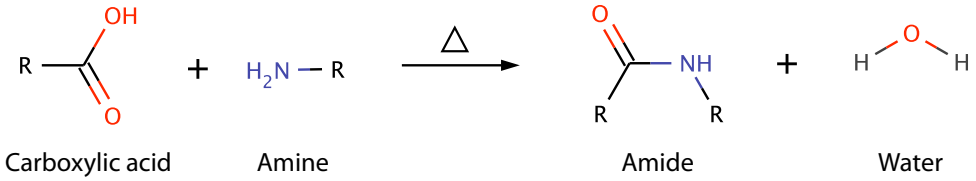

Figure 5.9 Reaction scheme of amide formation via condensation of a carboxylic acid and an amine.

For the preparation of the outer well, alternating monolayers of cadmium and selenium were grown analogue to the ZnS layers. A lower reaction temperature of 210–220 $°C$ was chosen, due to the higher reactivity of CdSe precursors relative to the ZnS precursors. After the final layer was added, the reaction was allowed to cool to 80 $°C$ at which point the particles were purified following the methods outlined in Chapter 2.

5.4.2 Amine Concentration

A high initial amine concentration was found to be mandatory to sufficiently activate the zinc oleate precursor and thus, facilitating the ZnS barrier growth [16, 35]. Furthermore it was found that the addition of OM in a 1:1 molar ratio relative to the introduced oleic acid with each metal precursor injection promoted the ZnS shell growth. It is known that carboxylic acids undergo condensation reactions under anhydrous conditions and high temperatures [36] which can lead to amide formation in the presence of free amines (see Figure 5.9). As this would lead to a reduction of free amine in the reaction solution (decreasing the zinc precursor reactivity) the addition of oleylamine aims to account for this, keeping the free amine concentration constant.

5.4.3 Homogeneous Nucleation

Another issue was the appearance of homogeneous nuclei (HN) during ZnS shell deposition which manifested itself by the emergence of a PL feature at ∼430 nm. This was confirmed through TEM analysis, as shown in Figure 5.10. Previously discussed in Chapter 3, HN generally occurs during shelling reactions when the growth rate is too low and free precursor accumulates in the reaction solution rising the supersaturation above the threshold to HN. Thus TBPh was supplemented to control the sulphur precursor supersaturation, as described for Type–I heterostructures. A supplementation of TBPh with a 0.4:1 mole ratio to sulphur was found to successfully suppress HN while allowing for good shell growth, while higher ratios resulted in insufficient ZnS deposition.

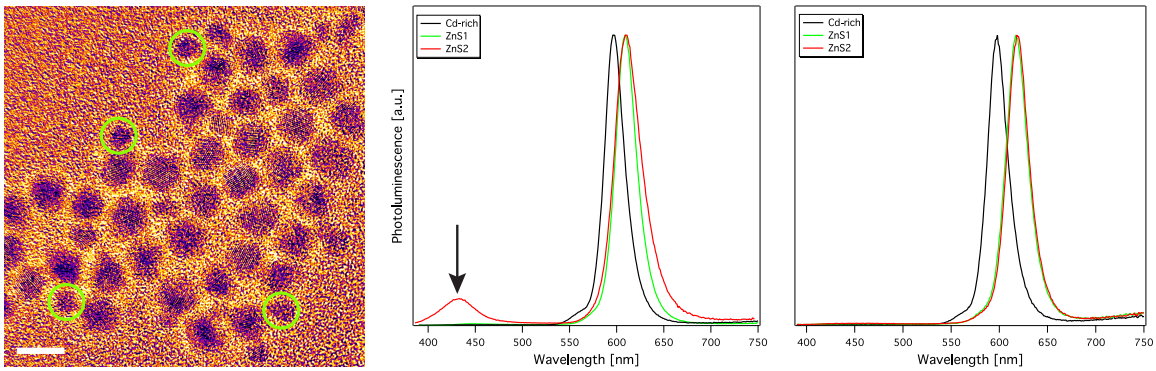

Figure 5.10 TEM image and PL spectra of CdSe/ZnS core/shell particles exhibiting homogeneous nucleation (HN) during ZnS Barrier growth. The green circles in the TEM image (left) mark ZnS nuclei (scale bar = 10 nm) which result in the emergence of a PL feature around 430 nm (centre). Addition of TBPh was found to successfully suppress HN (right).

5.4.4 The Selenium Precursor

Considering the deposition of the CdSe outer well, it appeared from numerous trials that only the use of Se–TBP as selenium source led to successful well growth and the emergence of the second emission feature under the present reaction conditions. Other attempts employing Se–TOP and Se–ODE [33] did not result in appreciable shell deposition and no well emission could be detected. This selectivity can be ascribed to the superior reactivity of Se–TBP compared to the other two precursors which is necessary to overcome the adverse effects of lattice strain and low particle surface reactivity.

5.4.5 The Effect of Metal Complexing Ligand

To investigate the suitability of phosphonic acid ligands for the DQS synthesis, the previously employed TMPPA metal precursors were tested. Utilising this ligand system superior control over shell growth and improved uniformity compared to pure oleic acid was reported for the deposition of thick CdS shells [30, 34, 37]. For direct comparison of the effects of OA and TMPPA on the DQS preparation all reaction conditions were kept identical except the metal oleate precursors were substituted by Cd–TMPPA and Zn–TMPPA (1:4 molar ratio) which were prepared as outlined in Chapter 3. Figure 5.11 displays the photoluminescence evolution during ZnS barrier growth for both ligand systems. Comparing the graphs (A) and (B), a substantial difference in PL intensity development between the two ligand systems is observable. As directly compared in plot (C), starting from the cadmium rich sample, the PL of the OA reaction drops significantly with ZnS1 deposition and recovers gradually

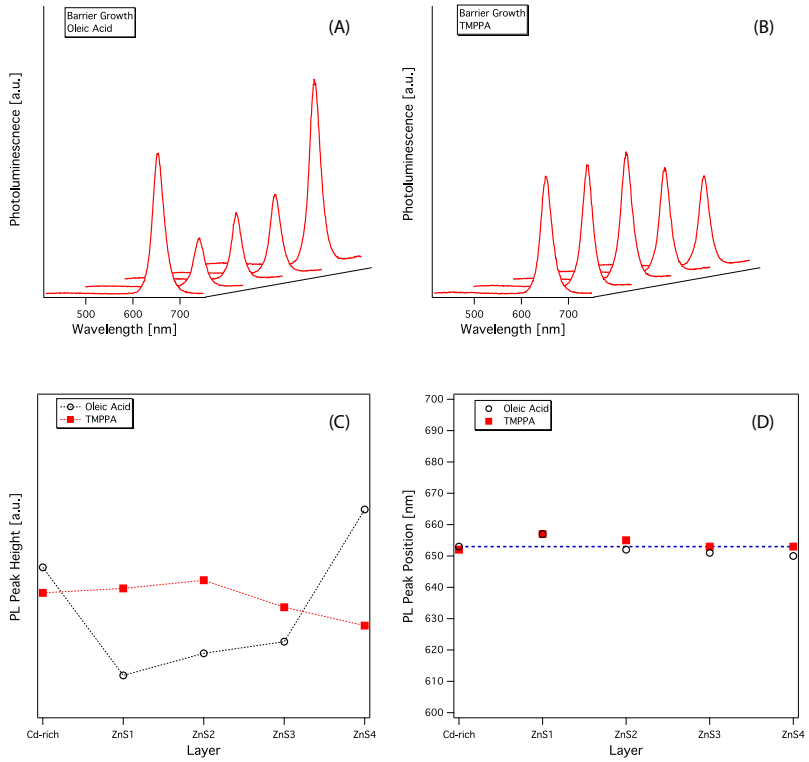

Figure 5.11 PL spectra of CdSe/ZnS core/shell particles. The waterfall plots illustrate the PL evolution during ZnS barrier growth utilising oleate (A) and TMPPA (B) metal precursors. The traces from front to back correspond to the layers of cadmium rich followed by ZnS 1–4 respectively. All spectra were normalised to their absorbance at the excitation wavelength (400 nm). The bottom graphs summarise the trends for PL intensity (C) and energy (D) development.

before experiencing a substantial gain after growth of the fourth ZnS monolayer. In contrast, the PL of the TMPPA system increases slightly up to the growth of two ZnS monolayers before continuously decreasing with the third and fourth ZnS shell deposition. Considering the spectral shifts during shell growth, both reactions show only minor shifts relative to the original CdSe core emission energy (653 nm), as depicted in graph (D), suggesting sufficient confinement.

The mechanisms for the different PL intensity developments is currently not clear. Considering the difference in surface passivation of the particles, one would expect a consistently higher surface coverage in the OA system based on the smaller steric hindrance of this ligand. However, this should lead to a higher PL intensity for all shells grown with the oleate precursors relative to their TMPPA counterparts, which is not observed. In contrast up to ZnS3 the TMPPA synthesised particles exhibit a higher PL intensity relative to the OA reaction. Therefore the two trends must be related to differences in shell growth. A possible scenario

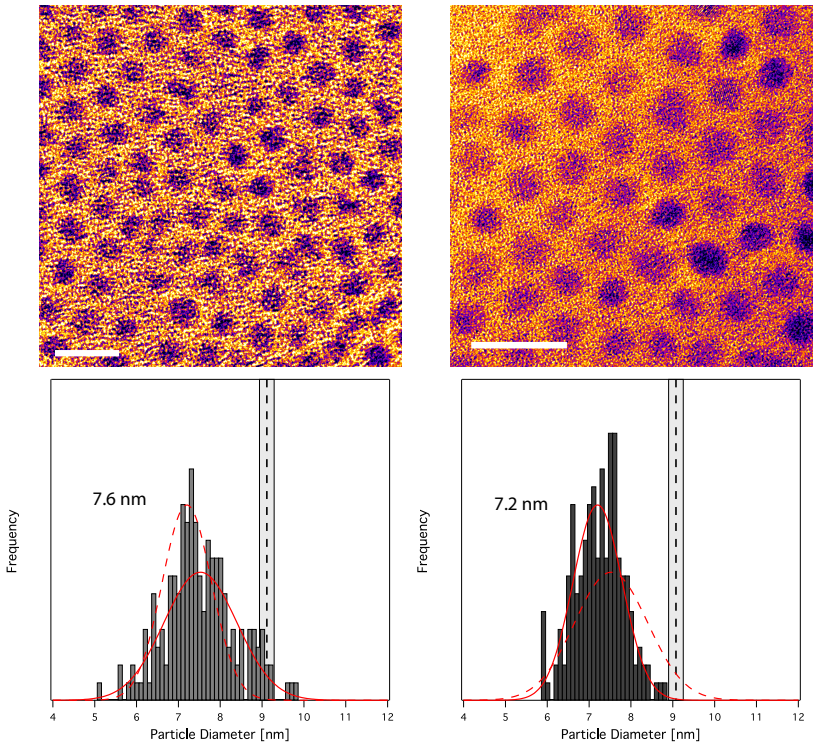

Figure 5.12 HRTEM images of CdSe/ZnS heterostructures grown with oleate (left) and TMPPA (right) metal precursors. (Scale bars = 20 *nm*). The corresponding histograms of measured particle sizes were fitted to Gaussian distributions (red lines) to recover mean size and standard deviation. For direct comparison, the respective fitted distribution of the other ligand system (dashed red line) was added to the plots. The dashed black lines and grey boxes indicate the theoretically predicted particle size along with its error.

could be the following: As Zn-oleate possesses a higher reactivity than TMPPA, ZnS may grow faster but less controlled for the early layers. This would lead to a higher number of crystal defects at the core/shell interface and in the shell, resulting in an increased number of non–radiative recombination centres effectively decreasing the observed PL intensity. As the reaction progresses, the particle surface reactivity diminishes leading to slower growth. This combined with continuous annealing at elevated temperatures would reduce the number of crystal defects and eventually resulting in the observed PL increase with the final ZnS layer. In the case of TMPPA ligands, slower but epitaxial growth would lead to a continuous increase in PL from the first ZnS shell. However due to the lower precursor reactivity and stronger surface passivation the shell growth may eventually stop under the present reaction conditions leading to a thinner overall barrier.

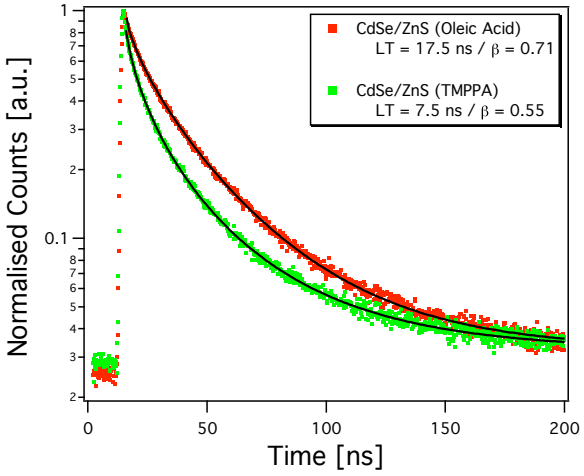

Figure 5.13 Fluorescence lifetime decay curves of CdSe/ZnS core/shell NCs with a 4 ML ZnS shell taken from the OA and TMPPA samples after annealing of the final ZnS layer. The β and τ values (inset) were obtained from stretched exponential fits to those traces.

Figure 5.12 depicts TEM images and corresponding PSD histograms for both systems. By comparing the histograms it was observable that the final CdSe/ZnS heterostructures grown with Zn-oleate indeed exhibit a slightly larger mean diameter. However, at the expense of a distinct broadening in size distribution compared to the TMPPA sample. Both reactions did not reach the expected theoretical particle size, which highlights the challenges of thick barrier growth under the conditions of large lattice mismatch and reduced surface reactivity of large core NCs. Nevertheless, the spherical morphology of the initial CdSe cores was retained to a great extent, supporting isotropic shell growth.

Figure 5.13 compares the the fluorescence lifetime of the OA and TMPPA samples after the final ZnS layer deposition and annealing. Fitting the decay curves to a stretched exponential function yields a significantly longer lifetime for the OA sample of 17.5 ns compared to 7.5 ns in the TMPPA case, while the β values indicate an increased number of (non–radiative) recombination pathways (β=0.55) for the TMPPA synthesised NCs compare to the OA system (β=0.71). As both reactions are extensively annealed at the point of measurement, the longer lifetime and higher β value of the particles prepared with OA was attributed to the reduced number of available trap states based on the slightly thicker ZnS barrier and superior surface passivation of OA ligands. A higher number of available fast non–radiative decay channels, present in the TMPPA synthesised NCs (indicated by the lower β value), naturally explains then the observed shortening in fluorescence lifetime.

Finally after growing the outer CdSe well for both reactions, PL spectroscopy revealed another issue related to the stronger binding TMPPA ligand. Figure 5.14 shows the emission

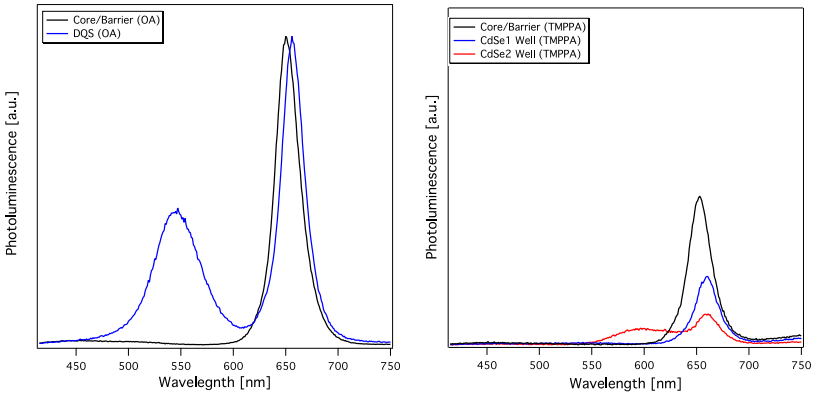

Figure 5.14 Photoluminescence spectra taken before and after CdSe well deposition for the OA (left) and TMPPA (right) reaction.

spectra taken after the growth of the outer CdSe well for both reactions. The oleate experiment exhibits the predicted second PL feature upon well growth and only minor changes of the core emission peak. In contrast, the already lower emission band of the TMPPA reaction becomes further reduced upon CdSe deposition and only a very broad, low intensity, shoulder appears on the blue side of the core emission peak after growth of the second CdSe layer. The deterioration of the core emission band and lack of a defined well peak indicates insufficient and non–epitaxial deposition of CdSe on the TMPPA passivated core/barrier particles. This is likely caused by the strong bond between TMPPA and the surface zinc sites, effectively preventing ligand displacement and further shell growth. Thus the optical and structural characterisation presented in the following section is exclusively based on DQS particles prepared with the OA ligand system.

5.5 Optical and Structural Characterisation

5.5.1 Electron Microscopy

To verify the successful synthesis of DQS particles, samples from certain stages of the reaction were subject to structural analysis via TEM. Figure 5.15 shows representative HRTEM images and the corresponding histograms obtained from the the utilised core CdSe nanocrystals (left), the CdSe/ZnS core/barrier heterostructure (middle) and the final Dual Quantum System NCs (right). The histograms and PSD were obtained following the methods outlined in Chapter 2. For direct comparison, the theoretically predicted mean size (dashed line) of the NCs with its associated error (grey shaded box) is plotted alongside its corresponding histogram.

As observed previously, the HRTEM images reveal that the particles are overall of spherical morphology which is maintained throughout the reaction. Furthermore the high resolution

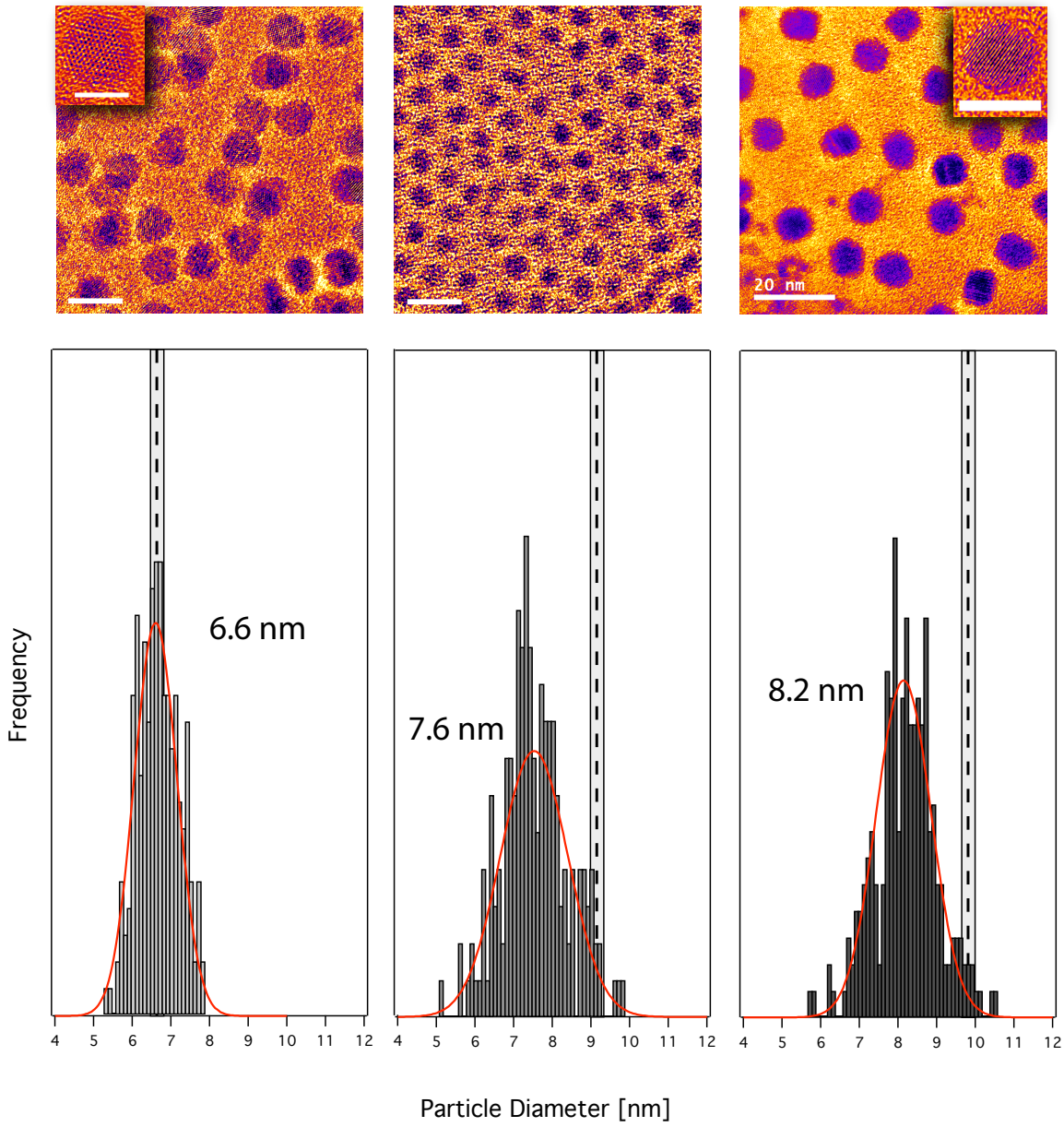

Figure 5.15 Bright field TEM images at different stages of the DQS synthesis (top) and corresponding histograms of the measured particle sizes (bottom). Samples from the initial CdSe cores (left), after the ZnS barrier growth (center) and final DQS (right) were analysed. The dashed lines indicate the expected size of the nanocrystals, with the grey box outlining the associated error of $\pm 0.175\ nm$ (one c–lattice plane of CdSe). Gaussian distributions were fitted to the histograms to obtain the mean diameter (stated) and PSD. Scale bars: Cores (10 nm) and Inset (5 nm); Core/Barrier (20 nm); DQS (20 nm) and Inset (10 nm).

images of individual core and DQS crystals (insets) demonstrate the high degree of crystallinity preserved during epitaxial shell growth. Upon inspection of the histograms, it can be seen that the PSD broadens slightly with addition of the ZnS barrier but narrows again with the subsequent well shelling. The PSD of the barrier particles have a FWHM typically 0.7 nm greater than the original cores, whereas the final DQS samples exhibit a FWHM broadening of just 0.4 nm. Those broadening effects are common during NC shelling and can be attributed to variations in reactivity between individual particles. By comparing the peaks of the Gaussian distributions (mean particle size) to their corresponding predicted sizes, it can be observed that the CdSe core values are in excellent agreement. In contrast, examination of the CdSe/ZnS values shows that the ZnS barrier increased the average diameter by just $\sim$1 nm compared to the predicted 2.5 nm (4 ML) gain, which reflects the difficulties of thick ZnS barrier growth directly onto the CdSe cores. Consequently the mean diameter of the final DQS particles is smaller than the predicted final size, too. However the relative size increase of $\sim$0.6 nm (1 ML) after the CdSe outer well growth is in good agreement with the predicted gain of 0.702 nm which is attributed to the greater precursor reactivity of Cd–oleate and Se–TBP compared to Zn–oleate and S–ODE.

5.5.2 Absorbance and Fluorescence Studies

Figure 5.16 displays the spectroscopic properties of the Dual Quantum System and highlights the importance of the right size parameters in order to observe dual emission. The spectra and theoretical calculations compare two DQS samples with a 2 nm CdSe core radius / 3 ML ZnS barrier (left column) and a 3.2 nm core radius / 4 ML barrier (right column). The absorbance and emission spectra show the traces of the initial cores, after growth of the ZnS barrier and the final DQS with the outer CdSe well deposited.

The band edge absorption of the small core sample shows a distinct red shift of $\sim$10 nm upon ZnS shell growth, whereas the large core sample shifts only to a minor extent owing to the weaker confinement in those cores. The difference on those shifts can be explained by the EMA calculations. In the small core case, the $1S$ electron (red solid trace) possesses a significant probability to deeply penetrate the ZnS shell which leads to a weakened exciton confinement and therefore to the observed red shift. In contrast, the model for the large core sample shows a sufficiently fast decline of the $1S$ electron density after entering the ZnS barrier domain, effectively confining the exciton into the core region. For both samples an absorbance increase at higher energies relative to the band edge absorption is observed following the growth of the ZnS barrier. This may be attributed to the enlarged absorption cross–section of the resultant heterostructure.

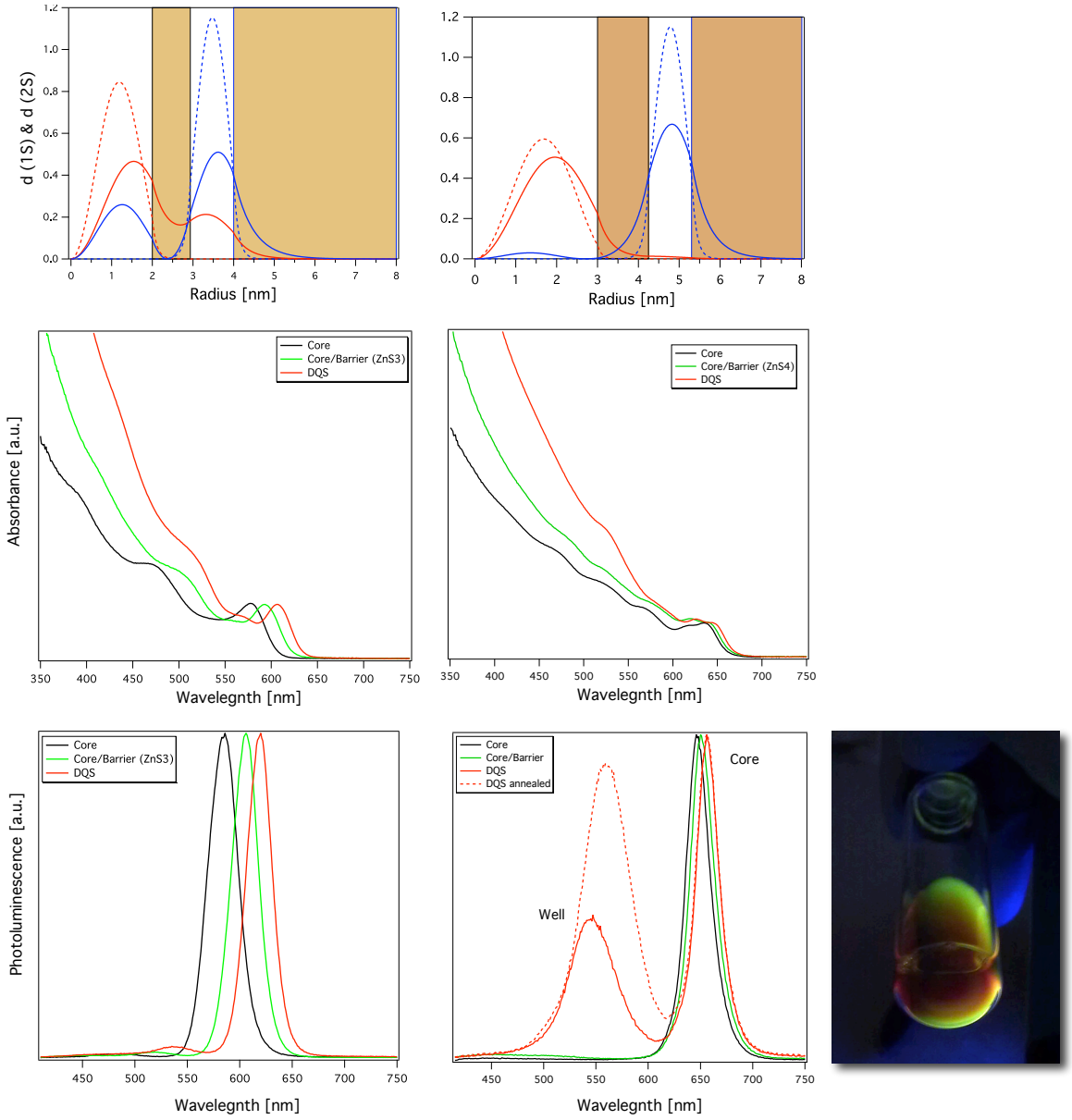

Figure 5.16 Calculated density probabilities (top), normalised absorption spectra (middle) and corresponding PL spectra (bottom) of DQS samples with a 2 *nm* CdSe core radius / 3 ML ZnS barrier (left column) and a 3.2 *nm* core radius / 4 ML barrier (right column). The outer CdSe well has a thickness of 2 ML for both samples. The solid and dashed traces in the top plots assign the electron and hole densities respectively, while red and blue color codes represent the $1S$ and $2S$ excitons accordingly. The absorbance and emission spectra are taken at different stages of the reaction: Cores (black), after ZnS barrier growth (green) and after final CdSe well growth (red). The PL spectra were recorded under excitation at 400 *nm*. The photograph shows the dual–emitting NCs dispersed in chloroform under UV excitation.

Upon growth of the CdSe outer well, a substantial gain in absorbance below $\sim 525\ nm$ was detected. This increase was assigned to the absorption onset of the 2D well system, in accordance with the results by Battaglia et al. [16]. Another viable explanation for the increase at this spectral region could be the formation of homogeneous nuclei. However this possibility could be ruled out through HRTEM analysis exhibiting just one population of particles. The possibility of absorbance from reaction by–products was also dismissed as no changes were observed after purification of the particles.

The band edge absorption of the system with the smaller core size was further red-shifting after the CdSe well growth which supports the fact that the core exciton is not sufficiently confined and can expand beyond the barrier into the outer well. In contrast, the absorption of the large core sample with a slightly thicker ZnS barrier stays virtually constant. Comparing the PL spectra of those two samples, it was experimentally found, that this lack of core exciton confinement correlates directly with the extent of the second emission feature from the 2D exciton. Following the CdSe well growth, only a weak feature along with a further $\sim$10 nm red-shift of core emission was found in the case of the small core sample. In contrast, a well resolved second emission peak emerges at higher energies for the large core sample. With prolonged annealing at 240 $°C$ a significant increase of its intensity relative to the core peak along with a progressive red shift was detected. The boost in intensity is likely a result of reduced crystal defects and improved ligand surface coverage. The mechanism of the observed red shift is not completely understood. However a possible explanation could be a reduction in band gap offset at the barrier/well interface with continuous annealing. As the atomic rearrangement improves the epitaxy at the interface, the lattice parameters of the two materials approach each other, effectively reducing the potential offset. This would result in a diminished confinement in the well region which is experimentally observed as a red shift in emission. The different optical response of these two samples is in accordance with the theoretical density distributions. While the $1S$ and $2S$ electron densities of the small core sample are delocalised over the whole system (and likely to interact), they are well confined and separated in the large core structures enabling independent exciton recombination.

As shown on the photograph of Figure 5.16, both PL colours of the dual–emitting particles in solution can be observed when excited under UV light. This phenomenon can be explained through re–absorption effects. Close to the inner wall of the vial, the path length of emitting photons is short and the well emission (green) is readily observable. However, in the center of the solution the well emission has a high probability of being re–absorbed by the surrounding NCs and only the core emission (red) is visible.

Further evidence for the independence of the 0D and 2D exciton recombination centres is given by photoluminescence excitation (PLE) and lifetime decay spectra taken from the PL maxima of core and well emission of the large–core DQS sample (see Figure 5.17). The

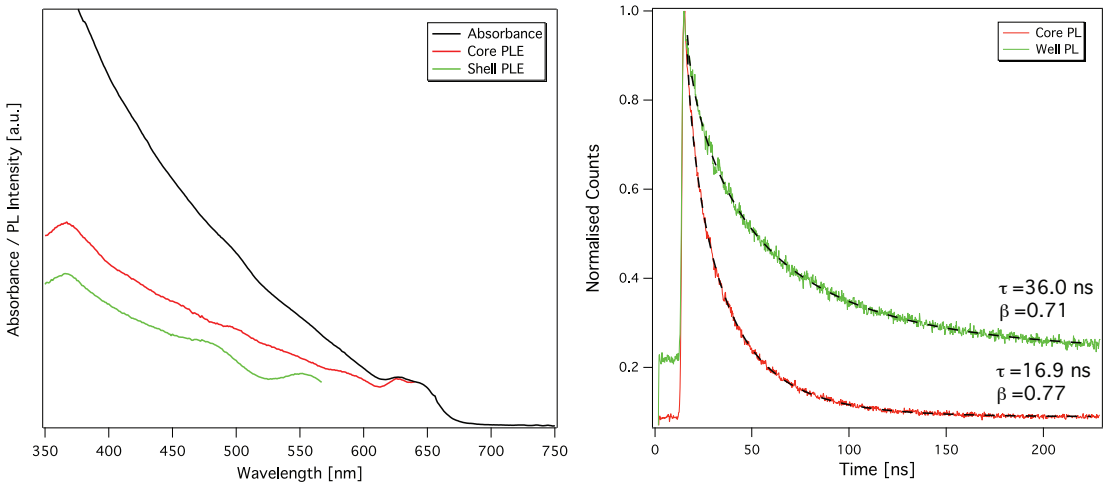

Figure 5.17 Left: Absorption and PLE spectra for the 3.2 nm CdSe core radius / 4 ML ZnS barrier / 2 ML CdSe well sample. Right: Lifetime traces of the same sample, taken from the core and well emission bands. The β and τ values were obtained from stretched exponential fits of those traces.

PLE spectra (red and green lines) of the two PL peaks support that the low–energy peak is associated with the core exciton and the high–energy one with the well exciton, exhibiting step like features of a 2D confinement system [15]. The PLE of the core PL peak followed the absorption spectrum (black line) at the low–energy part and showed significantly low intensity at the high–energy region, where the absorbance of the 2D well system resided. The different features in the core and well PLE traces are a strong indicator that the 0D and 2D exciton recombinations arise from independent states.

The uncorrelated nature of the two recombination channels was also supported by the fluorescence lifetime analysis of the two emission peaks. While both decay traces exhibit a similar β value, the well exciton decay time with 36 ns is more than twice as long as the core decay of $\sim$ 17 ns. If the two emission states would be coupled to some degree, one would expect to observe very similar lifetimes, unlike the observations presented here. Since the lifetime is related to the localisation of electron and hole, the longer decay time in the well can be explained by a higher delocalisation of the $2S$ charge carriers in the two–dimensional confinement system. Moreover, the EMA simulations indicate, that the $2S$ electron is generally stronger delocalised than its $1S$ counterpart which could also account for the significant difference in lifetimes.

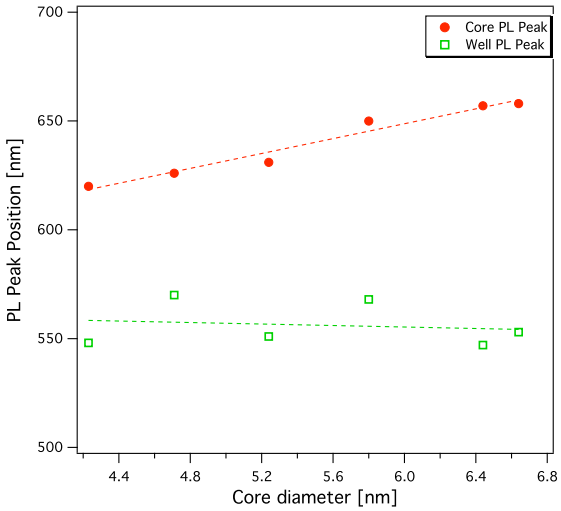

Figure 5.18 The effect of CdSe core size on the final energies of core (red) and well (green) emission bands.

5.5.3 Effects of Core Size and Barrier

The theoretical calculations presented previously permitted insights into the effects of core size and barrier thickness on charge carrier localisation within the DQS heterostructure. However due to the mentioned approximations of the EMA model, it was not possible to predict accurate exciton energies or further photo–physical properties. The experimentally observed effect of CdSe core size on the final emission energies of core and well exciton recombination is displayed in Figure 5.18. The final peak emission of the core emission band follows a linear behaviour with increasing core size in accordance with the results by Battaglia et al. [16]. In contrast, no distinct trend could be observed considering the well PL.

While the red shifting core emission is expected and well understood, studies on exciton confinement in spherical 2D well systems are rare. Assuming sufficient exciton localisation through the ZnS barrier, the effects of increasing core size on the outer well system should be negligible. A decrease in curvature and a gain in overall volume of the 2D region as a function of core size suggests a confinement reduction which may result in a red–shift of well emission. This is not observed, as the peak energies range from $\sim$ 550–570 nm, but do not correlate with the increasing core diameter. The wide range of detected emission energies can be attributed to the high sensitivity of well confinement on the quality and thickness of the few atomic monolayer region, whose outcome is prone to slight variations between reactions.

Next to the core size, the effect of the barrier was experimentally investigated. Figure 5.19 depicts the behaviour of lifetime (left) an emission energies (right) as a function of intermediate barrier type. All three structures were grown from the same CdSe nanocrystal batch with a

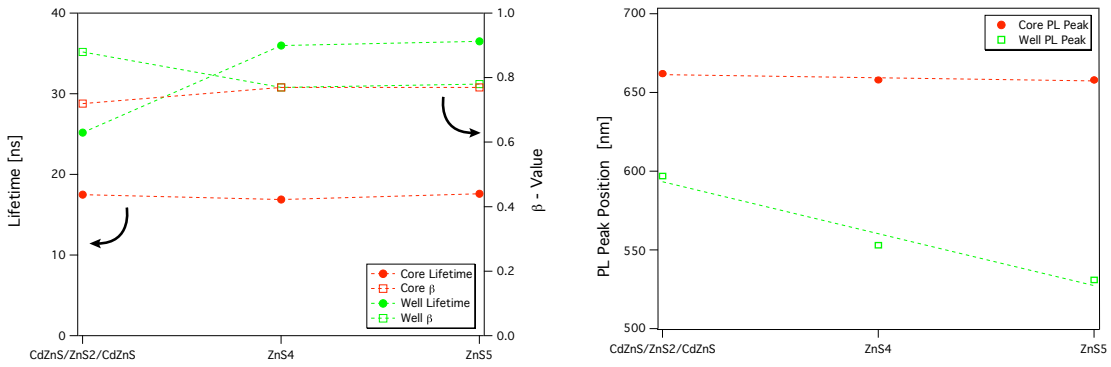

Figure 5.19 The effect of barrier type on the final fluorescence lifetime (left) and emission energies (right) of radiative exciton recombination in core (red) and well (green).

mean particle diameter of 6.4 *nm*. In this study a *graded* CdZnS/ZnS/CdZnS barrier with two central ZnS monolayers was compared to the traditional pure ZnS systems. The Hybrid CdZnS layers with a 1:1 ratio of Cd:Zn were introduced to mediate the lattice strain at the CdSe interfaces and facilitate epitaxial shell deposition. Earlier studies [32] showed that such a graded transition in core/multishell heterostructures can lead to enhanced epitaxy and improved uniformity in shell deposition. However, due to the introduction of cadmium into those layers, one would also expect a hybridised band gap falling in between the values of CdS and ZnS, effectively reducing the conduction and valence band offset relative to CdSe.

The lifetime analysis reveals that the recombination kinetics in the core domain are largely unaffected by changes in the barrier thickness or potential with values of ∼17 *ns* and β–values of ∼0.75 for all samples. On the other hand, the fluorescence lifetime of well emission shows a distinct dependence on the barrier type between the graded and traditional barrier, while being virtually identical with increasing barrier thickness from 4 to 5 ML of ZnS. The higher β–value (0.88) of the graded barrier compared to the pure ZnS shell (0.77) indicates a reduction of recombination channels which can be related to a lower number of available trap states due to the improved epitaxy. As the total decay rate is a sum of radiative and non–radiative decay rates

$$\Gamma_{tot} = \Gamma_{rad} + \Gamma_{nrad} \quad , \tag{5.4}$$

the reduction of fast non–radiative recombination channels should result in a longer observed mean lifetime. This is in stark contrast with the detected value of ∼25 *ns* compared to a mean LT of ∼36 *ns* for pure ZnS barrier nanocrystals. To model the graded barrier system was beyond the scope of this work as it required to simulate four additional boundaries. The shortened radiative lifetime in graded barrier DQS particles suggests an enhanced electron–hole

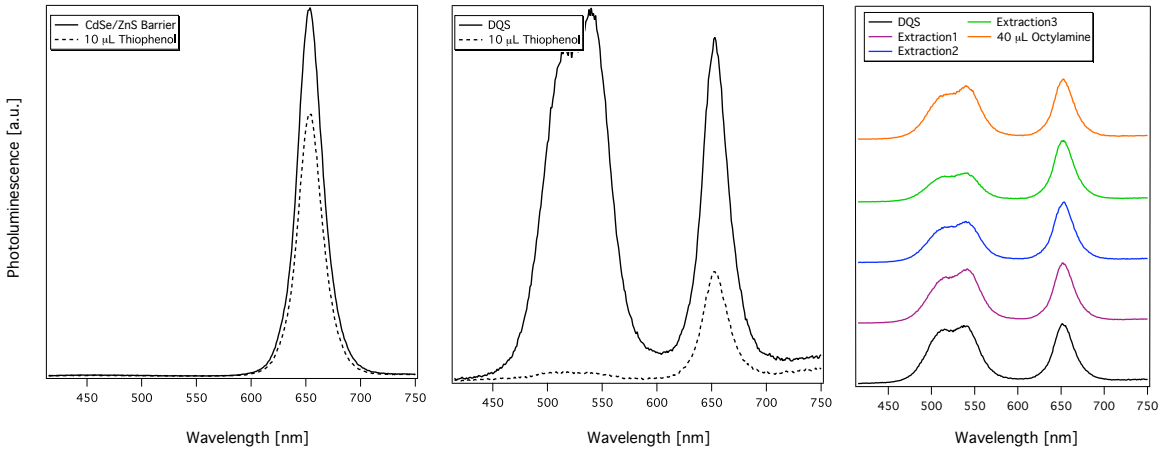

Figure 5.20 PL spectra of CdSe/ZnS (left) and CdSe/ZnS/CdSe DQS (center) nanocrystals both before and after the addition of 10 μL thiophenol. Right: PL spectra of the DQS sample after several purification steps and the addition of 10 μL octylamine.

overlap in the well of those structures, however to establish a mechanism for this behaviour further studies are required.

Photoluminescence spectra of the three DQS structures confirmed the independence of core excitons on barrier type and thickness. For all samples the emission peak was detected at ∼660 nm within experimental error. In contrast, an evident dependence of well emission energy as a function of barrier potential was observed. From the graded 4 ML barrier over the 4 ML pure ZnS barrier to a 5 ML ZnS barrier, the first appearance of well emission gradually blue shifted indicating an increase in exciton confinement in the well region. This can be explained by the enhanced charge carrier localisation with increasing barrier potential, in accordance with the calculations for different ZnS barrier thicknesses.

5.5.4 Effects of Post–Synthetic Treatment

In general the well emission was found to be highly sensitive to any post–synthetic treatment, which is expected as the surface constitutes the majority of the 2D well region. Figure 5.20 illustrates the optical response upon addition of thiophenol, octylamine and repeated washing. The ability of high band gap shells to insulate the core from its local environment can be tested by PL spectroscopy through the use of quenching agents that absorb to the NC surface. Any detected drop in PL upon addition of the quencher is direct consequence of charge tunnelling through the shell. Therefore the extent of quenching reflects the efficiency of the shell to confine the charge carriers.

The left and middle spectra of Figure 5.20 show PL traces of the same heterostructure after barrier (4 ML ZnS) and well growth (2 ML CdSe) respectively. To both samples 10 μL

thiophenol were added and allowed to establish equilibrium for $\sim 15\ min$ before the PL was monitored again. In both cases a distinct drop in emission intensity was observable, however the PL of the core/barrier particles decreased only by ∼30 % whereas in the DQS the core emission dropped by ∼80 % and the well PL was completely quenched. The drastic effect on the well emission is expected as the thiol quencher binds effectively to cadmium sites and has direct access to the unprotected well surface. However the increased quenching efficiency of core emission in the DQS sample is somewhat surprising, as one would expect the opposite as a result of additional shell thickness between the core and the surface. Although the exact mechanism for this behaviour is unknown, the simulations presented previously could provide a feasible explanation. As shown in Figure 5.4, growth of the CdSe well actually facilitates the delocalisation of charge carriers from the core into the well region, given they posses a sufficient probability to tunnel through the barrier. TEM analysis revealed that the growth of thick ZnS shells is not quantitative and the actual barrier thickness is below the theoretically predicted one. Following these arguments, the increased quenching efficiency of the core emission in DQS particles compared to the core/barrier sample would be explicable by the promoted charge carrier delocalisation upon well growth.

Another method to highlighted the sensitivity of well emission in regards to surface ligand passivation is shown in the right plot of Figure 5.20. In this experiment PL spectra were taken after several washing steps and the addition of octylamine. As discussed in Chapter 1, surface ligand passivation of bare CdSe cores with amines results in the removal of non–radiative recombination sites effectively enhancing their luminescence. Since those capping ligands only bind reversibly to the NC surface, a PL decline upon purification is observed. This trend was confirmed as the well emission declined progressively following repeated extractions, whereas the core emission remained unaffected by this treatment. After addition of 10 μL octylamine, effectively re–passivating the particle surface, the well PL band could be mostly recovered.

This surface sensitivity made the particles extremely difficult to utilise for any optical applications that required substantial dilution or thorough purification. Attempts to passivate the outer CdSe well with another ZnS shell were successful to some degree. However a substantial red shift was detected upon ZnS growth resulting in an increased overlap of well and core emission.

5.6 Conclusion

This chapter constitutes a comprehensive report on the theoretical and experimental investigations of a Dual Quantum System based on a CdSe/ZnS/CdSe core/barrier/well model structure. Exploring a wide parameter space of core sizes, barrier and well thicknesses by means of an EMA model, Section 5.3 presented the various effects of these structural features

on charge carrier localisation. This study yielded the fundamental requirements to successfully observe dual–emission. The synthesis of these complex heterostructures posed multiple challenges, due to the adverse effects of low particle surface reactivity and large lattice mismatch. It was found that a generally high amine concentration, oleate metal precursors as well as reaction temperatures above 240 $°C$ were imperative to achieve appreciable shell growth. The optical studies presented in Figure 5.16 highlight the importance of large cores to efficiently contain the $1S$ exciton in order to observed dual–emission. PLE and lifetime analysis of the two PL bands arising from core and well strongly support the uncorrelated nature of the two recombination channels (see Figure 5.17). Studying the effects of core size and barrier width, the PL band of the core emission exhibited the expected correlation to core size while being independent from the barrier width. Interestingly, the opposite behaviour was found to be true for the PL emission band arising from the well region. Finally, post–synthetic treatment revealed the high surface sensitivity of DQS particles, rendering the well emission feature extremely unstable. This drawback must be addressed in further investigations in order to make these materials suitable for any practical applications.

Bibliography

[1] A. Mews, A. Eychmueller, M. Giersig, D. Schooss and H. Weller. Journal of Physical Chemistry **98**, 934 (1994).

[2] A. Eychmüller, A. Mews and H. Weller. Chemical Physics Letters **208**, 59 (1993).

[3] H. Borchert, D. Dorfs, C. McGinley, S. Adam, T. Moller, H. Weller and A. Eychmuller. Journal of Physical Chemistry B **107**, 7486 (2003).

[4] F. Koberling, A. Mews and T. Basché. Physical Review B **60**, 1921 (1999).

[5] R. Little, C. Burda, S. Link, S. Logunov and M. A. El-Sayed. Journal of Physical Chemistry A **102**, 6581 (1998).

[6] A. Mews, A. V. Kadavanich, U. Banin and A. P. Alivisatos. Physical Review B **53**, R13242 (1996).

[7] V. F. Kamalov, R. Little, S. L. Logunov and M. A. El-Sayed. The Journal of Physical Chemistry **100**, 6381 (1996).

[8] K. Chang and J.-B. Xia. Physical Review B **57**, 9780 (1998).

[9] W. Jaskólski and G. W. Bryant. Physical Review B **57**, R4237 (1998).

[10] G. W. Bryant. Physical Review B **52**, R16997 (1995).

[11] D. Schooss, A. Mews, A. Eychmüller and H. Weller. Physical Review B **49**, 17072 (1994).

[12] W. W. Yu and X. Peng. Angewandte Chemie International Edition **41**, 2368 (2002).

[13] Z. A. Peng and X. Peng. Journal of the American Chemical Society **123**, 183 (2001).

[14] J. J. Li, Y. A. Wang, W. Guo, J. C. Keay, T. D. Mishima, M. B. Johnson and X. Peng. Journal of the American Chemical Society **125**, 12567 (2003).

[15] D. Battaglia, J. J. Li, Y. Wang and X. Peng. Angewandte Chemie International Edition **42**, 5035 (2003).

[16] D. Battaglia, B. Blackman and X. Peng. Journal of the American Chemical Society **127**, 10889 (2005).

[17] H. V. Demir, S. Nizamoglu, E. Mutlugun, T. Ozel, S. Sampra, N. Gaponik and A. Eychmüller. Nanotechnology **19**, 335203 (2008).

[18] S. Nizamoglu, E. Mutlugun, T. Ozel, H. V. Demir, S. Sapra, N. Gaponik and A. Eychmuller. Applied Physics Letters **92**, 113110 (2008).

[19] S. Sapra, S. Mayilo, T. A. Klar, A. L. Rogach and J. Feldmann. Advanced Materials **19**, 569 (2007).

[20] S. Nizamoglu and H. V. Demir. Opt. Express **16**, 3515 (2008).

[21] B. O. Dabbousi, J. Rodriguez-Viejo, F. V. Mikulec, J. R. Heine, H. Mattoussi, R. Ober, K. F. Jensen and M. G. Bawendi. Journal of Physical Chemistry B **101**, 9463 (1997).

[22] S.-H. Wei and A. Zunger. Applied Physics Letters **72**, 2011 (1998).

[23] H. Fu, L.-W. Wang and A. Zunger. Physical Review B **57**, 9971 (1998).

[24] J. Schrier and L.-W. Wang. Physical Review B (Condensed Matter and Materials Physics) **73**, 245332 (2006).

[25] L.-W. Wang. Physical Review Letters **88**, 256402 (2002).

[26] S. Yang, D. Prendergast and J. B. Neaton. Nano Letters **10**, 3156 (2010).

[27] A. M. Smith, A. M. Mohs and S. Nie. Nature Nanotechnology **4**, 56 (2009).

[28] J. Berezovsky, O. Gywat, F. Meier, D. Battaglia, X. Peng and D. D. Awschalom. Nat Phys **2**, 831 (2006).

[29] C. Bullen and P. Mulvaney. Langmuir **22**, 3007 (2006).

[30] J. van Embden, J. Jasieniak and P. Mulvaney. Journal of the American Chemical Society **131**, 14299 (2009).

[31] E. A. Dias, A. F. Grimes, D. S. English and P. Kambhampati. Journal of Physical Chemistry C **112**, 14229 (2008).

[32] R. Xie, U. Kolb, J. Li, T. Basche and A. Mews. Journal of the American Chemical Society **127**, 7480 (2005).

[33] C. Bullen, J. van Embden, J. Jasieniak, J. E. Cosgriff, R. J. Mulder, E. Rizzardo, M. Gu and C. L. Raston. Chemistry of Materials **22**, 4135 (2010).

[34] J. van Embden, J. Jasieniak, D. Gomez, P. Mulvaney and M. Giersig. Australian Journal of Chemistry **60**, 457 (2007).

[35] L. S. Li, N. Pradhan, Y. Wang and X. Peng. Nano Letters **4**, 2261 (2004).

[36] H. Liu, J. S. Owen and A. P. Alivisatos. Journal of the American Chemical Society **129**, 305 (2006).

[37] J. van Embden and P. Mulvaney. Langmuir **21**, 10226 (2005).

6 Concluding Remarks

Shell deposition onto semiconductor nanocrystals is certainly proving to be one of the milestones in the synthetic history of quantum dot preparation. The enhanced control over spatial charge carrier localisation in these core/shell heterostructures, not only enables one to significantly improve the stability and photoluminescence properties of bare NCs, but it allows to fundamentally change and extend the optical and electronic characteristics of those materials.

In this thesis, we have explored several core/shell and core/multi–shell material configurations both theoretically and experimentally to extend the understanding of their structure related characteristic. The finite potential well model, presented in Chapter 1, was found to be suitable to qualitatively describe the charge carrier localisation in core and core/shell nanocrystals, with the predicted trends being in good agreement with experimental observations. However, the neglect of lattice mismatch at material interfaces resulted in a significant overestimation of confinement potentials. Here, first–principle atomistic models, which take this mismatch amongst other factors into account, have shown to yield more accurate descriptions.

The fundamental effects of shell growth on the electronic properties of CdSe/CdS Type–I heterostructures were experimentally investigated. Based on established synthetic protocols, which are known to yield accurate and quantitative shell growth, data on a wide range of CdSe core sizes with various CdS shell thicknesses has been reported. The quantitative analysis of the band edge as well as higher order transitions for this parameter space provides a valuable platform from which quantum mechanical models may be developed.

The experimental data presented in this thesis has shown that the epitaxial deposition of uniform shells is an intricate process. Reaction conditions must be strictly controlled at every stage of the synthesis to maintain appreciable deposition rates while preventing uncontrolled growth, leading to the formation of homogeneous nuclei and anisotropic shells. Preparing various core/shell combinations, our results highlight the significant effect of lattice mismatch on the uniformity and optical properties of the final structures. As the degree of this mismatch is inversely related to the band gap offset between materials, this trade–off was found to be one of the major challenges to overcome in the synthesis of high quality Type–I heterostructures.

The presented studies, comparing the structural and confinement characteristics of CdSe/CdS and CdSe/ZnS nanocrystals illustrate this trade–off. While CdSe/CdS systems revealed superior growth uniformity and retention of a narrow size distribution due to a small lattice mismatch, CdSe/ZnS samples offered improved quantum confinement based on the larger

band gap offset relative to CdSe. To remedy this compromise, the graded seal CdSe/CdS/ZnS core/shell/shell structure, presented in Chapter 4, has shown to successfully combine the advantages of both configurations. The presented data, strongly supports the benefits of an intermediate 'buffer' shell to mediate lattice strain, which resulted in improved shell uniformity and extremely bright and stable emitters. Our results clearly point towards the minimisation of internal crystal defects at the material interfaces as one of the key requirements for highly luminescent core/shell quantum dots.

The extrema of charge carrier localisation in complex core/shell heterostructures were explored in a colloidal Dual Quantum System. By means of band gap engineering our results demonstrated the successful formation of two de–coupled exciton recombination centres in one nanocrystal heterostructure, which yielded two well resolved emission bands in the steady state photoluminescence spectrum. The theoretical investigation of this system revealed a delicate balance of structural parameters to by crucial for dual–emission. Although these requirements posed significant synthetic challenges due to large lattice mismatch and low particle reactivity, successful preparation was possible through careful adjustment of the reaction conditions at hand. This proves the powerful flexibility provided by the SILAR layer–by–layer deposition technique.

Given the continuously expanding knowledge on nanocrystal ligand chemistry and the ability to systematically modify the characteristics of core/shell heterostructures, by altering the material combination or structural parameters — such as core size, shell thickness or particle geometry — the preparation of even more complex and highly optimised nano–materials is easily foreseeable.

A Shell Growth Spreadsheet

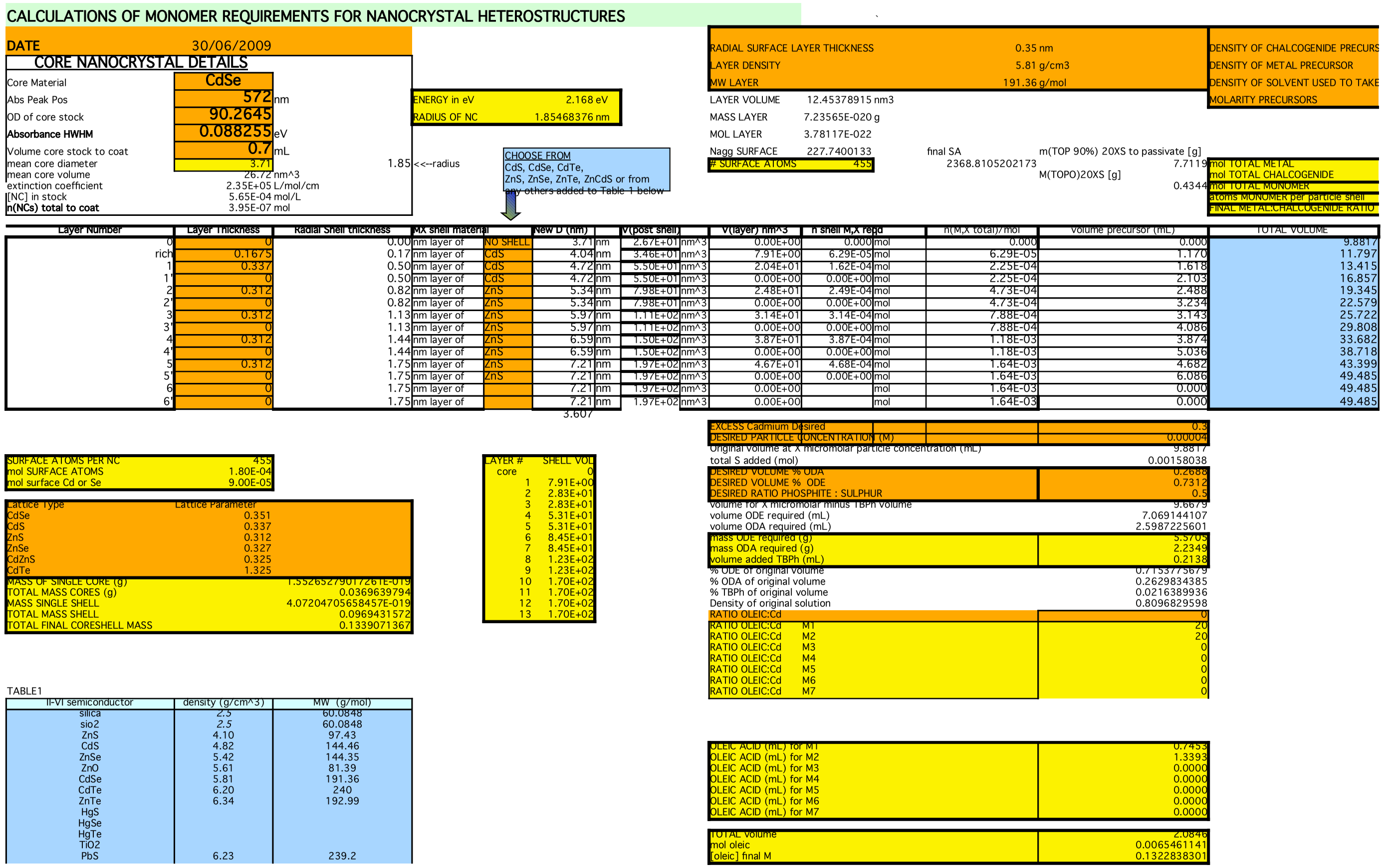

CALCULATIONS OF MONOMER REQUIREMENTS FOR NANOCRYSTAL HETEROSTRUCTURES

DATE 30/06/2009

CORE NANOCRYSTAL DETAILS

Core Material	CdSe	
Abs Peak Pos	572	nm
OD of core stock	90.2645	
Absorbance HWHM	0.088255	eV
Volume core stock to coat	0.7	mL
mean core diameter	3.71	
mean core volume	26.72	nm^3
extinction coefficient	2.35E+05	L/mol/cm
[NC] in stock	5.65E-04	mol/L
n(NCs) total to coat	3.95E-07	mol

1.85 <<--radius

ENERGY in eV 2.168 eV
RADIUS OF NC 1.85468376 nm

CHOOSE FROM
CdS, CdSe, CdTe,
ZnS, ZnSe, ZnTe, ZnCdS or from
any others added to Table 1 below

RADIAL SURFACE LAYER THICKNESS	0.35	nm
LAYER DENSITY	5.81	g/cm3
MW LAYER	191.36	g/mol
LAYER VOLUME	12.45378915	nm3
MASS LAYER	7.23565E-020	g
MOL LAYER	3.78117E-022	
Nagg SURFACE	227.7400133	
# SURFACE ATOMS	455	

final SA
2368.8105202173

m(TOP 90%) 20XS to passivate [g] 7.7119
M(TOPO)20XS [g] 0.4344

DENSITY OF CHALCOGENIDE PRECURS
DENSITY OF METAL PRECURSOR
DENSITY OF SOLVENT USED TO TAKE
MOLARITY PRECURSORS

mol TOTAL METAL
mol TOTAL CHALCOGENIDE
mol TOTAL MONOMER
atoms MONOMER per particle shell
FINAL METAL:CHALCOGENIDE RATIO

Layer Number	Layer Thickness	Radial Shell thickness	MX shell material		New D (nm)		V(post shell)		V(layer) nm^3	n shell M,X reqd		n(M,X total)/mol	Volume precursor (mL)	TOTAL VOLUME
0	0	0.00	nm layer of	NO SHELL	3.71	nm	2.67E+01	nm^3	0.00E+00	0.000	mol	0.000	0.000	9.8817
rich	0.1675	0.17	nm layer of	CdS	4.04	nm	3.46E+01	nm^3	7.91E+00	6.29E-05	mol	6.29E-05	1.170	11.797
1	0.337	0.50	nm layer of	CdS	4.72	nm	5.50E+01	nm^3	2.04E+01	1.62E-04	mol	2.25E-04	1.618	13.415
1'	0	0.50	nm layer of	CdS	4.72	nm	5.50E+01	nm^3	0.00E+00	0.00E+00	mol	2.25E-04	2.103	16.857
2	0.312	0.82	nm layer of	ZnS	5.34	nm	7.98E+01	nm^3	2.48E+01	2.49E-04	mol	4.73E-04	2.488	19.345
2'	0	0.82	nm layer of	ZnS	5.34	nm	7.98E+01	nm^3	0.00E+00	0.00E+00	mol	4.73E-04	3.234	22.579
3	0.312	1.13	nm layer of	ZnS	5.97	nm	1.11E+02	nm^3	3.14E+01	3.14E-04	mol	7.88E-04	3.143	25.722
3'	0	1.13	nm layer of	ZnS	5.97	nm	1.11E+02	nm^3	0.00E+00	0.00E+00	mol	7.88E-04	4.086	29.808
4	0.312	1.44	nm layer of	ZnS	6.59	nm	1.50E+02	nm^3	3.87E+01	3.87E-04	mol	1.18E-03	3.874	33.682
4'	0	1.44	nm layer of	ZnS	6.59	nm	1.50E+02	nm^3	0.00E+00	0.00E+00	mol	1.18E-03	5.036	38.718
5	0.312	1.75	nm layer of	ZnS	7.21	nm	1.97E+02	nm^3	4.67E+01	4.68E-04	mol	1.64E-03	4.682	43.399
5'	0	1.75	nm layer of	ZnS	7.21	nm	1.97E+02	nm^3	0.00E+00	0.00E+00	mol	1.64E-03	6.086	49.485
6	0	1.75	nm layer of		7.21	nm	1.97E+02	nm^3	0.00E+00		mol	1.64E-03	0.000	49.485
6'	0	1.75	nm layer of		7.21	nm	1.97E+02	nm^3	0.00E+00		mol	1.64E-03	0.000	49.485
					3.607									

SURFACE ATOMS PER NC	455
mol SURFACE ATOMS	1.80E-04
mol surface Cd or Se	9.00E-05

Lattice Type	Lattice Parameter
CdSe	0.351
CdS	0.337
ZnS	0.312
ZnSe	0.327
CdZnS	0.325
CdTe	1.325

MASS OF SINGLE CORE (g)	1.55265279017261E-019
TOTAL MASS CORES (g)	0.0369639794
MASS SINGLE SHELL	4.07204705658457E-019
TOTAL MASS SHELL	0.0969431572
TOTAL FINAL CORESHELL MASS	0.1339071367

LAYER #	SHELL VOL
core	0
1	7.91E+00
2	2.83E+01
3	2.83E+01
4	5.31E+01
5	5.31E+01
6	8.45E+01
7	8.45E+01
8	1.23E+02
9	1.23E+02
10	1.70E+02
11	1.70E+02
12	1.70E+02
13	1.70E+02

EXCESS Cadmium Desired	0.3
DESIRED PARTICLE CONCENTRATION (M)	0.00004
Original volume at X micromolar particle concentration (mL)	9.8817
total S added (mol)	0.00158038
DESIRED VOLUME % ODA	0.2688
DESIRED VOLUME % ODE	0.7312
DESIRED RATIO PHOSPHITE : SULPHUR	0.5
volume for X micromolar minus TBPh volume	9.6679
volume ODE required (mL)	7.069144107
volume ODA required (mL)	2.5987225601
mass ODE required (g)	5.5705
mass ODA required (g)	2.2349
volume added TBPh (mL)	0.2138
% ODE of original volume	0.7153775679
% ODA of original volume	0.2629834385
% TBPh of original volume	0.0216389936
Density of original solution	0.8096829598
RATIO OLEIC:Cd	0
RATIO OLEIC:Cd M1	20
RATIO OLEIC:Cd M2	20
RATIO OLEIC:Cd M3	0
RATIO OLEIC:Cd M4	0
RATIO OLEIC:Cd M5	0
RATIO OLEIC:Cd M6	0
RATIO OLEIC:Cd M7	0

OLEIC ACID (mL) for M1	0.7453
OLEIC ACID (mL) for M2	1.3393
OLEIC ACID (mL) for M3	0.0000
OLEIC ACID (mL) for M4	0.0000
OLEIC ACID (mL) for M5	0.0000
OLEIC ACID (mL) for M6	0.0000
OLEIC ACID (mL) for M7	0.0000

TOTAL volume	2.0846
mol oleic	0.0065461141
[oleic] final M	0.1322838301

TABLE1

II-VI semiconductor	density (g/cm^3)	MW (g/mol)
silica	*2.5*	60.0848
sio2	*2.5*	60.0848
ZnS	4.10	97.43
CdS	4.82	144.46
ZnSe	5.42	144.35
ZnO	5.61	81.39
CdSe	5.81	191.36
CdTe	6.20	240
ZnTe	6.34	192.99
HgS		
HgSe		
HgTe		
TiO2		
PbS	6.23	239.2

Figure A.1 The Excel spreadsheet utilised for SILAR shell deposition.

B Excitation Dependence of Single Particle Photoluminescence

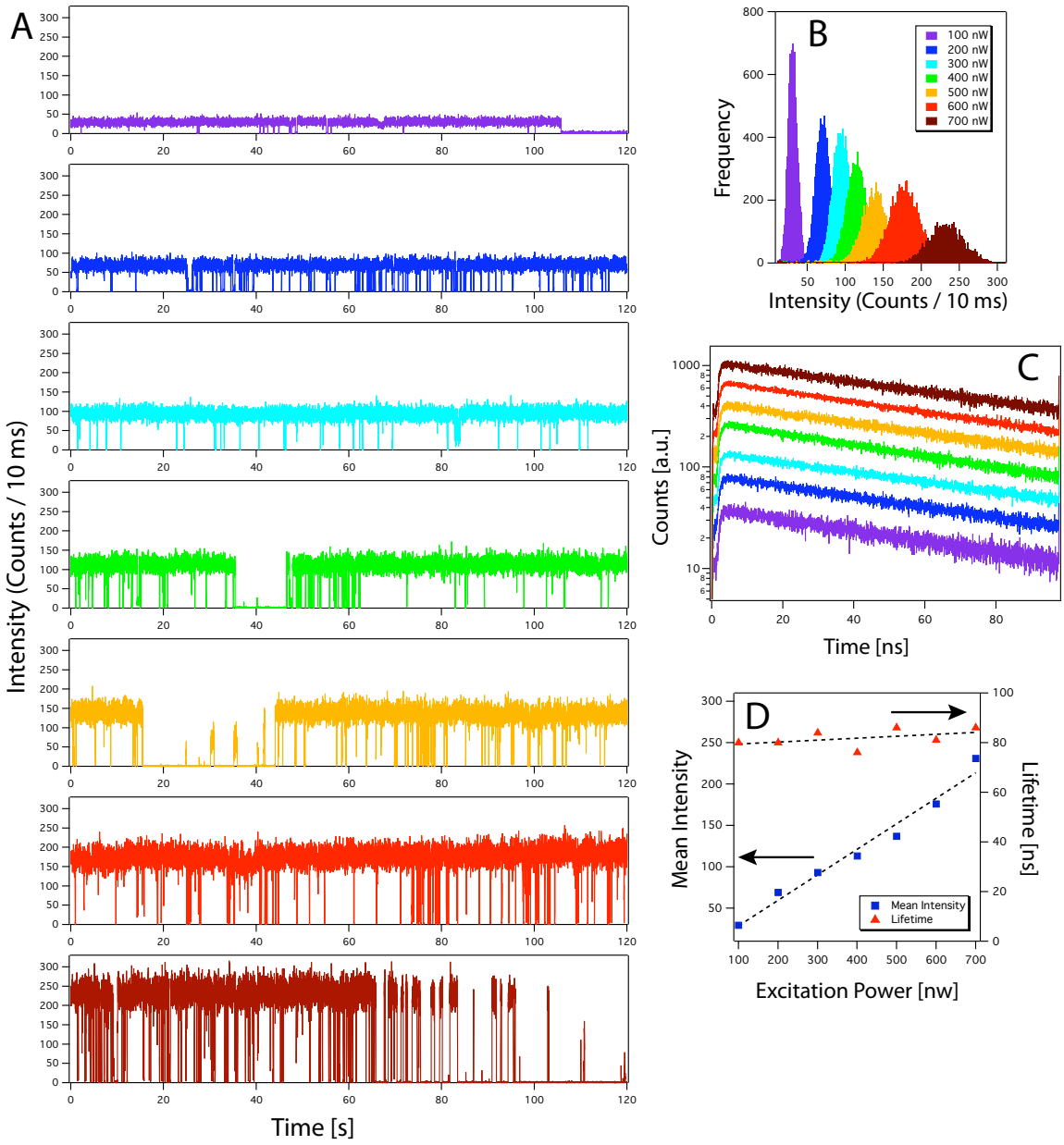

Figure B.1 Collected photoluminescence time trajectories from the same single CdSe/CdS/ZnS nanocrystal at different excitation powers. The traces from top to bottom were successively recorded with increasing excitation power from 100 nW to 800 nW in 100 nW steps ($\lambda_{exc} = 466\ nm$).

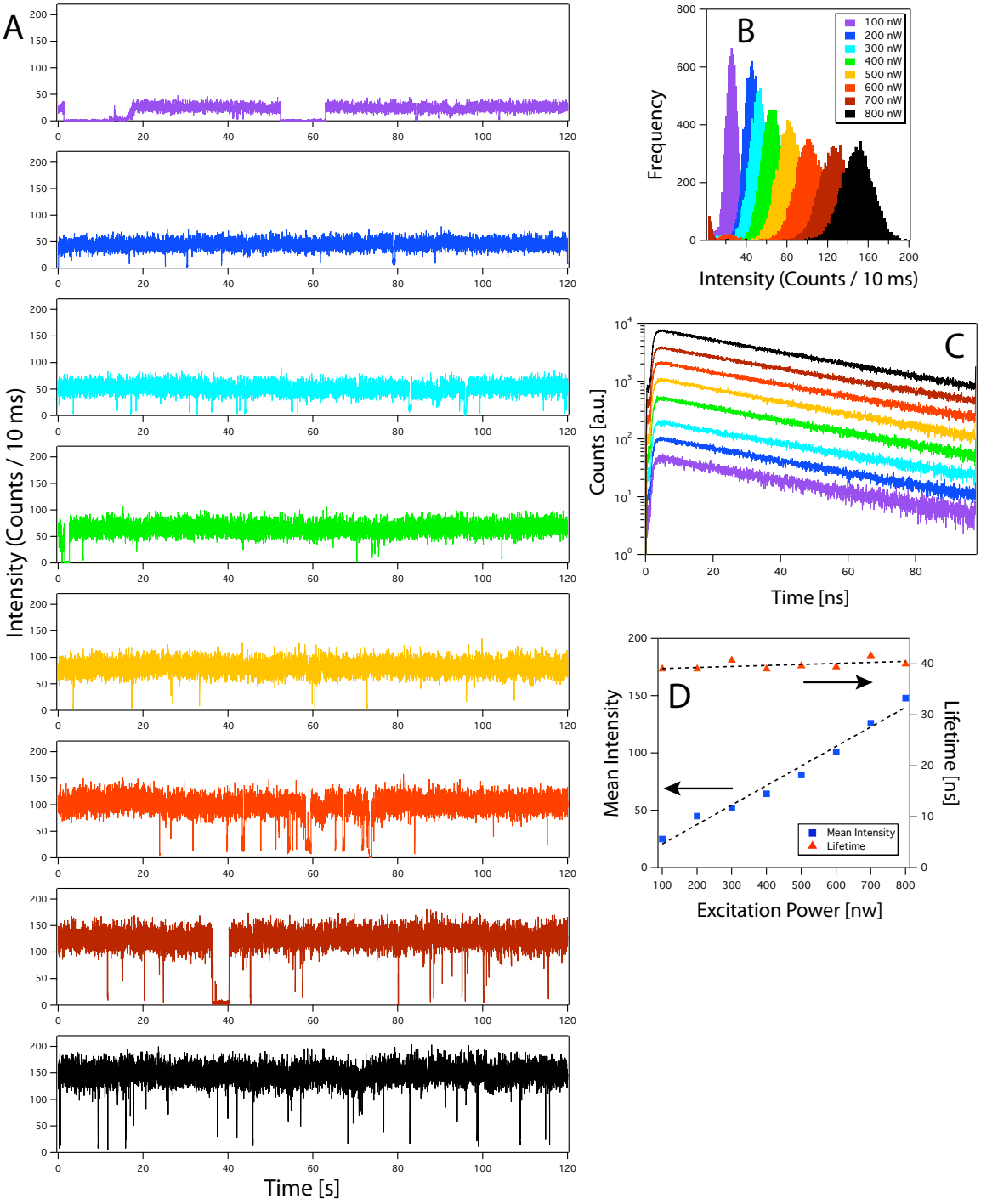

Figure B.2 Collected photoluminescence time trajectories from the same single CdSe/CdS/ZnS nanocrystal at different excitation powers. The traces from top to bottom were successively recorded with increasing excitation power from 100 nW to 800 nW in 100 nW steps ($\lambda_{exc} = 466\ nm$).

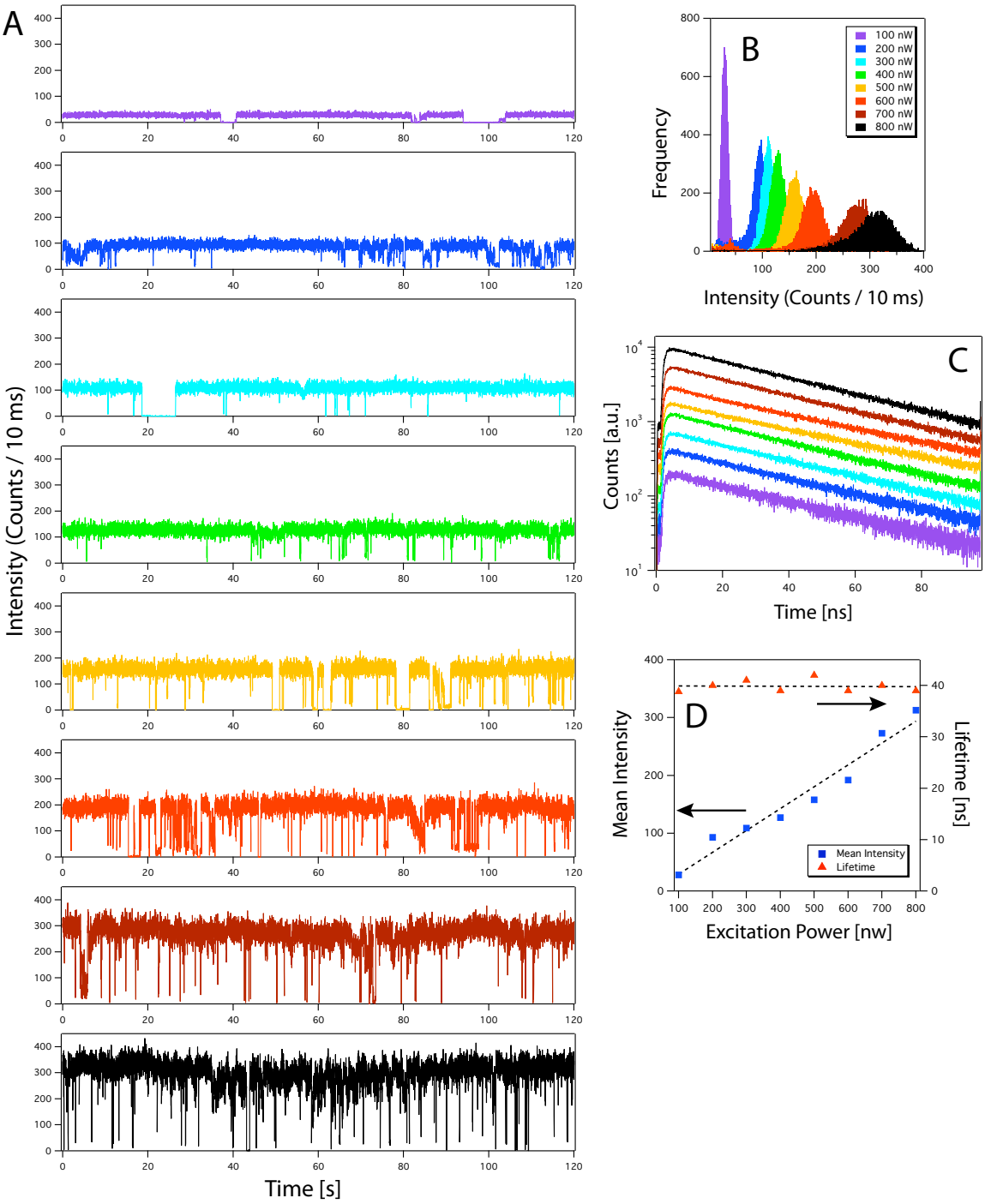

Figure B.3 Collected photoluminescence time trajectories from the same single CdSe/CdS/ZnS nanocrystal at different excitation powers. The traces from top to bottom were successively recorded with increasing excitation power from 100 nW to 800 nW in 100 nW steps ($\lambda_{exc} = 466\ nm$).

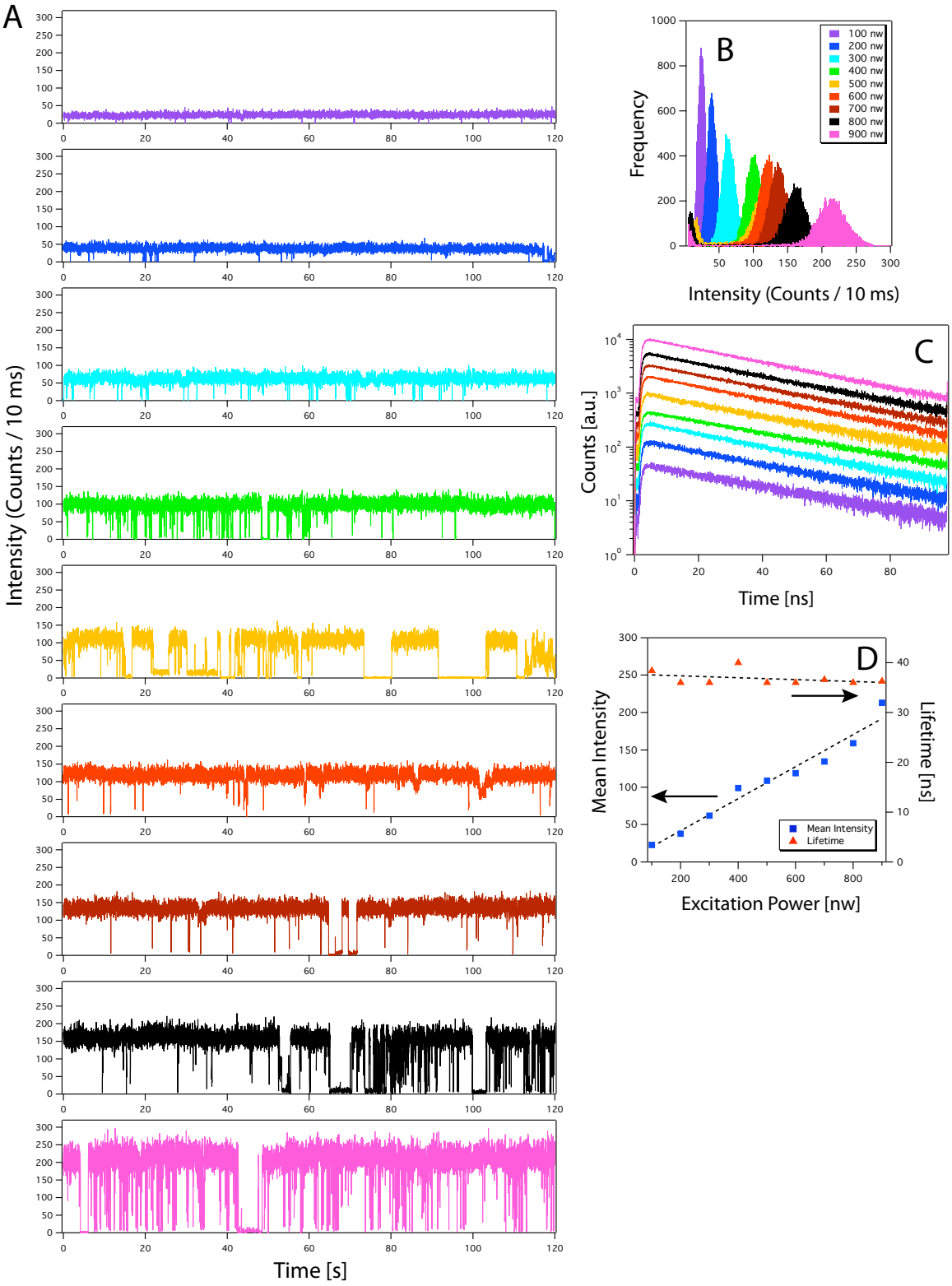

Figure B.4 Collected photoluminescence time trajectories from the same single CdSe/CdS/ZnS nanocrystal at different excitation powers. The traces from top to bottom were successively recorded with increasing excitation power from 100 nW to 800 nW in 100 nW steps ($\lambda_{exc} = 466\ nm$).